PAUL SCHERRER INSTITUT

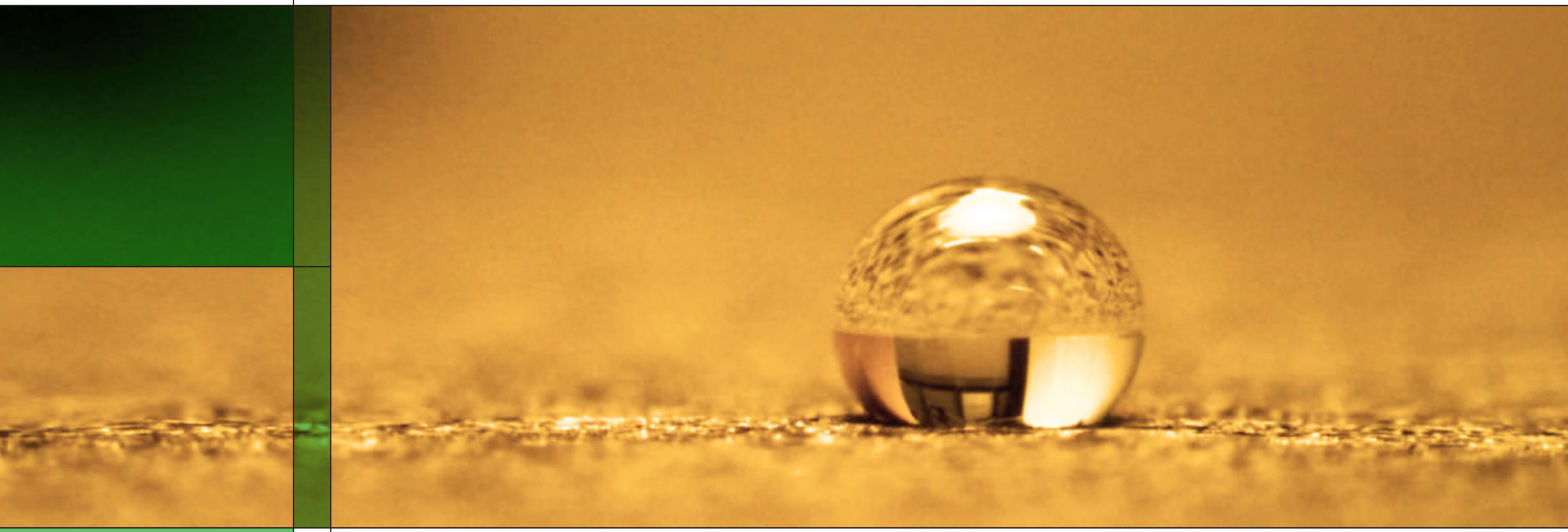

Annual Report 2012

Electrochemistry Laboratory

www.psi.ch/lec

COVER PHOTO:

Water droplet on surface of gas diffusion layer for
fuel cells during contact angle measurement

© Paul Scherrer Institut

DOI: 10.3929/ethz-a-007047464

Electrochemistry Laboratory

Annual Report 2012

Hardcopies of this report are available from:
Cordelia Gloor (cordelia.gloor@psi.ch)
Paul Scherrer Institut
5232 Villigen PSI
Switzerland

A full version of this report is also available on the web:
www.psi.ch/lec

Paul Scherrer Institut
Electrochemistry Laboratory
5232 Villigen PSI
Switzerland

Secretary
Phone +41 56 310 29 19
Fax +41 56 310 44 15

Publisher
Electrochemistry Laboratory
Paul Scherrer Institut
5232 Villigen PSI

Editorial Team
Felix Büchi
Cordelia Gloor
Rüdiger Kötz
Thomas J. Schmidt

Printing
Paul Scherrer Institut

ISSN 1661-5379
DOI: 10.3929/ethz-a-007047464
PSI Electrochemistry Laboratory – Annual Report 2012

© Paul Scherrer Institut

CONTENTS

1 **EDITORIAL**
T.J. Schmidt

2 **THE ELECTROCHEMISTRY LABORATORY AT A GLANCE**

4 **ELECTROCHEMICAL ENERGY RESEARCH FOR A FUTURE ENERGY SYSTEM**

7 **SCIENTIFIC ACHIEVEMENTS 2012**

FUEL CELLS - MATERIALS

9 Performance enhancements of the PSI Gen2 radiation grafted membrane

11 Grafting of glycidyl methacrylate (GMA) onto ETFE and post-sulfonation

13 Investigation of comonomer effects on proton conductivity

15 Analysis of the degree of hydrolysis in styrene / acrylonitrile co-grafted membranes tested in PEFCs

16 Study of the degradation of nitrile containing membranes in PEFC

19 **FUEL CELLS - SYSTEMS & DIAGNOSTICS**

21 Exploring the high power density possiblities of H_2/O_2 PEFC systems

23 Dynamic properties of H_2/O_2 PEFC systems

24 Towards high accuracy water transfer measurement in differential PEFCs

25 Distinction of liquid water and ice based on dual spectrum neutron imaging

27 *In situ* X-ray tomography of PEFC at isothermal freeze – start at -10 ℃

29 Influence of feed gas humidity and current density on the 3D water distribution in PEFC

31 First results of HT-PEFC X-ray tomographic microscopy

32 *In situ* FTIR microscopy measurements in high temperature PEFCs: experiment and first results

33 Spatially resolved start/stop measurements in high temperature PEFCs

35 Non-uniform degradation of the catalyst support during fuel cell start-up and shutdown in PEFC

37 Degradation processes at membrane defects in PEFC

39 Local impact of the flow field design onto the PEFC's performance

41 **BATTERIES & SUPERCAPACITORS - MATERIALS**

43 Graphene as electrode material for supercapacitors?

45 Graphene layers supported by partially pyrolized nanodiamonds: a suitable composit material for supercapacitor electrodes?

47 Recent progress on Li-O_2 batteries at PSI

49 Effect of sulphur type and graphitized carbon nanofibers on the performance of Li–S cells

51 New composites for Li-S batteries

52 Influence of conductive carbon additives on the performance of $LiCoO_2$ electrodes

54 Thin-layer electrodes of overlithiated NCM material for model lithium-ion batteries

55 Ageing of overlithiated NCM positive electrode material upon exposure to water vapour

57 Phase boundary alignment in graphite during lithium intercalation

58 New high energy materials for negative electrodes of lithium based batteries

59 **BATTERIES & SUPERCAPACITORS - DIAGNOSTICS**

61 *Ex situ* X-ray absorption spectroscopy on $M_{0.5}TiOPO_4$ (M=Fe, Cu)

63 Investigation of HE-NCM by differential electrochemical mass spectrometry to elucidate reactions occuring at high potentials

65 *In* and *ex situ* Raman microscopy applied to the mechanistic study of HE-NCM

67 Dynamics of ionic liquids in porous carbon electrodes investigated by quasi-elastic neutron scattering

CONTENTS

69 Core level data of ionic liquids: monitoring charging by *in situ* EC XPS

71 ELECTROCATALYSIS & INTERFACES

73 Tin oxide as support for Pt-based oxygen reduction electrocatalysts in PEFC

75 Oxide semiconductor-based catalysts for application as cathode materials in polymer electrolyte fuel cells (PEFCs)

77 Iridium-titanium oxide as a stable support for Pt catalyst in PEFC cathodes

79 Investigation of model Pt catalysts: from nanoparticles to extended surfaces

81 On-line mass spectrometry for electrochemical reduction of CO_2 on copper electrodes

83 Preparation of thin platinum films by pulsed laser deposition

85 THE ELECTROCHEMISTRY LABORATORY - FACTS & NUMBERS

86 Structure 2012

87 ECL-Personnel 2012

88 Dissertations 2012

88 Exchange students, diploma theses, summer students, guest scientists

90 Seminar, invited speakers

91 Awards

92 Conferences – Symposia

94 Review activities of the laboratory

95 Industrial partners

97 Documentation

EDITORIAL

2012 again was a very successful year for PSI's Electrochemistry Laboratory in terms of both organization and scientific research although we also needed to master some challenges. In that respect, the last year can be considered as a transitional year in which existing R&D projects have been successfully finished and, at the same time, new topics and projects have been kicked-off. Within the last 12 months we could seed first projects on water electrolysis within our R&D portfolio. This allows us to address the important question of hydrogen production as a way of chemical energy storage of renewable energy sources making use of our great experience from the field of polymer electrolyte fuel cells. At the same time, we considerably strengthened our research on electrocatalysts for different electrochemical energy conversion systems.

Especially the Section and Group Leaders of the Laboratory succeeded in guiding new researchers and incorporating them into their teams: The Laboratory was growing from 36 employees in January to 48 employees in December 2012, respectively.

Scientifically, we also can report important results. Two PhD students from the laboratory graduated at ETH Zürich (see p. 88) during 2012 and we certainly wish both all the best for their future. At the same time, we have 18 ongoing PhD projects pointing to the major emphasis we are placing on education of students in the field of electrochemical energy conversion and storage. Contributions from PhD students and scientists summarizing our main 2012 achievements can be found in this report. These short communications presented here are the basis of the 43 peer-reviewed papers and book chapters our researchers have been written, demonstrating the impact of the high-level R&D we are performing in the Electrochemistry Laboratory.

The traditional One-Day-Symposium on topics in Electrochemistry which has been held in May 2012 again was well attended from more than 100 interested persons from all over Europe. With the topic *Electrochemistry for Renewable Energy Storage* one of the most important aspects of current and future energy research was addressed by internationally renowned scientists. In the contributions from D. Chartouni (ABB Baden), A. Reiner (Siemens AG Erlangen), R.F. Savinell (Case Western Reserve University, Cleveland), C. Dustmann (Battery Consult, Meiringen), S. Fiechter (Helmholtz Zentrum Berlin), and G. Andersson (ETH Zürich) different views on resolving the prospective mismatch between energy supply and demand on a temporal and regional scale in an energy system using renewable energy sources have been given. At the same time, all speakers pointed to the need of new developments in the energy and electricity storage sector.

Quite clearly, electrochemical energy conversion and storage devices will play a major role for these new developments and, as can be seen by reading through this annual report, our Laboratory, therefore, is perfectly setup to accept these challenges and will also successfully contribute to their future solutions.

Thomas Schmidt

Thomas J. Schmidt

THE ELECTROCHEMISTRY LABORATORY AT A GLANCE

Our Mission

Advancement of electrochemical energy storage and conversion by

- **developing novel electrochemical materials, cells and devices**
- **providing insights into electrochemical materials, cells and device properties**

PSI's Electrochemistry Laboratory is Switzerland's largest Center for Electrochemical Research with around 50 employees. Our mission is to advance the scientific and technological understanding of electrochemical energy storage and conversion specifically in the context of a sustainable energy system, in which renewable energy is required to be stored in secondary batteries or chemicals as e.g., hydrogen and (re-)converted into electricity. Our applied fundamental R & D, hence, is focused on devices like secondary batteries - specifically Li-based systems -, supercapacitors, polymer electrolyte fuel cells and electrolyzers, respectively.

As a research institute's laboratory we are bridging the gap between fundamental science and applied engineering by combining both academically as well as industrially relevant questions. For all outlined devices we not only develop fundamental understanding of materials on atomic and molecular level (electrochemical materials sciences and electrocatalysis), but also on the applied development of technical cells and devices, e.g., fuel cell systems.

On all technical complexity levels, we are developing and utilizing advanced *in situ* diagnostic tools to gain insights on properties and processes from the nanometer to the centimeter scale, respectively, often making use of PSI's unique large scale facilities.

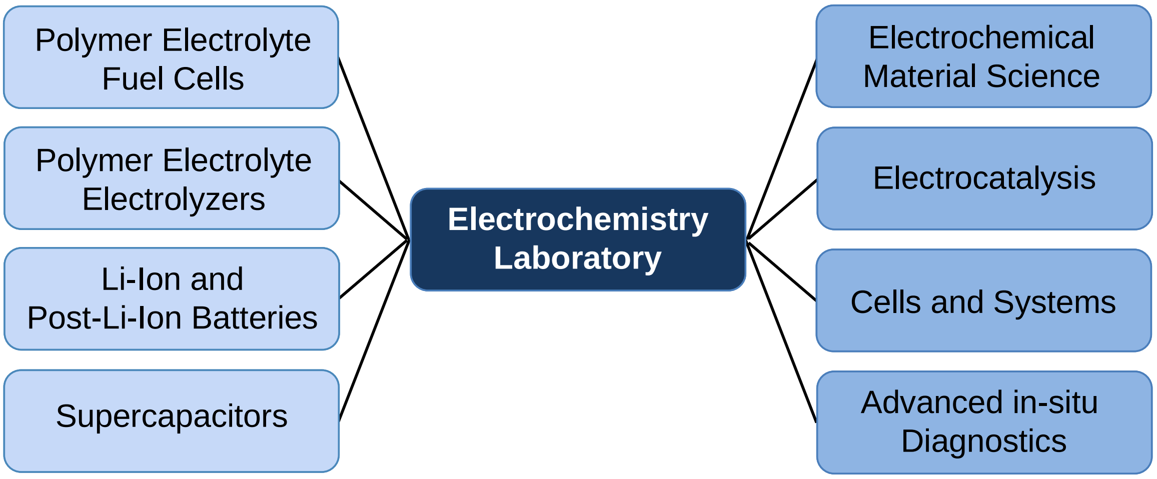
Polymer Electrolyte Fuel Cells
Polymer Electrolyte Electrolyzers
Li-Ion and Post-Li-Ion Batteries
Supercapacitors
Electrochemistry Laboratory
Electrochemical Material Science
Electrocatalysis
Cells and Systems
Advanced in-situ Diagnostics

Electrochemical Energy Storage

The vision of the Electrochemical Energy Storage Section is the development of the best energy storage system.

We work on rechargeable batteries, mainly lithium based. The scientific goal is a profound understanding of electrochemical processes in complex nonaqueous systems. In particular, of utmost scientific interest are the numerous interactions of all components of electrochemical energy storage systems (batteries, supercapacitors, and hybrids) determining the safety and life time of such systems.

Modern multi-channel battery testing facilities.

The work equally considers the synthesis of novel materials for electrochemical energy storage and the modification of known materials (e.g., carbon), and material characterization, keeping in mind the entire span from basic science to industrial applications. To answer the scientific questions, we develop various sophisticated *in situ* methods for use in the field of nonaqueous solid-state electrochemistry and investigate the physical and electrochemical properties of insertion materials and electrochemical interfaces *in situ*. Also, we do electrochemical engineering work on three-dimensional electrodes and characterize industrial batteries and battery systems.

Electrochemical Energy Conversion

The Electrochemical Energy Conversion Section is focused on the development and in-depth understanding of materials, processes and devices for the conversion of renewable energy into electricity or chemical energy carriers. Especially in the context of a sustainable energy system utilizing hydrogen as an energy carrier and its electrochemical energy conversion is of particular importance.

In this topical context our goal is the in-depth understanding of technologies like Polymer Electrolyte Fuel Cells (PEFC), Polymer Electrolyte Electrolyzer Cells (PEEC) for water electrolysis and processes like the co-electrolysis of CO_2 and water, respectively.

The R&D strategy involves activities on four pathways: *i)* system, stack and cell engineering; *ii)* membrane development based on PSI's own radiation-grafting technology and the development of cell components; *iii)* research in electrocatalysis and the reaction kinetics of the important reactions (e.g., the oxygen electrode reactions) for improved understanding of intrinsically limiting factors; and *iv)* the development and application of advanced *in situ* diagnostic tools on stack, cell and component levels including analyses of the electrode-electrolyte interface.

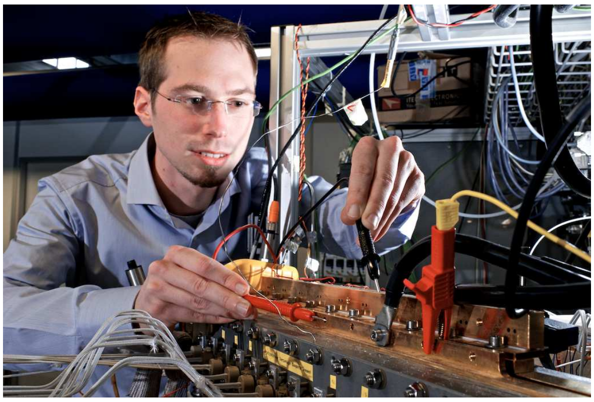

Characterization of a Polymer Electrolyte Fuel Cell with locally resolved analytical tools.

In addition, we are working on new materials for advanced electrochemical double layer capacitors (EDLC), which includes the application of ionic liquids or graphene-type carbons for high power EDLCs.

ELECTROCHEMICAL ENERGY RESEARCH FOR A FUTURE ENERGY SYSTEM

Electrochemical Energy Research becomes an increasingly important field for addressing the challenges of the future energy system consisting largely of intermittent renewable energy. Electrochemical energy storage and conversion are considered to play significant roles and have been both focus areas in PSI's Electrochemistry Laboratory for more than two decades. Our integrated approach on electrochemical materials science, the R&D of components, systems and devices as well as the development of important diagnostic tools in the field of secondary batteries, supercapacitors, polymer electrolyte fuel cells and water electrolysis allows us to significantly contribute to challenges of future energy systems.

The future of the Swiss energy supply, after the nuclear energy phase out, will heavily rely on intermittent renewable energies such as solar or wind. To guarantee the continuous (both temporal and regional), reliable, and cost-efficient supply of power, heat, and fuels derived from these energy sources for Switzerland in a European context, it is critical to develop the science and technology of energy storage and conversion devices for both stationary and mobile applications. While electrochemical energy conversion and storage will play a significant role in this future to allow for energy supply intermittency, the Electrochemistry Laboratory with its over twenty years of experience in these fields will contribute to shaping the future of the overall energy system. Our multidisciplinary and internationally renowned research team combined with an integrated R & D approach on both the fundamentals and applications of secondary batteries, supercapacitors, polymer electrolyte fuel cells, and water electrolysis is the basis for our present and prospective research and development results, respectively.

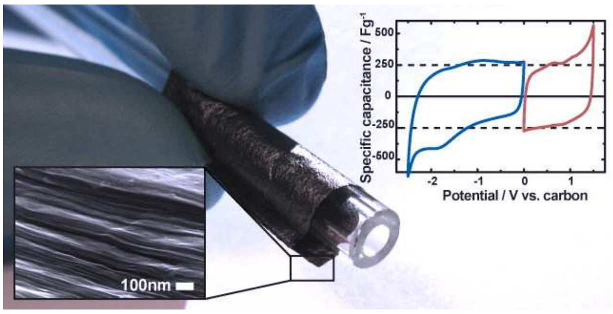

Figure 1. *Electrochemical behavior of 25 μm partially reduced graphite oxide paper electrode, alongside with an electron micrograph, allowing for both high energy and power supercapacitors.*

Materials Development

Electrochemical materials science is one of the key aspects in the development of advanced devices. One of our continuous efforts around the preparation and in-depth understanding of electrodes for supercapacitors resulted in the successful development of 25 μm graphite paper based on partially reduced graphite oxide (a graphene-type material) as self standing, binder-free and flexible electrode allowing for both high energy and power supercapacitors, figure 1 [1].

Besides the energy storage in super-capacitors, our research focus is on next generations of high energy batteries, e.g., the Li-S system. We successfully demonstrated a composite positive electrode material based on graphitized carbon fibers and sulfur with significantly improved cycle life (figure 2).

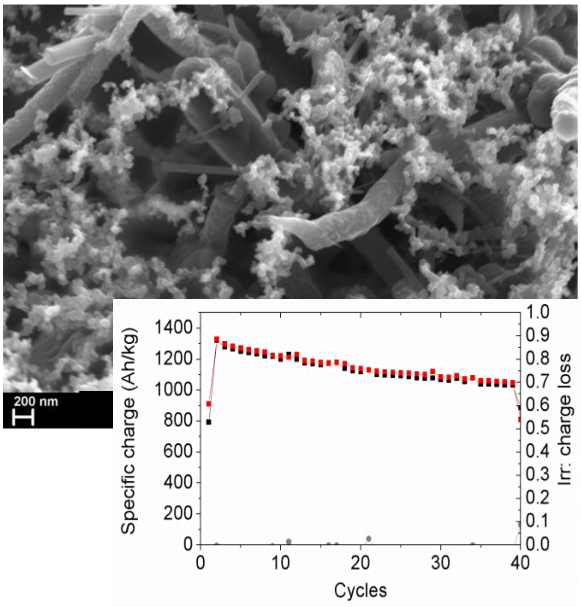

Figure 2. *Cycle stability of our proprietary composite electrode for Li-S batteries shown in the micrograph.*

Over several years, one of our targets has been the development of a low-cost proton conducting membrane for polymer electrolyte fuel cells. Within the ongoing successful collaboration with Belenos CPH, we have leap-frogged several steps in the development in order to achieve technologically important results. Figure 3 illustrates the matching performance of a fuel cell operated with our GEN 2 radiation grafted membrane as compared to DuPont's state-of-the-art Nafion membrane material. At the same time, accelerated *in situ* aging of membrane electrode assemblies (MEA) using potential cycling (strongly oxidizing conditions) resulted in a clear outperforming of stabilized Nafion membranes, with MEAs consisting of our GEN2 membrane still being operational whereas the Nafion-based MEAs all failed in this accelerating aging test.

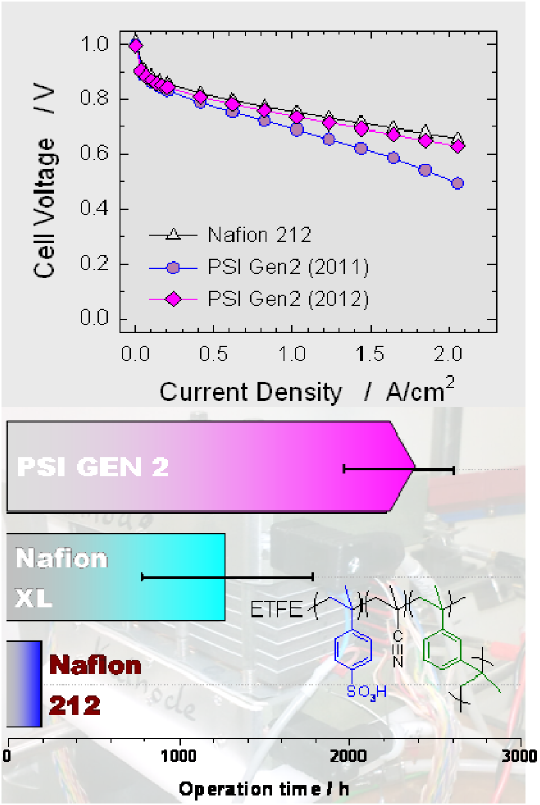

Figure 3. *Performance of our GEN 2 radiation grafted membrane inside a fuel cell as well as its high in situ stability as compared to state-of-the-art Nafion membranes in accelerating aging test.*

In situ Diagnostics

Modern materials development and understanding is only possible with the use of advanced diagnostics tools helping not only to improve materials but also to get insights into relevant failure modes. As an example, figure 4 demonstrates, for the first time, the mechanistic elucidation of an important membrane and MEA failure mode in technical devices upon membrane pin hole formation during fuel cell operation using a combination of x-ray tomographic and infrared microscopy at the respective beamlines of the Swiss Light Source (SLS) [4].

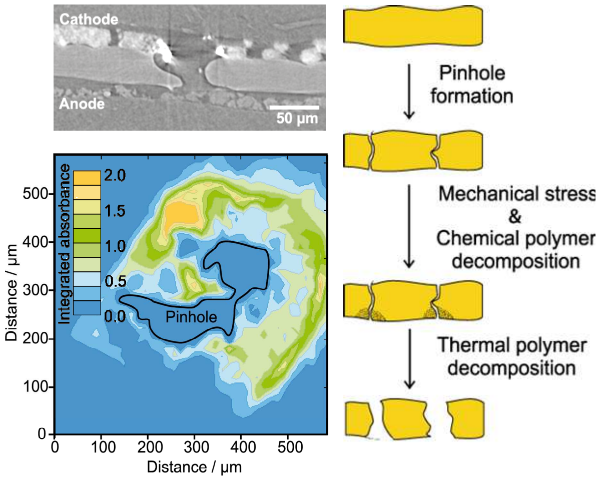
Cathode
Anode
50 µm
Distance / µm
500
400
300
200
100
0
Integrated absorbance
2.0
1.5
1.0
0.5
0.0
Pinhole
0
100
200
300
400
500
Distance / µm
Pinhole formation
Mechanical stress & Chemical polymer decomposition
Thermal polymer decomposition

Figure 4*. Elucidation of membrane pin hole formation inside a fuel cell using a combination of x-ray tomographic and infrared microscopy at the SLS, respectively.*

Conclusion

PSI's Electrochemistry Laboratory is well setup to take the challenge of future R&D of energy conversion and storage, not only by the accumulated experience and know-how of its personnel, but also based on its strategic position within the General Energy Department and PSI with its high-level large scale facilities. At the same time, we are contributing to the future by educating young scientist currently averaging more than 20 doctoral and master students, respectively.

References

[1] PSI Electrochemistry Laboratory - Annual Report 2011, p. 53, DOI: 10.3929/ethz-a-007047464.

[2] S. Kreitmeier, M. Michiardi, A. Wokaun, F.N. Büchi, Factors determining the gas crossover through pinholes in polymer electrolyte fuel cell membranes, Electrochim. Acta (2012) 240-247.

SCIENTIFIC ACHIEVEMENTS 2012

FUEL CELLS

MATERIALS

Performance enhancements of the PSI Gen2 radiation grafted membrane

L. Bonorand, P. Reichel, J. Thut, L. Gubler

phone: +41 56 310 2132, e-mail: lukas.bonorand@psi.ch

For economic viability of polymer electrolyte fuel cells (PEFC), its components, such as the proton exchange membrane (PEM), need to fulfil technical and operational requirements, as well as meet cost targets [1]. State of the art membranes based on perfluorosulfonic acid (PFSA) type chemistries, such as Nafion®, offer excellent performance and durability, but are associated with high cost, owing to the complex fluorine chemistry involved in their synthesis. To face the challenge of meeting low cost requirements, alternative membrane chemistries are subject to ongoing research since many years. Hydrocarbon (HC) membranes, such as sulfonated polyetherketones or polysulfones, offer low cost and are known for their good thermal and mechanical stability, but often suffer from excessive swelling, poor phase separation and lack of conductivity at low relative humidity, making them poor candidates for powering automobiles of the future.

Radiation grafted membranes offer several combined key benefits of PFSA's and hydrocarbon membranes. Similar to PFSA type chemistries, the apolar backbone bearing pendant ionic groups promotes the formation of ionic aggregates which phase separate from the polymer backbone to allow the formation of favorable proton conducting channels. Also, low swelling and hydrolytic stability are key attributes of PFSA and radiation grafted membranes. On the other hand, low cost potential and designability are benefits in line with HC membranes.

However, one drawback of radiation grafted membranes is their sensitivity to preparation steps and processing. These membranes are synthesized via copolymerization of monomers onto pre-irradiated pre-formed dense films. Although an advantage from a manufacturing point of view, this process is sensitive to inhomogeneities of the functionality throughout the thickness of the membrane. Reduced functionality at either the surface or the interior will lead to increased resistance in protonic flux and can therefore reduce the performance of the membrane in an operating fuel cell.

Our 'Generation 2' (Gen2) radiation grafted membrane has demonstrated durabilities in excess of commercial state of the art PFSA membranes (Nafion® XL-100) under simulated vehicle drive cycle conditions [2], as well as has the potential to be an order of magnitude lower in cost than current Nafion® type membranes [3]. This is especially attractive at low production volumes, since the membrane can make up half of the stack cost.

In situ fuel cell performance, however, has been below commercial benchmarks. In this context, we have investigated routes and implemented strategies to improve performance to be comparable to current commercial benchmarks by (a) processing improvements and (b) modification of the monomer/co-monomer chemistry. In this framework we report on the processing parameters.

Experimental

The membrane synthesis is described elsewhere [4].

Results

In contrast to most other membrane technologies, the synthesis of the PSI radiation grafted membrane is a diffusion controlled process. As illustrated in Figure 1, an irradiated pre-formed dense polymer film is exposed to a polymerizable monomer, which is incorporated into the film as a graft copolymer to then carry the ion exchange functionality. Since the irradiated film does not swell considerably in the monomer, the initial reaction takes place at the film surface. Layer by layer of growing polymer chains are added from the surface towards the center of the film until the entire substrate is homogenously grafted. Due to this type of front mechanism the initial surface grafting is highly sensitive and can strongly govern the final membrane quality.

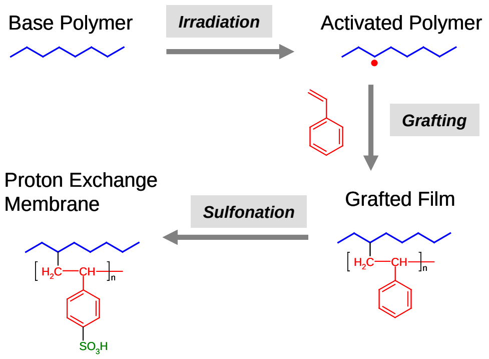

Figure 1. *Synthesis route for the preparation of radiation grafted Membrane prepared at PSI, using styrene.*

The generated reactive free radicals in the irradiated film are intended to be used for initiating growing chains. However, due to their non selective nature, free radicals are prone to undergo undesired side reactions with species other than the monomers. Scavenging reactions inhibit or prematurely terminate growing chains, leading to a reduced level of functionality in the membrane. This sensitivity is most pronounced at the surface of the film, since (a) this part is exposed to environmental conditions, and (b) due to the nature of the grafting front mechanism, radical scavengers or impurities in the monomers or solvents will predominantly affect the initial phase of polymerization at the surface. This results in membranes with insufficient surface functionality.

During the preparation of radiation grafted membranes, the following steps have been identified as key issues:

Step A: Irradiation and subsequent storage of films. Antioxidants and stabilizers in storage bags used for irradiation, scavenge surface radicals of irradiated films.

Step B: Film preparation prior to grafting process. Irradiated films are exposed to environmental factors while handled and assembled into the grafting reactor, which can lead to radical decays at the film surface.

Step C: Grafting reaction. Stabilizers in monomers can act as radical scavengers and chain terminators, mostly at the initial phase of the graft copolymerization, affecting predominantly the film surface.

Grafted films have been prepared by altering the above processing steps to minimize losses of active surface radicals. The films were characterized in terms of grafting level at the surface relative to the bulk of the film via FTIR-ATR spectroscopy. *In situ* fuel cell testing revealed the surface properties of the membrane in an operating fuel cell. Figure 2 shows a section of the FTIR spectrum containing the relevant absorbance bands that were used to quantify the grafting level. These absorbance bands were chosen to ensure similar penetration depth for surface measurements, as well as high absorbance for reliable quantification.

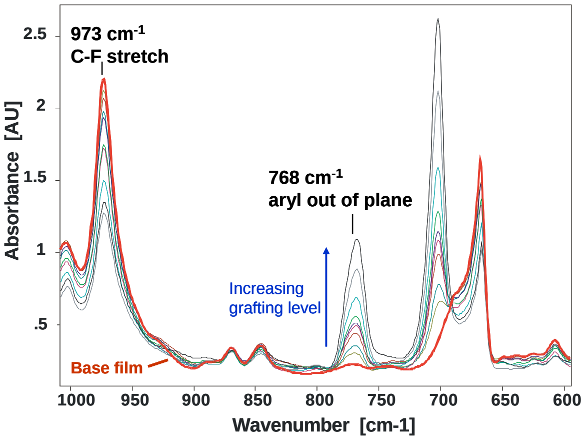

***Figure 2.** FTIR spectra of grafted films containing various grafting levels, measured in transmission mode.*

The absorbance ratio between 768 cm^{-1} (aryl out of plane) and 973 cm^{-1} (C-F stretch) provided, through a calibration curve, the grafting level. The relative extent of surface grafting was then calculated by taking the ratio of grafting level measured in ATR mode (surface) over the grafting level in transmission mode (bulk).

Figure 3 illustrates the effect of minimizing the loss of active surface radicals prior to grafting on the relative surface grafting level (FTIR-ATR), as well as on *in situ* fuel cell performance of the resulting membrane.

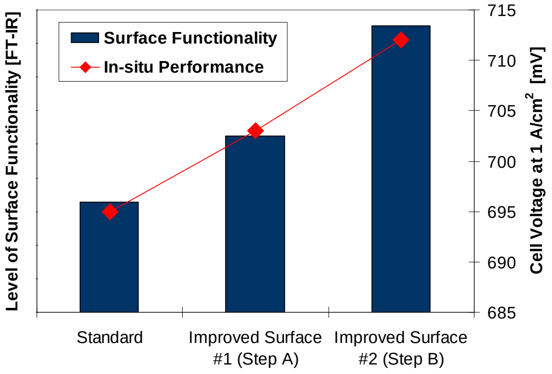

***Figure 3.** Effect of surface functionality of grafted membranes, measured by FT-IR, on in situ cell voltage at 1 A/cm^2.*

These implemented modifications provide enhanced surface grafting leading to enhanced functionalities at the membrane surface and, accordingly, improved *in situ* fuel cell performance of the final membranes.

Figure 4 displays polarization curves of membranes that result from various surface improvement strategies. The tests were done in a 30 cm^2 H_2/O_2 single cell at 80°C, 100% relative humidity, 2.5 bar absolute pressure.

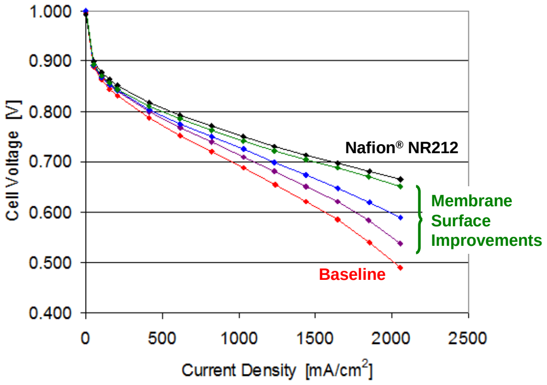

***Figure 4.** Polarization curves of radiation grafted membranes bearing various improvements in their surface functionality.*

The modifications during the grafting reaction (Step C), such as removing stabilizers in the monomers, as well as using high purity solvents, demonstrated to have the most pronounced effect on surface functionality and therefore membrane performance, as shown in Figure 5. Also, when improvement strategies are combined, the effects can be additive (Step B+C).

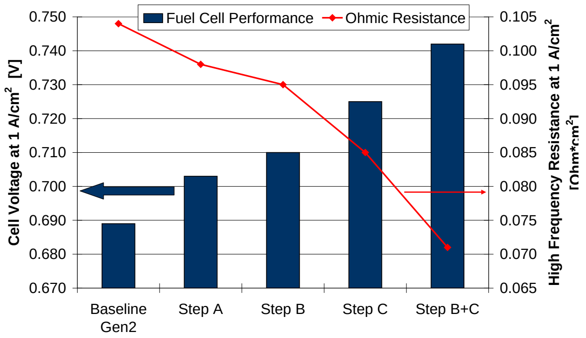

***Figure 5.** Effect of membrane processing modifications on fuel cell performance and resistance. (Commercial benchmark Nafion® NR212 performs at 0.740-0.750 V, with a resistance of 0.066 Ohm·cm^2 under identical fuel cell operating conditions).*

Conclusion

Radiation grafted membranes offer great advantages to other membrane technologies, however, are sensitive to their preparation technique. Maintaining active surface radicals is a key attribute to ensuring optimal membrane functionality in an operating fuel cell.

Acknowledgement

Financial support by Belenos Clean Power AG (Biel) is gratefully acknowledged.

References

[1] U.S. Department of Energy (EERE), Fuel Cell Technologies (FCT) Program – Pathways to Commercial Success - 2012.

[2] L. Gubler, L. Bonorand, J. Thut, G.G. Scherer, PSI Electrochemistry - Annual Report 2011, 17-18, DOI: 10.3929/ethz-a-007047464 (2012).

[3] L. Bonorand, G.G. Scherer, L. Gubler, PSI Electrochemistry - Annual Report 2011, 5-6, DOI: 10.3929/ethz-a-007047464 (2012).

[4] L. Gubler, G.G. Scherer, in: Handbook of Fuel Cells, Vol. 5, W. Vielstich, H.A. Gasteiger, H. Yokokawa (Editors), John Wiley & Sons, Chichester (UK), 313-321 (2009).

Grafting of glycidyl methacrylate (GMA) onto ETFE and Post-Sulfonation

Y. Buchmüller, G.G. Scherer, A. Wokaun, L. Gubler

phone: +41 56 310 5450, e-mail: yves.buchmueller@psi.ch

Radiation grafting is a versatile technique to introduce desired properties into polymers [1, 2]. Advantages are the wide range of commercially available monomers and the relatively easy control of the graft component by the appropriate choice of the irradiation dose, monomer concentration in the grafting solution, solvent and additives, the reaction time and temperature. Radiation grafting can be performed to obtain ion-exchange membranes for variable applications: proton conductive membranes for fuel cells [1], separation membranes for water purification [3] or membranes for the removal of heavy metal ions [4].

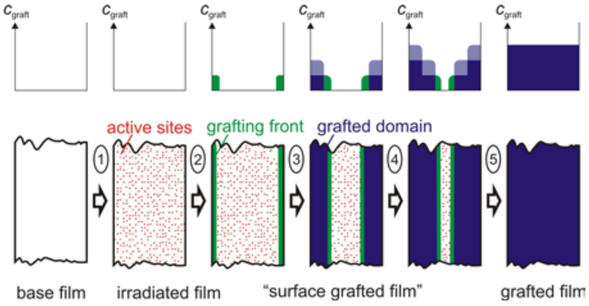

Figure 1. *Schematic representation of grafting fronts [5].*

Polymer electrolyte membranes for fuel cell application are used under chemically and electrochemically harsh conditions and need to exhibit long term chemical stability and mechanical integrity. State of the art are perfluorinated sulfonic acid (PFSA) membranes, e.g, Nafion®, Flemion®. These are aliphatic polymers with good mobility of the polymer chains leading to acceptable proton conductivities at relatively low sulfonic acid contents. In contrast, in ETFE grafted with polystyrene sulfonic acid (ETFE-*g*-PSSA) the mobility of the side chains is restricted, due to the stiffness of the pendant aromatic styrene groups. To improve the mobility of the grafted chains, styrene could be replaced by a more saturated monomer, e.g., glycidyl methacrylate (GMA).

The grafting of monomers into a base film is a reaction and diffusion controlled process [6]. If the diffusion of the monomer into the film is faster than the reaction, grafting occurs quasi-simultaneously across the film. In case that the reaction rate is higher than the diffusion rate, grafting initially only takes place at the surface of the film. When the monomers diffuse into the base film over time, polymerization starts in the bulk of the film gradually. For grafting of monomers into a base material, this mechanism is referred to as "front mechanism" (Figure 1) [5, 7].

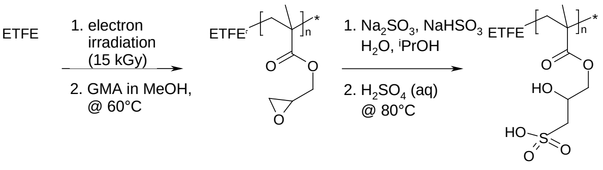

Figure 2. *Schematic representation of grafting GMA onto ETFE with subsequent sulfonation to obtain a proton conductive membrane.*

In this work, grafting of glycidyl methacrylate (GMA) onto poly(ethylene-*alt*-tetrafluoroethylene) (ETFE) base film is presented. GMA contains a functional group (electrophile) and a polymerizable double bond. Functionalization of the grafted films was performed with sulfite: sulfonation of the epoxy group in GMA yields an alternative proton exchange membrane (Figure 2).

Experimental

GMA was grafted onto ETFE film of 25 μm thickness. The graft level (GL) is an important parameter to characterize graft copolymers:

$$GL = \frac{m_{\mathrm{grafted}} - m_{\mathrm{basefilm}}}{m_{\mathrm{basefilm}}} \cdot 100\,\% \qquad (1)$$

where *m* is the mass. The ETFE base films were electron beam irradiated (Studer Leoni, Däniken) with a dose of 15 kGy, the stabilizing agent in GMA was extracted using an inhibitor remover column and the grafting solution consisted of MeOH and GMA at a volumetric ratio of 9/1. The grafting reaction was performed at 60°C. All films were characterized with FTIR and gravimetrically.

The influence of the graft level and time on the sulfonation reaction of the epoxide group of GMA was studied. The sulfonation solution consisted of 10 m% Na_2SO_3, 3 m% $Na_2S_2O_5$, 10 m% ^{i}PrOH, and 77 m% H_2O [8]. The sulfonation was carried out at 80 °C for 8 h and 24 h, respectively. Films of graft levels ranging from 10% to 300% were sulfonated.

The membranes were swollen in water, frozen in liquid nitrogen and broken for the analysis of the cross-sections with scanning electron microscopy and energy dispersive X-ray analysis (SEM EDX).

Results

The kinetics for the grafting of GMA onto ETFE is described elsewhere [9]. The grafting shows a linear dependence on the grafting time. GLs of 300 m% could be reached within 6 hours.

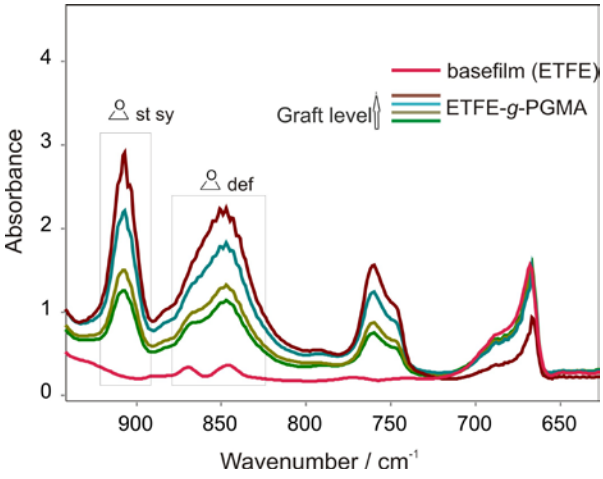

Figure 3. *FTIR spectra of ETFE-*g*-PGMA films at different GL.*

All films were characterized with FTIR (Figure 3). The epoxide bands at 853 cm^{-1} and 902 cm^{-1} and the band of the α–methyl group at 1388 cm^{-1} were used for quantification of the GMA content.

Sulfonation of the epoxide group was performed to analyze the conversion of nucleophilic attack in the bulk polymer film. The number of $–SO_3H$ groups in the film was determined with acid-base titration (Figure 4). Additionally, the measured through-plane conductivity is an indication of base film functionalization across the entire thickness, which is a prerequisite for fuel cell application. The obtained membranes will be tested in fuel cells in forthcoming experiments. The degree of sulfonation seems to stabilize at around 90% at graft levels higher than 80 m%. There was no detectable difference in the conversion to the sulfonic acid after 8 or 24 h of reaction time.

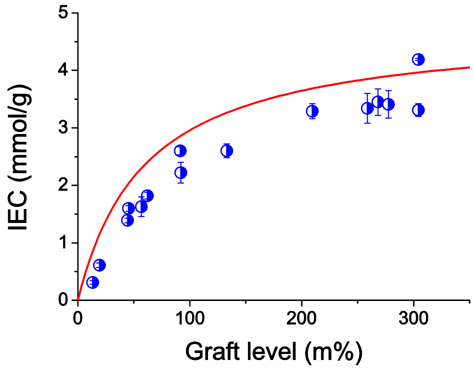

Figure 4. *IEC vs. GLs of the sulfonated ETFE*-g-*PGMA. The line represents the theoretically possible IEC (100% sulfonation of the GMA side chains).*

The through-plane conductivity measurements revealed a kind of threshold value for its dependence on the ion exchange capacity (IEC) (Figure 5). Below this value the membranes show no through-plane conductivity. The measured values above this threshold are acceptable to high. This behavior, combined with high conversion of the sulfonation reaction, suggests a front mechanism for the grafting of GMA onto ETFE.

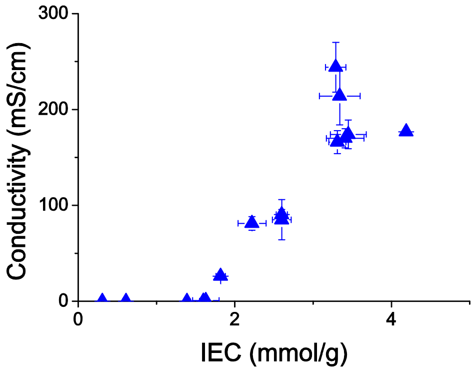

Figure 5. *Proton conductivity of sulfonated ETFE*-g-*PGMA membranes in water swollen state at room temperature as a function of the IEC. The membranes show no through-plane conductivity below an IEC of 1.8 mmol/g*

Several cross-sections of membranes of different GLs were analyzed with SEM/EDX to verify this assumption. Two SEM images and the corresponding EDX mappings for sulfur are shown in Figure 6. The SEM images show cross-sections with three distinctive areas: the center appears to be plastically deformed, whereas the outer areas show no deformations. This suggests a non-grafted polymer in the center and brittle outer sections of the membrane. The shown sulfur mappings support this assumption, showing no sulfonic acid groups in the center part of the analyzed samples. The sample with higher GL shows a smaller non-grafted portion of the membrane, indicating a front mechanism for grafting of GMA onto ETFE.

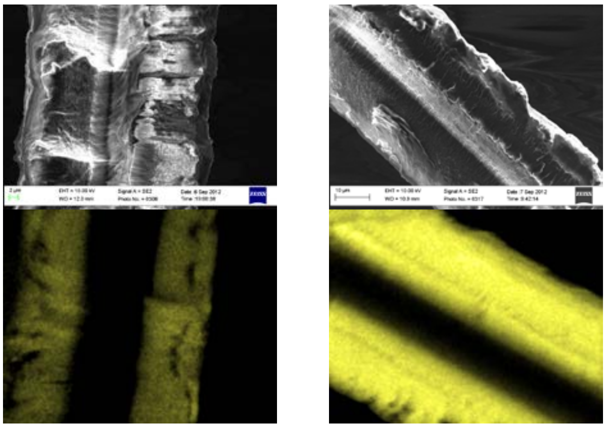

Figure 6. *SEM images (top) and corresponding EDX maps of cross-sections of sulfonated ETFE*-g-*PGMA of different GLs. Left: GL = 57 m%. Right: GL = 92 m%. The yellow domains indicate the concentration of sulfur.*

Conclusion

GMA was grafted onto ETFE. It showed a linear grafting behavior. ETFE-*g*-PGMA films were sulfonated using a sulfite solution. The degree of sulfonation showed a dependence on the graft level: for films with graft levels higher than 80 m%, the conversion seems to stabilize at around 90%. The high conversion, combined with a threshold value for the through-plane conductivity (vs. IEC) suggests a front mechanism for grafting of GMA onto ETFE. The SEM-EDX analysis supports this hypothesis.

References

[1] S. Alkan-Gürsel, L. Gubler, B. Gupta, G.G. Scherer, Adv. Polym. Sci. **216**, 157-217 (2008).

[2] A. Bhattacharya, B.N. Misra, Progr. Polym. Sci. **29** (8), 767-814 (2004).

[3] M.M. Nasef, O. Güven, Progr. Polym. Sci. **37** (12), 1597-1656 (2012).

[4] R. Ishihara, K. Fujiwara, T. Harayama, Y. Okamura, S. Uchiyama, M. Sugiyama, T. Someya , W. Amakai, S. Umino, T. Ono, A Nide, Y. Hirayama, T. Baba , T. Kojima, D. Umeno, K. Saito, S. Asai, T. Sugo, J. Nucl. Sci. Technol. **48**, 1281-1284 (2011).

[5] F. Wallasch, M. Abele, L. Gubler, A. Wokaun, K. Müller, G.G. Scherer, J. Appl. Polym. Sci. **125**, 3500-3508 (2012).

[6] A. Chapiró, Radiation chemistry of polymeric systems; Interscience Publishers, New York, London, 1962.

[7] A. Dobó, A. Somogyi, T. Czvikovszky, J. Polym. Sci. C **4**, 1173-1193 (1963).

[8] M. Böhme, PhD thesis, TU Clausthal (2005).

[9] Y. Buchmüller, G.G. Scherer, A. Wokaun, L. Gubler, PSI Electrochemistry - Annual Report 2011, 7-8,
DOI: 10.3929/ethz-a-007047464 (2012).

Investigation of comonomer effects on proton conductivity

K. Jetsrisuparb, B. Miserere-Janssens, Z. Zhang, A. Wokaun, L. Gubler

phone: +41 56 310 2162, e-mail: kaewta.jetsrisuparb@psi.ch

The radiation grafted membrane is an alternative material to the state-of-the-art perfluorosulfonic acid (PFSA) membrane in fuel cells. In addition to the potential cost reduction, the main technological challenge to be addressed is membrane durability. Radiation grafted membranes are commonly prepared by grafting of styrene or its derivatives into a polymer matrix and subsequent sulfonation to introduce proton conductivity. The use of styrene derivatives, e.g., α,β,β-trifluorostyrene (TFS) or α-methylstyrene (AMS), as grafted monomers was found to increase membrane durability compared to the styrene analog. However, the common drawback of these styrene derivatives is their slow grafting kinetics.

The use of styrene based membranes has been motivated by its easy polymerization and sulfonation. To increase the durability of such membranes in the fuel cell, a proper comonomer can be introduced into the system. Incorporation of methacrylonitrile (MAN) as styrene's comonomer in the grafted membrane led to more than a fourfold increase in the lifetime of the membrane electrode assembly (MEA) [1]. As a consequence, an understanding of the co-monomer effects is required to establish a basis for an alternative membrane design. Except the durability, the effect of the presence of a comonomer on the fuel cell relevant properties has not been investigated. Here, we will highlight the effect of various comonomers with the main focus on proton conductivity.

Experimental

ETFE base film with 25 µm thickness was electron beam irradiated in air to generate active sites to initiate grafting. The pre-irradiated films (1.5-15 kGy) were exposed to the grafting solution containing 20 vol% monomer mixture and 80 vol% solvent. The monomer mixture consisted of styrene and its comonomer (Figure 1). The grafting reaction was carried out at 60ºC under N_2 atmosphere. Sulfonation of grafted films was performed subsequently in 2 vol% chlorosulfonic acid in dichloromethane at room temperature for 5 hours. Then hydrolysis was carried out in 80ºC water for 8 hours. FTIR analysis and solid state NMR were applied to investigate the polymer composition before and after sulfonation. The degree of sulfonation was determined as described in [2]. The amount of sulfonic acid groups in the membrane is defined by the ion exchange capacity (IEC) as:

$$IEC = \frac{n(H^+)}{m_{dry}}$$

Where $n(H^+)$ is the molar number of protons in the membrane and m_{dry} is the dry mass of the membrane.

Results and Discussion

The nature of the co-monomer affects the membrane preparation in several stages. We observed that the type of co-monomer influences the grafting behavior, such as the grafting rate. Therefore, the irradiation doses of the base film were adjusted accordingly to obtain reasonable grafting time. A higher dose can increase the grafting rate, yet also damage the base film [3]. In this study, the dose was limited to 15 kGy to prevent excessive chain scissions resulting from radiation. It is reasonable to anticipate that the small differences in the dose applied for different membrane systems should not lead to significant changes in base film properties.

Five different membrane types were prepared by sulfonation of the grafted films (Figure 1). Key properties such as ion exchange capacity, water uptake and proton conductivity of these membranes were investigated.

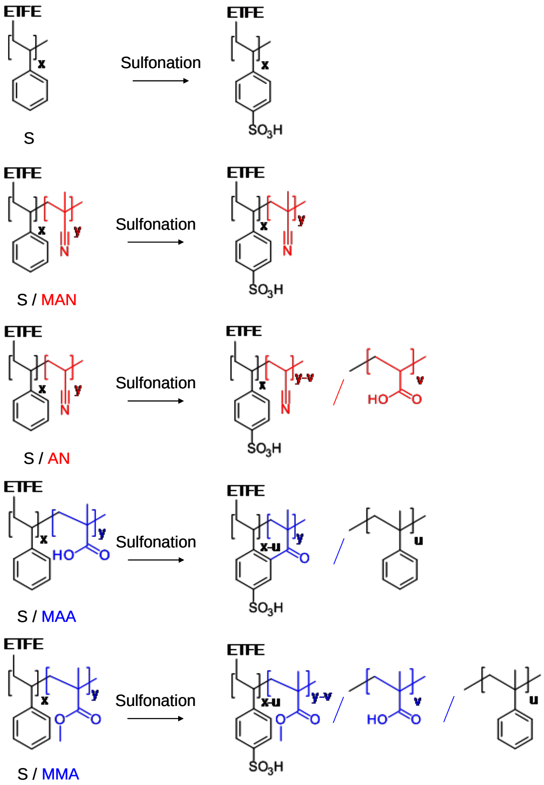

Figure 1. *Sulfonation of radiation grafted films leads to membranes containing sulfonic acid groups in the aromatic ring of styrene (S). Styrene's comonomers are methacrylonitrile (MAN), acrylonitrile (AN), methacrylic acid (MAA), and methyl methacrylate (MMA). Copolymerization kinetics of these systems suggest that the grafted polymers have a tendency to form alternating chains.*

FTIR analysis showed that the presence of a comonomer not only affects the grafting kinetics, it can also lead to formation of hydrolyzed products during sulfonation. The presence of an α-methyl group in the hydrolyzable comonomer was found to increase the resistance to hydrolysis due to the inductive electron donor effect.

Complete sulfonation was achieved in pure styrene grafted membranes, S / MAN and S / AN cografted membranes, while only 80% of the styrene units were sulfonated in the presence of MAA and 70% in case of MMA under the same conditions. In addition, the MAA underwent Friedel-Crafts acylation forming a conjugated ketone as product [4]. Extending the reaction time or increase in temperature may help to increase the degree of sulfonation in S / MMA and S / MAA membranes.

After sulfonation, the membranes became hydrophilic and absorbed water. An increased IEC and comonomer content were accompanied by an increased water uptake. We found that pure MAN and pure MAA grafted films hardly swell in water, implying that the amount of water absorbed by the membrane is mostly governed by the acid groups. The comonomer may play a role as a spacer that helps to accommodate the water molecules associated with the sulfonic acid.

Generally, the conductivity of the membranes is strongly dependent on their hydration state since it is directly connected to the proton mobility. Surprisingly, the increased water uptake of the cografted membranes in water swollen state hardly affects the proton conductivity compared to the pure styrene grafted membrane with the same IEC (Figure 2). The proton conductivity of the membranes in the liquid water equilibrated state depends primarily on the IEC.

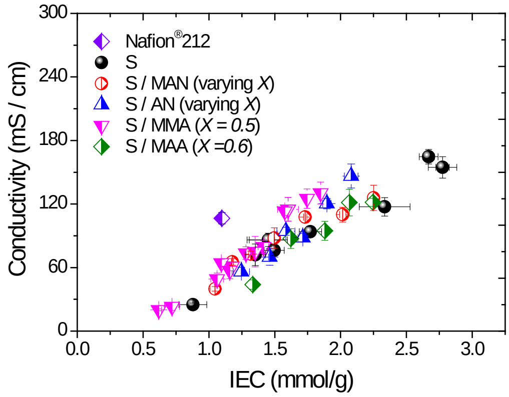

Figure 2. *The proton conductivity of water swollen cografted membranes containing styrene and different comonomers as a function of the IEC at room temperature. X is the molar fraction of styrene with respect to the total graft copolymer content in the membrane. Nafion® 212 and pure styrene grafted membranes (S) are included for comparison.*

Although the presence of a comonomer did not promote the proton conductivity of the membranes in water, an increased water uptake may be advantageous for proton conductivity at reduced humidity by providing increased proton mobility. We selected different membranes with similar IEC and investigated the corresponding proton conductivity over a range of relative humidities. The graft copolymer of the cografted membranes contained a styrene to comonomer molar ratio of approximately 1:1. By reducing the relative humidity, the water content in the membrane decreases and hence the proton conductivity is reduced.

Surprisingly, all cografted membranes showed a higher loss in proton conductivity compared to the pure styrene grafted membrane with comparable IEC (Figure 3). In addition, the differences in the chemical structure of the comonomer did not seem to play a role in the proton conductivity at reduced humidity. We presume that incorporation of a comonomer during grafting affects the morphology of the membranes and contributes to the decrease in proton conductivity at reduced humidity. To gain some insights into the structure of the membranes at reduced humidity and its influence on the proton conductivity, we started to investigate the membrane morphology in the dry state using small angle x-ray scattering (SAXS). Detailed studies are ongoing to identify the effect of the comonomer functionalities on the nanoscale structure.

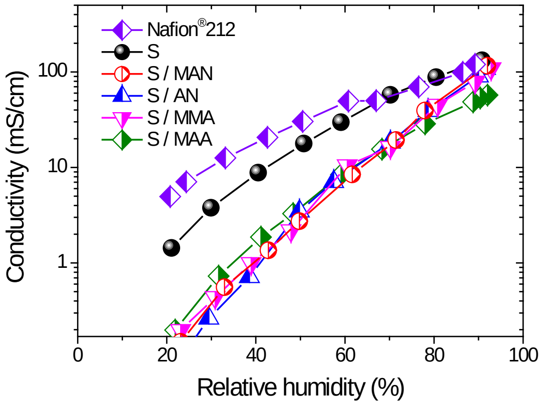

Figure 3. *Comparison of the proton conductivity as a function of relative humidity of different grafted membranes with similar IEC (~1.5 mmol/g). The styrene molar fraction in the cografted membranes containing styrene and different comonomers is similar. Nafion® 212 is given here for comparison.*

Conclusions

Cografted membranes containing styrene and four different comonomers were prepared by radiation grafting. Incorporation of a comonomer resulted in increased water uptake in water swollen membranes. The additional water does not lead to improved proton conductivity, though. In the water swollen state, all membranes have similar proton conductivity at a given IEC. However, the presence of a comonomer leads to a pronounced loss in proton conductivity at reduced humidity. The cografted membranes containing similar styrene molar fraction and IEC showed the same proton conductivity at reduced relative humidity regardless of the type of comonomer. Although the functionality of the comonomer does not lead to any considerable effect on proton conductivity, an appropriate comonomer should be selected for stability reasons [5].

Acknowledgement

Solid-state NMR investigation of S / MAA membranes by the LEPMI group at the Université de Savoie (France) is gratefully acknowledged.

References

[1] H. Ben youcef, L. Gubler, S. Alkan Gürsel, D. Henkensmeier, A. Wokaun, G.G. Scherer, Electrochem. Commun. **11**, 941-944 (2009).

[2] K. Jetsrisuparb, H. Ben youcef, G.G. Scherer, A. Wokaun, L. Gubler, PSI Electrochemistry Laboratory - Annual Report 2009, ISSN 1661-5379, 9-11 (2010).

[3] H. Ben youcef, S. Alkan Gürsel, A. Buisson, L. Gubler, A. Wokaun, G.G. Scherer, Fuel cells, **10**, 401-410 (2010)

[4] K. Jetsrisuparb, H. Ben youcef, G.G. Scherer, A. Wokaun, L. Gubler, PSI Electrochemistry Laboratory - Annual Report 2011, ISSN 1661-5379, 11-12 (2012).

[5] Z. Zhang, K. Jetsrisuparb, B. Miserere-Janssen, A. Wokaun, L. Gubler, PSI Electrochemistry Laboratory - Annual Report 2012, 16 (2013).

Analysis of the degree of hydrolysis in styrene / acrylonitrile co-grafted membranes tested in PEFCs

Z. Zhang, K. Jetsrisuparb, B. Miserere-Janssen, A. Wokaun, L. Gubler

phone: +41 56 310 4188, e-mail: zhuoxiang.zhang@psi.ch

It has been discussed that the loss of functional groups in radiation grafted membranes during an accelerated stress test (AST) in the fuel cell can be calculated via *post mortem* analysis based on FTIR spectroscopy [1]. Since we observed the impact of hydrolysis on the loss of nitrile for styrene / acrylonitrile (AN) co-grafted membranes, it is useful and necessary to quantitatively analyze the degree of hydrolysis of the nitrile units. The quantification of the characteristic groups is achieved by peak area integration and intensity normalization to a peak area associated with the ETFE base film.

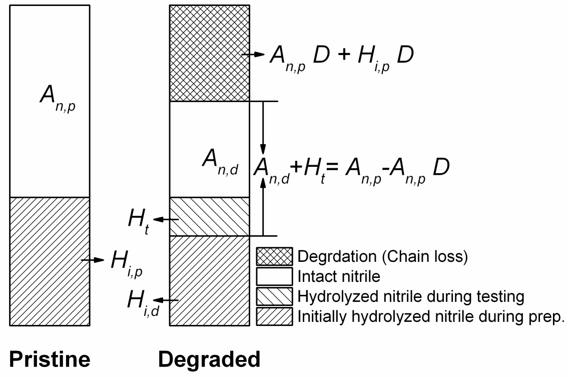
$A_{n,p}$
$A_{n,p}\,D + H_{i,p}\,D$
$A_{n,d}$
$A_{n,d}+H_t= A_{n,p}-A_{n,p}\,D$
H_t
$H_{i,p}$
$H_{i,d}$
Degrdation (Chain loss)
Intact nitrile
Hydrolyzed nitrile during testing
Initially hydrolyzed nitrile during prep.
Pristine
Degraded

Figure 1. *Illustration of the calculation of the degree of nitrile hydrolysis.*

$$Degree\ of\ hydrolysis = \frac{H_t}{H_t + A_{n,d}} \tag{1}$$

$$H_t + A_{n,d} = A_{n,p} - A_{n,p} \cdot D \tag{2}$$

$$Degree\ of\ hydrolysis = 1 - \frac{A_{n,d}}{A_{n,p}(1-D)} \tag{3}$$

In order to clearly show the calculation procedure for the degree of hydrolysis, Figure 1 is used to illustrate the composition of the pristine and degraded membrane, respectively. As shown in Equation 1, we define the hydrolysis degree of nitrile groups during the fuel cell test as the content of hydrolyzed nitrile (H_t in Figure 1) after the test with respect to the remaining content ($A_{n,d}$+H_t in Figure 1) of nitrile in the pristine membrane ($A_{n,p}$ in Figure 1). $A_{n,d}$ represents the area of the peak characteristic of the intact nitrile in the tested membrane. H_t is the hypothetical peak area of the nitrile groups that are hydrolyzed during the AST. Since H_t is not measurable by FTIR spectroscopy, we need to deduce the expression using the relationship shown in Equation 2, where the area of the peak associated with C☰N vibration in the pristine membrane is indicated by $A_{n,p}$ and D is the extent of degradation calculated based on the loss of styrenesulfonic acid (SSA) units [1]. This relationship is based on the assumption that the SSA and the co-monomer units in the grafted chains are decomposed proportionately. This assumption can actually be supported by the consistency between the degree of SSA degradation and the degree of nitrile loss in the case of the styrene/methacrylonitrile co-grafted membrane [1].

Combining Equations 1 and 2, we obtain the final expression for the calculation of the degree of hydrolysis (Equation 3). Both $A_{n,p}$ and $A_{n,d}$ can be directly obtained from transmission FTIR spectra with peak areas normalized to the band at 1325 cm^{-1} associated with the ETFE base film. In the calculation, we neglect the initial degree of hydrolysis ($H_{i,p}$ and $H_{i,d}$ Figure 1) which takes place during membrane preparation, because we wish to distinguish between hydrolysis resulting from preparation (around 35%) and hydrolysis during testing. The obtained results based on the aged styrene/AN co-grafted membranes are shown in Table 1.

Duration of AST (h)	**24**	**48**	**96**	**130**
Degree of hydrolysis (%)	29±6	36±8	48±6	57±5

Table 1. *The calculated degree of nitrile hydrolysis due to testing in styrene/AN co-grafted membranes over different time periods of operation in the fuel cell.*

The fate of the nitrile units in the degraded and hydrolyzed membranes with increasing operation time is displayed in Figure 2. The pristine membrane only contains the intact nitrile and the nitrile hydrolyzed during preparation, both of which are reduced in proportion with increasing testing duration due to chain degradation. The fraction of the nitrile hydrolyzed during testing remains approximately constant in a range between 17% and 14%. The decomposed fraction increases dramatically with time, while the nitrile remaining intact only accounts for around 11% of the initially grafted units after130 h.

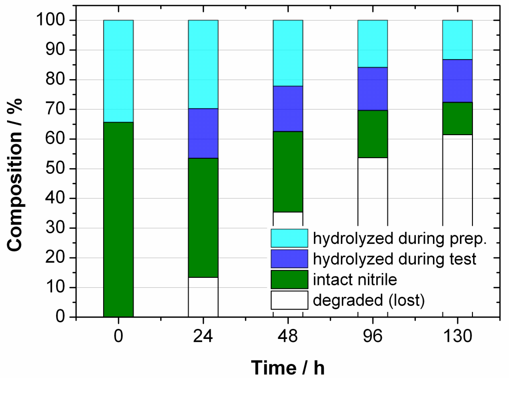

Figure 2. *The analysis of the fate of the original nitrile units in styrene/AN co-grafted membranes aged in an AST in the fuel cell over different time periods of operation.*

A calculation method for quantifying the degree of hydrolysis of nitrile groups during testing was established, based on the principle of area integration of the characteristic IR-vibrational bands. With this method, we can gain an insight into the fate of the nitrile units of the styrene/AN co-grafted membrane over the testing time.

References

[1] Z. Zhang, K. Jetsrisuparb, B. Miserere-Janssen, A. Wokaun, L. Gubler, this PSI Electrochemistry Laboratory Annual Report 2012, 16 (2013).

Study of the degradation of nitrile containing membranes in PEFCs

Z. Zhang, K. Jetsrisuparb, B. Miserere-Janssen, A. Wokaun, L. Gubler

phone: +41 56 310 4188, e-mail: zhuoxiang.zhang@psi.ch

Durability and cost are two key issues for the commercialization of polymer electrolyte fuel cells (PEFCs). In the development of PSI membranes, methacrylonitrile (MAN) was used as co-monomer to promote the grafting of α-methylstyrene, and the obtained membranes displayed a significantly higher durability in the fuel cell compared to pure styrene grafted membranes [1]. Having the advantage of versatility, the radiation grafting method can allow the copolymerization between styrene based monomers and diverse low-cost co-monomers [2], such as MAN and acrylonitrile (AN). In this study, we discuss and evaluate the effect of the nitrile containing co-monomers on membrane chemical degradation through testing styrene/MAN and styrene/AN co-grafted membranes (Figure 1) in the single fuel cell at accelerated degradation conditions. The extent of membrane degradation as function of the testing duration is quantified by *post mortem* analysis using FTIR spectroscopy.

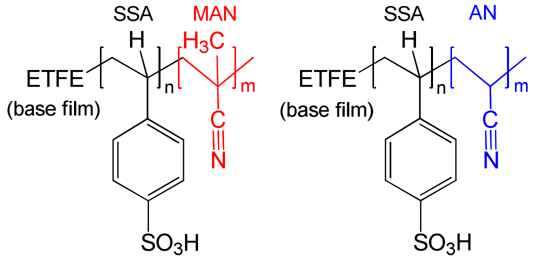

Figure 1. *Schematic of the architectures of the membranes used in the study. SSA: styrenesulfonic acid.*

Experimental

The membranes were prepared by co-grafting styrene (S) and MAN or AN onto pre-irradiated ETFE film (25 µm thickness) followed by sulfonation. Some relevant *ex situ* properties of membranes are shown in Table 1.

#	Grafted chain composition	Graft level (%)	Styrene molar fraction in the grafts	Thickness (µm)
1	S-*co*-MAN	~40	~0.5	46±1
2	S-*co*-AN	~42	~0.5	45±2

Table 1. *Graft level, composition of the grafts and thickness (water saturated state) of the used membranes.*

The membranes were laminated together with gas diffusion electrodes (type ELE162, Johnson Matthey Fuel Cells) with a platinum loading of 0.4 mg/cm^2 to form membrane electrode assemblies (MEAs) in a hot-press at defined temperature, load, and duration (110 ℃ / 40 kN / 180 s). Subsequently, the MEAs were assembled into a graphite single cell with an active area of 16 cm^2. Accelerated stress tests (ASTs) of the single cell were carried out at 80 ℃ under open circuit voltage (OCV) conditions. H_2 and O_2, both fully humidified, were fed to the anode and cathode, respectively, at 600 mL min^{-1} each and at a backpressure of 2.5 bar$_a$. *In situ* characterization of the single cell was performed by means of online measurements of cell voltage and high frequency resistance (HFR) at 1 KHz as a function of operation time.

At the end of test, the MEA was taken out of the fuel cell hardware. The electrodes were carefully peeled off the membrane and the surface of the membrane was cleaned from remaining catalyst particles in a mixture of demonized water and ethanol. The protons present in the degraded membranes were exchanged with K$^+$ by immersing the membrane in 0.5 M KCl solution overnight. The active area on the membrane was divided into 12 sections, each of which was probed by the FTIR analysis instrument. Therefore, the entire active area can be analyzed.

Results and Discussion

With respect to radiation grafted membranes, measuring membrane resistance *in situ* is the most advisable way of monitoring the ‘state-of-health’ of the membrane during fuel cell tests [3]. We performed the measurement of membrane resistance by the high frequency resistance (HFR) method using an AC mOhm tester for fuel cells (Tsuruga 3566-01) and were thereby able to follow the evolution of the membrane resistance as a function of the operating time during OCV hold tests. The durability of the nitrile containing membranes can be evaluated and compared by the evolution of the HFR for the corresponding membranes as function of time.

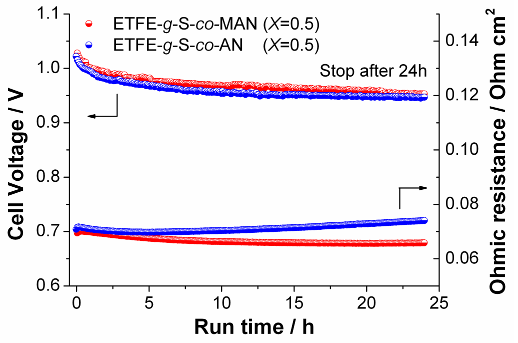

Figure 2. *Evolution of cell voltage and membrane resistance (measured by HFR) vs. time of operation in the H_2/O_2 fuel cell at 80 ℃ for membranes tested for 24 hours.*

The resulting *in situ* characterizations of cell voltage and ohmic resistance for the single cells with two kinds of nitrile containing membranes are shown in Figure 2. We observe that both styrene/MAN and styrene/AN co-grafted membranes showed steady profiles of ohmic resistance over the investigated time domain. Within an OCV duration of 24 h, a slow decrease in HFR from 70 mΩ cm^2 to 66 mΩ cm^2 was found for the cell with the styrene-*g*-MAN membrane. The resistance of the styrene-*g*-AN membrane, whose initial value was 72 mΩ cm^2, increased with a rather small slope to 74 mΩ cm^2 at the end of the durability test. The result implies that the durability of these two kinds of nitrile containing membranes is comparable within the investigated time domain.

Transmission FTIR spectroscopy on the tested membranes was performed in the *post mortem* analysis. This method can be used to characterize membrane degradation due to the fact that the intensities of the peaks corresponding to functional groups (e.g., styrenesulfonic acid and nitrile) diminish during OCV durability tests, owing to the chemical attack by reactive oxygen species on the grafted chains followed by detachment from the ETFE backbone.

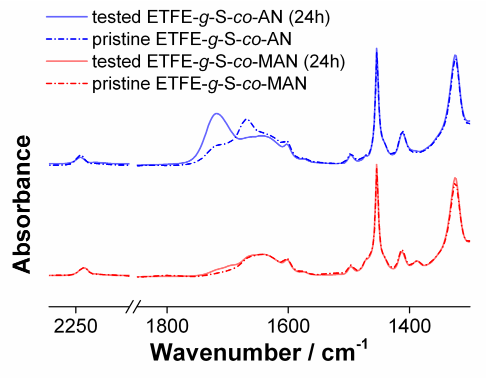

Figure 3. *FTIR spectra of pristine and tested membranes after 24 h OCV operation. Graft component relevant peaks: CΞN stretch vibration at 2234 cm^{-1}, C=C aromatic skeleton stretch vibration at 1600 cm^{-1} and 1494 cm^{-1}, -CH$_2$ deformation vibration at 1411 cm^{-1}, -CH$_3$ deformation vibration at 1388 cm^{-1}.*

The FTIR results for the styrene-*g*-AN membrane and styrene-*g*-MAN membrane before and after the 24 h OCV durability test is displayed in Figure 3. The good stability of both kinds of nitrile containing membranes found in the evolutions of their ohmic resistance during testing can be confirmed by the fact that the intensities of the absorption bands at 1600 cm^{-1} and 1494 cm^{-1} show a rather small decrease after the test. The spectra of the styrene-*g*-AN membrane reveals that the nitrile groups were partially hydrolyzed into amide and carboxylic acid (the bands in the region near 1700 cm^{-1}), whereas the hydrolysis of the nitrile in the styrene-*g*-MAN membrane was negligible. Accordingly, the change of the absorption band at 2234 cm^{-1} (assigned to CΞN vibration) is less significant for the styrene-*g*-MAN membrane than for the styrene-*g*-AN membrane.

The extent of degradation (*D*) can be quantified by the peak area integration. Yet, the peak area associated with the particular grafted component needs to be normalized to that associated with the ETFE base film. This is because the loss of the grafted component leads to a lateral contraction and a decrease in thickness of the membrane undergoing degradation, which results in a "concentration" of the vibronic states in the probed volume. The normalization can take into account the effects owing to the area contraction of the tested membrane.

$$D = 1 - \frac{\tilde{A}_t}{\tilde{A}_p} \qquad (1)$$

The used expression for calculating the extent of degradation extent of each grafted component is shown in Equation 1. $\tilde{A}_p$ and $\tilde{A}_t$ represent the normalized values of A_p and A_t, which are the integrated areas of peaks associated with grafted components (typically aromatic vibration at 1494 cm^{-1} and CΞN vibration at 2234 cm^{-1}) for pristine and tested membranes, receptively. The references are $A_{ETFE,p}$ and $A_{ETFE,t}$, respectively, indicating the areas of the peak characteristic of ETFE (typically at 1325 cm^{-1}). Thus, $\tilde{A}_p = A_p / A_{ETFE,p}$ and $\tilde{A}_t = A_t / A_{ETFE,t}$.

For the nitrile containing membranes used in this study, the degradation degree of SSA and the degree of nitrile loss are quantified for a set of continuous OCV durability tests with increasing operating time (24 h, 48 h, 96 h and 130 h) (Figure 4). It is worth pointing out that four pristine membranes of each category, which were synthesized in the same grafting reactor, were used in the individual tests. The degrees of degradation for SSA in both kinds of membrane gradually increase with time, with around 60% of grafted styrene detached from the backbone after 130 h OCV durability test. Moreover, their rates of degradation of SSA units are comparable within the investigated time domain, which again demonstrates their similar stability. However, the styrene-*g*-AN membranes always show more loss in nitrile units than the styrene-*g*-MAN membranes, which results in about 84% of lost grafted nitrile after 130 h. The more pronounced loss of nitrile in the styrene-*g*-AN membranes is due to the combination of the chemical attack of reactive oxygen species on the grafted chains and the hydrolysis of nitrile groups to amide and carboxylic acid. Another interesting observation from the result of styrene-*g*-MAN membranes is that there is a consistency between the degree of SSA degradation and the degree of nitrile loss. It suggests that, for styrene-*g*-MAN membranes, the SSA units and nitrile units are decomposed proportionately during OCV hold tests. Obviously, this is not the case for the styrene-*g*-AN membranes, where the hydrolysis results in more nitrile loss.

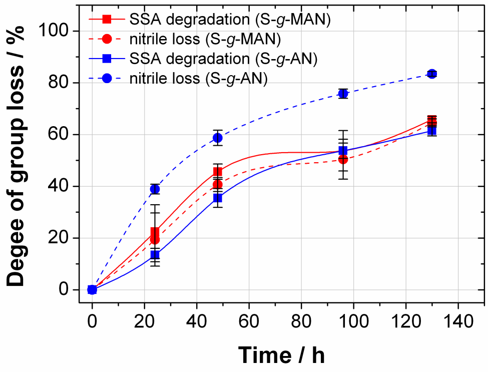

Figure 4. *Degradation of the graft component in styrene-g-MAN and styrene/AN co-grafted membranes aged at OCV over different time periods of operation.*

Conclusion

Two kinds of nitrile containing membranes prepared by radiation grafting were tested under accelerated stress conditions in the fuel cell. Over the investigated testing time, they showed very comparable durability, which was demonstrated by *in situ* characterization and *post mortem* analysis. The degrees of the loss of the grafted components were quantified and compared between the two kinds of membranes as a function of time. The styrene-*g*-AN membranes are more prone to hydrolysis compared to the styrene-*g*-MAN membranes.

References

[1] L. Gubler, M. Slaski, A. Wokaun, G.G. Scherer, Electrochem. Commun. **8,** 1215-1219 (2006).

[2] L. Gubler, S. Alkan-Gürsel, G.G. Scherer, Fuel Cells **5**, 317-335 (2005).

[3] F.N. Büchi, B. Gupta, O. Haas, G.G. Scherer, Electrochim. Acta **40**, 345-353 (1995).

FUEL CELLS

SYSTEMS & DIAGNOSTICS

Exploring the high power density possiblities of H_2/O_2 PEFC systems

F.N. Büchi, M. Hofer, J. Bernard, U. Hannessen[1], R. Gashi[1], A. Closset[1], P. Dietrich

phone: +41 56 310 2411, e-mail: felix.buechi@psi.ch

Oxygen reduction is the main loss mechanism in acidic low temperature fuel cells (PEFC). The Tafel equation relates the kinetic loss, termed overvoltage η, to the exchange current density i_0

$$\eta = b \cdot \log\left({}^{i}\!/_{i_0} \right) \tag{1}$$

with b a constant in the order 70 mV/dec and i the current density. The exchange current density i_0 in turn depends on the geometric catalyst surface A (i.e. loading times specific surface) the catalyst activity expressed as specific exchange current density $i_{0,S}$ (in terms of A/cm^2 of catalyst surface) and the oxygen partial pressure p_{O2} as

$$i_0 = 10 \cdot A \cdot i_{0,S} \cdot \left({}^{p_{O2}}\!/_{p_{O2}^{ref}} \right)^{\gamma} \tag{2}$$

The exponent γ is not precisely known, but measurements indicate a range of $\gamma \approx 0.5 - 1$ (see i.e. [1, 2]). For reducing the cathodic overvoltage η, the exchange curent density i_0 needs to be increased. As deduced from equation (2) three basically different routes are available:

- increasing the catalyst loading. Thus A and i_0 in equation (2) increase, and the overvoltage in equation (1) drops. However due to cost and mass transport limitations in the catalyst layer, this is a limited option;
- increasing the catalysts activity (i.e. $i_{0,S}$ in eq. (2)). This is the main path pursued and thus a broad research field [3]. In the past 20 years, the development of alloy catalysts has lead to an increase of $i_{0,S}$ by about a factor of 2.
- increasing the oxygen partial pressure. This is easiest when using pure oxygen. This increase is typically about an order of magnitude (0.3 to 3 bar). Which is equivalent to an increase of the catalyst activity by about a factor of three to ten, depending in the constant γ.

Thus the use of pure oxygen at the cathode allows for unrivalled high current densities as compared to the operation of the PEFC with air as the oxidant. Pure oxygen fed to the cathode generally also reduces other losses in the cell. The transport overvoltage is reduced because the inter-diffusion of diluted oxygen in nitrogen falls away and the ohmic losses decrease because the membrane is kept easier in a humid, well conducting state without the high volume flow of nitrogen at the cathode.

Results

Figure 1 shows an i/E curve of a 230 cm^2 single cell obtained in the test bench environment with gases in flow through configuration. It is demonstrated that already at a moderate pressure of 3.5 bar, current densities in excess of 2.5 A/cm^2 can be obtained at 0.6 V with conventional electrochemical components on the technical scale. Specific power densities of about 1.6 W/cm^2 are reached.

Similar experiments were performed on the system level with a 24 cell short stack. System components had been optimized for the 30 kW level and are therefore not perfectly adapted for the reduced power. In particular gas recirculation and cooling are over-dimensioned. This will be reflected mainly in the system efficiency where the higher parasitic power leads to somewhat reduced values. The system is shown in Figure 2.

In the system configuration the attained current densities are slightly smaller than in the test bench setup. This is due to a gas utilization close to unity in the system setup which is obtained through recirculation and leads to different gas purity and entrance humidity than in the test bench. However, as shown in Figure 3, also in the system configuration, the stack can be operated at high current densities of up to 2 A/cm^2. This is about a factor of 2 higher than what today's air systems achieve at comparable cell voltages.

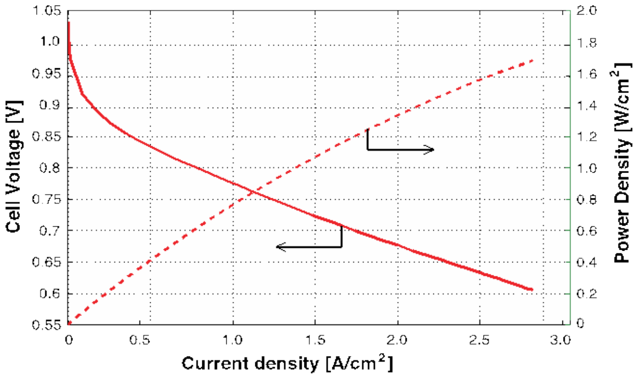

***Figure 1**. i/E characteristics of H_2/O_2 230 cm^2 single cell.*

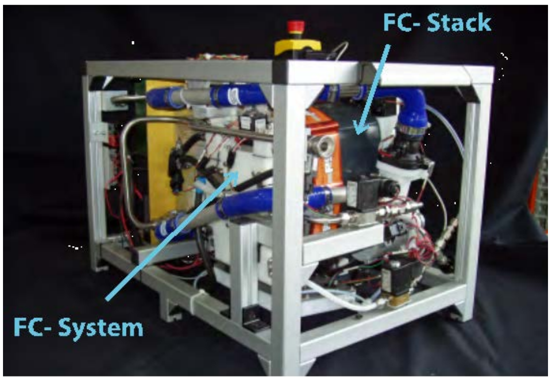

***Figure 2**. H_2/O_2 system with 24-cell stack as indicated.*

[1] Belenos Clean Power Holding, Marin, CH

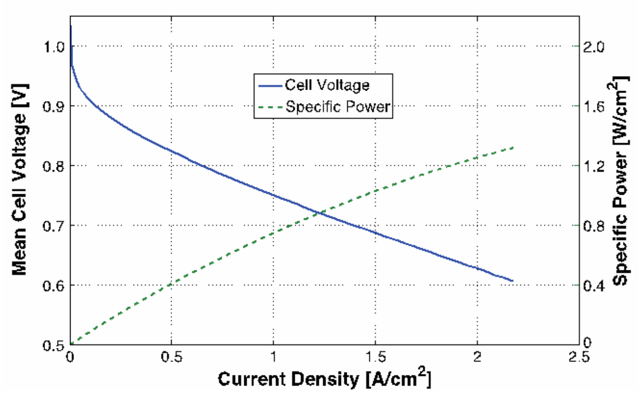

***Figure 3**. i/E characteristics of 24 cell stack in H_2/O_2 system. The power at 2 A/cm^2 is about 7 kW.*

At this current density a specific power density of about 1.3 W/cm^2 is achieved. The high specific current and power densities have a significant influence on the cost of the fuel cell system because the stack size may be reduced accordingly.

It has previously been shown [4] that on the 25 kW power level, systems with pure oxygen as the oxidant, can achieve peak efficiencies of up to 70% (LHV).

Figure 4 shows the efficiency data of the present test system. Peak values in the order of 60% (LHV) are achieved. for this comparably low value, it has to be considered that for the present test system the same balance of plant components (pumps, valves) have been used as in the previously described 25 kW system [3]. In systems fed with pure oxygen, the coolant pump is the main parasitic power consumer and for this test system it has been considerably over-dimensioned, so resulting efficiencies in the present 7 kW$_{peak}$ system are lower than published previously for larger system power.

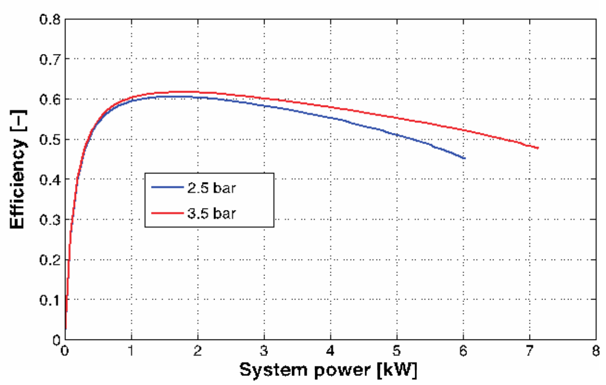

***Figure 4.** Efficiency of H_2/O_2 fuel cell system operated at current densities up to 2 A/cm^2, using non-optimized (oversized) system components developed for 30 kW level systems.*

Conclusions

The losses from the oxygen reduction reaction in PEFC can be reduced when increasing the oxygen partial pressure by using pure oxygen as the oxidant. It is shown that also on the system level, high current and power densities, in excess of 2 A/cm^2 and 1.2 W/cm^2, respectively can be obtained at interesting system efficiencies.

This opens up the application of H_2/O_2 systems for various niche applications.

Acknowledgement

These results have been obtained in course of a joint project between PSI and Belenos Clean Power. Financial support by Belenos Clean Power is gratefully acknowledged.

References

[1] K.C. Neyerlin, Wenbin Gu, Jacob Jorne, and Hubert A. Gasteiger, J. Electrochem. Soc. **153**, A1955-A1963 (2006).

[2] A. Parthasarathy, S. Srinivasan, A.J. Appleby and C.R. Martin, J. Electrochem. Soc. **139**, 2856-2862 (1992).

[3] H.A. Gasteiger, S.S. Kocha, B. Sompalli, F.T. Wagner, Appl. Catal. B Environ. **56,** 9–35 (2005).

[4] F.N. Büchi, J. Bernard, M. Hofer, U. Hannessen, P. Dietrich, PSI Electrochemistry Laboratory Annual Report 2011, 37–38 (2012).

---

[1] Belenos Clean Power Holding, Marin, CH

Dynamic properties of H_2/O_2 PEFC systems

M. Hofer, F.N. Büchi, J. Bernard, U. Hannessen[1], A. Closset[1], P. Dietrich

phone: +41 56 310 2411, e-mail: felix.buechi@psi.ch

In conventional fuel cell systems, oxygen from the ambient air is consumed at the cathode. In most system designs, in particular for those used in road transport applications, the air is fed into the cathode using a blower or compressor.

In these system designs the air compressor is the limiting factor in dynamic response when increasing the system power. Finite time is required for accelerating the moving parts in the compressor and the air in the dead volume of stack and piping in order to satisfy the rising air mass flow demand. Consequently several 100 ms up to some seconds are typically necessary for large steps of power increase.

The absence of a compressor and a minimized dead volume in pressurized oxygen fed systems is therefore a major advantage for dynamic operation. The pressure regulating valve and it’s control feedback loop become the limiting factors. However these components exhibit a considerably lower lag than those of the air supply path. Highly dynamic power changes with minimal pressure excursions become thus possible.

Results

In order to demonstrate the dynamic possibilities of oxygen systems, the prototype system presented recently [1] with a 182 cell stack has been evaluated in a dynamic test protocol (see Figure 1). Current steps of different size, up to idling to full rated power of 25 kW have been prescribed to the system. The rising current step at 180 s has a transient time of 20 ms and at 190s a falling time of again 20 ms. The pressure excursions are moderate and remain below 100 mbar.

Figure 2 shows the stability of the system at the transients at 180 and 190 s. In this Figure time 0 denotes the time of the rising transient. The top row shows the voltage of the fuel cell system, for the fast power increasing transient no undershoot is observed in the voltage (for the given 10 Hz sampling rate), after the power decreasing transient a relatively slow increase to regain the idling voltage in the order of 1V/cell is observed.

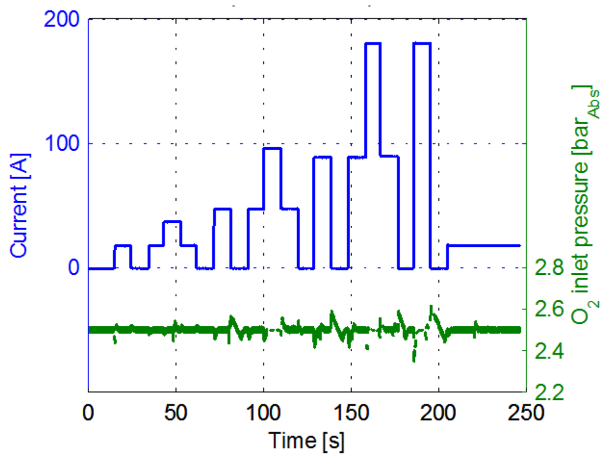

Figure 1*. Dynamic operation of 25 kW H_2/O_2 system based on 182-cell stack*

The middle and bottom row of Figure 2 show the maximum and minimum single cell voltages of the 182 cell stack and the standard deviation of the individual cell voltages, respectively. The data shows that after the power increase the homogeneity of the cell voltage distribution worsens only slightly. The standard deviation increases from 2.5 to less than 5 mV and the deviation between the highest and lowest cell does not exceed 25 mV at any time.

In conclusion, the presented data show the excellent dynamics, which can be obtained with a H_2/O_2 fuel cell system in the 25 kW class.

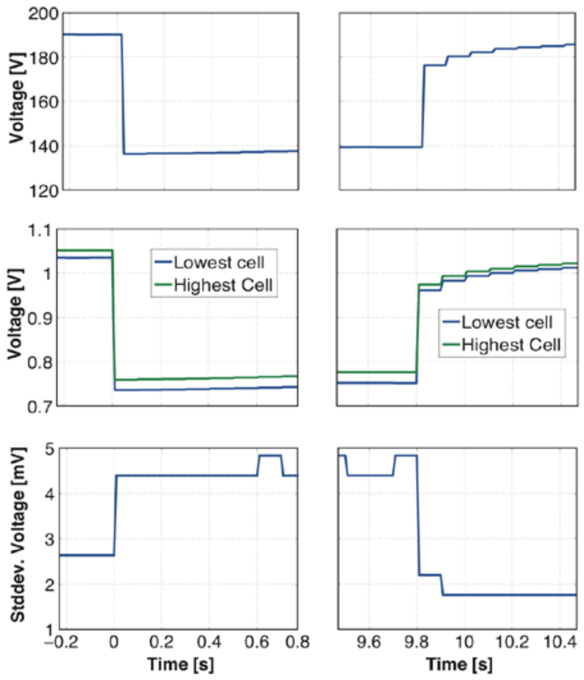

Figure 2*. Dynamic response at transients at 180 s and 190s in Figure 1 of (top) system voltage, (middle) highest and lowest cell voltage and (bottom) std. deviation of voltage.*

Acknowledgement

These results have been obtained in course of a joint project between PSI and Belenos Clean Power. Financial support by Belenos Clean Power is gratefully acknowledged.

References

[1] F.N. Büchi, J. Bernard, M. Hofer, U. Hannessen, P. Dietrich, PSI Electrochemistry Laboratory Annual Report 2011, 37-38 (2012).

---

[1] Belenos Clean Power Holding, Bienne, CH

Towards high accuracy water transfer measurement in differential PEFCs

P. Boillat, P. Oberholzer, F. Bernauer, T.J. Schmidt, A. Wokaun

phone: +41 56 310 2743, e-mail: pierre.boillat@psi.ch

As water management is a key issue in the development of polymer electrolyte fuel cells (PEFCs), many researchers have addressed the question of measuring the water transfer characteristics in operating cells (e.g. [1,2]). Such measurements are very challenging in so called *differential cells* – small scale cells operated on high stoichiometries, in order to ensure a homogeneous distribution of parameters – as the difference of humidity between the inlets and outlets are very small [3]. Measurements based on the difference of two absolute humidity sensors will suffer from important errors, and a measurement principle which is intrinsically differential is expected to yield better results. Our proposed method consists in measuring the open cell voltage in a H_2/H_2 concentration cell. Due to the coupling between proton and water transport by electro-osmotic drag, water can be considered as a part of the electrochemical reaction [4] and the open cell voltage calculated by the Nernst equation depends on the H_2O partial pressures on both sides of the concentration cell. We present here a summary of the results obtained with this method, which are published in ref. [5].

Experimental

The final proposed method consists in measuring the differential humidity between the anode inlet and outlet (setup shown in superimposition in Figure 1). However, the measurements reported here were conducted with a validation setup implying no operating cell. In this setup, a small flow of dry hydrogen is mixed with the main flow of humidified hydrogen at the position where the anode of the operating cell would be. This allows generating precise differences of humidity based on the known gas flows.

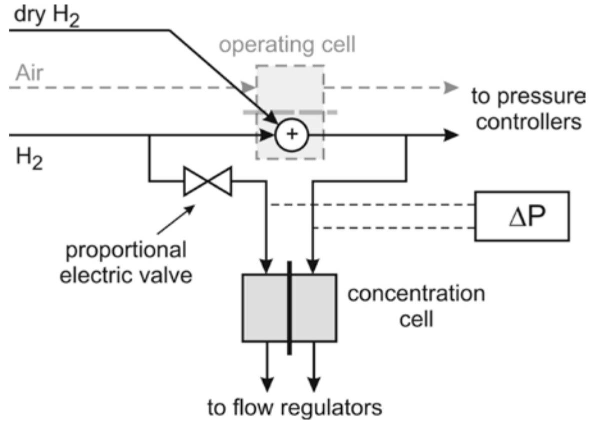

Figure 1. *Experimental setup used for the validation measurements reported here. The position where the operating cell would be in the final method is shown in light gray.*

Additionally, a control valve was included in one of the gas flows, allowing a change of the differential pressure between both sides of the concentration cell. As detailled in ref. [5], the sensitivity of the concentration cell can be calibrated based on the voltage change measured as a response to pressure changes. Thus, with this setup, no preliminary calibration is necessary. The results reported here were obtained at a temperature of 26˚C and with a hydrogen dew point of 14˚C. The main gas flow was 4 nlm and the mixed dry gas flow was between 0 and 0.2 nlm to produce values of differential humidity between 0 and 5%. Additional conditions are published in ref. [5].

Results

The comparison of the measured differential humidity with its "real" value (calculated on the base of the known gas flows) is presented in Figure 2. A very good agreement is obtained, and the analysis of transitions also shows a reasonable dynamic response (stabilization of the measurements in 10-15 seconds after the change).

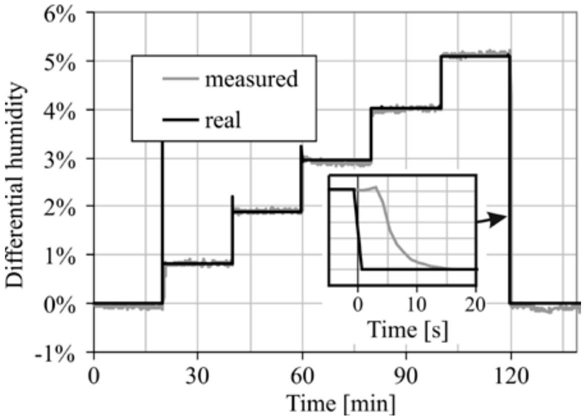

Figure 2. *Comparison of the differential humidity measured with our proposed principle with the "real" value.*

For this experiment (running over 16 hours without any preliminary calibration), the maximal error based on values averaged over 1 minute periods fell comfortably within the target range of +/-0.25%. This precision on the differential humidity is required for obtaining a 5% precision on the water transfer in a cell with 5% differential humidity between the inlet and outlet. At higher temperature (experiments reported in ref. [5]), an increased bias was observed. However, with a preliminary calibration and for experiments running over a period of 5 days, the target accuracy of 0.25% could be obtained as well.

In summary, the realized work has shown that the proposed differential humidity measurement principle has a high potential for performing water transfer measurement with a good accuracy, even in the very challenging case of differential cells.

References

[1] K.-H. Choi, D.-H. Peck, C.S. Kim, D.-R. Shin, and T.-H. Lee, *J. Power Sources* **86**, 197 (2000).

[2] T. Colinart, A. Chenu, S. Didierjean, O. Lottin, and S. Besse, *J. Power Sources* **190**, 230 (2009).

[3] P. Sauriol, D.S. Nobes, X.T. Bi, J. Stumper, D. Jones, and D. Kiel, *J. Fuel Cell Sci. Tech.* **6**, 041014 (2009).

[4] T.F. Fuller and J. Newman, *J. Electrochem. Soc.* **139**, 1332 (1992).

[5] P. Boillat, P. Oberholzer, F. Neuschütz, T.J. Schmidt, A. Wokaun, *Electrochem. Commun.* **22**, 12 (2012).

Distinction of liquid water and ice based on dual spectrum neutron imaging

J. Biesdorf, P. Boillat, P. Oberholzer, F. Bernauer, A. Kaestner, E.H Lehmann, T.J. Schmidt

phone: + 41 56 310 57 27, e-mail: johannes.biesdorf@psi.ch

To be able to replace combustion engines in automotive applications, polymer electrolyte membrane fuel cells (PEFCs) have to resist against various weather conditions, such as subfreezing temperatures. Polymer electrolyte membranes have a reasonable proton conductivity in sub zero temperatures, allowing start up without preliminary heating, but the frozen product water can block the electrodes. In a previous study [1], the role of super-cooled water was highlighted and a relation between the freezing of water and a sudden shutdown of the cell was established. As the freezing of water shows a statistical fluctuation [1], it is crucial to improve the understanding of this process. In this context, the possibility of a direct visualization of the aggregate state (liquid or solid) of water is highly desired.

In the last decade, neutron imaging has shown its usefulness as a non-destructive imaging technique, visualizing the water distribution inside PEFCs [1,2]. Some studies [3,4] addressed the energy-dependent attenuations of neutrons for liquid water and for ice. Differences were reported in the lowest energy range, starting at a wavelength of approx. 3Å and increasing for longer wavelengths. As an important portion of the spectrum of the ICON beamline at PSI [5] covers the range below 3Å, no significant deviations between liquid and solid phase are identifiable when using the white beam. Introducing a polycrystalline beryllium filter in the neutron beam, the neutrons underneath a wavelength of 3.95A are removed. This is expected to emphasize the lowest energy range, which will increase the contrast between the phase transitions between liquid water and ice.

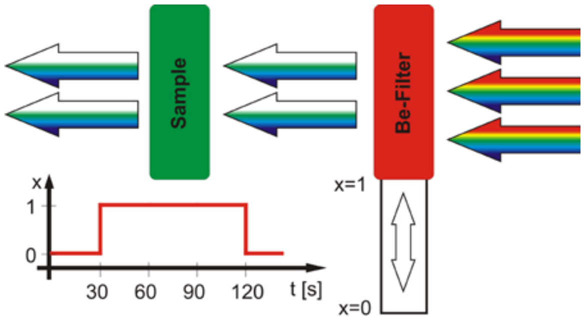

Figure 1. *Illustration of the technical implementation of dual spectrum measurements using a polycrystalline beryllium filter. A motorization of the filter allows consecutive images with and without filter.*

Experimental

Measurements with the filtered beam alone do not allow the identification of the aggregate state, because neither the molar density nor the thickness of water is known. Therefore, the analysis is based on relative attenuations, comparing exposures of the filtered and unfiltered beam at the same conditions. As the water distribution inside a fuel cell may change over time, consecutive images with and without filter (dual spectrum) were acquired (see figure 1). Keeping in mind that neutrons below a certain wavelength λ_c are scattered, the flux is reduced passing through the filter. In order to have a similar image quality for both images, longer exposure times were used for the filtered beam. Therefore, acquisition intervals of 90s and 30s were chosen for the exposure with and without filter, respectively (see figure 1).

In order to determine reference values for the relative attenuations, measurements with a cylindrical water column (Ø1.7x10mm) have been realized. Additionally to expected attenuation changes, this sample facilitates the observation of phase transitions due to volumetric expansions. The measurement protocol consists of freezing at -15°C and subsequent measurements of one hour duration at different temperatures.

Measurements with a differential fuel cell (using the fuel cell setup described in ref. [1] but with a lower imaging resolution) were performed as well. In contrast to the previous sample, water is only partly filling the available space. Volume expansion due to freezing will occur locally and the average water thickness will not change. In the present study, the analysis is focused on the flow channels of the cathode, as the resolution of the used setup is too limited to address other regions of the fuel cell such as the gas diffusion layer (GDL).

Temperature-dependent attenuations of water and ice have been published in ref. [4]. To avoid any effect of temperature differences, the subsequent procedure to form super-cooled water at a constant temperature T_{wrk} in a PEFC has been elaborated:

I. Current production (0.1 Acm^{-2}) at T_{wrk} (0.5h)
II. Imaging in super-cooled state at T_{wrk} (1h)
III. Freezing at T=-15°C (0.5h)
IV. Imaging in frozen state at T_{wrk} (1h)

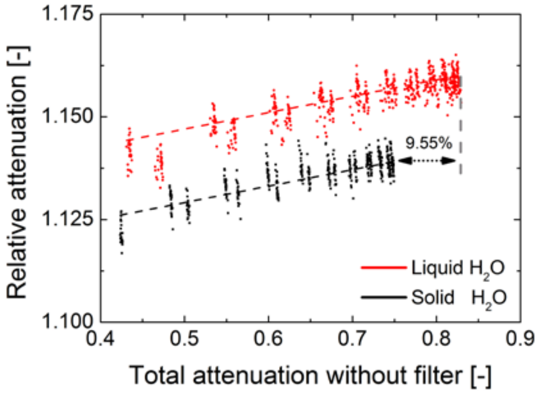

Figure 2. *Ratio between the attenuation of neutrons by H_2O with and without filter at liquid and solid phase as a function of the total attenuation without filter. A difference of about 1.8% can be found between the two phases.*

Results

In the following paragraph, the results obtained with the cylindrical water column are presented. Figure 2 defines reference values of the ratio between the neutron attenuation by H_2O with and without filter. The ratio is plotted for different positions in the cylinder as a function of the total attenuation without filter. A shift on the horizontal axis of 9.5% can be observed between ice and water, resulting from the volumetric expansion during freezing. As expected, due to the decreasing attenuation of H_2O with increasing energy [3], the attenuation ratio is higher than 1. A variation of the attenuation ratio as a function of thickness is observed, which might be related to different beam hardening effects in the filtered and unfiltered beam. As targeted, an effect of the aggregate state on the attenuation ratio is measured, with a higher value for liquid water (~1.8%) than for ice.

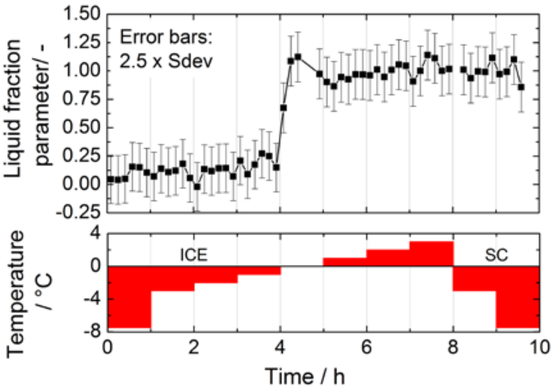

Figure 3. *Liquid fraction parameter indicates the aggregate state of water inside a cylindrical water column. At subfreezing temperatures values around 0 (ice) are obtained, whereas the value of the function increases to 1(liquid) passing through the freezing point of water.*

Based on this data, a liquid fraction parameter is introduced as a linear combination of the attenuation ratio and the attenuation without filter, referencing the average functions (see figure 2 dashed lines) towards 0 (ice) and 1 (liquid). Figure 3 illustrates the temporal evolution of this parameter during a temperature ramp from -7.5°C to 3°C. At each function value, an average over the entire volume of the cylinder is calculated during 10 minutes. As expected, a single-phase transition occurred at 0°C. No phase transformation can be observed during the last two measurements at -3°C and -7.5°C, where the water is in super-cooled state.

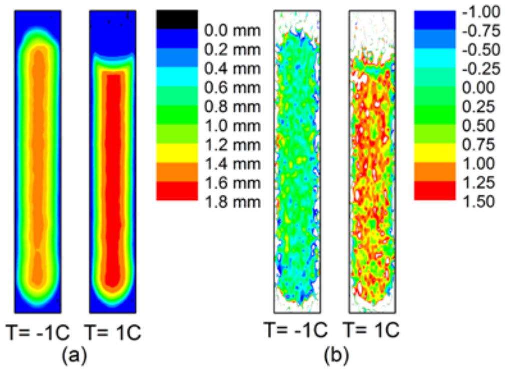

Figure 4. *(a) Distribution of equivalent thickness of liquid water inside the cylindrical water column at frozen and liquid phase. (b) Distribution of the liquid fraction parameter for the same experiments.*

The measured spatial distribution of the water equivalent thickness (WET), corresponding to the thickness measured based on the attenuation coefficient of liquid water, is illustrated in figure 4 (a) for two different states (liquid water and ice). Because of the lower density of ice, the WET is reduced at -1°C. Figure 4 (b) shows the spatial resolution of the previously presented liquid fraction parameter. Although the result is relatively noisy, a general picture of the spatial distribution can be obtained with the long integration time used here (1 hour).

In the following paragraph, the average liquid fraction parameter inside the flow channels of a fuel cell is presented (see figure 5). Three different experiments were performed at working temperatures T_{wrk} of -7.5°C, -5°C and -2.5°C. After the third test, a supplementary temperature ramp has been performed.

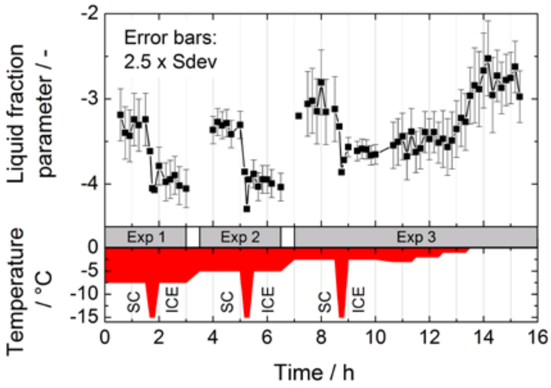

Figure 5. *Temporal evolution of the liquid fraction parameter inside the flow channels of a fuel cell.*

Even though the values obtained are significantly outside of the allowed range (0.0 – 1.0), phase transitions can clearly be identified at all three working temperatures, as well as during the 0˚C crossing in the temperature ramp. In contrast to measurements with the cylindrical water column, the spatial distribution of the liquid fraction parameter shows strongly inhomogeneous values, which is not physically expected. The reasons for the discrepancies with the water column experiment are still under investigation.

In summary, the distinction of liquid water from ice using dual spectrum neutron imaging has been demonstrated using a cylindrical water column. The results of measurements on water droplets in a fuel cell show important discrepancies with these reference measurements, preventing an absolute measurement of the aggregate state. Despite this, phase transitions in the fuel cell can clearly be identified.

References

[1] P. Oberholzer, P. Boillat, R. Siegrist, R. Perego, A. Kästner, E. Lehmann, G.G. Scherer, A. Wokaun, Journal of the electrochemical society **159**, B235-B245 (2012).

[2] P. Boillat, D. Kramer, B.C. Seyfang, G. Frei, E. Lehmann, G.G. Scherrer, A. Wokaun, Y. Ichikawa, Y. Tasaki, K. Shinohara, Electrochemistry Communications, **10**, 546-550 (2008).

[3] L. Torres, J.R. Granada, J.J. Blostein, Nuclear Instruments and Methods in Physics Research B, **251**, 304-305 (2006).

[4] L. Josic, E.H. Lehmann, D. Mannes, N. Kardjilov, A. Hilger, Nuclear Instruments and Methods on Physic Research A, **670**, 68-72 (2012).

[5] A.P. Kaestner, S. Hartmann, G. Kühne, G. Frei, C. Grünzweig, L. Josic, F. Schmid, E.H. Lehmann, Nucl. Instr. Meth. *A* **659**, 387 (2011).

In situ X-ray tomography of PEFC at isothermal freeze – start at -10 °C

J. Roth, M. Zurbrügg, F.N. Büchi

phone: +41 56 310 5396, e-mail: joerg.roth@psi.ch

Fuel cell start-up at temperatures below freezing represents still a challenge for polymer electrolyte fuel cell powered devices. Engineering solutions, primarily dealing with shutdown strategies prior to freezing are state of the art to deal with freezing induced degradation. Yet, at start–up below freezing temperature, the product water removal is a major challenge since ice can limit the gas transport in the channel, GDL and catalyst layer. Under non-isothermal conditions, the start-up is successful if the self-generated heat is sufficient to thaw the cell before ice-formation. This depends on the temperature of the environment and the power profile at start-up.

Experiments under isothermal conditions below 0 °C show that the cell operates for a certain time, and then the power drops to an extremely low level. The runtime depends on the current density and temperature. The isothermal freeze-start is investigated by means of X-ray tomographic microscopy to explore the circumstances of freezing induced termination of electric power production. This study aims at quantitative imaging of the solid/liquid water distribution during start-up which can finally lead to improved material/operating condition to enable reliable fuel cell system start-ups under freezing conditions.

Experimental

To visualize ice during isothermal freeze start-up, the following sequence was applied: after drying the cell by purging (membrane resistance: 0.25 Ωcm^2) and cooling the cell is started in potentiostatic mode (0.5 V) at -10 °C and ambient pressure. The cell is fed with pure oxygen and hydrogen at flow rates of 8 ml min^{-1} of 16 ml min, respectively. This corresponds to gas channel velocities of 0.8 ms^{-1} and 1.6 ms^{-1}. The potential and the temperature are held constant for the duration of the current production. Tomographic images are taken during the start-up until the current drops below 20 mAcm^{-2}. One minute after start-up the first image is taken. Successive scans are taken until the shutdown criterion is reached. Since the images have no contrast between water and ice, it is not possible to distinguish the phases. After the shutdown a gas purge (gas channel velocity at cathode: 22 ms^{-1}) is applied to remove liquid water from the flow field channels and several scans are taken under purge conditions.

The fuel cell design is accustomed to the requirements of the X-ray tomographic microscopy (XTM) experiment: it can rotate freely in front of the microscope and allows for high contrast images and extended exposure times. The heat management is based on an external air/nitrogen stream as thermofluid for heating and cooling. Figure 1 shows the XTM- setup and the heat management system. The cell was operated at the TOMCAT beamline of the Swiss Light Source [1] with the fast tomography setup in combination with the 2-4x microscope and the "Edge" camera system.

The cell is assembled with a Nafion 212 membrane coated with gas diffusion electrodes (0.6 mg cm^{-2} Pt total) and Toray 060 gas diffusion layers, impregnated with 10% PTFE but no MPL. The flow fields have an S-shaped single pass meander and are made of graphite (BMA5, SGL).

Threshold segmentation of subtracted images (dry images subtracted from wet image) was applied to post process the images (described in more detail by Eller et al. [2]). A volume of 4.8 mm^{-3} comprising the cathode GDL and the cathode flow channel is used to calculate the total water/ice mass.

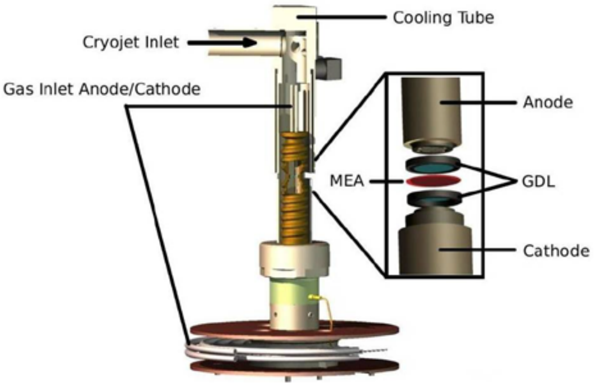

Figure 1. *Model of the differential cell with the cooling tube allowing for freezing experiments down to -20 °C. The cell and the cooling setup are customized to meet the requirements for XTM-imaging.*

Results

Isothermal - potentiostatic freeze starts have the general characteristic of increasing current, followed by a more or less sharp current drop. The duration of this period is highly variable. In the experiment shown here, the cell operates for 6 minutes (see Figure 2).

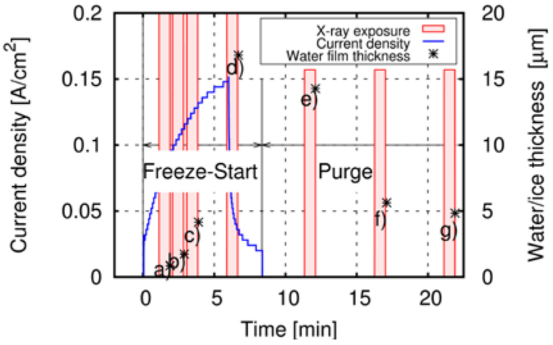

Figure 2. *Freeze-start response at -10°C, 0.5~V and isothermal conditions. The labels refer to the data presented in Figures 3 and 4.*

At the freeze-start, the current increased up to about~0.15 Acm^{-2}. Beyond this point, the current drops off sharply because of the ice/water induced effects. The ice/water volume, obtained from imaging, increases. Due to the water adsorption capability it its likely that membrane/catalyst layer stores water in the similar order of magnitude. The imaging revealed that the condensed water appears only in the cathode part of the cell under

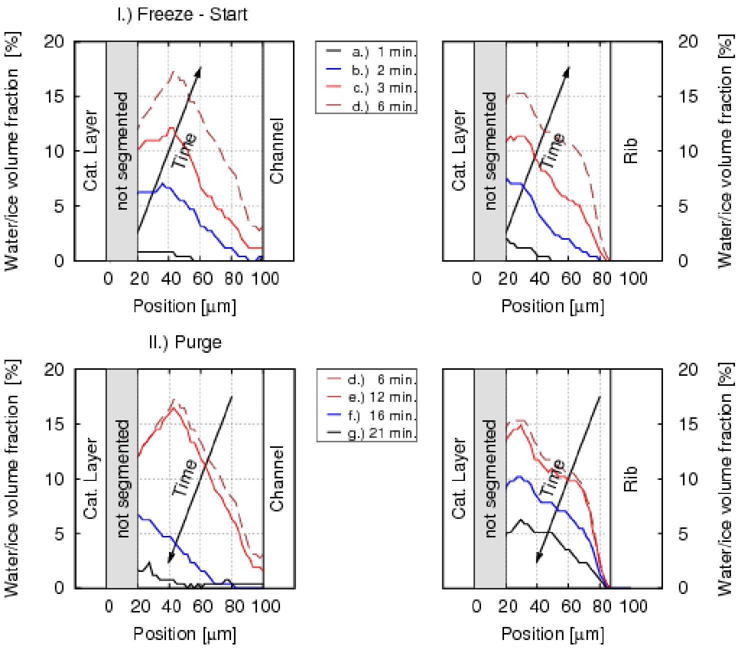

Figure 3. *Development of water volume fraction across the GDL for the channel (left) and rib (right) during the freeze-start (top) and purge (bottom) at -10°C. The time labels refer to the positions marked in Figures 2.*

the given test conditions, therefore only the cathode compartment is discussed further.

The water profile in the GDL is examined in detail for a rib/channel combination. Figure 3 shows the time dependent water profiles as ice/water volume fractions for the channel (left) and rib (right) locations for the freeze-start (upper image) and the purge (lower image).

The profiles show that the water fraction in the GDL has a peak at around 50 µm from the catalyst layer. With increasing duration of the experiment, the water fraction increases while the peak position varies only little. During the current production phase, first (e.g. 3 after minutes), water accumulates in the GDL under rib and channel with a similar rate. However, at the time of the current shutdown after about 5 min, slightly more water in the GDL is found under the channel (0.20 mg/cm^2, a peak water fraction in the GDL of 17%) as compared to the rib (0.18 mg/cm^2 a peak of 15%), respectively. The zone next to the catalyst layer is not segmented due to the enhanced noise level in the image caused by the platinum.

The purge phase was analysed the same way. It turned out that purging removes the condensed water phase primarily from the channel area.

A further analysis shows that the accumulated water/ice the cathode compartment (GDL and channel) film thickness (volume/area) grows up to 16.5 µm. About 46% of the total water is located in the GDL at shutdown resulting in a saturation of about 12%.

The purge experiment, aimed at investigating, if the water in the channel was liquid after the shut-down of the current. It had been postulated (e.g. in [3]) that the water reaches the channel in super cooled form and may thus be removed with high gas speed. However 4 minute purge at 22 ms^{-1} gas channel velocity does not remove a significant fraction of water from the channel. After 10 minutes of purging, the condensed water phase in the channel has disappeared, probably by sublimation as the water vapour pressures over super cooled water and ice are similar. In the GDL the ice fraction levels off at about 70 % of it's maximum value. The further decrease of water mass between 10 minutes and 15 minutes is probably due to sublimation.

Conclusions

The XTM study revealed that the produced water at -10°C penetrates the GDL and reaches the channel. This is an indication that it is in liquid phase initially. Within 6 min of operation the cathode GDL saturates up to 12%. Since the purge 4 min after shutdown did not clear the channel to a large extent, it is reasonable to assume that the water is frozen at shutdown. The ice/water build-up occurs with an intensity and dynamic in the GDL largely independent from the rib/channel boundary condition, while the purge affects primarily the GDL under the channel.

Acknowledgements

Precise machining work by M. Hottiger, software and electronic support by T. Gloor, support at the beamline by J. Eller, T. Fedtke, I. Weissensteiner, S. Kreitmeier, the SLS TOMCAT Team, namely F. Marone, S. Irvine, and M. Stampanoni (all PSI) and last but no least the financial support by Belenos and BFE are gratefully acknowledged.

References

[1] J. Eller, T. Rosén, F. Marone, M. Stampanoni, A. Wokaun, F.N. Büchi, J. Electrochem. Soc. 158, B963 (2011).

[2] M. Stampanoni, TOMCAT, Beamline Layout, Optics. http://www.psi.ch./sls/tomcat/optics (2011).

[3] P. Oberholzer, P. Boillat, R. Siegrist, R. Perego, A. Kästner, E. Lehmann, G.G. Scherer, A. Wokaun, J. Electrochem. Soc. 159, B235 (2012).

Influence of feed gas humidity and current density on the 3D water distribution in PEFC

J. Eller, R. Gaudenzi, J. Roth , S. Irvine F. Marone, M. Stampanoni, F.N. Büchi

phone: +41 56 310 2411, e-mail: felix.buechi@psi.ch

Efficient water removal and water management is crucial for the performance of polymer electrolyte fuel cells (PEFC), especially at high load operation. The two phase properties of the gas diffusion layer (GDL) in PEFC are therefore characterized by visualization of the liquid water pattern and local saturation by *in situ* by X-ray tomographic microscopy (XTM) [1]. Cells are operated close to the optimal performance point at 80 °C (dew point of reactant gases 74 °C). A variation of ± 8 °C of the feed gas dew point leads to significant saturation and performance changes. The water saturation and permeability of the liquid phase of the cathode are determined and analyzed for different current densities.

Method and Experimental

A specially designed two-channel (0.8 mm width, 0.3 mm depth) PEFC with vertical MEA orientation and cell active area of 16 mm² was used for the XTM experiments. The two-channel design is required to obtain saturation and water distribution data in the rib region without boundary bias, as the case in a single channel cell. Two different flow field designs, differing only in the rib width (0.8 and 1.6 mm) were used (see Figure 1). H200 (Umicore, Germany) catalyst coated membrane (CCM, 2-mil Nafion® membrane with Pt loading of 0.2/0.4 mg/cm^2 at anode/cathode) and Toray TGP-H060 paper GDLs with micro porous layer (MPL) were used. The MEA's were compressed to 450 µm between the ribs of the flow field, corresponding to a GDL compression to about 75% of their initial thickness.

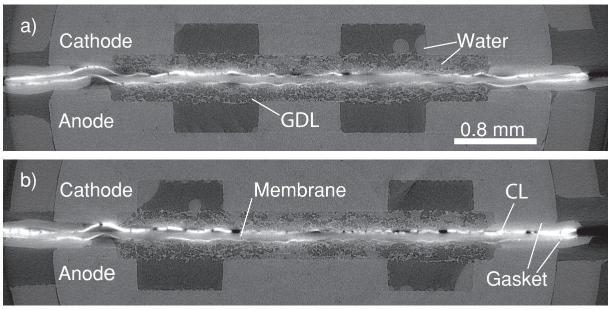

Figure 1. *XTM ortho-slices in through-plane direction of a) cell with narrow ribs (0.8 mm), at set point A03; b) cell with wide rib (0.8 mm) at set point A13. Reproduced from Eller et al. [1] with permissions of the Electrochemical Society. Copyright 2012 The Electrochemical Society.*

At the TOMCAT beamline at SLS a fast camera based on CMOS technology (pco.Dimax, Germany) is available. The chip has 2016 × 2016 pixels with a pitch of 11 µm. The exposure time ranges from 1.5 µs to 40 ms allowing ultra fast XTM scans to be realized within half a second [2]. The pco.Dimax camera was mounted on a microscope (ELYA solutions, Czech Republic) equipped with a continuous zoom objective providing magnification ranging from 2× to 3.9×. At the highest magnification and for a full chip readout, this combination provides a pixel size of 2.9 × 2.9 µm², about 5.8 × 5.8 mm² field of view and 2.44×10^{-17} m³ voxel size (2.44×10^{-2} pL).

In situ XTM scans in absorption contrast mode with 2.9 µm pixel edge length were acquired at 13.5 keV beam energy. The exposure time per projection was 10 ms, so rotating the cell 180° while taking 1001 radiographic projections led to a total SR exposure of 10 s per scan.

In order to provide the required operating conditions with dew points of the reactants around 80 °C, the set-up was equipped with in-house designed heated gas tubes which allow the cell to turn without exerting too much torque to allow for an undisturbed imaging process.

At the beamline, the cells were operated at constant current at 80 °C cell temperature in differential mode with H_2/Air or H_2/O_2 (100 Nml/min each; stoichiometries > 10) humidified at the required dew point. All data was obtained at atmospheric gas pressures. During the experiments the 1 kHz high frequency resistance (HFR) of the cells was monitored with a Tsuruga E3566 AC milliohm meter as a measure of membrane resistivity and thereby membrane humidification.

Table 1 gives an overview of the cell parameters for the operation points where XTM images were recorded. For the cells and operating conditions with air at the cathode (A*nn*), the influence of dew point of the gases (at ± 8 °C around the optimal performance point of 74 °C) and the width of the rib on cell potential and water distribution was studied at a current density of 0.75 A/cm^2. One cell was also operated with oxygen as the cathode reactant in order to access a large range of current densities. For the conditions with oxygen (O*n*), the water phase was therefore imaged at four different current densities between 0.75 and 3.0 A/cm^2 at the optimum humidification condition found for the H_2/Air case at 0.75 A/cm^2.

Experiment ID	Cathode Gas	Dew point [°C]	Current Density [A/cm^2]	Rib Size
O1	Oxygen	74	0.75	Narrow
O2	Oxygen	74	1.50	Narrow
O3	Oxygen	74	2.25	Narrow
O4	Oxygen	74	3.00	Narrow
A01	Air	66	0.75	Narrow
A02	Air	74	0.75	Narrow
A03	Air	82	0.75	Narrow
A12	Air	74	0.75	Wide
A13	Air	82	0.75	Wide

Table 1. *Cell and set point characteristics.*

The segmented data of the MPL-free GDL domain was evaluated using the GeoDict Software [3] package for through-plane permeability of the gaseous phase in the cathode GDL for wet and dry conditions, as well as for the liquid phase permeability of the wet case.

Results

At the optimal performance point (dew points 74°C, 78% rH, see Figure 2) for the current density of 0.75 A/cm^2 no liquid water was detected in the rib area of the cathode GDL in the cell with the narrow rib. However, in the cell with the wide rib a maximum saturation of 0.4 is found (see Figures 3 and 4). At 8°C above the optimal humidification temperature (108% rH) a cathode GDL saturation in the order of 25% (channels) and 50% (ribs) was observed at cell voltage drop of about 70 mV. When increasing the current density at the optimal humidification point for H2/Air operation and 0.75 A/cm^2 the saturation increased, reaching values up to 60% under the rib with H2/O2 operation at 3.0 A/cm^2 (see bottom of Figure 4).

Numerous small water clusters with a volume below 0.5 nl are identified both under ribs and channels, but the overall GDL saturation is determined by few clusters with volumes above 1 nl. Under the ribs water clusters with a volume of up to 120 nl have been identified in the GDL. Under the channels the cluster size reached a maximum of 20 nl at over-saturated conditions and only water clusters with a volume of at least 0.2 nl contribute to through-plane liquid transport paths towards the channel.

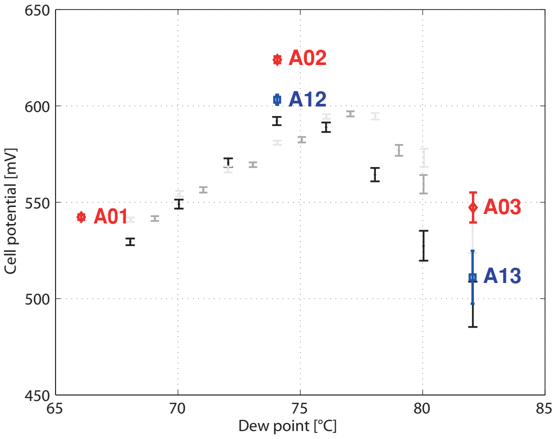

Figure 2. *Cell voltage for H_2/Air operation at 0.75 A/cm^2 as function of gas dew point; labels refer to conditions imaged by XTM; gray symbols (right) indicate pre-characterization results for different cells. Reproduced from Eller et al. [1] with permissions of the Electrochemical Society. Copyright 2012 The Electrochemical Society.*

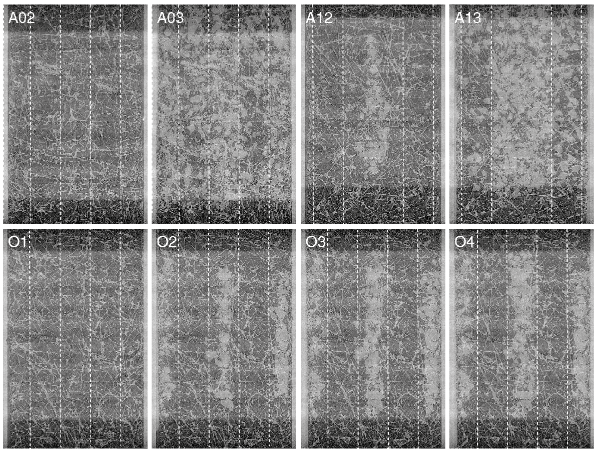

Figure 3. *In plane slices through the cathode GDL for different imaging conditions; white dashed lines indicating the edges of the flow field ribs/channels; gas flow direction was from bottom to top; active area of the cells can be identified by a brighter area over the whole slice width (in case of the wide rib cell (A12, A13), the active area was slightly higher positioned compared to the other cells). Reproduced from Eller et al. [1] with permissions of the Electrochemical Society. Copyright 2012 The Electrochemical Society.*

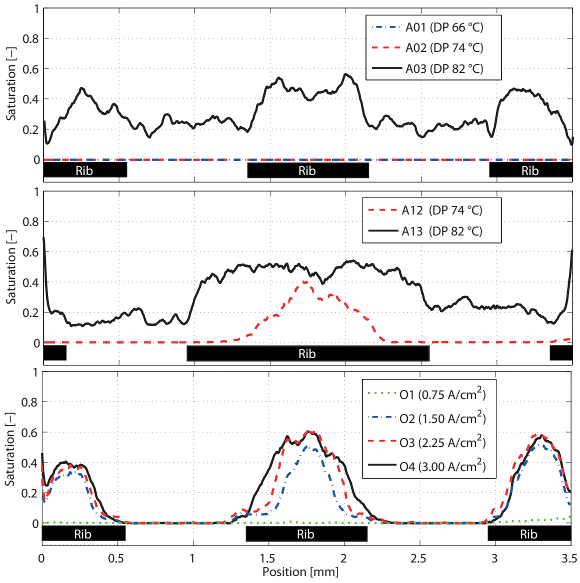

Figure 4. *Saturation profiles of cathode GDL across the cell width averaged along the active area (4.5 mm) and for a height of 90µm of the GDL from the channel/rib-GDL interface.*

The through-plane liquid phase permeability shows a positive correlation to the water saturation (see Figure 5). The highest absolute and relative water permeability was observed for the wet conditions in the GDL under the wider rib. A cubic power law description $\kappa_{rl} = s^3$ is clearly underestimating the relative liquid permeability under the ribs and probably also under the channels. For the relative gas phase permeabilities the dependency $\kappa_{rg} = (1 - s)^3$ seems to be valid also at higher gas feed humidities and current densities (see Figure 5).

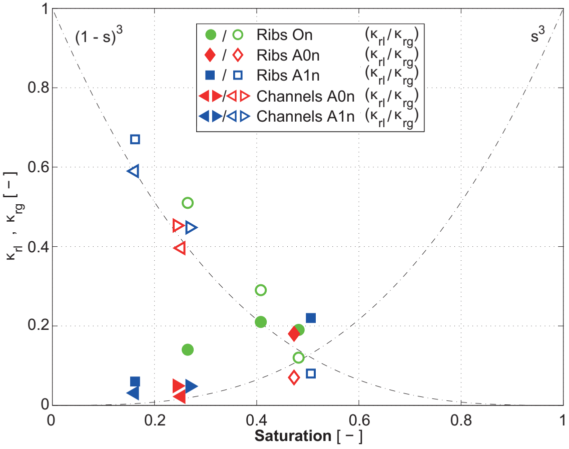

Figure 5. *Through-plane relative liquid (κ_{rl}, filled symbols) and gaseous (κ_{rg}, empty symbols) permeabilities for rib and channel domains of conditions with GDL saturation different than zero.*

References

[1] J. Eller, J. Roth, R. Gaudenzi, S. Irvine, F. Marone, M. Stampanoni, A. Wokaun, F.N. Büchi, ECS Trans. **50**, 477-486 (2012).

[2] R. Mokso, F. Marone, M. Stampanoni, AIP Conf. Proc. **87**, 1234 (2010).

[3] GeoDict. http://www.math2market.com/.

First results of HT-PEFC X-ray tomographic microscopy

S.H. Eberhardt, F.N. Büchi, T.J. Schmidt

phone: +41 56 310 2541, e-mail: sebastian.eberhardt@psi.ch

High temperature polymer electrolyte fuel cells (HT-PEFCs) exhibit an increased CO-tolerance of up to 2% in the anode feed [1] due to faster CO-oxidation kinetics at operating temperatures of 160-190°C. In order to sustain the high temperatures membranes based on a polybenzimidazole backbone doped with phosphoric acid (PA) [2] are used. The high CO tolerance, compared to (low temperature) PEFCs, is a significant system advantage of HT-PEFCs allowing to use H_2 rich reformate gas without expensive clean-up.

A major factor to allow for commercialization of PEFC for co-generation applications is to achieve a lifetime of more than 40'000 h without losing significant performance. Several degradation mechanisms have been investigated and reported in literature [2]. Electrode (Pt-particle detachment and agglomeration and carbon corrosion), membrane (thinning and pinhole formation) and GDL degradation (structural change and flooding) as well as evaporation of phosphoric acid electrolyte have been identified as the most critical life-limiting factors. Acid evaporation and redistribution is exclusive to HT-PEFCs and its *in situ* characterization is of importance for a better understanding of the underlying mechanisms. Therefore, X-ray tomographic microscopy (XTM) has been applied to visualize the acid inventory and movement in the GDL for correlation with performance. The ability to quantify the amount of phosphoric acid as well as to distinguish between different concentrations are key factors for evaluating performance degradation.

Experimental

BASF Celtec B 2611 membrane-electrode-assemblies with a SGL 34BA (5% PTFE) carbon cloth and an active area of 0.28 cm^2 were visualized *ex situ* at the TOMCAT beamline of the Swiss Light Source (SLS). A beam energy of 20 keV and an exposure time of 25 ms (nnn projections) were applied. For the reconstruction of the different projections a PACT reconstruction algorithm [3] was used. The anode flow field was replaced by a Kapton cylinder with four holes of 1 mm diameter which were used for reference fluids: ortho-phosphoric acid with 40 and 85 wt%, demineralized water and air.

Results

Figure 1 shows the comparison of the greyscale images for the phosphoric acid wetted carbon fibres of the GDL close to the membrane and close the flow field. The darkest greyscale represents the void while brighter greyscales represent carbon fibres, PA and the microporous layer (MPL) with phosphoric acid filled pores. The phosphoric acid shows a significant through-plane saturation gradient with high saturation close to the membrane and lower saturation at the flow field interface.

The resulting greyscale plot of the two images in Figure 1 as well as the reference with phosphoric acid of different concentrations and water are plotted in Figure 2. The peaks of the reference fluids (green line) from low to high greyscale values are air (void), Kapton, water, o-phosphoric acid 40 wt% and 85 wt%. The contrast between the two phosphoric acid peaks gives rise to a possible quantitative threshold segmentation strategy. For the greyscale plot of the image in Figure 1 close to the membrane (red line) a broad additional peak for carbon at greyscale values between 28'000 and 34'000 is observed which overlaps partially with the phosphoric acid peak visible between 34'000 and 60'000 (blue line). MPL is also visible in the GDL pore space with a similar absorption as phosphoric acid. Additionally, a shift of the void peak to higher absorption values can be observed for the image taken close to the membrane, which can be explained by the high absorption of the Pt-catalyst in this region. The challenges for a quantitative threshold segmentation are, therefore, not only the overlapping of carbon and acid peaks but also the poor contrast of the MPL.

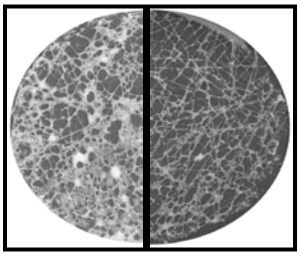

Figure 1. *16-bit greyscale images of the GDL (left: membrane side, right: flow field side).*

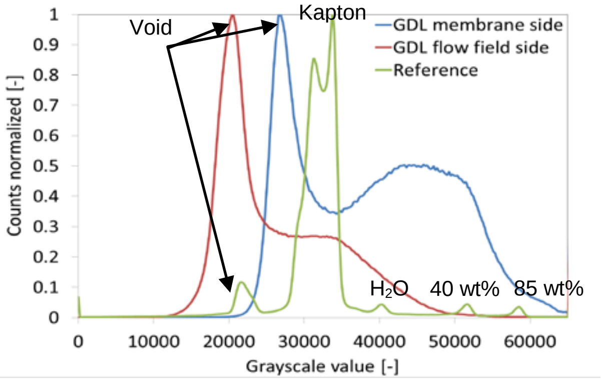

Figure 2. *Greyscale histogram of the GDL and the reference sample.*

Acknowledgments

Financial support by BASF is greatly acknowledged.

References

[1] T.J. Schmidt, J. Baurmeister, ECS Transactions **3**, 861-869 (2006).

[2] T.J. Schmidt, High-Temperature PEFC Durability Insights in Polymer Electrolyte Fuel Cell Durability, F.N. Büchi, M. Inaba, T.J. Schmidt (Eds.), Springer, NY, 199–221 (2009).

[3] G.R. Myers, D.M. Paganin, T.E. Gureyev, S.C. Mayo, Optics express **16**, 908–19 (2008).

In situ FTIR microscopy measurements in high temperature PEFCs: experiment and first results

G. Neophytides[1], A. Orfanidi[2], F. Büchi[1], L. Quaroni[3], S.G. Neophytides[2], T.J.Schmidt[1]

phone: +41 56 310 2165, e-mail: george.neophytides@psi.ch

High temperature PEFCs offer a complex system of the interface to study. The presence of phosphoric acid and the elevated temperatures creates an interesting environment for which little is known. We have recently designed and carried out experiments to investigate the species found on the Pt catalyst in a high temperature PEFC using FTIR microscopy. The first results show potential for further investigating and understanding of the processes that take place on the catalyst surface.

Experimental

The experiments have been carried out at the infrared beamline of the Swiss Light Source using a Hyperion 3000 microscope and a Vertex V70 spectrometer. The reactor used was designed in-house and is shown in Figure 1. The experiments have been carried out in reflection mode since Pt has been deposited directly on the membrane electrolyte as nanoparticles, forming a layer which acts also as a mirror. Therefore information is collected directly on the Pt surface which is controlled as the working electrode.

Discussion

CO adsorption has been studied at various conditions in order to understand the mechanism of the surface poisoning. The novel optical configuration yielded interesting results, regarding the optical effects that govern the absorbance spectrum. As can be seen in Fig. 2 the gaseous CO signal appears in positive absorbance units at 2143 cm^{-1} (more light is absorbed) while for the surface adsorption a negative peak (less light is absorbed by the sample) appears in a position approximately 80 cm^{-1} lower,at 2065 cm^{-1} as expected [1].

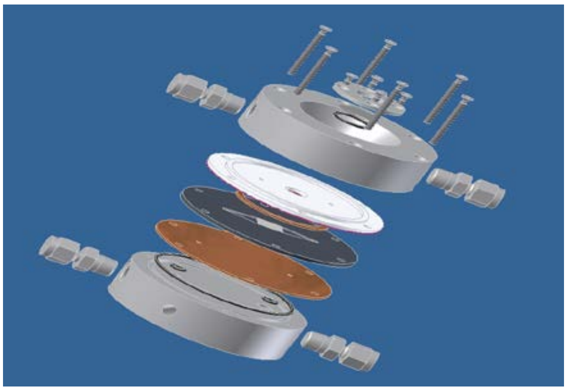

Figure 1. *Explosion image of the in situ cell design.*

This negative peak can be identified as CO since it disappears when the CO is electrochemically removed from the surface. The appearance of the negative peak is discussed in the literature as being associated with anomaleous dielectric properties of aggregated nanoparticles [2], but further explanations are still to be defined.

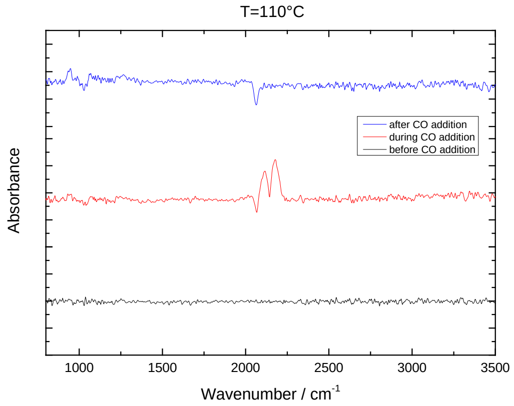

Figure 2. *Absorbance spectra of CO adsorption at 110 °C.*

Conclusions and Outlook

Spectroelectrochemical measurements have been carried out in several cases in the past but only in model systems and thin electrolyte layers. It is the first time that this kind of experiments has been carried out in a nearly technical system and at relevant temperature conditions. More studies need to be carried out in order to clarify different aspects of the electrochemical system. Also screening of the surface by phosphoric acid species can be investigated in order to understand the electrode electrolyte interface and the challenges that can arise for properly engineering an electrode and in general an MEA.

References

[1] S. Zafeiratos, G. Papakonstantinou, M. Jacksic, S. Neophytides, J. Catal. **232** 127-136(2005).

[2] S. Park, A. Wieckowski, M. J. Weaver, J. Am. Chem. Soc. **125** 2282-2290 (2003).

[1] Electrochemistry Laboratory, Paul Scherrer Institut
[2] Institute of Chem. Eng. and High Temp. processes, Greece
[3] Infrared beamline, Swiss Light Source, Paul Scherrer Institut

Spatially resolved start/stop measurements in high temperature PEFCs

G. Neophytides, F.N. Büchi, T.J. Schmidt

phone: +41 56 310 2165, e-mail: george.neophytides@psi.ch

Start/Stop cycling is a degradation protocol developed to simulate the start up and shut down of fuel cell stacks in real life cycles. Cycling involves the exchange between hydrogen and oxygen on the fuel side of the cell which leads to a propagating front of either of the gasses. This triggers carbon corrosion on the oxidant side as it can be seen from Fig. 1. Resolving the transients in combination with locally resolved current measurements, can yield important information on how and where the degradation occurs.

Experimental

The 9-fold segmented cell setup that was used is well established and has been used in numerous experiments in the past [1]. The operation temperature was 170ºC, and the cell was kept at all times in open circuit conditions. The degradation protocol involved the exchange of the gasses between hydrogen and air on the anode side under a given flow rate. The switch occurred every 30 seconds throughout the experiments. On the cathode side there was a steady flow of air of the same value and direction as the anodic flow. The flow rate varied from 50 to 600 mL/min thus changing the residence time of the formed front from 1.9 to 0.16 seconds.

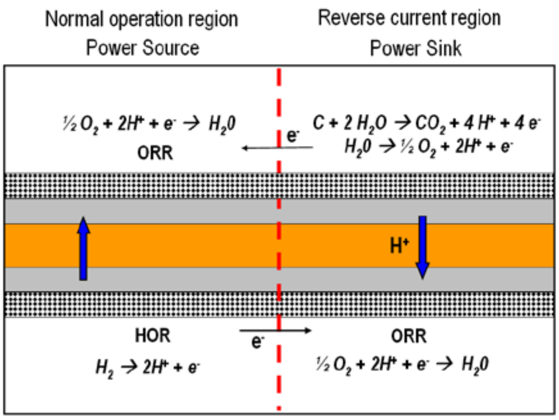

Figure 1. *Reactions in the cell during the front passing.*

Discussion

In Fig. 2 the local current density of the internal currents of the cathode during a start is shown for the individual segments, where segment 1 is at the gas inlet and segment 9 at the gas outlet. During the passing of the front through the cell there are negative and positive currents evolving. The positive currents are cathodic. The negative, anodic currents are responsible for the carbon corrosion occuring [2]. As it can be clearly seen the residence time of the front in the gas channels of the cell does not match the duration of the internal currents. This aspect is most clearly observed when the residence time of the front is further reduced (see Fig. 3) and can be compared with the duration of the current flows in the cell.

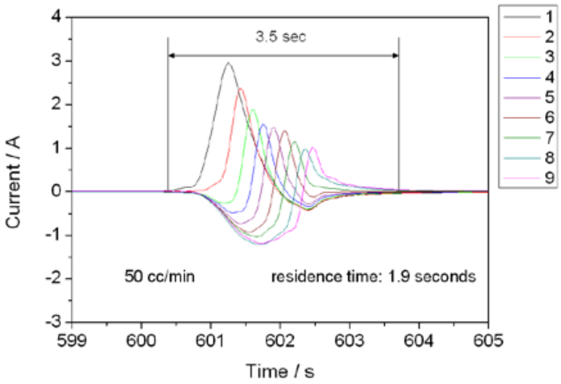

Figure 2. *Start transient currents of the air side.*

This mismatch can be explained by the diffusion limitations under the ribs of the flowfield as shown in the work of von Dahlen et al. [3]. Also Gu et al. have proposed a very comprehensive model regarding the start/stop phenomena in relation to the residence times and the relative position of the front in the cell [2]. The model predicts pseudocapacitative effects that cause the mismatch and has been verified by experiments for low temperature PEFCs [4]

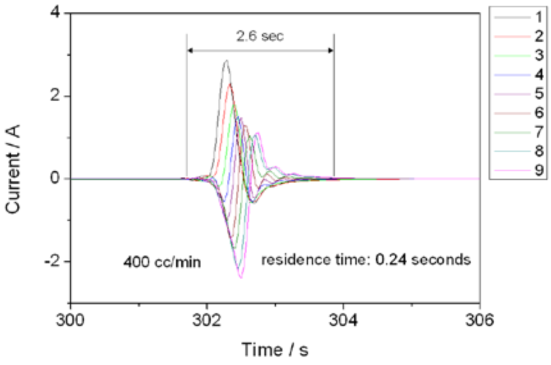

Figure 3. *Start transient currents of the air side for lower residence time of the front.*

Changing the residence time of the front is not only affecting the timescale on which the corrosion takes place but also affects the locality and the intensity of the phenomenon. As it can be seen from Fig. 4 the corrosion charge is reducing as the residence time is lowered. This strong dependence of the corrosion charge from the residence time has led to the proposal of using low residence times to inhibit the corrosion mechanisms that enhance the degradation of the system [4]. Moreover the pseudocapacitance of the catalytic layer leads to lowering the carbon corrosion reaction rates. The effect during start though is smaller than during stop and therefore the corrosion is smaller in the latter case, (seen Fig. 4). Furthermore the corrosion shifts from the inlet to the outlet region when decreasing the residence time.

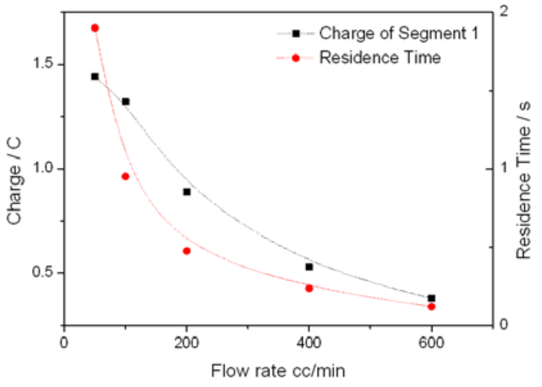

Figure 4. *Correlation of the residence time of the H_2/Air front and the corrosion charge.*

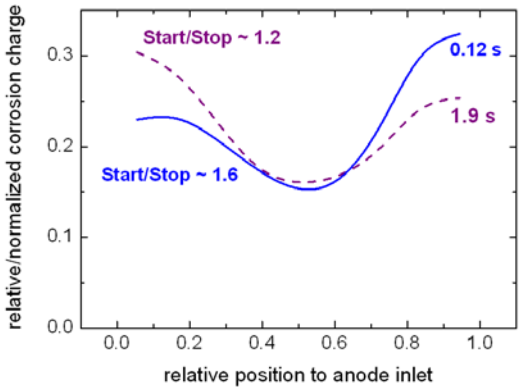

Figure 4. *Correlation between the residence time of the H_2/Air front and the locally resolved relative corrosion charge.The ratio of corrosion between start and stop changes.*

In case of long residence times the start vs. stop corrosion is more or less similar and it significantly changes by increasing the flow rate of the gases. This occurs due to the limited capacitance owing to the high residence time of the front and leads to significant differences from start to stop [2]. This has also been observed in the work of Hartnig and Schmidt [5] where the low flow rates and high residence times of the front led to the exclusion of the pseudocapacitative effects from their analysis of simulated start/stop degradation in high temperature PEFCs.

Conclusions and outlook

In this work it has been shown that start/stop cycling protocols, when applied in high temperature PEFCs have very similar behavior to models and experiments developed for low temperature PEFCs. The similarities can be found in the behavior of the corrosion currents between different residence times. The change in residence time of the propagating front leads to significant changes in degradation. This comes from the fact that with high residence times, pseudocapacitance does not affect the processes taking place due to its limited size. On the other hand when the residence time is lowered then the pseudocapacitative processes affect heavily carbon corrosion and more specifically the carbon corrosion during the stop cycle. It also leads to the shifting of the corrosion from the inlet to the outlet regions of the cell. Therefore it can be said that high temperature PEFCs behave similarly during start/stop cycling and the phenomena occurring can be described with previously developed models for low temperature PEFCs.

References

[1]. I.A. Schneider, H. Kuhn, A. Wokaun, G.G. Scherer, J. Electrochem. Soc. **152**, A2092-A2103 (2005).

[2]. W. Gu, R.N. Carter, P.T. Yu, H.A. Gasteiger, ECS Transactions. **11**, 963-973 (2007).

[3]. I.A. Schneider, S. von Dahlen, Electrochemical and Solid-State Letters. **14**, B30-B33 (2011).

[4]. S. Kreitmeier, A. Wokaun, F.N. BÃ¼chi, J. Electrochem. Soc. **159**, F787-F793 (2012).

[5]. C. Hartnig, T.J. Schmidt, Journal of Power Sources. **196**, 5564-5572 (2011).

Non-uniform degradation of the catalyst support during fuel cell start-up and shutdown in PEFC

S. Kreitmeier, A. Wokaun, F.N. Büchi

phone: +41 56 310 2127, e-mail: stefan.kreitmeier@psi.ch

Carbon supported platinum is the most frequently used catalyst in PEFCs. During fuel cell start-up and shutdown, a high potential can be formed at the cathode that electrochemically oxidizes carbon to carbon dioxide and thus degrades the catalyst. Before start-up, the anode and cathode are usually filled with air, since gas diffusion settles any imbalance between the atmosphere and the anode and cathode compartments, even if they are nominally closed to the environment. When hydrogen is introduced into the air-filled anode for start-up, a hydrogen/air front is formed [1, 2]. This phenomenon also appears during shutdown if the anode is purged with air to remove the remaining hydrogen quickly (for safety reasons). The coexistence of hydrogen and oxygen in the anode induces a high cathode potential by the reverse current mechanism first proposed by Reiser *et al.* [2].

Most studies on carbon corrosion during start-up and shutdown were carried out in laboratory fuel cells with active areas of 25–50 cm^2. However, the scale-up of these results to technical size cells requires careful consideration, as carbon corrosion rates vary with the position in the flow field [3]. Therefore, in this work the catalyst support degradation was investigated locally in a fuel cell of technical size during start-up and shutdown. This way, a fundamental understanding of *local* carbon corrosion and the influence of the major operating conditions can be elaborated.

Experimental

Local catalyst support degradation during fuel cell start-up and shutdown was investigated by analyzing the l*ocal* CO_2 concentration in the cathode channel. Fuel cell start-up and shutdown were simulated by alternately purging the anode with hydrogen (99.995 vol.%) or synthetic air (80/20 vol.% N_2/O_2). Synthetic air had to be used to eliminate the natural CO_2 background.

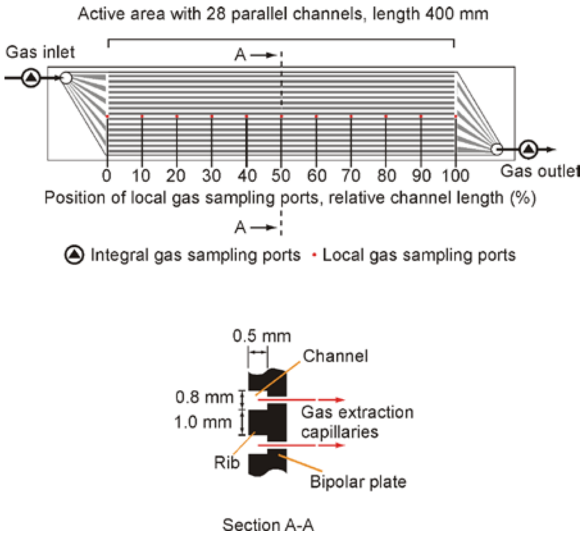
Active area with 28 parallel channels, length 400 mm
Gas inlet
A
Gas outlet
0
10
20
30
40
50
60
70
80
90
100
Position of local gas sampling ports, relative channel length (%)
A
Integral gas sampling ports
Local gas sampling ports
0.5 mm
Channel
0.8 mm
1.0 mm
Gas extraction capillaries
Rib
Bipolar plate
Section A-A

Figure 1. *Schematic drawing of the flow field plate of the segmented cell, adapted from [4].*

This allowed to analyze the carbon corrosion-derived CO_2 with concentrations in the range of 10–500 ppm. No load was applied to the cell to facilitate carbon corrosion. The experiments were carried out in a segmented cell of technical size. The cell has a linear flow field with channel dimensions of 0.8x0.5x400 mm, an active area of 200 cm^2 and has been equipped with fully heated gas extraction lines, as depicted in Figure 1. Electrochemical components used are Nafion NR 211 membranes and H400 (Solvicore) carbon paper gas diffusion electrodes with a catalyst loading of 0.4 mg cm^{-2} and 0.1 mg cm^{-2} for cathode and anode, respectively. For local gas analysis, 11 gas extracting ports are aligned along the center channel of the linear cell described above and two integral gas ports are installed in the flow field plate. 30 µL min^{-1} of gas can be extracted from each gas port during fuel cell operation and be analyzed using a quadrupole mass spectrometer (Pfeiffer Prisma 200M1).

Results

Online mass spectrometry was employed to investigate *local* CO_2 production during fuel cell start-up and shutdown in order to provide a fundamental understanding of the relevant carbon corrosion processes [5]. This method was preferred over electrochemical methods because the latter cannot discriminate between currents produced by the oxidation of carbon, water or platinum, nor can it distinguish between irreversible and reversible carbon oxidation, i.e. decomposition of the carbon support versus formation of surface oxides. Carbon support corrosion is non-uniform across the active area during fuel cell start-up and shutdown, as shown in Figure 2A. During start-up, the rate of carbon corrosion increases along the channel, while it decreases during shutdown. The carbon losses vary by a factor of up to 4 along the channel. Typically, the corrosion rate is highest at the outlet due to enhanced corrosion associated with the start process, followed by the inlet (shutdown-related corrosion) and lowest in the center. This pattern is in excellent agreement with modeling work from Gu *et al.* [3] for identical operating conditions (Figure 2B).

Due to carbon loss, the catalyst layer collapses and is reduced in thickness, as depicted in Figure 3. While the catalyst layer thickness is 11.4±3.0 µm for a pristine MEA (A), it is reduced to 3.7±1.1 µm for the degraded MEA at the inlet (B), 6.4±1.4 µm at the center (C) and 2.0±1.6 µm at the outlet (D). The reduction in the catalyst layer thickness qualitatively agrees with the local carbon loss data obtained from mass spectrometry. As the carbon particles collapse, the density of the catalyst support increases, limiting mass transport and thus lowering cell performance. To show the spatial effect of such mass transport limitations, the limiting current density was also analyzed locally. Figure 2C shows the limiting current density ratio between end of life (EOL) and beginning of life (BOL) after applying 500 start/stop cycles at the given conditions (see figure caption). The limiting current density profile (Figure 2C) is consistent with the local carbon loss profile (Figure 2A);

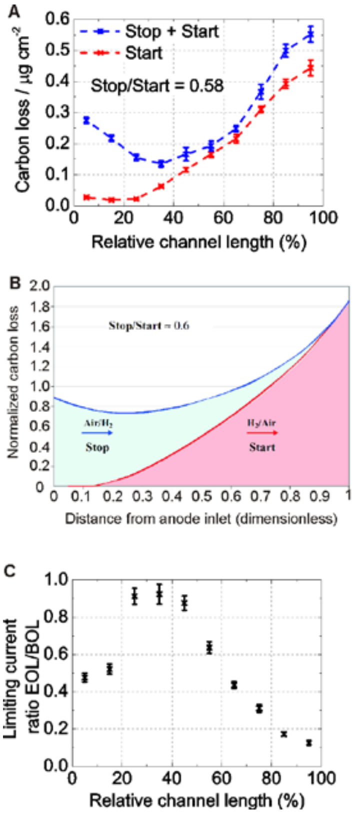

Figure 2. *Local carbon losses per start/stop cycle during start-up and shutdown. A) experimentally determined carbon loss at 80 °C, ambient pressure, 70% RH and a nominal anode gas velocity of 0.6 m* s^{-1}*; B) model of the local carbon loss [3]; C) ratio of the limiting current after (EOL) and prior (BOL) to start/stop cycles. Reproduced from [5].*

The current density decline is highest at the outlet, with intermediate losses at the inlet and the least decline in the center.

The ratio of the carbon corrosion rate between start-up and shutdown and thus between inlet and outlet is controlled by two opposite mechanisms: the pseudo-capacitive effect of the platinum electrode and diffusive mass transport limitations in the gas diffusion electrode. The pseudo-capacitance dampens carbon corrosion, while mass transport limitations increase carbon corrosion. The gas exchange by diffusive transport is slower during shutdown (oxygen replaces hydrogen) than during start-up (hydrogen replaces oxygen). This increases carbon corrosion during shutdown as compared to start-up. In contrast, the pseudo-capacitive effect mitigates the carbon corrosion for both processes. During shutdown platinum is oxidized at the cathode and at the anode, while it is only oxidized at the cathode during start-up (pseudo-capacitive effect). As platinum oxidation is a parallel reaction to carbon oxidation, carbon corrosion is mitigated by the pseudo-capacitive effect. However, the attenuation is more effective during shutdown. The combination of the pseudo-capacitive effect and the effect of the diffusive mass transport limitations, i.e. addition of their relative magnitude, sets the corrosion ratio between start-up and shutdown. Depending on the operating conditions and on the cell design and material properties of the gas diffusion electrode, the effect of both mechanisms is different yielding a specific, non-uniform degradation pattern. As an example, the effect of the rib width of flow fields on the carbon corrosion during start-up and shutdown is illustrated in Figure 4. The pseudo-capacitive effect is independent of the rib width, while diffusive mass transport limitations are smaller for narrow ribs and larger for wide ribs, leading to lower (Figure 4A) or higher (Figure 4B) corrosion rates during shutdown. The set of parameters investigated in this work are a basis to evaluate and predict local carbon support corrosion rates during fuel cell start-up and shutdown for different operating conditions.

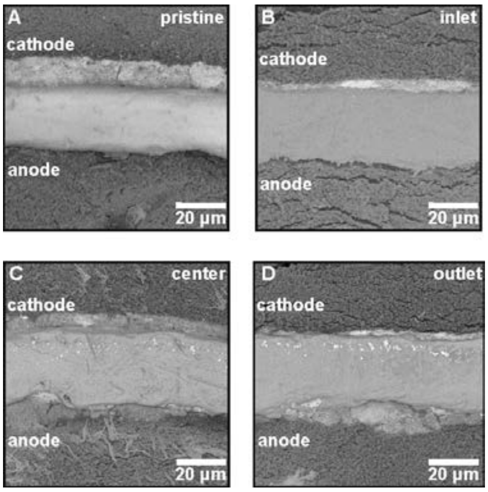

Figure 3. *MEA cross-sections visualizing carbon loss by the reduction of catalyst layer thickness; A) pristine MEA; degraded MEA B) at the cell inlet, C) at the center and D) at the cell outlet. MEA was degraded at 70% RH, ambient pressure and at a nominal gas velocity of 0.3 m* s^{-1} *for 500 cycles. Reproduced from [5].*

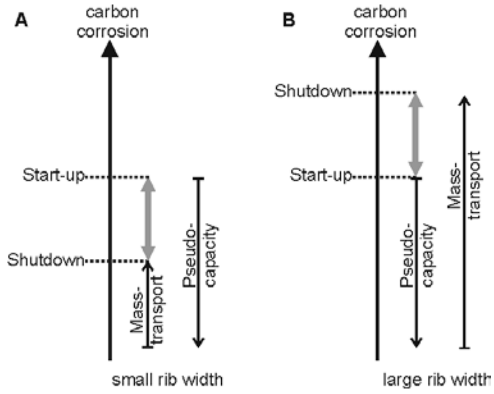

Figure 4. *Influence of the pseudo-capacitive effect and diffusive mass transport on the carbon corrosion ratio between start-up and shutdown. A) a small rib width and B) large rib width affect the diffusive mass transport, but not the pseudo-capacitance of the platinum electrode. The combination of the two effects may lead to either higher carbon corrosion during start-up (A) or shutdown (B). Reproduced from [5].*

References

[1] N. Linse, PhD Thesis, ETH No. 20132, ETHZ, Zürich, 2012.

[2] C.A. Reiser, L. Bregoli, T W. Patterson, J.S. Yi, J.D. Yang, M.L. Perry, T.D. Jarvi, Electrochem. Solid-State Lett. **8** A273–A276 (2005).

[3] W. Gu, R.N. Carter, P.T. Yu, H.A. Gasteiger, ECS Trans. **11**, 963-973 (2010).

[4] G.A. Schuler, A. Wokaun, F.N. Büchi, J. Power Sources **195**, 1647-1656 (2010).

[5] S. Kreitmeier, A. Wokaun, F.N. Büchi, J. Electrochem. Soc. **159**, F787-F793 (2012).

Degradation processes at membrane defects in PEFC

S. Kreitmeier, A. Wokaun, F.N. Büchi

phone: +41 56 310 2127, e-mail: stefan.kreitmeier@psi.ch

Polymer electrolyte membranes undergo chemical, mechanical and thermal degradation during fuel cell operation. Gas crossover is the key element of membrane degradation, triggering two out of three possible degradation mechanisms: chemical and thermal degradation. The hydrogen and oxygen crossover is the primary source of oxygen radical species that chemically decompose the polymer via the unzipping reaction mechanism, as described by Curtin *et al.* [1]. The carboxyl group (COOH) is a key function of this mechanism and therefore often used as an indicator for chemical polymer decomposition. At the same time, the crossover can initiate thermal membrane degradation if the temperature increases due to permeated hydrogen and oxygen that combust catalytically at the catalyst layer. The gas crossover is too low in pristine membranes for this to occur, but the crossover at defects may be sufficient to locally initiate this process [2]. Both, chemical and thermal polymer decomposition lead to a loss in the gas separation and thus an enhancement of the gas crossover, so a positive feedback loop is created that accelerates these degradation processes. Because of this, the loss of the gas separation capability is the most detrimental degradation in polymer electrolyte membranes.

Unlike for non-stabilized perfluorosulfonic acid membranes, membrane thinning was not observed and did not contribute to the increase of the gas crossover in Nafion NR 211 membranes [3]. The main reason for the loss of the gas separation is rather the mechanical formation of pinholes induced by humidity fluctuations and imperfections of the GDE. In this case, the gas crossover is locally increased and expected to accelerate degradation processes [4], that were systematically investigated in this study in order to generate a database that allows for the elaboration of an overall degradation mechanism at membrane defects.

Experimental

As the native formation of membrane defects is a slow process, and the evolving defects differ in size and shape, pinholes were implemented artificially in membranes using focused ion beam milling [4]. This allowed for the investigation of degradation processes at membrane defects under well known conditions. MEAs of the perforated membranes were operated in a fuel cell under adequate stress tests to accelerate chemical, mechanical and thermal degradation processes. Degradation at membrane defects was investigated post mortem using synchrotron based X-ray tomographic microscopy and FTIR spectro-microscopy. To study the evolution of membrane defects, the gas crossover was monitored online using a tracer gas concept [2]. At the anode 10 vol. % helium is fed to the hydrogen flux and the helium concentration is measured at the cathode. This allowed to analyze gas permeation online during fuel cell operation, which is not possible by conventional electrochemical analysis of the hydrogen crossover.

Results

MEAs with artificially implemented membrane defects (10 µm in diameter) were degraded under different accelerated stress tests and analyzed post mortem by X-ray tomographic microscopy. Figure 1 illustrates the effect of the direction of the gas crossover. In case of hydrogen crossover (Figure 1B), the catalyst layer and the membrane degrade at the cathode. Thermal degradation processes seem to dominate which is indicated by catalyst sintering and polymer melting. In contrast, in case of oxygen crossover (Figure 1A) only the membrane degrades at the anode side, where etching processes seem to decompose the polymer indicating that chemical degradation processes are dominating. In this case, the low potential at the anode probably facilitates the formation of oxygen species radicals via hydrogen peroxide. Note that in both tests the pinhole became larger, but the degradation rate is much faster for hydrogen crossover than for oxygen crossover (see caption of Figure 1).

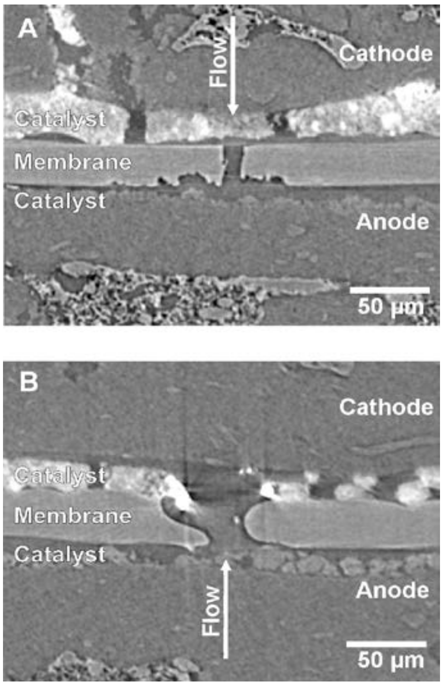

Figure 1. *MEAs with 10 µm pinholes in the membrane were degraded by operating the fuel cell at H_2/O_2 in OCV mode, 80 °C, 150 kPa and humidity cycles. A) XTM cross-section of a MEA degraded 232 h with the cathode pressure 0.5 kPa higher than the anode pressure and B) degraded only 50 h with the cathode pressure 0.5 kPa lower than the anode pressure.*

FTIR spectro-microscopy was applied to study chemical polymer decomposition in the vicinity of membrane defects. Figure 2 shows IR spectra of degraded Nafion 111 (black data set) and degraded Nafion 211 (blue data set) next to defects (10×10 μm^2 scan area). Both spectra show the characteristic peaks of the ether group (COC, 983 cm^{-1}), sulfonic acid group (SO_3, 1060 cm^{-1}), fluorocarbon backbone (CF_2, 1080–1380 cm^{-1}) and absorbed

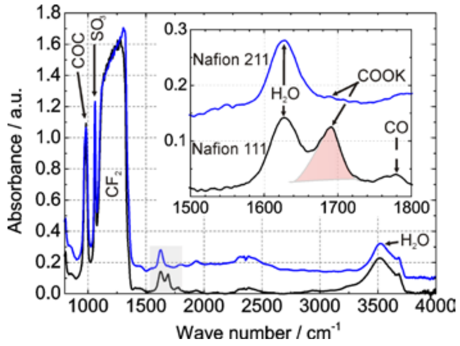

Figure 2. *FTIR spectra of Nafion 211 (blue data set) and Nafion 111 (black data set) next to an artificially implemented pinhole degraded under H_2/O_2 in OCV mode at 80 °C, 150 kPa and cycling the humidity between 0% and 70% RH.*

water (H_2O, 1628 $cm^{-1}$and 3350–3700 cm^{-1}) [5]. Additional peaks are observed at 1689 cm^{-1} and 1772 cm^{-1}, which can be assigned to the carboxyl group (COOK, 1689 cm^{-1}; CO, 1772 cm^{-1}) [6]. Unlike Nafion 111, the COOK absorbance of Nafion 211 is barely recognizable for the given degradation protocol (see Figure 2). Nafion 211 is end-group stabilized improving its chemical stability as compared to Nafion 111. Therefore, Nafion 111 was used to further investigate chemical polymer decomposition using FTIR analysis.

Figure 3 shows a 2D map of the distribution of the integrated COOK absorbance for the degraded Nafion 111 membrane. The degraded defect has dimensions of 100–200 µm and is indicated by a black line. The integrated COOK absorbance is zero in the pinhole, shows a maximum intensity in the vicinity of the pinhole and decays with increasing distance.

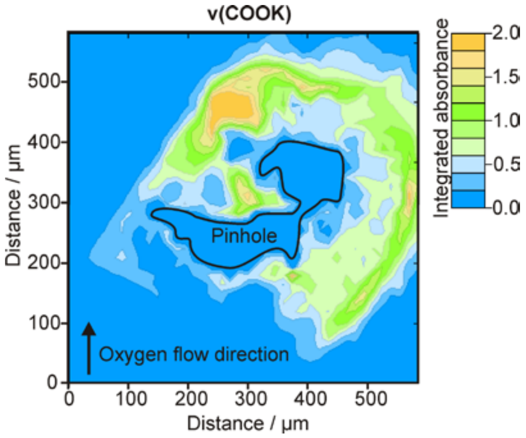

Figure 3. *2D-FTIR map of the integrated COOK absorbance for a degraded Nafion 111 membrane at a defect. A 25 µm pinhole was previously implemented artificially and degraded 25 h at H_2/O_2, 80 °C, 150 kPa and cycling the humidity from 0–70% RH. A hydrogen crossover was forced through the membrane by a pressure gradient between anode and cathode of 10 kPa.*

Polymer decomposition is highest at the oxygen downstream side and the maximum intensity is not at the pinhole edge. As shown in Figure 1B, the catalyst is lost at the cathode near the defect, so hydrogen can accumulate in the vicinity of the membrane defect. A reaction zone is formed, the dimensions of which depend on the hydrogen crossover rate and the catalyst availability. Because of this fact, the highest radical formation rate is not necessarily next to the pinhole edge, so the polymer does not decompose in an expanding ring. Instead, larger areas can decompose simultaneously. Since significant amounts of the catalyst and the microporous layers are lost at the defect, even a small pressure gradient of the oxygen flux in the flow direction will transport the permeated hydrogen downwards the channel. Thus, the polymer is mainly decomposed in oxygen flow direction.

Polymer decomposition close to the pinhole leads to pinhole growth. However, it is not clear how the pinhole is growing. To study the evolution of membrane defects, artificially implemented pinholes were degraded in a stress test that accelerate chemical (OCV mode; H_2/O_2) and mechanical (humidity cycles) degradation processes, while the helium crossover was monitored online by mass spectrometry. As illustrated in Figure 4, the helium crossover increases exponentially over time, with stepwise jumps occurring when mechanical stress was applied by humidity cycles.

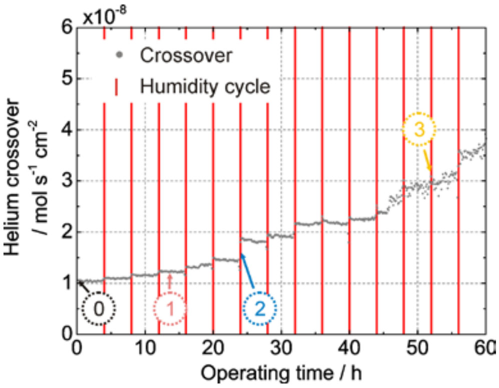

Figure 4. *Online helium crossover of an MEA with pinholes in the membrane that was aged during fuel cell operation at H_2/O_2 in OCV mode, 80 °C, 150 kPa and cycling the humidity between 0% and 70% RH. Numbers in the figure refer to different degradation phases.*

From the results, an overall degradation mechanism at membrane defects was deduced [2]. When pinholes are formed mechanically (phase 0), the locally elevated gas crossover induces chemical polymer decomposition (phase 1), that weakens the polymer around defects. Large parts of the partially decomposed polymer will suddenly fracture, i.e. gas crossover jumps are observed (phase 2), if mechanical stress induced by humidity fluctuations exceeds the local membrane strength. For pinholes larger than about 15-30 µm, permeated hydrogen starts to combust catalytically at the cathode electrode, inducing thermal degradation processes (phase 3). The combination of degradation processes causes a synergetic effect which accelerates the degradation at membrane defects exponentially, as shown in Figure 4.

References

[1] D.E. Curtin, R.D. Lousenberg, T.J. Henry, P.C. Tangeman, M. E. Tisack, J. Power Sources **131**, 41-48 (2004).

[2] S. Kreitmeier, A. Wokaun, F.N. Büchi, ECS Trans. **50**, (2012).

[3] S. Kreitmeier, G.A. Schuler, A. Wokaun, F.N. Büchi, J. Power Sources **212**, 139-147 (2012).

[4] S. Kreitmeier, M. Michiardi, A. Wokaun, F.N. Büchi, Electrochim. Acta **80**, 240-247 (2012).

[5] V. Di Noto, R. Gliubizzi, E. Negro, G. Pace, Phys. Chem. B **110**, 24972-24986 (2006).

[6] Y. Akiyama, H. Sodaye, Y. Shibahara, Y. Honda, S. Tagawa, S. Nishijima, J. Power Sources **195**, 5915-5921 (2010).

Local impact of the flow field design onto the PEFC's performance

P. Oberholzer, P. Boillat, R. Siegrist, A. Kaestner, E.H. Lehmann, G.G. Scherer, A. Wokaun

phone: +41 56 310 5637, e-mail: pierre.oberholzer@psi.ch

The flow field is an important component of the Polymer Electrolyte Fuel Cell (PEFC) as it ensures the current (and heat) collection, the reactant distribution and the water removal. A large variety of studies address flow field designs (i.e. channel/rib size and shape) mainly by considering the optimization of the water management at the scale of full-size cells [1] while keeping reasonable manufacturing costs. However, the precise characterization at the local scale of the effect of the channel and ribs dimensions on the performance and the water distribution remains widely unexplored in the state-of-the-art research.

In the present study, *differential cells* (small-size cells supplied with high stoichiometry gases) are used to emulate a local area of the full-size cell. Three different flow fields are characterized by means of voltage-current dependency under air, during which helox and oxygen pulses are applied [2], using the multi-cell setup recently developed [3]. The aim of the study is to simplify the diffusive pattern of oxygen across the porous media, as explained below, to gain a more accurate insight about the loss mechanisms.

Experimental

All experiments presented here were realized on differential cells at 70°C temperature, with H_2 and air at pressures of 2 and 2.1 bar_{abs} respectively. Samples were made of a Gore Primea 5710 catalyst coated membrane and GDLs (gas diffusion layers) of type 24BC from SGL carbon (i.e. with microporous layer). Three different types of flow field are tested (Figure 1).

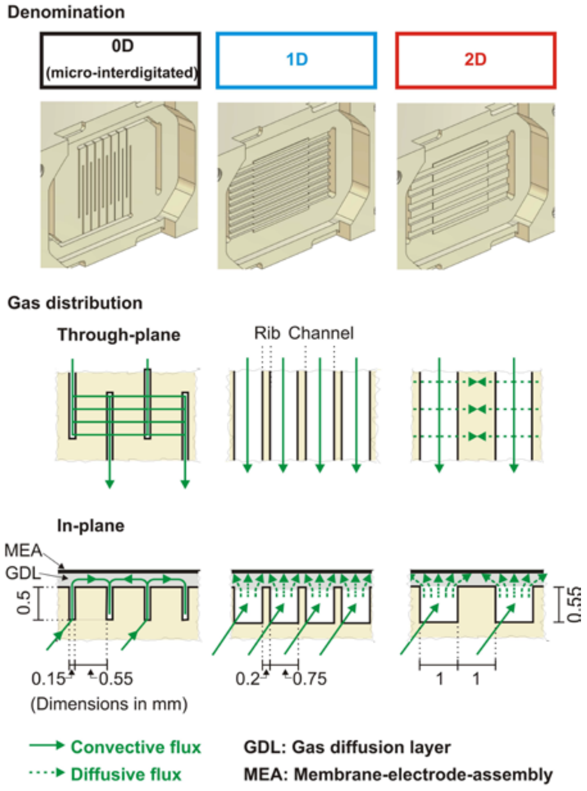

Figure 1. *Flow field patterns investigated.*

The denominations "0D", "1D" and "2D" refer to the diffusive pattern of oxygen expected across the gas GDL on cathode side. In the "2D" structure, the channel and the rib widths are the same. It represents the typical flow field design used in technical stacks because of its low manufacturing costs. However, it can lead to a strongly inhomogeneous current distribution [4] due to the limited diffusion of oxygen under the rib zones of the GDL. By reducing the rib width, a more homogeneous distribution of oxygen can be expected, that tends to a "1D" distribution of the current, though at the expenses of higher resistive losses (see Results). In the "0D" flow field the diffusive flow of oxygen in the GDL is replaced by a convective flow thanks to the micro-interdigitated design of dead-end channels, in which the gas flow is forced to throughout the GDL by convection.

Results

Two voltage-current characterizations were realized: under "wet" (Figure 2; relative humidity = 100% on both sides) and "optimal" conditions (Figure 3; relative humidity = 100% on anode and 0% on cathode). Water contents were measured using in-plane neutron imaging at the ICON beam line of PSI [5].

By looking first at the voltage in "wet" condition (Figure 2.a) it can be observed that the "2D" cell has the poorest performance at higher current densities. Other indicators can be considered to refine the analysis. On the second graph (Figure 2.b), the ohmic losses, calculated by the product of the current by the high frequency resistance, are observed to be identical for all cells (Figure 2.b). Moreover, the voltage recorded under pulsed oxygen using the method described in ref. [2] is reported, and the ohmic contribution is removed from this voltage (by adding the ohmic loss). The $U_{O2} + ir$ value obtained allows checking that differences of kinetic losses between the cells are negligible. Finally, the difference between the voltage measured during helox pulses (21% O_2 and 79% He) and the voltage under air operation is plotted (Figure 2.c). It can be interpreted as an indicator of mass transport losses induced by limited bulk diffusion of gases [2].

These results confirm the natural expectation according to which the "2D" flow field induces higher mass transport losses due to the longer pathway for oxygen diffusion under the ribs in the GDL. This effect is further increased by the presence of liquid water [2]. The advantage of the reduced rib width of the "1D" is obvious for that issue. At last, the "0D" cell demonstrates the best performance due to the convective nature of the gas flow and the mitigation of diffusive losses.

Let us consider now the experiment realized under another relative humidity condition, that is with a fully humidified anode and a dry cathode (Figure 3). This condition is called "optimal condition", since the best performance is obtained for all cells at this specific relative humidity regime. Contrary to the previous case, the mass transport losses of the "2D" cell are much smaller, yet higher than for the "1D" and the "0D" cells. For these two cells, the mass transport losses are identical.

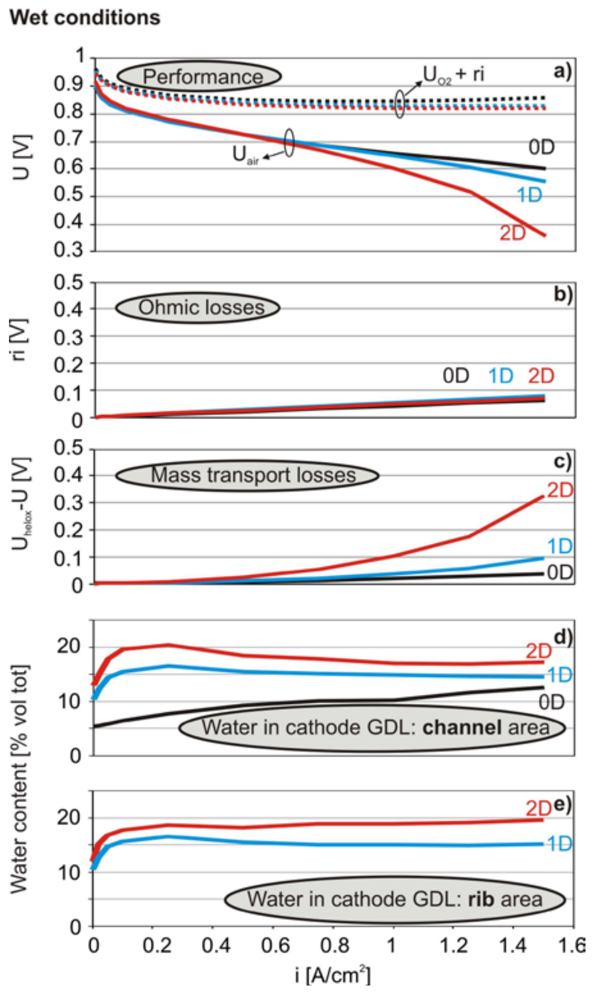

***Figure 2.** Performance indicators in wet condition (relative humidity is 100% on both sides).*

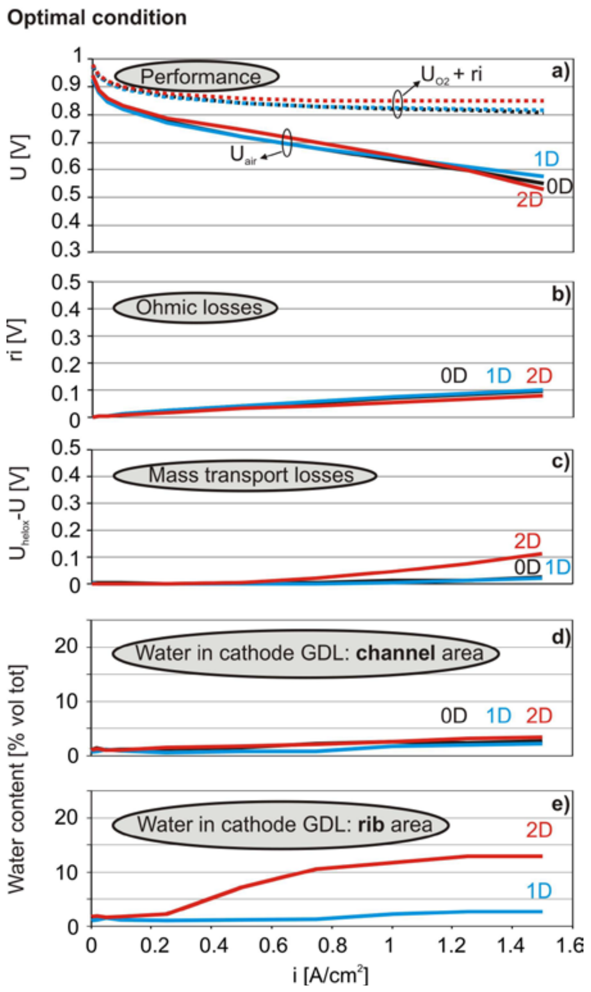

***Figure 3.** Performance indicators in dry condition (relative humidity is 100% on anode and 0% on cathode).*

Furthermore, the “2D” cell exhibits a much higher content of water than the “1D” cell under the rib area (Figure 3.e), which can be explained by the difficult removal of water vapor in that region due to the longer gas pathway. Whereas this accumulation is detrimental to the access of oxygen under the rib regions, it is reasonable to suggest that its impact will be mitigated, since the current density is probably strongly inhomogeneous and essentially concentrated in the active areas facing the channel regions, while being quite low under the ribs, as measured in ref. [4] and suggested in ref. [2]. Based on that, the major reason for the high mass transport losses of the “2D” cell under “wet” conditions (Figure 2.c) should rather be attributed to the strong effect of water accumulation under the channels due to a high current density in that region rather than to a value of water content higher than in the “1D” cell (Figure 2.d & 2.e).

Further comments can be made about the other flow fields. The “1D” cell shows identical water amounts in the channels and ribs in “wet” conditions and is almost dry under optimal conditions. The fact that the channel and rib regions contain the same amount of water tends to validate the “1D” behaviour desired for this cell. The very low mass transport losses of the “0D” cell, even in presence of important water amount (Figure 2.d), confirms that the target of this design was achieved, namely to mitigate (or even suppress) the effect of limited diffusion in the porous medium.

Conclusion

The effect of the flow field design on the performance and water content was investigated. Namely, model designs were realized with the aim of simplifying the diffusive pattern of oxygen across the gas diffusion layer, conceptually tending to “2D”, “1D”, and “0D” (micro-interdigitated) gradients of oxygen concentration. The “2D” effect could be pointed out (performance and water content) compared to a “1D” design of flow field that was validated. At last, the negligible diffusion losses in the “0D” cell confirm the goal of this design and let presage of an interesting diagnostic tool for electrode characterization in absence of gas diffusion.

References

[1] A. Aiyejina and M.K.S. Sastry, *J. Fuel Cell Sci. Tech.* **9**, 011011 (2012).

[2] P. Boillat, P. Oberholzer, A. Kaestner, R. Siegrist, E.H. Lehmann, G.G. Scherer, and A. Wokaun, *J. Electrochem. Soc.* **159**, F210 (2012).

[3] P. Oberholzer, P. Boillat, R. Siegrist, A. Kaestner, E.H. Lehmann, G. G. Scherer, and A. Wokaun, *Electrochem. Commun.* **20**, 67 (2012).

[4] I.A. Schneider, M.H. Bayer, and S. von Dahlen, *J. Electrochem. Soc.* **158**, B343 (2011).

[5] A.P. Kaestner, S. Hartmann, G. Kühne, G. Frei, C. Grünzweig, L. Josic, F. Schmid, E.H. Lehmann, *Nucl. Instr. Meth. A* **659**, 387 (2011).

SCIENTIFIC ACHIEVEMENTS 2012

BATTERIES & SUPERCAPACITORS

MATERIALS

Graphene as electrode material for supercapacitors?

R. Kötz, M.M. Hantel, D. Weingarth, A. Foelske-Schmitz

phone: +41 56 310 2057, e-mail: ruediger.koetz@psi.ch

Graphene has become a magic word in science in general and in electrochemistry in particular. Since the Nobel Prize of 2010 for Geim and Novoselov for the discovery of graphene the numbers of publications in electrochemistry with graphene is exploding.

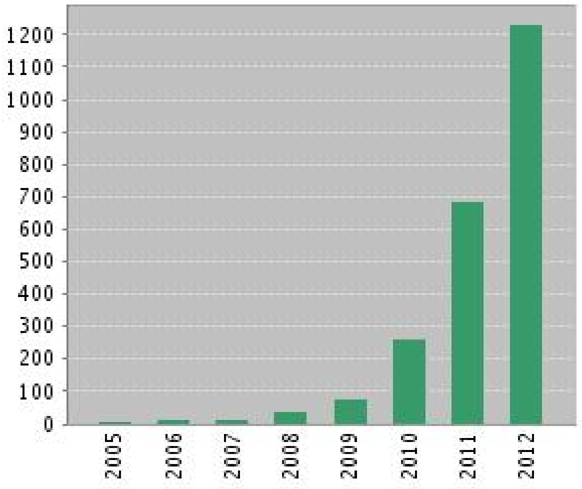

Figure 1. *Evolution of scientific publications for keywords " graphene AND electrochem* " from Web of Science January 2013*

The graphene material which is defined as a "single layer graphite" is supposed to have particular properties [1], some of which may be important for deployment of graphene in electrodes for energy applications, in particular electrochemical energy storage [2]. Graphene has the highest surface area possible for carbon materials. Considering both sides of the graphene sheet the surface area is 2630 m^2/g, not taking into account adsorption sites at the edges. Such a high surface area makes graphene especially attractive for electrochemical double layer electrodes. Assuming a specific double layer capacitance of the basal plane of graphite of 8 µF/cm^2 a specific capacitance above 200 F/g could be achieved for one capacitor electrode. This is significantly higher than for typical activated carbons used today.

However, in order to translate the high surface area into such high capacitance it is necessary that both sides of the graphene layer are capable of forming an electrochemical double layer with the mentioned specific capacitance of a graphite basal surfaces.

For activated carbon it has been demonstrated [3] that the solid side of the double layer contributes and even dominates the overall double capacitance. Due to the fact that carbon has a low density of electronic stated close to the Fermi level the respective conductance and screening is significantly reduced compared to a metal [3].

This situation is sketched in figure 2 for a carbon wall separating two pores in e.g. an activated carbon electrode. Based on the density of states (DOS) of graphite it could be calculated that the screening layer in the solid reaches into the bulk for about 5 Å on each side of the wall. In other words, in order to screen the electrochemical double layers on both sides the carbon wall has to have a thickness of minimum 1 nm.

For graphene one interesting particularity is the existence of the so-called Van Hove singularity [5]. As shown in figure 3 the consequence is a zero density of states at the Fermi level and a linearly increasing DOS with positive or negative charging. This, however, is only true for an ideal graphene layer without any distortion, defects, or impurities. When defects and impurities are considered the two-dimensional DOS at the Fermi level increases and the distribution of DOS approaches a parabola (see fig. 3).

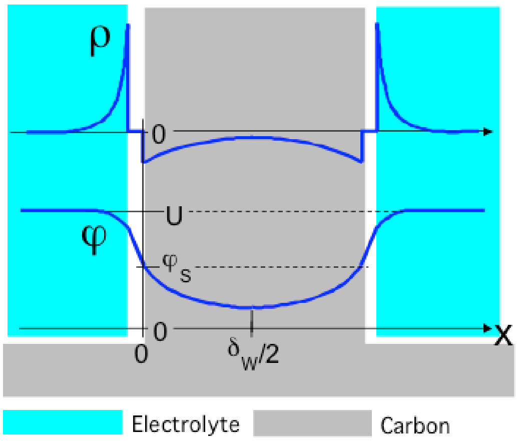

Figure 2. *Schematic presentation of the charge density ρ and potential φ in a pore wall and in the pore electrolyte on both sides. U is the electrode potential relative to the potential of zero charge. φs is the potential at the wall surface and δw is the wall thickness. Per definition φ = 0 within the uncharged carbon [4].*

The quantum capacitance based on the two dimensional DOS for an ideal graphene layer exhibiting the Van Hove singularity is reproduced in Figure 3. Uncharged graphene has a negligable DOS at the Fermi level and consequently in a non-charged state the space charge layer will be large and the quantum capacitance approaches zero. In reality, however, the graphene layer has defects caused by imperfections, voids, or adsorbates, which increase the DOS particularly in the uncharged state (Potential = 0 V).

The specific capacitance values calculated in figure 3 are in good agreement with what one usually measures for activated carbon or the basal plane of graphite at the potential of zero charge where the overall capacitance is determined by the space charge layer. With a typical double layer capacitance of 8 µF/cm^2 one would obtain a specific capacitance of about 210 F/g for a graphene electrode assuming a surface area of 2630 m^2/g for both sides of the grahene sheet. This number assumes that an electrochemical double layer can be formed on both sides of the graphene sheet.

Our investigations [7] of partially reduced graphite oxide (GOpr) in an aprotic electrolyte showed a specific capacitance of 220 F/g, which is close to the above mentioned 210 F/g. GOpr can be considered as stacked layers of slightly oxidised graphene.

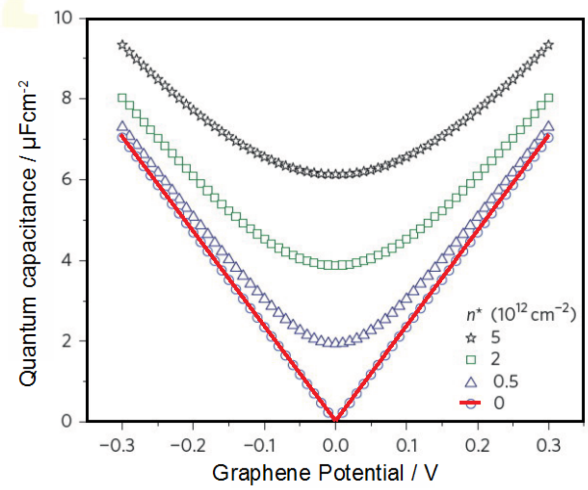

Figure 3 *Dependence of quantum capacitance on graphene. Simulated capacitance at different effective charged impurities n^* (0, 0.5, 2 and 5 x 10^{12} cm^{-2}). Reproduced from [6]*

An experimental answer to the question whether an electrochemical double layer can be formed on both sides of graphene was given by Ruoff et al [8], who performed a sophisticated experiment exposing a supported graphene sheet to electrolyte on one side and afterwards on both sides.

The results are reproduced in figure 4 and clearly demonstrate that exposing both sides of a graphene sheet to the electrolyte results in a decrease of the specific capacitance. In other words doubling the electrochemical interface by exposing front and backside of a graphene sheet does not double the capacitance. These experimental results of Ruoff et al. [8] indicate that a single graphene sheet cannot provide enough charge carriers to facilitate screening of both electrolyte Helmholtz layers within the bulk.

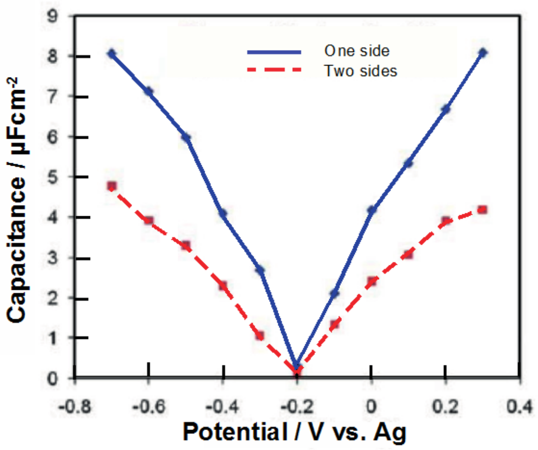

Figure 4*. Measured interfacial capacitance for one and two-sided graphene. Reproduced from [8].*

The two dimensional charge carrier density for a graphene sheet at 0 V is in the order of $D_{2d}(E_F) \approx 10^{11}$ cm^{-2} only. However, this two dimensional density increases to about $D_{2d}(E_F) \approx 10^{14}$ cm^{-2} for a positively or negatively charged graphene at ± 1V [5]. The 3d density can than be estimated to be about 10^{18} carriers per cm^3 at 0 V or 10^{21} cm^{-3} at ±1 V, just assuming 3x10^7 graphene sheets in one cm. This value is comparable to the estimated density for graphite which was 10^{20} cm^{-3} eV^{-1} [9] or for activated carbon 10^{21} cm^{-3} eV^{-1} [3]. Thus the minimum thickness of the carbon layer accepting electrochemical double layers on both sides of 1 nm for activated carbon [3] cannot be provided by a single graphene sheet. About 3 graphene layers are needed to screen both double layers.

In view of the above our recent results on partially reduced GOpr may be reconsidered. Probably the measured 220 F/g cannot be completely ascribed to double layer charging unless the oxygen containing surface functional groups still present between the graphene sheets cause a significant increase in the electronic density of states by at least one order of magnitude. Alternatively we have to assume that the huge specific capacitance arises from pseudocapacitive surface reactions of the electrolyte ions with the surface groups.

Conclusions

Considering the calculated density of charge carriers for graphene and activated carbon shows that the capacitance of graphene will be comparable to that of activated carbon. The interface capacitance of both, graphene and activated carbon are dominated by the space charge capacitance in the bulk of the material and not by the Helmholtz capacitance. It is hardly possible to form full electrochemical double layers on both sides of graphene.

Nevertheless, graphene may be beneficial for electrode materials used in electrochemical devices. The high surface area and unsurpassed strength of the material together with its optical properties and good conductance may result in new and improved electrodes.

References

[1] A. K. Geim, K. S. Novoselov, Nature Materials **6**, 183 (2007).

[2] J. Liu, Y. Xue, M. Zhang, L. Dai, MRS Bulletin **37**, 1265-1272 (2012).

[3] M. Hahn, M. Bärtschi, O. Barbieri, J-C. Sauter, R. Kötz, R. Gallay, Electrochemical and Solid-State Letters **7**, A33-A36 (2004).

[4] M. Hahn, M. Baertschi, O. Barbieri, J-C. Sauter, R. Kötz, GDCH Monographie Bd. **29**, 120-129 (2003) Gesellschaft Deutscher Chemiker 2004.

[5] T. Fang, A. Konar, H. Xing, D. Jena, Applied Phys. Lett. **91,** 092109-1-092109-3 (2007).

[6] J. Xia, F. Chen, J. Li N. Tao, Nature Nanotechnology **4**, 505-509 (2009).ß

[7] M.M. Hantel, T. Kaspar, R. Nesper, A. Wokaun, R. Kötz, Electrochem. Commun. **13,** 90-92 (2011).

[8] M.D. Stoller, C.W. Magnuson, Y. Zhu, S. Murali, J.W. Suk, R. Piner, R.S. Ruoff, Energy Environ. Sci. **4**, 4685-4689 (2011).

[9] H. Gerischer, J. Phys. Chem. **89**, 4249-4251 (1985).

Graphene layers supported by partially pyrolized nanodiamonds: a suitable composit material for supercapacitor electrodes?

M.M. Hantel, T. Kaspar[1], R. Nesper[1], V. Mochalin[2], Y. Gogotsi[2], A. Wokaun, R. Kötz

phone: +41 56 310 4189, e-mail: moritz.hantel@psi.ch

Graphene with a theoretical specific surface area of 2630 m^2g^{-1} [1] is a promising starting material for applications requiring high surface areas, like supercapacitors [2]. One way to utilize graphene for a supercapacitor electrode is by preparing a so called free-standing graphene paper (GP). Such a paper can be produced by a flow-directed filtration of a graphene dispersion [3], where the thickness of the paper can easily be tuned by the amount of graphene in the solution or by the filtration time. Another approach is to start from a dispersion of graphene oxide instead of graphene [4]. The resolved graphene oxide paper (GOP) shows similar morphology like the graphene paper, but has an increased interlayer distance between 6-8 Å which is approximately twice that of graphite [5]. As a drawback GOPs are not conductive and hence need to be further treated to regain conductivity.

Beside a large specific surface area the ion accessibility plays an important role when it comes to supercapacitor electrodes. Since the ion accessibility is directly connected to the rate capability a feasible strategy would be to introduce pillars within the graphene network to enhance the diffusion path ways. One promising candidate is detonation soot nanodiamond (ND). NDs are sp3 hybridized carbon with sizes in the range of 5 to 8 nm [6]. The idea is to combine ND with graphene oxide in dispersion and then follow the same synthesis route used for GOPs with a flow directed filtration. By applying a thermal reduction one can tune the resulting composite material in two directions. The first would be a low temperature reduction leading to partially reduced graphene oxide supported by non conductive nanodiamonds. The second would be a high temperature reduction leading to graphene supported by partially graphitized nanodiamonds, a process starting at pyrolysis temperatures close to 1000° C [6, 7].

Experimental

Starting from graphite oxide made from synthetic graphite (TIMREX SFG44, Timcal, Switzerland) a graphene oxide dispersion in water was prepared by sonication. 50 ml of de-aggregated NDs [8] were added to 250 ml of the prepared graphene oxide dispersion ($c_{GO} = 1\ gl^{-1}$). A flow-directed filtration of the dispersion was used to prepare the self-standing paper like ND supported graphite oxide film. The resolved membrane was thermally reduced under nitrogen atmosphere at temperatures of 200, 250, 800 and 1000 °C. Pieces punched out of these membranes with a diameter of 10 mm were attached to carbon coated aluminium and used as electrodes.

Cyclic voltammetry was performed using these electrodes with 1M $TEABF_4$ in acetonitrile (AN) at a scan rate of 1 mVs^{-1} utilising a VMP3 potentiostat (BioLogic, France). In addition, galvanostatic charge / discharge cycles were performed to characterize the rate capability of the electrodes.

The interlayer distance of the electrodes were characterized by XRD (D8 system, Bruker, Germany) measurements using a Bragg-Brentano diffraction mode. The morphology of the electrodes was investigated by SEM (FE-SEM Ultra55, Carl Zeiss, Germany) and TEM (CM 30 ST, Phillips, Netherlands).

Results and discussion

Figure 1 display the diffractogram patterns of the ND-graphene composite membrane. The reduced composite membranes show broadened peaks with decreased intensity due to a less ordered structure. This indicates that the NDs are not distributed in-between individual graphene sheets, but are allocated between small blocks of packed graphene layers. The calculated interlayer distances range form 7.55 Å for the oxidized membrane to 4.71, 4.41, 3.44 and 3.38 Å for the pyrolized membranes at temperatures of 200, 250, 800 and 1000° C. These values are comparable to partially reduced graphite oxide (GOpr) reduced at similar temperatures [9].

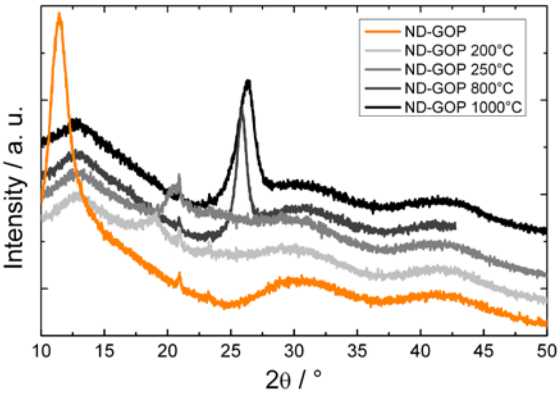

Figure 1. *XRD diffractograms of the graphene oxide based membrane (a) and the one based on the graphene oxide nanodiamond mixture (b). Each display the diffractogram of the untreated membrane as well as the ones for the different reduction temperatures of 200, 250, 800 and 100° C.*

The electrochemical performance of the ND-graphene composite membranes where characterized for the positive polarization using an activation cycle up 1.9 V vs. carbon followed by CV cycles between 0 and 1.5 V vs. carbon. The CVs were taken with 1 mVs^{-1} using 1M $TEABF_4$ / AN. In order to judge the performance of the ND-graphene composite membranes the same characterization was done for the graphene membrane reduced at the same temperatures. Figures 3 summarize the results from this characterization, showing the graphene membrane (GOP) in gray and the ND-graphene composite membrane (ND-GOP) in red. Starting with the GOP pyrolized at 1000° C one can see that the activation reaction seems to be hindered. The resulting specific capacitance of 19 Fg^{-1} is relatively small and indicates that the ions can not access the internal surface of the GOP. By decreasing the pyrolysis temperature both activation reaction and the achieved specific capacitance, are improved. The best result of this series is achieved for a GOP reduced at 250° C resulting in a specific capacitance of 147 Fg^{-1}. Compared to 195 Fg^{-1} achieved for GOpr [9] the graphene membrane yields approximately 25% less specific capacitance. The reason for this weak performance might be found within the thickness of the membrane. Both the GOP as well as the ND-GOP have a thickness of 100-200 μm which might lead to an increased resistance. This higher resistance might also explain the more elliptical shaped cyclic voltammetry of the 1.5 V cycles in Figure 3/4.

---

[1] Laboratory of Inorganic Chemistry, ETH Zürich, Switzerland
[2] A.J. Drexel Nanotechnology Institute, Drexel University, USA

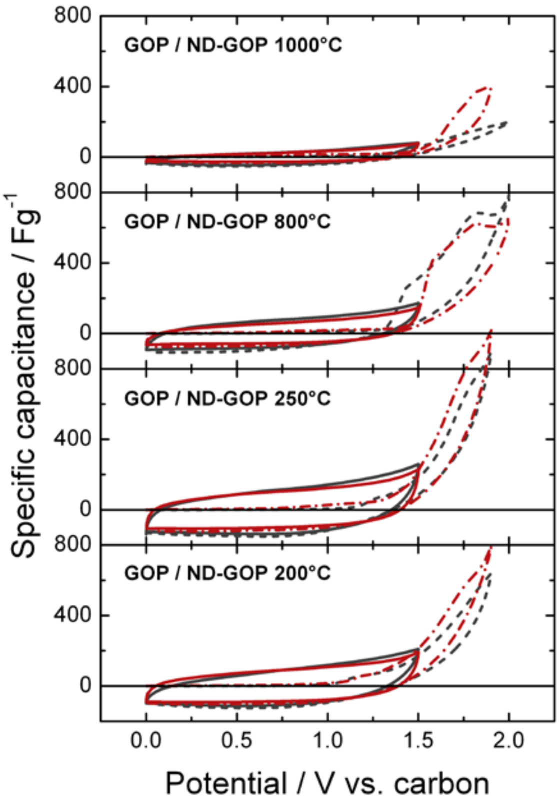

Figure 2. *First (dashed) and second (solid) cyclic voltammetry cycle for the positive polarization for GOP (gray) and ND-GOP (red) pyrolized at different temperatures of 1000°, 800°, 250° and 200° C. All the CVs were taken wit a sweep rate of 1 mVs^{-1} using 1M $TEABF_4$ / AN.*

Continuing with the ND-GOP (Figure 2 in red) it is obvious that it struggles from the same effects like the GOP (Figure 2 in gray). The observed electrochemical activations of the composite are similar to the GOP. This supports the observation from the XRD that the composite is based on graphene packages separated by NDs. Therefore the observed activation reactions in Figure 4 are related to graphene packages and not to NDs. As for the GOP the best specific capacitance is reached for the composite pyrolized at 250°C yielding 104 Fg^{-1}. This value is smaller than the one of the graphene membrane but this could be explained with the NDs within the graphene matrix which add mass but almost no capacitance.

Figure 3 compares the relative specific capacitance of the different GOPs and the ND-GOPs for two different discharge currents. The relative specific capacitance was calculated from the discharge current at 1 Ag^{-1} in relation to 0.1 Ag^{-1}. It can be seen that for all reduction temperatures the ND-GOP show a higher relative specific capacitance, i.e. a better rate capability.

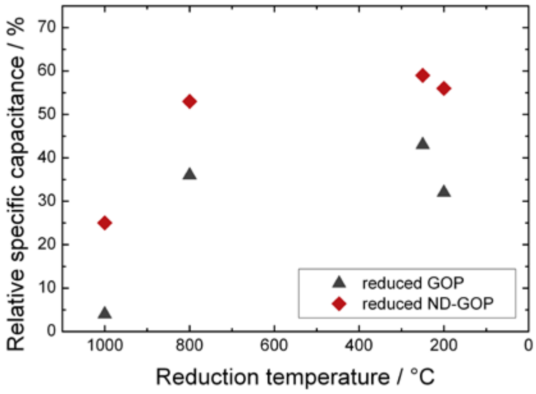

Figure 3. *Relative specific capacitance calculated from the discharge at 1 Ag^{-1} for GOP and ND-GOP reduced at different temperatures.*

Conclusions

The achieved ND-GOP proved the possibility of inserting a carbon based support material within a graphene matrix. However, XRD and cyclic voltammetry showed that the NDs are not homogenously spread but are concentrated between blocks of graphene packages. The electrochemical characterization indicates that partially pyrolized NDs have no positive effect on the achievable specific capacitance of the material. These results are comparable to graphene oxide nanodiamond composites described in literature [10] achieving approximately 140 Fg^{-1} using H_2SO_4. However, the direct comparison with a pure graphene membrane revealed an improved rate capability of the ND-graphene composite membrane.

Acknowledgement

The authors are grateful for the help of Ms. Amanda Pentecost, for milling the NDs, Ms. Annett Rabis, for doing the XRD and Swiss National Science Foundation for financial support (project # 200021_126855/1).

References

[1] A.K. Geim, K.S. Novoselov, *Nat. Mater.*, **6**(3), 183–191 (2007).

[2] R. Kötz, M. Carlen, *Electrochim. Acta*, **45**(15-16), 2483 – 2498 (2000).

[3] D. Li, M. B. Muller, S. Gilje, R. B. Kaner, G.G. Wallace, *Nat. Nanotechnol.*, **3**(2), 101–105 (2008).

[4] D.A. Dikin, S. Stankovich, E.J. Zimney, R.D. Piner, G.H.B. Dommett, G. Evmenenko, S. T. Nguyen, R.S. Ruoff, *Nature*, **448**(7152), 457–460 (2007).

[5] O.C. Compton, S.T. Nguyen, *Small*, **6**(6), 711–723 (2010).

[6] S. Osswald, G. Yushin, V. Mochalin, S.i O. Kucheyev, Y. Gogotsi, *J. Am. Chem. Soc.*, **128**(35), 11635–11642 (2006).

[7] V.L. Kuznetsov, Yu.V. Butenko, *Synthesis, Properties and Applications of Ultrananocrystalline Diamond - NATO Science Series*, **192,** 199–216 (2005).

[8] A. Pentecost, S. Gour, V. Mochalin, I. Knoke, Y. Gogotsi, *ACS Applied Materials & Interfaces*, **2**(11), 3289–3294 (2010).

[9] M.M. Hantel, T. Kaspar, R. Nesper, A. Wokaun, and R. Kötz, *Chem. Eur. J.*, **18**(29), 9125–9136 (2012).

[10] Y. Sun, Q. Wu, Y. Xu, H. Bai, C. Li, G. Shi, *J. Mater. Chem.*, **21**(20), 7154–7160 (2011).

Recent progress on Li-O_2 batteries at PSI

E.J. Berg, P. Novák

phone: +41 56 310 5736, e-mail: erik.jaemstorp-berg@psi.ch

The rechargeable lithium-air battery, or preferably Li-O_2 battery since lithium and oxygen are the reagents, has been subject to what has been described as a "gold rush" by researchers worldwide during the past years [1]. The high specific energy of the battery, sometimes boldly claimed to even approach that of gasoline [2], has rendered Li-O_2 batteries as one of the most attractive technologies for use in automotive and/or stationary applications.

The Li-O_2 cell mainly comprises a negative (e.g. Li metal) and positive (e.g. porous carbon) electrode separated by an electronically insulating, but Li^+ conducting layer. However, unlike conventional Li-ion batteries where the reagents are kept within a sealed cell, oxygen enters the cell from the outside (e.g. atmosphere), dissolves in the electrolyte and gets reduced at the positive electrode on discharge. Concurrently, Li-ions form at the negative electrode, diffuse through the electrolyte, and react with the reduced oxygen to form the discharge product (e.g. Li_2O_2) on the positive electrode. On charging, the discharge product is oxidized, the lithium ions return to the negative electrode and oxygen gas evolves. At PSI, a Li-O_2 cell for use particularly with non-aqueous aprotic electrolytes has been developed (Fig 1a). Cells operating with non-aqueous, as opposed to aqueous, electrolytes are commonly preferred, since they offer higher specific capacities [2]. The principal chemical reaction in non-aqueous electrolytes may thus be formulated as

$$2\mathrm{Li} + \mathrm{O_2} \leftrightarrow \mathrm{Li_2O_2} \qquad U^o = 2.96V,$$

although a sequence of intermediate steps is present [1]. Apart from the principal reaction, a range of undesired irreversible side reactions with the chemical environment are seen to occur [1]. These adverse reactions are currently the major hurdle to Li-O_2 battery development because they increase the overpotentials and limit the rechargability as well as the life time of the system. The life time of typical Li-O_2 cells are normally restricted to a few cycles with a rapid loss in cell capacity. However, an improved cyclability is nevertheless an inadequate measure to probe the rechargability [3]. It has been observed that even though the irreversible side reactions are ultimately detrimental to cell performance, they may not immediately influence the cyclability [3]. Therefore, the electrochemically active species have to be carefully monitored, e.g. by analyzing O_2 gas usage, before conclusions on the true rechargability of the cell can be drawn. For this purpose, a dedicated dosing differential electrochemical mass spectrometer (D-DEMS) has been developed to follow the oxygen gas being consumed and evolved during discharge and charge, respectively. In this report, first results with the PSI Li-O_2 cell and the D-DEMS are presented and discussed.

Experimental

Fig. 1 shows a simplified sketch of the PSI Li-O_2 cell and the D-DEMS. The Li-O_2 cell consists of Ti current collectors, a stainless steel spring to apply mechanical pressure on the electrodes and rubber O-rings for air-tight sealing; all assembled in a PEEK casing. The D-DEMS setup (Fig. 1b) operates with a quadrupole mass spectrometer (MS) for partial pressure measurements, a pressure transducer (PS) for cell pressure and volume determination, stainless steel gas pipes to connect the Li-O_2 cell, a set of solenoid valves and a membrane pump for efficient cell flushing. Apart from this: Ar, O_2 and calibration gas bottles (C1, C2) are connected (Fig. 1b). The carbon electrodes are prepared by dispersing 80% graphite (SFG6, TIMCAL), 20% Li-exchanged Nafion binder (LithION GmbH) in an NMP/EtOH solution to obtain a slurry with proper viscosity for doctor blade coating. The slurry is coated (200µm) directly on Celgard 2400 separator and vacuum-dried at 80°C over-night. Thereafter, electrodes are punched and again vacuum-dried over-night (at 95°C) along with the cell parts before introduction into the Ar filled glove-box. The cell is assembled according to Fig. 1a with the porous graphite electrode (Ø18mm, 6mg) ontop of 3 Celgard 2400 separators (Ø 24mm) and a Li metal foil (Ø 20mm); all soaked in 160µl electrolyte of 0.2 M LiTFSI in Diglyme (Novolyte Inc., H_2O < 10 ppm). Before starting an experiment, the cell is mounted in the D-DEMS (Fig 1b), flushed several times with Ar to remove gaseous contaminants, pressurized with Ar to determine cell headspace volume and finally left 1h to equilibrate at 1.1 bar abs. of pure O_2. The cell was subsequently galvanostatically discharged and charged (0.18mA) within a potential window of 2.0-4.7 vs. Li^+/Li.

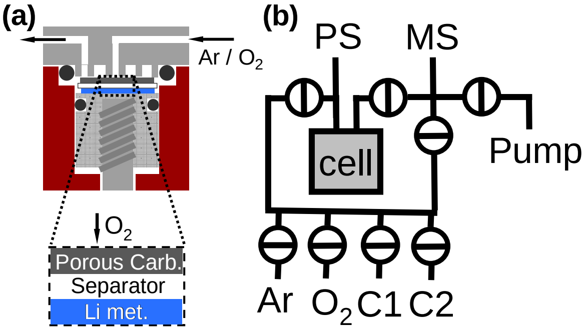

Figure 1. *Sketches of the* ***(a)*** *Li-O_2 cell and* ***(b)*** *dosing differential electrochemical mass spectrometer setup.*

Before the charging step, the cell is again flushed to create an Ar atmosphere in the cell headspace volume. During charging, the changes in the partial pressure of the cell are measured with 10 min time intervals. Each measurement point is recorded by opening and closing of the valves next to the cell in a sequential manner to let the gasses, which have accumulated in the cell, expand into the volume to which the MS is connected. The MS subsequently records the partial pressures and computes the amount of evolved gases. Before the next measurement point, the MS volume is again flushed and evacuated with the pump to remove any residual gases.

Results

Fig. 2a shows the potential profile of the first discharge and charge cycle. During the discharge, a potential plateau at ~2.6 V vs. Li^+/Li is observed and is mainly attributed to reduction of O_2 in the presence of Li-ions to form Li_2O_2; however with an overpotential (denoted η_{dis}) compared to the thermodynamic potential E^o (*2.96*V vs. Li^+/Li, Eq. 1). The magnitude of η_{dis} is consistent with previous studies [1] of similar systems, but its origin is not yet clear. The discharge capacity was found to be 95 mAh/g_{carbon} and is normalized with respect to the weight of the porous-carbon-positive-electrode only, thus disregarding the weight of the discharge products formed on the carbon surface. This capacity is reasonable with respect to previous studies [2], considering that the specific surface area of the graphite (16 m^2/g, SFG6, TIMCAL) is comparably [2] low and, as a consequence, the space for Li_2O_2 formation is limited. The charging potential monotonically increases from slightly above E^o up to the cut-off of 4.7V. The increasing overpotential (denoted η_{cha}) has been suggested to originate from side-products (e.g. Li_2CO_3, etc) covering the Li_2O_2 and therefore act as a potential barrier to further oxidation [3].

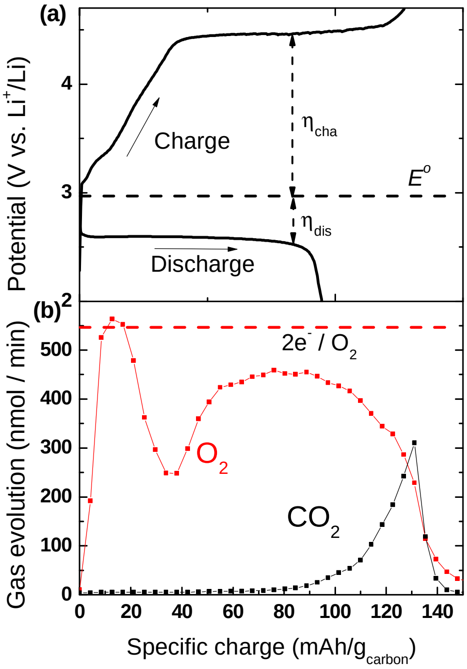

Figure 2. ***(a)*** *Potential profiles during galvanostatic discharge and charge of porous carbon electrode vs Li in 0.2 M LiTFSI in Diglyme.* ***(b)*** *O_2 and CO_2 gas evolution during charging.*

Fig. 2b shows the evolution rate of O_2 and CO_2 during charging. Interestingly, oxygen is observed already at very low η_{cha} and is in the beginning of the charging seen to reach an evolution rate of $2e^- / O_2$, which would correspond to Li_2O_2 oxidation. However, the oxygen evolution rate reduces thereafter and the current/O_2 ratio remains at $e^-/O_2 > 2$ for the rest of the charging step. The presence of competing electrochemical processes during charging is more clearly observable at higher potentials, e.g. with the appearance of CO_2 evolution at a potential of ~4.3V vs Li^+/Li. Although the oxygen dominates the gas evolution up to ~4.6V, where the formation rate of CO_2 rapidly takes over, the presence of parasitic reactions during almost the whole charging step is clearly evidenced already in the first cycle with the D-DEMS. However, the stability of the electrolyte itself has also to be considered, since it could to be compromised at these high potentials. Therefore, the importance of further research into reduction of the observed overpotentials during charging should be emphasized.

Conclusions

Judging from the first results, both the developed Li-O_2 cell and the D-DEMS are promising tools to study the performance of Li-O_2 systems. Reproducible and consistent results comparable to previously reported data has been achieved. The new setup enables the detailed observation of the oxygen evolution during charging, thus allowing assessment of the rechargability of the Li-O_2 cell. The reversible formation of Li_2O_2 is one of the major challenges for the Li-O_2 battery concept and more fundamental studies of the oxygen reduction and oxidation reactions (ORR/OER) in the presence of Li-ions in non-aqueous electrolytes are needed.

Acknowledgments

BASF SE is gratefully acknowledged for financial support within the framework of “BASF Network”. The authors wish to express gratitude to the group of H. Gasteiger at the Technical University in München (TUM) for many useful discussions. H. Kaiser and C. Junker are also particularly acknowledged for cell design and technical assistance.

References

[1] L.J. Hardwick, P.G. Bruce, *Curr. Opin. Solid. St. M.* **16**, 178-185 (2012).

[2] J. Christensen, P. Albertus, R. Sanchez-Carrera, T. Lohmann, B. Kozinsky, R. Liedtke, J. Ahmed, A. Kojic, *J. Electrochem. Soc.* **159**, R1-R30 (2012).

[3] B.D. McCloskey, A. Speidel, R. Scheffler, D.C. Miller, V. Viswanathan, J.S. Hummelshøj, J.K. Nørskov, A.C. Luntz., *J. Phys. Chem. Lett.* **3**, 997–1001 (2012).

Effect of sulphur type and graphitized carbon nanofibers on the performance of Li–S cells

S. Urbonaite, P. Novák

phone: +41 56 310 5775, e-mail: sigita.urbonaite@psi.ch

Lithium–sulphur (Li–S) batteries are considered to provide one of the most realistic pathways to reach the increased energy densities needed in new battery applications. Sulphur as the active material has a high specific charge of 1678 mAh/g. Furthermore, it is abundant and cheap. Despite these clear advantages, some challenges remain to be overcome before Li–S technology is ready for commercialization. One challenge is sulphur's isolating nature, making it important to identify both the optimal particle size for lithiation and a suitable conductive additive [1].

A number of different conductive additives can be used, but all of them have the same role — to connect all the sulphur present in the electrode into the conductive network and thus allow full sulphur utilization during the electrochemical charge and discharge.

In this work, the effect of sulphur-particle size (sulphur type) on the performance of Li–S cells has been tested under different conditions. Moreover, the use of graphitized carbon nanofibres (GCNF) as a conductive additive was explored, with the goal of improving both the electric and thermal conductivity, which is important for cycling stability of sulphur-composite electrodes.

Experimental

Sulphur electrodes have been prepared by mixing components such that standard final component ratios are as follows: 60% sulphur, 30% carbon (Super P or/and GCNF), 10% polyethylene oxide (PEO, M = 4,000,000 g/mol). Components were mixed using turbo stirring.

In case of S–GCNF composites 80% of the material is mixed with 10% Super P and 10% PEO. The S–GCNF composites were prepared in an autoclave by adding 20% GCNF and 80% of refined sulphur. The mixture was then kept at 125ºC for 24 h.

Electrolytes were either 1M LiTFSI in DME:Diox (2:1) or 1M LiTFSI in DME:Diox + 0.5 M LiNO$_3$, where LiTFSI is Lithium bis(trifluoromethane sulfone)imide, DME is dimethoxyethane, and Diox is 1,3-dioxolane.

Galvanostic cycling conditions: voltage window 1.8-2.7 V vs. Li, C-rate is defined as 1C = 1678 mA/g.

Electrodes with three different types of sulphur — sublimed, refined and precipitated — were prepared using PEO as a binder and contained 60% of sulphur.

Results

Among the three types of sulphur tested, sublimed sulphur has the largest particle size, refined sulphur is of intermediate size and the smallest particle size is found in precipitated sulphur powder. From Fig. 1 it can be seen that the biggest particles in the sublimed-sulphur electrode are extruded on the surface, whereas the refined and precipitated sulphur particles look similar. At higher magnifications (not shown here) it is clearly visible, however, that precipitated sulphur is agglomerated in the composite electrode. From this observation, it seems that refined sulphur should have the most favourable distribution in the carbon matrix.

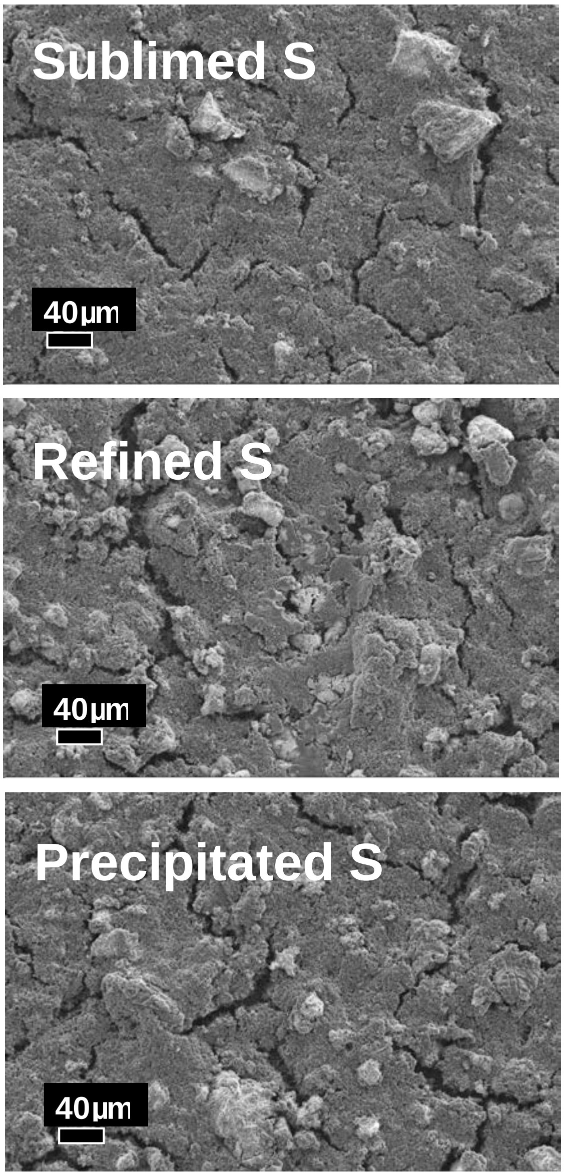

Figure 1. *SEM micrographs of sulphur/Super-P composite electrodes.*

The electrochemical behaviour was tested by galvanostatic cycling. In Fig. 2 the cycling behaviour of the S–Super-P composite electrodes under different conditions is shown for all three types of sulphur used. All electrodes were cycled under the same conditions; the only difference is that in the upper graph, the cycling performance is presented for the standard electrolyte, whereas in the data shown in the lower graph, LiNO$_3$ was used as an additive to the electrolyte, to help reducing irreversible-charge loss and to passivate metallic lithium [2]. As can be seen in Fig. 2, no size/type effect for the three kinds of sulphur particles is observed.

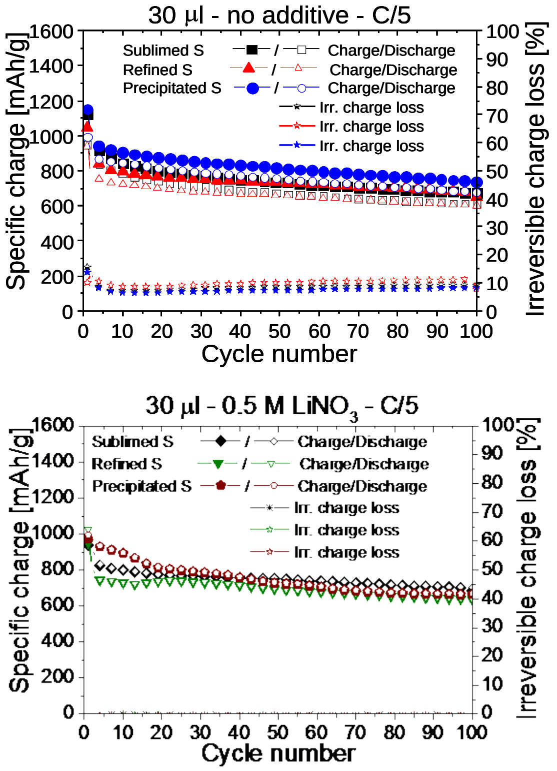

Figure 2. *Cycling performance of the composite sulphur/Super-P electrodes containing three types of sulphur tested under different conditions.*

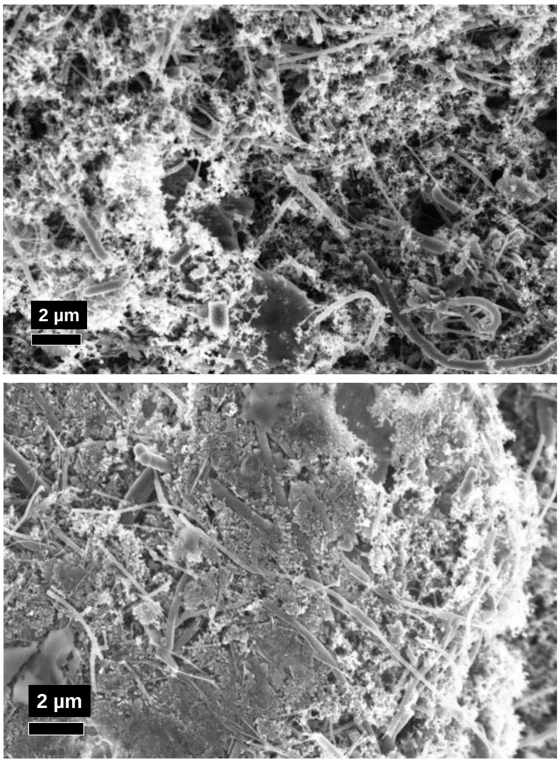

Figure 3. *SEM micrographs of S-GCNF/Super-P composite electrodes.*

Incorporation of GCNF into the electrode architecture resulted in well-interconnected, randomly wired carbon nanofibre network, as can be seen in the images shown in Fig. 3, with well-dispersed sulphur particles. However, it did not have the desired effect on the specific charge of the composite electrodes, which was already lower from the beginning than in electrodes prepared without GCNF, and remained so during all 100 cycles (see upper graph in Fig. 4). Therefore, the next step was to densify electrodes, and give GCNF a preferred orientation by calendering, SEM micrograph of this material is shown in the lower part of Fig. 3. However, the specific charge remained the same for all experimental condition and the irreversible capacity did not improve. Nonetheless, the specific charge stability over cycling was improved and after about 10–20 cycles, specific charge fading subsided. As in previous work, reported in last year's report, it is clearly confirmed that using a lower amount of electrolyte improves the specific charge and the stability during long term cycling.

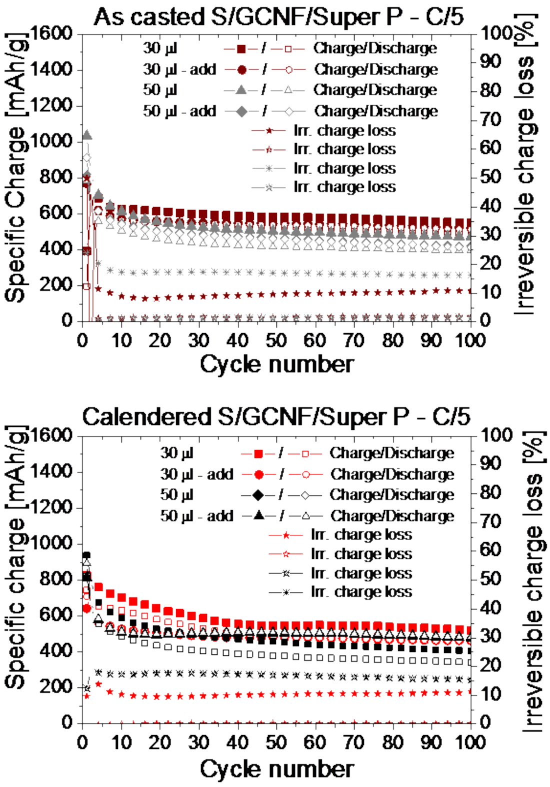

Figure 4. *Cycling performance of composite S-GCNF/Super-P electrodes.*

Conclusions

Despite reports in the literature of contrary trends [1], our experiments showed that sulphur type/particle size influence neither the practical specific charge nor cycling stability of Li-S cells. The incorporation of two-dimensional conductive additives, such as GCNF, does not improve the specific charge, but stabilizes and eliminates fading during extended cycling.

Acknowledgement

We thank BASF SE for financial support within the framework of "BASF Network".

References

[1] S. Evers, L.F. Nazar, Acc. Chem. Res. in press (2012) DOI: 10.1021/ar3001348.

[2] D. Aurbach, E. Pollak, R. Elazari, G. Salitra, C.S. Kelley, J. Affinito, J. Electrochem. Soc. **156**, A694−A702 (2009).

New composites for Li-S batteries

C. Villevieille, S. Urbonaite, P. Novák

phone: +41 56 310 2410, e-mail: claire.villevieille@psi.ch

Safety, low-cost and high-energy-density are the main requirements for the new generation of batteries, and one of the most promising candidates for new storage devices is the lithium sulphur battery. The reaction mechanism of Li-S batteries differs from conventional lithium-ion cells, which operate on the basis of topotactic intercalation reactions. The redox couple described by the reaction $S_8 + 16Li \rightarrow 8Li_2S$ leads to a theoretical specific charge of 1675 Ah/kg of S. Thus, compared with intercalation based batteries, Li/S cells can provide a significantly higher energy density with values close to 2500 Wh/kg, assuming complete lithiation to Li_2S [1]. Despite its considerable advantages, the Li/S cell has many latent challenges that prevent its practical application yet. The main drawback is that the sulphur is highly electrically and ionically insulating. To enable a reversible electrochemical reaction at high current rates, the sulphur must maintain intimate contact with electrically conductive additives. Various carbon-sulphur composites have been used for this purpose but they have limitations owing to the scale of the contact area. Typical reported specific charge values are between 500 and 700 Ah/kg at moderate rates [2]. In this work we present a new carbon-sulphur composite able to reach almost the theoretical specific charge during the first cycle and which then remains above 1000 Ah/kg during 40 cycles.

In order to explore new composite materials we were mixing by different ways the active material (refined sulphur) with conductive agents (carbon fibres, Super P carbon). The synthesis was performed by heating the mixture in the autoclave during 24h.

The advantage of our approach, compared to the other composites described in the literature, is that the autoclave method with the carbon fibres is not destructive and none of the carbon fibres were broken leading thus to a homogeneous composite material with a sulphur well attached to the carbon fibres, as seen in Figure 1.

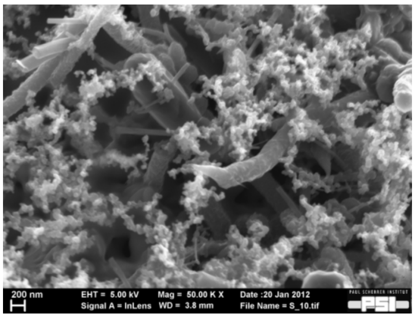

Figure 1. *SEM picture of the sulphur/carbon-fibres composite synthesized in autoclave.*

As we can see from the electrochemical results of the reference material, refined sulphur/Super P electrode (Figure 2, top), the specific charge at C/10 rate decreases and fades to less than 800 Ah/kg after 40 cycles. With the standard electrolyte without an additive, the irreversible charge loss is close to 10% every cycle. The most impressive specific charge was obtained for the composite (refined sulphur + carbon fibres) at C/10 rate with only 30 µl of standard electrolyte. After more than 40 cycles the specific charge is close to 1000 Ah/kg. Moreoever, at the beginning of cycling, the specific charge was very close to the theoretical one (Figure 2, bottom). Most surprising is the fact that the irreversible capacity is virtually 0%. It seems that we were able to create an intimate composite between the carbon fibres and the sulphur when using the autoclave for the synthesis.

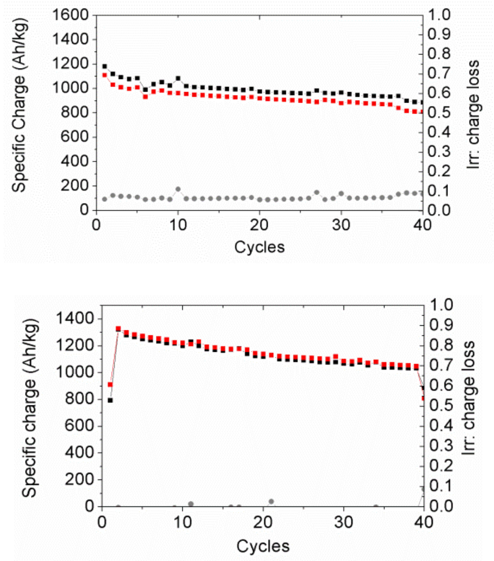

Figure 2. *Galvanostatic cycles of lithium sulphur cells at C/10 rate with 30 µl of LiTFSI based electrolyte, (top) of refined sulphur only, (bottom) of the sulphur/carbon-fibre composite.*

In short, here we show the importance to identify the best composite material and composite synthesis method in order to improve the conductivity of the sulphur based composite and to obtain the perfect interpenetration of carbon and sulphur.

Acknowledgement

We thank BASF SE for financial support within the framework of “BASF Network”.

References

[1] D. Peramunage, S. Licht, Science **261**, 1029-1032 (1993).

[2] S. Holger, A. Garsuch, A. Panchenko, O. Gronwald, N. Janssen, P. Novák, J. Power Sources. **205**, 420-425 (2012).

Influence of conductive carbon additives on the performance of $LiCoO_2$ electrodes

C. Bünzli, J.L. Gómez-Cámer, D. Cericola[1], P. Novák

phone: +41 56 310 2161, e-mail: christa.buenzli@psi.ch

To meet the demands of electric and plug-in hybrid electric vehicles for high energy densities at high power levels, research efforts have to concentrate both on active material development as well as on electrode engineering. In order to fully exploit a material's potential, optimisation of the electrode design is of utmost importance [1]. As many active materials for the positive electrode in lithium-ion batteries exhibit low electronic conductivity, conductive additives (CAs) are a crucial part of an electrode's composition. Carbon-based additives are commonly used as the CA due to their good electronic conductivity and chemical stability.

Here, the commercially available carbon blacks (CBs) SuperP® Li (SP), C-NERGY™ SuperC65 (SC65) and C-NERGY™ SuperC45 (SC45) were studied and compared. Graphites are also used as CAs and in addition, synergistic effects of the combined addition of CB and graphite have been reported [2,3]. Therefore, the CBs were investigated in combination with the graphite C-NERGY™ KS6L (KS6L) as CAs. These carbons have recently been developed as CAs in batteries and their properties like morphology, electrical resistivity of dry powder mixtures and surface group chemistry have been investigated [3]. However, their cycling performance under battery cycling conditions has not yet been fully explored. As has been shown, good electronic conductivity of an electrode does not necessarily translate directly into good battery cycling performance, most likely due to ionic conductivity restrictions [1].

In this contribution, the electrode preparation was not engineered, i.e. the preparation method was kept constant for the various electrodes with different CA composition. However, for an effective conductive carbon network, not only the nature and the amount of the carbon additives are important. The connectivity of the carbons is also affected by the preparation method, the viscosity of the slurry, the level of dispersion of the CAs, thermodynamic interactions between the CA and the polymer and the ionic strength of the medium [3,4]. It is noted that, for optimal performances of the electrodes, the conditions for each composition would have to be optimised with respect to all of the above-mentioned parameters.

Experimental

$LiCoO_2$ (LCO) is the most commonly employed positive electrode material in nowadays rechargeable batteries [5] and was chosen as an exemplary active material with intrinsically low conductivity. Composite electrodes consisting of 87 wt% LCO (Umicore), 3 wt% carbon black (TIMCAL), 3 wt% C-NERGY™ KS6L (TIMCAL) and 7 wt% PVDF (KF polymer L#1320, Kureha) as the binder material were prepared. The following carbon blacks were employed: SuperP® Li, C-NERGY™ SuperC65 and C-NERGY™ SuperC45. Additional *N*-methylpyrrolidone (NMP) was added to obtain a viscous slurry. The mixture was homogenised for 2 minutes using a POLYTRON® PT 2100 homogeniser (Kinematica AG) at 22'000 rpm. After 45 minutes on a roller table, the slurries were casted by a doctor blade technique onto aluminium foil. The electrodes were dried under vacuum at 80° C overnight. Scanning electron microscopy (SEM) images of the as-prepared electrodes were taken on a Carl Zeiss Ultra 55 microscope. Electrodes of a geometrical area of 1.3 cm^2 were punched out and calendered. In order to minimise influences from electrode parameters, the macroscopic properties of the electrodes were kept within small deviations from each other as shown in Table 1.

CA (+ 3 wt% KS6L)	Active mass [mg]	Height [µm]	Density* [g/cm^3]
3 wt% SC45	9.07 ± 0.09	38.0 ± 1.8	2.1 ± 0.1
3 wt% SC65	9.46 ± 0.12	37.8 ± 1.5	2.2 ± 0.1
3 wt% SP	9.40 ± 0.11	37.8 ± 1.5	2.2 ± 0.1

*taking total film mass into account

Table 1. *Macroscopic properties of the calendered electrodes.*

The electrodes were dried under vacuum at 120° C overnight before they were assembled in an argon filled glovebox. The coin-type cells comprised a 0.75 mm thick Li foil (Alfa Aesar) as a counter electrode, a glass fiber fleece as a separator and were filled with 500 µl of 1 M $LiPF_6$ in ethylene carbonate : dimethyl carbonate = 1 : 1 by weight (Ferro). Galvanostatic cycling was performed by a computer controlled cell capture system (CCCC, Astrol Electronic AG) in a temperature controlled chamber at 25° C between 3.0 and 4.2 V vs. Li^+/Li, at consecutive rates of C/3, 1C, 5C, 10C, C/3, 1C (taking 1C as 150 mA/g). Each galvanostatic phase was followed by a potentiostatic step until the current dropped to a value corresponding to C/30.

Results

Figure 1 shows a representative SEM image of the composite electrode. The active LCO material particles are surrounded by the CA network of CB and graphite particles. The smaller size of the CB particles allows them to fill the voids between the larger LCO particles and hence

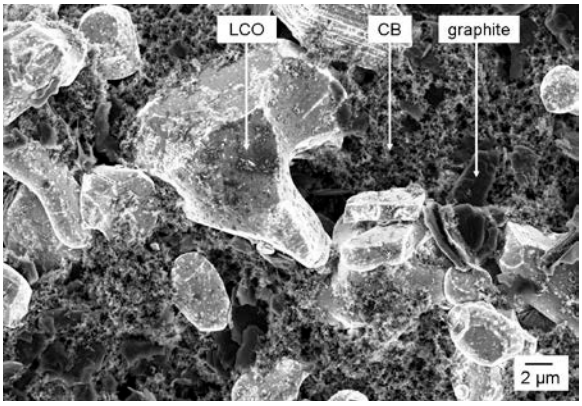

Figure 1. *SEM image of a pristine electrode with 3 wt% SC65 and 3 wt% KS6L as additives to LCO.*

---

[1] R&D Electrochemical Applications, TIMCAL Ltd., Bodio, Switzerland

increases the electronic contact area to the active material.

Figure 2 shows that the total specific charges of the various electrode combinations were the same within the error of the measurement. Furthermore, the total specific charge did not depend on the cycle rate as the same cut-off current corresponding to C/30 was used in the potentiostatic step and the electrodes could therefore compensate during this phase for shortcomings in the galvanostatic step. Only a slight fading of the total specific charge was observed over the first 55 charge / discharge cycles.

The galvanostatic charge parts clearly decreased with C-rate. At 5C, the electrodes were at their limit regarding galvanostatic cycling and exhibited a huge dispersion. A cycle rate of 10C was too high to allow galvanostatic charging for all the investigated electrodes. These fast cycle rates did not provide relevant information for the comparison of the different CAs and are therefore not shown. However, it should be noted that the electrodes exhibited a good recovery of their galvanostatic charging after the fast cycling rates.

The comparison of the galvanostatic parts of the different carbon additives shows that at the beginning at a cycling rate of C/3, the performance of the electrodes with different CAs was the same, which is in agreement with their morphological and electrical resistivities in dry powder mixtures [3]. With prolonged cycling and especially at faster cycling rates, small differences became apparent. The galvanostatic charge part decreased in the order of SP > SC65 > SC45. This was mainly due to a larger loss in the galvanostatic charge part of the electrodes with SC45 and SC65 while the SP-containing electrodes retained better its ability of galvanostatic charging. This trend was reflected in the potential profile of the charging of the LCO electrodes with different CB additives shown in Figure 3. Electrodes with a lower galvanostatic charge part exhibited a higher overpotential and the limiting potential of 4.2 V vs. Li^+/Li consequently was reached at a lower charge value. A more pronounced difference between the CAs is expected at even longer cycling time and at cycling rates between 1 and 5C. Why some of the CAs slow down electrode degradation more than others is not clear at this moment.

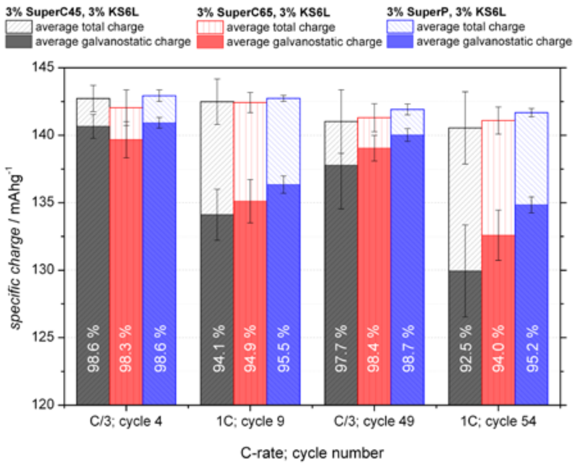

Figure 2. *Different carbon blacks are compared as 3 wt% additives to LCO electrodes in combination with 3 wt% of the graphite KS6L. The total specific and the galvanostatic charges are shown at various cycle numbers and cycling rates. The corresponding percentages of the galvanostatic part with respect to the total charge are given.*

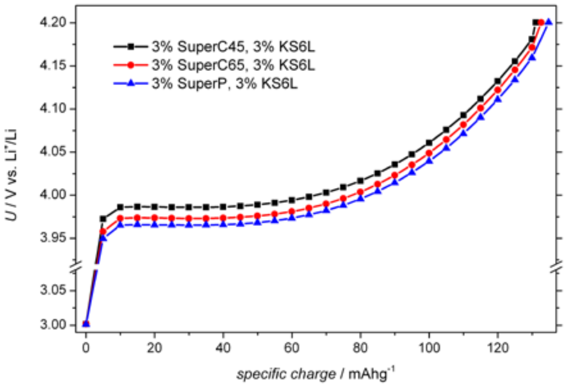

Figure 3. *Representative evolution of the potential during the charge of the 54th cycle at a cycling rate of 1C.*

This study showed that, under the employed electrode preparation conditions, i.e. keeping the same preparation procedure for the different electrode compositions, electrodes with SP as carbon black CA exhibited a marginally better performance at fast cycle rates in combination with a slighly better cycle life than electrodes containing SC65 or SC45. So far, the findings are just of observative nature. In the future, the present results will be compared to electrochemical impedance spectroscopy of the respective electrodes.

Acknowledgment

The authors thank TIMCAL SA for financial support.

References

[1] H. Zheng, R. Yang, G. Liu, X. Song, V. Battaglia, J. Phys. Chem. C **116**, 4875-4882 (2012).

[2] S. Cheon, C. Kwon, D. Kim, S. Hong, H. Kim, S. Kim, Electrochimica Acta **46**, 599-605 (2000).

[3] M. Spahr, D. Goers, A. Leone, S. Stallone, E. Grivei, J. Power Sources **196**, 3404-3413 (2011).

[4] D. Guy, B. Lestriez, R. Bouchet, D. Guyomard, J. Electrochem. Soc. **153**, A679-688 (2006).

[5] R. Marom, S. Amalraj, N. Leifer, D. Jacob, D. Aurbach, J. Mater. Chem. **21**, 9938-9954 (2011).

Thin-layer electrodes of overlithiated NCM material for model lithium-ion batteries

C. Villevieille, M. Heβ, P. Novák

phone: +41 56 310 2410, e-mail: claire.villevieille@psi.ch

Higher energy density materials such as the ‘Li-excess’ layered-layered NCM formed as structural defect (monoclinic domains) between Li_2MnO_3 and $LiMO_2$ [1] (where M = Ni, Mn, and Co) are promising candidates for future cathode materials in vehicle applications. They deliver higher specific charge (> 220 Ah/kg) once ‘activated’. This activation process involves the charging of the cathode to more positive potentials (> 4.5 V), thus removing both Li ions as well as a certain amount of oxygen. It was found previously that the activation process comes from the monoclinic domains of Li_2MnO_3, which occurs at very positive potentials above 4.5 V and leads to a release of oxygen during cycling [2]. Currently, it is still unknown what the local disorder in the overlithiated NCM is made of. The material still suffers from a capacity fading detectable after circa 50 cycles, which is probably due to the fact that i) the high voltage for the cycling involves electrolyte decomposition and generates more acidic solution (due to the formation of HF) leading to an increased manganese disproportionation [3], ii) oxygen release during cycling with the consequence of increasing pressure inside the cell and lowering electronic conductivity and iii) the structural rearrangements due to the oxygen lost.

We were making a thin-layer (TL) electrode of the overlithiated NCM material in order to improve the cycling stability (less amount of materials).

In figure 1 (left), the specific charge of the TL and a standard electrode (SE) are presented at different C-rates, C/10 and 1C, respectively. In the C/10 rate specific charge plot, we cannot observe a significant difference between the SE and TL both delivering a specific charge close to 275 Ah/kg. However, we can already notice the better capacity retention for the TL in comparison with the SE, and the better stability along cycling with less than 0.5% irreversible specific charge.

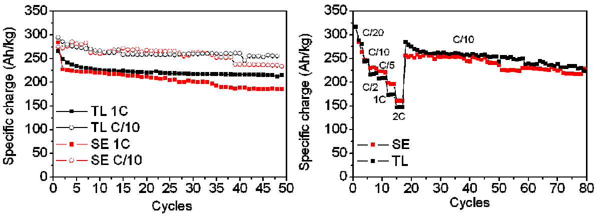

Figure 1. *Specific charge of a TL and a standard electrode of overlithiated NCM; left) at different C-rates; right) at different rates applied to the same electrode.*

For the 1-C rate, the results are similar except that the fading for the SE occurs faster after less than 10 cycles. After 50 cycles, a fading of more than 15% in respect to the initial cycle occurs for the SE, however, the TL electrode suffers only 3% specific charge loss. We designed an experiment to test the kinetic conditions during cycling, as shown in figure 1 (right). During the first twenty cycles different C-rates were applied between C/20 until 2C. There is no difference between C/20 and C/10 for the SE and TL electrode. In contrast, for rates between C/5 until 2C, the specific charge is higher for the SE than for the TL. This difference can be interpreted as slow kinetics or at least a slow adaptation to the new rate for the TL. Our hypothesis comes from the fact that the “SEI” on the surface of the TL hinders the cycling kinetics. Then, after 20 cycles, the rate was decreased back to C/10. Surprisingly the TL reached not only the original specific charge, it was a little bit higher than that before changing the rate. For the SE electrode, the specific charge reached again the starting values but started to fade quite fast.

The post mortem analyses of both TL and SE electrodes are shown in figure 2. The SEM pictures confirm our hypothesis that there are substantial cracks on the surface of the SE particles and no visible surface modification for the TL particles. But as we already suspected, there is a thick polymer layer on the surface of the TL (most probably due to the electrolyte decomposition).

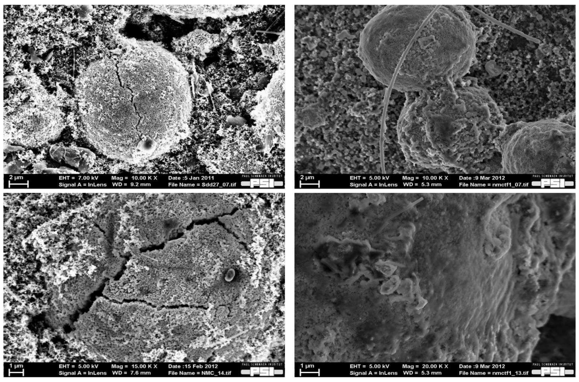

Figure 2. *SEM pictures of the overlithiated NCM after 50 cycles, left) the standard electrode, right) TL electrode.*

Acknowledgement

We thank BASF SE for financial support.

References

[1] M.M. Thackeray, S.H. Kang, C.S. Johnson, J.T. Vaughey, R. Benedek, S. A. Hackney, Journal of Materials Chemistry **17**, 3112-3125 (2007).

[2] V. A. Godbole, J. F. Colin, P. Novák, Journal of the Electrochemical Society **158**, A1005-A1010 (2011).

[3] J. Vetter, P. Novák, M.R. Wagner, C. Veit, K.C. Möller, J. O. Besenhard, M. Winter, M. Wohlfahrt-Mehrens, C. Vogler, A. Hammouche, Journal of Power Sources **147**, 269-281 (2005).

Ageing of overlithiated NCM positive electrode material upon exposure to water vapour

C. Villevieille, P. Lanz, P. Novák

phone: +41 56 310 2410, e-mail: claire.villevieille@psi.ch

The layered transition-metal oxide overlithiated '5V' NCM is a very promising replacement for $LiCoO_2$ in rechargeable Li-ion batteries [1]. However, extensive use of NCM requires knowledge of its long-term stability. Exposure to humidity is an important factor as it affects the specific charge of the material. Layered lithiated compounds and, in fact, all common cathode materials, are hygroscopic to a certain degree [2]. This phenomenon is caused by the high reactivity of Li towards H_2O, which results in delithiation of the surface layer over a thickness of a few nanometers.

Figure 1 summarizes some basic ageing mechanisms during cycling of NCM. The mechanisms of capacity fading and their prevention are of growing interest and not completely understood yet. A number of changes at the positive electrode may influence the life-time of a lithium-ion cell:

- Ageing of active material
- Degradation or changes in electrode components, such as conducting agents, binder, and current collector (corrosion)
- Oxidation of electrolyte components and surface film formation
- Interaction of ageing products with the negative electrode

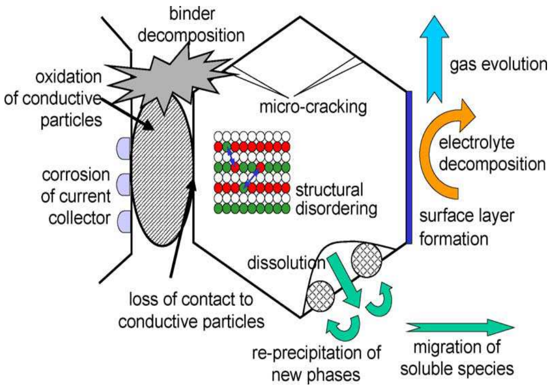
binder decomposition
oxidation of conductive particles
corrosion of current collector
micro-cracking
structural disordering
gas evolution
electrolyte decomposition
surface layer formation
dissolution
loss of contact to conductive particles
re-precipitation of new phases
migration of soluble species

Figure 1. *Ageing mechanisms of an NCM composite electrode and its interfaces during electrochemical cycling [3].*

These effects do not occur in isolation and cannot be discussed independently of one another. They are very sensitive to specific electrode compositions and are influenced by cycling and storage conditions.
In general, charge capacity fading of positive active material can occur according to three basic principles:

- Structural changes during cycling
- Chemical decomposition/dissolution reactions
- Surface film modification

We decided to investigate the effect of H_2O on overlithiated NCM upon ageing in a humid atmosphere by structural and electrochemical analysis as well as by infrared spectroscopy.

It was observed that both immersion of NCM in H_2O and exposure of NCM to a humid atmosphere led to rapid degradation that manifested itself in the delithiation of the surface layer of the particles. After ageing, about 80-90% of the initial specific charge was retained after 30 cycles at 1C in a potential window of 3.0–4.7V. But at a rate of C/10 the capacities were the same for the fresh material (FM) and for the aged material (AM).

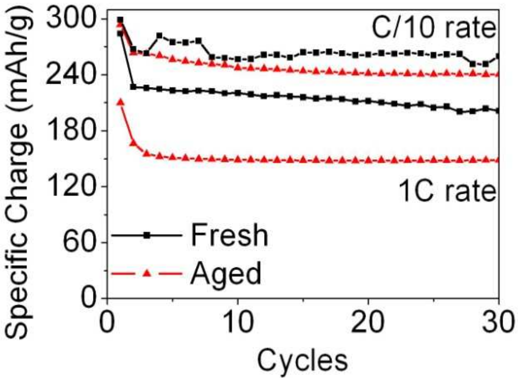

Figure 2. *Specific charge of overlithiated NCM before and after ageing with H_2O at different C-rates.*

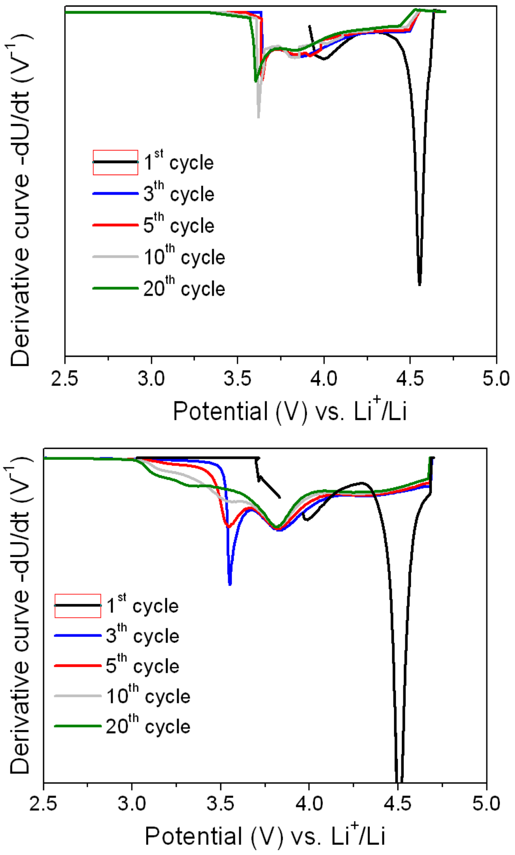

Figure 3. *Derivative curves of the galvanostatic curves for fresh NCM (top) and for aged NCM (bottom).*

We decided to have a closer look at the galvanostatic cycles for both FM and AM and, more specifically, at the derivative curves during the first 20 cycles. The curves are presented in figure 3, and it can be seen that there is no phenomenon between the potential windows of 3.0V and 3.5V *vs.* Li^+/Li during the first 20 cycles. If we now compare this with the derivative curves of the aged sample, it is clearly visible that a new phenomenon appears between 3.0V and 3.5V *vs.* Li^+/Li.

This new phenomenon increases after each cycle, which means that the respective current rises. Therefore, this new phenomenon is involved in the cycling process. If we now combine the observed specific charges with this new phenomenon, we know that we have lithium diffusion limitation.

Figure 4 shows the post mortem SEM pictures of AM and FM. It is clear that the layer on the surface of the AM is thicker and composed of relatively small, round particles. The EDX mapping analysis indicates that the layer is composed of decomposition products of the electrolyte.

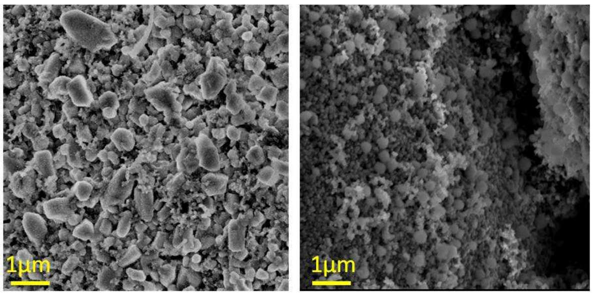

Figure 4. *SEM pictures after 20 cycles. Left: FM, right: AM.*

Nevertheless, it is well known that the surface of the lithiated sample reacts with air and moisture to form LiOH and Li_2CO_3 [4]. The corresponding infrared spectra are presented in figure 5. On FM no Li_2CO_3 is visible. However, if we increase the time of exposure to humidity, the Li_2CO_3 peak grows as well, indicating increasing thickness of the carbonate film.

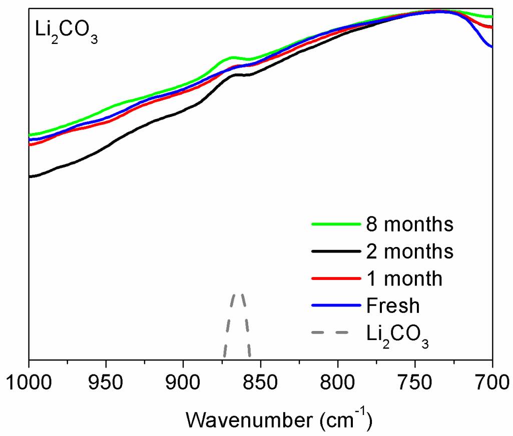

Figure 5. *Infrared spectra of the different aged NCM materials.*

Thus, we understand perfectly why the specific charge decreases when we apply a fast cycling rate. At low rates (C/10) lithium diffusion is not a limiting factor but when we increase the rate (1C) lithium is not able to diffuse through the layer at sufficient speed and we lose practical specific charge. Diffusion is reduced due to the carbonate layer as well as the layer generated by electrolyte decomposition.

The layer of electrolyte decomposition products is thicker in the case of aged NCM due to fast degradation at the surface which is full of adsorbed water, and consequently blocks the diffusion of lithium to a higher degree. AM suffers from various side reactions, such as accelerated Mn disproportionation (observed by XPS and EDX). Most of these side reactions are currently under investigation by *in situ* infrared spectroscopy, X-Ray photoelectron spectroscopy, and electrochemical impedance spectroscopy.

Acknowledgement

The authors are very grateful for the financial support from BASF SE.

References

[1] N. Yabuuchi, Y. Koyama, N. Nakayama, T. Ohzuku, J. Electrochem. Soc. **152** (2005) A1434.

[2] J. Cho, Y. Kim, S.S. Zhang (Ed.), Advanced Materials and Methods for Lithium-ion Batteries, Transworld Research Network Publ, 2007, p. 49.

[3] J. Vetter, P. Novák, M. R. Wagner, C. Veit, K. C. Möller, J. O. Besenhard, M. Winter, M. Wohlfahrt-Mehrens, C. Vogler, A. Hammouche, J. Power Sources **147** (2005) 269.

[4] G.V. Zhuang, G. Chen, J. Shim, X. Song, P.N. Ross Jr., T.J. Richardson, J. Power Sources **134** (2004) 293.

Phase boundary alignment in graphite during lithium intercalation

M. Heß, D.A. Cogswell[1], P. Novák, M.Z. Bazant[1]

phone: +41 56 310 2176, e-mail: michael.hess@psi.ch

Graphite is widely used in today's rechargeable lithium-ion batteries. The thermodynamic stage transitions have been investigated and presented in the last annual report. During the lithiation of graphite, first stage 1L develops which is the solid-solution phase of graphite with ~5% lithium in every interslab of graphite in a disordered (liquid-like) state. Further lithiation leads to a phase separation between stages 1L to 4L where lithium is ordered in every fourth interslab in a liquid-like manner. The following stage transitions to stage 3L and 2L are still under debate but order every third and second interslab. A phase separation from stage 2L to 2 leads to a densification of the in-plane density of Li in graphite to form LiC_6 in every other interslab. The final stage transition leads to stage 1 with LiC_6 in-plane density in every interslab.

But to be able to describe the stage transitions completely, the orientation of the phase boundary between the different stage transitions of graphite have to be investigated. Calculations of Cogswell and Bazant [1] have revealed the phase boundary alignment in $LiFePO_4$ using the calculations of Khachaturyan [2]. These calculations have been adapted for the Li-graphite system and are present here.

Results

The elastic strain energy can be calculated [2]:

$$B(\vec{n}) = C_{ijkl}\varepsilon^0_{ij}\varepsilon^0_{kl} - \vec{n}_i\sigma^0_{ij}\Omega_{jl}(\vec{n})\sigma^0_{lm}\vec{n}_m$$

where B is the elastic strain energy of a flat interface with the interfacial normal n, the elastic Green tensor Ω, the elastic stiffness tensor C and strain field ε. DFT calculations [3] have been used for the elastic stiffness tensor C. Since only the elastic constants of graphite and stage 1 have been investigated in the literature [3], linear combinations of them have been used for the intermediate stages. The strain field ε has been calculated from experimental data [4]. Figure 1 shows the elastic strain energy along the crystal orientations for the transition between stage 1 and 2.

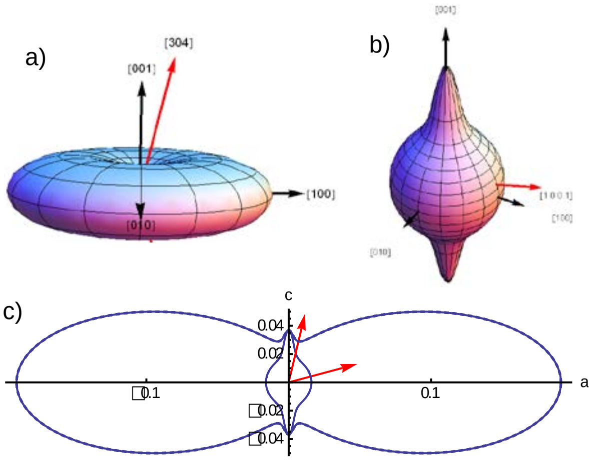

Figure 1. *Elastic strain energy of Li-graphite intercalation compound along crystal directions, a) coherent interface, b) incoherent interface in c-direction, c) cross-section of a) and b).*

The phase boundary will align along the minimal energy. For the stage 1 to 2 transition with a coherent interface (Fig. 1a) the minimum of the elastic strain will align at ~77°. All five different stage transitions will align close to 70° with respect to the graphene layers of graphite (table 1). Furthermore, the energy minimum is very well defined so that misalignments to the relative minimum will be energetically expensive.

A loss of coherency in different crystal directions might lead to a change in the elastic strain energy and therefore rotate the phase boundary (Fig. 1b). Losses of coherency have been modelled by having no strain in the respective crystallographic direction. An incoherent interface might come from a small defect in the crystal. Such a loss of coherency in c-direction would lead to a significant change in strain energy as depicted in Figure 1b. Table 2 shows that the phase boundary will align around 20° but has a very weakly defined minimum, so that misalignments can occur easily. A loss of coherency in a-, or b- direction will not change the strain energy much, so that the phase boundary will align close to 72° which is very close to the alignment for the coherent interface.

Phase Boundary	**Alignment vs. a,b- plane**	**±1% energy deviation**
Stage 1-2	77°	74° - 79°
Stage 2-2L	66°	62° - 70°
Stage 2L-3L	73°	70° - 76°
Stage 3L-4L	65°	59° - 70°
Stage 4L-1L	75°	71° - 77°

Table 1. *Calculated alignment of phase boundary to minimize elastic strain energy for coherent interface between stages.*

Phase Boundary	**Loss in [001] $\varepsilon_3 = 0$**	**±1% energy deviation**	**Loss in [100] $\varepsilon_1 = 0$**	**±1% energy deviation**
Stage 1-2	15°	0° - 40°	78°	76° - 80°
Stage 2-2L	20°	0° - 46°	67°	67° - 67°
Stage 2L-3L	20°	0° - 46°	75°	73° - 78°
Stage 3L-4L	22°	0° - 49°	67°	65° - 69°
Stage 4L-1L	23°	0° - 51°	76°	74° - 77°

Table 2. *Calculated alignment of phase boundary to minimize elastic strain energy with incoherent interfaces in a) c-direction [001], and b) a,b-direction [100] or [010].*

References

[1] D.A. Cogswell, M.Z. Bazant, ACS nano **6**, 2215 (2012).

[2] A.G. Khachaturyan, Sov. Phys. Solid State **8**, 2163 (1967).

[3] K.R. Kganyago, P.E. Ngoepe, Phys. Rev. B **68**, 205111 (2003).

[4] D. Billaud, F.X. Henry, M. Lelaurain, P. Willmann, J. Phys. Chem. Solids **57**, 775 (1996).

---

[1] Massachusetts Institute of Technology, Cambridge 02139, USA

New high energy materials for negative electrodes of lithium based batteries

C. Villevieille, J.L. Gómez-Cámer, P. Novák

phone: +41 56 310 2410, e-mail: claire.villevieille@psi.ch

During the 20 years since the commercialization of lithium-ion batteries, continuous progress in intercalation materials was made, and alternative materials including NCM, $LiFePO_4$ and $Li_4Ti_5O_{12}$ have reached the market at different levels, bringing incremental improvements in performance. Nonetheless, all these materials have intrinsic limitations in terms of specific charge, which are coming from their redox mechanism and structural aspects. Interest was therefore focused on alternatives like metals and semimetals that can electrochemically form alloys with lithium. Such materials are investigated as high specific charge electrode materials [1]. The specific charge that can be achieved from these alloying reactions can reach extremely high values both by weight and by volume, e.g., 8365 mAh/cm^3 and 3590 Ah/kg for silicon compared to 975 mAh/cm^3 and 372 Ah/kg for graphite. However, the practical utilization of these reactions has been severely handicapped by the huge volume changes associated to the (de)alloying process, which results in the introduction of high strains in the particles of active material and, in general, in the entire composite electrode. Upon cycling, such changes lead to a progressive decohesion, particle shuffling, and, subsequently, to a capacity loss [2]. The strategies used to circumvent these issues have recently been reviewed [3]. They always entail limiting the effects of these volume changes, mainly through the modification of the content ratios of active material, conductive additive, and polymeric binder in the electrode formulation.

In this contribution we test another way to solve the volume changes problem by creating an already lithiated matrix able to confine particles reacting with the lithium. This matrix shows very promising properties such as high conductivity and low potential, due to the lithium containing constitution.

As we can see from figures 1 and 2, the specific charge for materials containing Si-Sn and Si-P is higher than 1000 Ah/kg and 2500 Ah/kg, respectively, for the first cycle at a fast rate 1C.

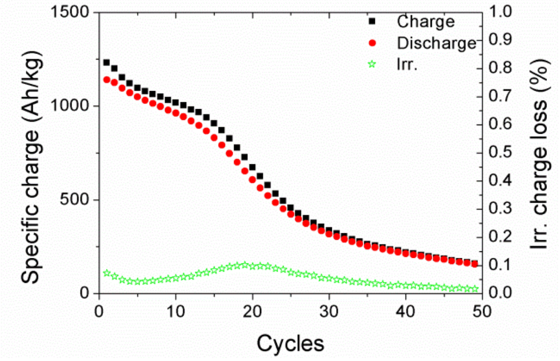

Figure 1. *Cycling of a lithiated matrix containing 2 active elements Sn & Si.*

More surprising is the fact that the irreversible charge loss is less than 10% for the Si-Sn based materials, which is low compared to other alloy materials such as Sn or Si. The fading for the subsequent cycles is presumably due to the fact that no engineering of the electrode was done, the materials were used as synthesized, without binder, and were mixed by hand with 10% Super-P carbon in order to improve the conductivity of the electrode mass

In figure 3 we compare the first half cycle of both materials at 1C rate, and confirm that the potential during cycling is less than 1V vs. Li$^+$/Li and that 90% of the capacity is coming from the potential window [0V-1V].

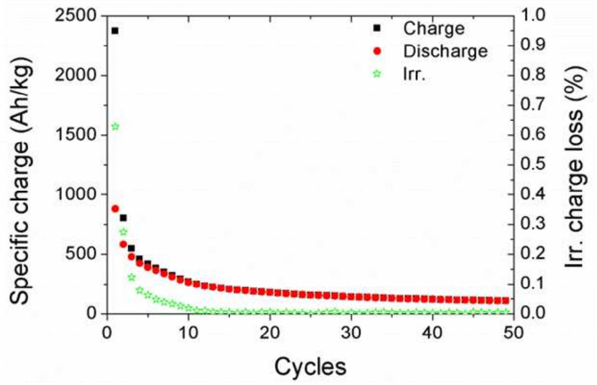

Figure 2. *Cycling of a lithiated matrix containing 2 active elements Si & P.*

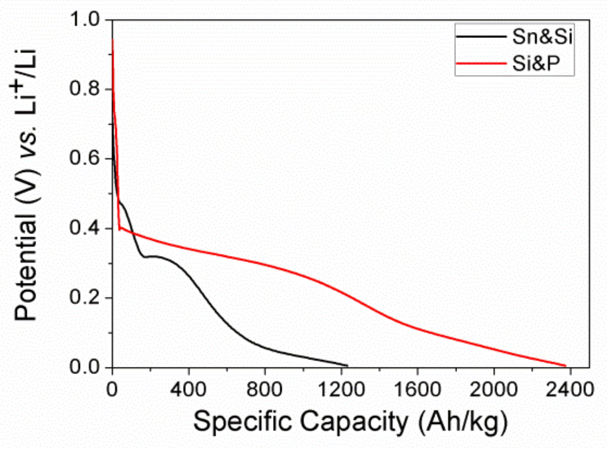

Figure 3. *First lithiation curve of Li-Si-Sn and Li-Si-P samples.*

Acknowledgement

We thank BASF SE for financial support within the framework of “BASF Network”.

References

[1] A.N. Dey, J. Electrochem. Soc. **118**, 1547, (1971).

[2] A. Timmons, J.R. Dahn, J. Electrochem. Soc., **153**, A1206, (2006).

[3] D. Larcher, S. Beattie, M. Morcrette, K. Edström, J.C. Jumas, J.M. Tarascon, J. Mater. Chem., **17**, 3759, (2007).

SCIENTIFIC ACHIEVEMENTS 2012

BATTERIES & SUPERCAPACITORS

DIAGNOSTICS

Ex situ X-ray absorption spectroscopy on $M_{0.5}TiOPO_4$ (M=Fe, Cu)

P. Bleith, C. Villevieille, P. Novák

phone: +41 56 310 2797, e-mail: peter.bleith@psi.ch

In order to increase the specific energy of battery materials, new materials are synthesised and tested as electrode materials in Li-ion batteries. To further improve the materials it is important to know the reaction mechanism of the materials. One characterization technique to elucidate the reaction mechanism is the study of the change of the oxidation state by X-ray absorption spectroscopy (XAS). In our studies, $Cu_{0.5}TiOPO_4$ and $Fe_{0.5}TiOPO_4$ were investigated by following the shift of the K_α absorption edge of copper, iron and titanium with the lithiation state of $M_{0.5}TiOPO_4$.

Experimental

$Cu_{0.5}TiOPO_4$ was synthesised from a solution of $NH_4H_2PO_4$ and $Cu(NO_3)_2$. $TiCl_4$*2THF dissolved in ethanol was added to this solution. The precipitate from this mixture was dried and subsequently heated to 200 °C, 450 °C and 900 °C. $Fe_{0.5}TiOPO_4$ was synthesised from $Cu_{0.5}TiOPO_4$ by an ion exchange with Fe powder at 900 °C in an evacuated silica tube. The Cu was removed from the $Fe_{0.5}TiOPO_4$ by washing with HNO_3 [1].

Ex situ samples were prepared by mixing $Cu_{0.5}TiOPO_4$ or $Fe_{0.5}TiOPO_4$ with 10 w% Super-P carbon. The samples were then cycled to different key-potentials in an electrochemical test cell with a lithium counter electrode and a 1:1 mixture of ethylene carbonate and dimethyl carbonate with 1 M $LiPF_6$ as electrolyte. The cycled powder was then taken out of the cell in an Ar-filled glove box, dried and filled in a capillary that was afterwards sealed with wax. Reference samples, Cu_2O, CuO, $FeSO_4$, Fe_2O_3, TiO, Ti_2O_3 and TiO_2 were also filled in capillaries. For the metals, a corresponding metal-foil was used as reference. *Ex situ* XAS measurements were done at Super-XAS beamline at SLS by recording spectra at the Cu-, Fe- and Ti-K_α-edge. Afterwards XRD measurements were performed on the filled capillaries on a PANalytical Empyrean diffractometer with a Mo X-ray source.

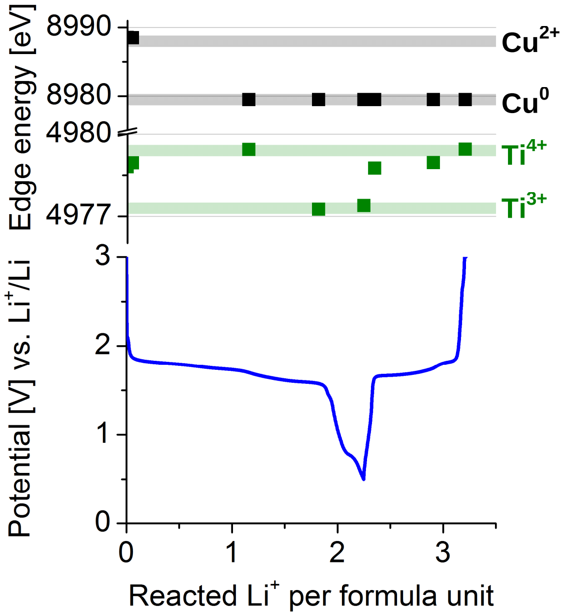

Figure 1: *Change of energy of the K_α absorption edge of copper and titanium in ex situ XAS measurements for $Cu_{0.5}TiOPO_4$ upon lithiation and delithiation.*

Results

If the local coordination of the central atoms is not changed, the position of the absorption edge of atoms changes with the oxidation state of the atom. The comparison to the edge-position of reference samples enables the determination of the oxidation state of the elements in the sample. For $Cu_{0.5}TiOPO_4$ it can be seen in Figure 1 that in the first reaction step, at 1.78 V vs. Li^+/Li, Cu^{2+} is reduced to Cu^0 and in the second step, at 1.7 V vs. Li^+/Li, Ti^{4+} is reduced to Ti^{3+}. Reactions at potentials negative to 1.5 V vs. Li^+/Li do not change the oxidation states of copper and titanium, so this reaction could be ascribed to the decomposition of the electrolyte. Upon delithiation, Ti^{3+} gets oxidised to Ti^{4+}, while copper is not reoxidised. Thus, based on these results, the reduction of copper is the irreversible process.

This hypothesis is supported by the *ex situ* XRD patterns (Figure 2). After the first lithiation step, mainly two phases can be detected: $LiTiOPO_4$ and metallic Cu (Cu^0). Cu^0 does not change significantly with further lithiation or delithiation. $LiTiOPO_4$ changes upon lithiation to a similar but as yet unknown structure, which could be Li_2TiOPO_4. Upon delithiation, this structure changes back to $LiTiOPO_4$.

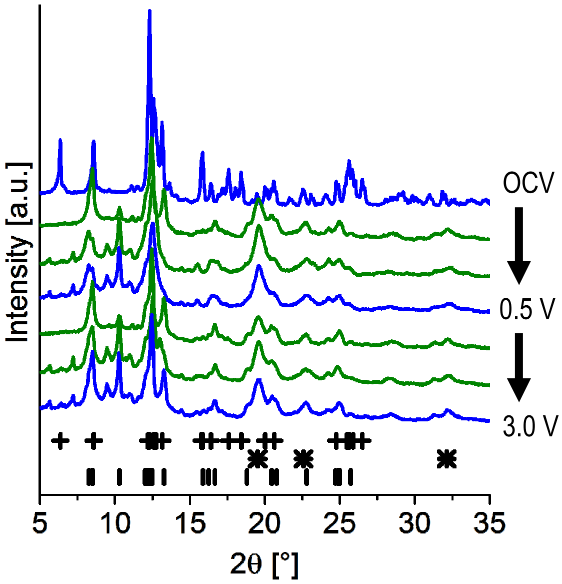

Figure 2: *Ex situ XRD patterns of $Cu_{0.5}TiOPO_4$ upon lithiation and delithiation; most intense reflexes of $Cu_{0.5}TiOPO_4$ (+), Cu (✳) and $LiTiOPO_4$ (|) are indicated.*

Similar studies were performed on Fe0.5TiOPO4, it can be seen in Figure 3 that here the first reaction, at 1.7 V vs. Li^+/Li, is the reduction of Ti^{4+} to Ti^{3+}, followed by the reduction of Fe^{2+} to Fe^0 at 0.7 V vs. Li^+/Li. At more negative potentials, Ti^{3+} seems to be reduced further. Upon delithiation, Fe^{0} is oxidised back to Fe^{2+}, and titanium to Ti^{4+}. Iron does not completely react back to the starting oxidation state. This could be explained by a partial quantity of Fe^{3+} in the starting phase as reported by Lasri et al. [2]. But it could also be due to an irreversible reaction, since the edge energy at full delithiation after the 2nd cycle (not shown in Figure 3) is also a bit lower than the one after the first cycle. More investigations are needed to validate one of those hypotheses.

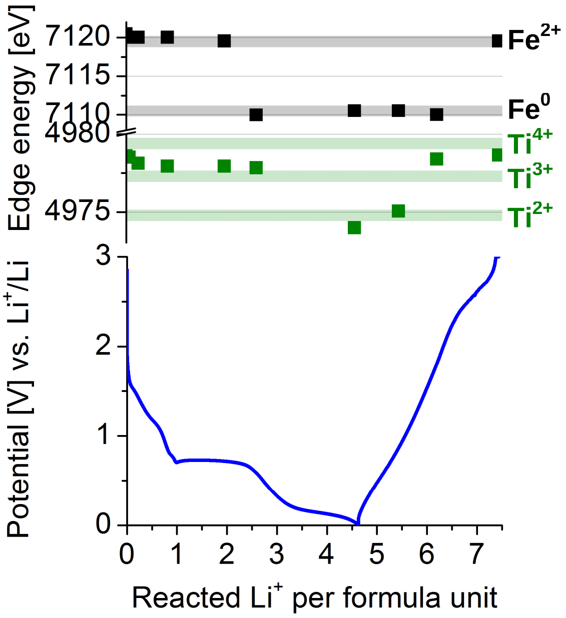

Figure 3: *Change of energy of the* K_α *absorption edge of iron and titanium in ex situ XAS measurements for* $Fe_{0.5}TiOPO_4$ *upon lithiation and delithiation.*

Ex situ XRD patterns of $Fe_{0.5}TiOPO_4$ (Figure 4) show a different behaviour of the material in comparison to $Cu_{0.5}TiOPO_4$ (Figure 2). In the case of $Fe_{0.5}TiOPO_4$, no metallic iron can be detected by XRD, because either the particles are not extruded or, more likely, the extruded particles are too small to be detected by XRD. After the first lithiation step, another, yet unknown phase appears. It is very similar to $Fe_{0.5}TiOPO_4$ and could be $LiFe_{0.5}TiOPO_4$. After the second lithiation step, an amorphisation occurs and the crystalline structure is lost. The only remaining reflexes can be ascribed to the dried electrolyte that was not washed away. Upon delithiation, the structure is not reconstructed and the sample stays amorphous. The amorphisation can also be the reason for the partly irreversible reaction, since particles might be electronically disconnected from the electrode during that process.

Conclusion

The reactions of $Cu_{0.5}TiOPO_4$ and $Fe_{0.5}TiOPO_4$ are different even if the materials are isostructural. Cu° is extruded out of $Cu_{0.5}TiOPO_4$ without an amorphisation of the structure and a lithium insertion in that structure occurs upon further lithiation. $Fe_{0.5}TiOPO_4$ first inserts one lithium-ion into the structure, before iron is reduced to Fe^{0} and the structure turns amorphous.

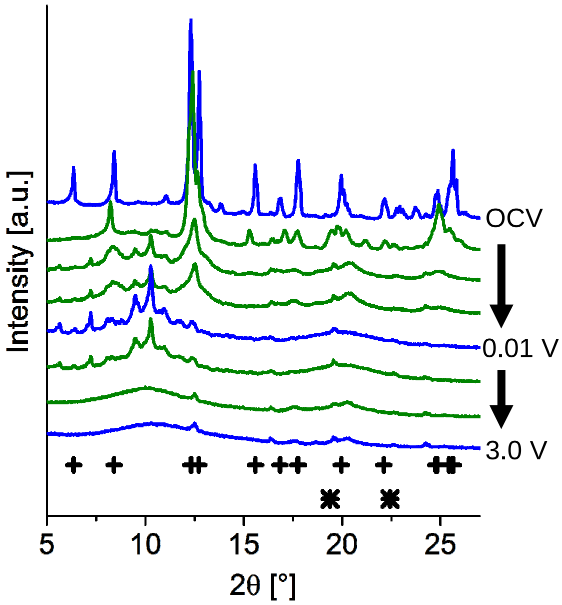

Figure 4: *Ex situ XRD patterns of* $Fe_{0.5}TiOPO_4$ *upon lithiation and delithiation; most intense reflexes of* $Fe_{0.5}TiOPO_4$ *(+) and Fe (✱) are indicated.*

Acknowledgment

Swiss National Science Foundation is thanked for financial support (project no 200021_129508). The support of Olga Safonova from the Super-XAS beamline was highly appreciated.

References

[1] S. Benmokhtar, A. El Jazouli, J.P. Chaminade, P. Gravereau, A. Wattiaux, L. Fournes, J.C. Grenier, D. Waal, J. Solid State Chem. **179**, 3709-3717 (2006).

[2] K. Lasri, I. Saadoune, Y. Bentaleb, D. Mikhailova, H. Ehrenberg, L. Häggström, K. Edström, Solid State Ionics **224**, 15-20 (2012).

Investigation of HE-NCM by differential electrochemical mass spectrometry to elucidate reactions occuring at high potentials

E. Castel, E. Jämstorp Berg, C. Villevieille, P. Novák

phone: +41 56 310 4542, e-mail: elias.castel@psi.ch

Widely used in the past twenty years, lithium-ion rechargeable batteries (LIBs) provide power for most of the portable electronic devices and nowadays, they are poised to enable the substitution of gasoline fuelled vehicles by hybrid systems (HEVs). Beyond consumer electronics, LIBs are also growing in popularity for military and aerospace applications. Research is yielding a stream of improvements to LIBs, focusing on high energy density, cycling performance, safety and cost.

To achieve higher energy, cathode materials with high specific charge and high voltage windows must be identified. The overlithiated NCM (HE-NCM), also formulated Li_2MnO_3-$Li(Ni_xCo_yMn_z)O_2$, displays a higher specific charge (~250 Ah/kg) and a higher volumetric energy density in comparison with other cathode materials. [1]. A potential plateau is observed on the first charge curve at 4.5V vs. Li^+/Li. This initial charging removes Li_2O from Li_2MnO_3, activating it for the subsequent cycling. [2] Although HE-NCM offers a higher energy density, several challenges remain such as the first cycling capacity loss of ~40 Ah/Kg and limited performances at high rates. Furthermore, the mechanism of Li_2MnO_3 oxidation is not fully understood. Differential electrochemical mass spectrometry (DEMS) is an analytic method used to detect gaseous and volatile reaction products from a battery during cycling. This technique was used to investigate the HE-NCM at high potentials.

Experimental

The working principle and setup of the mass spectrometer and the DEMS cell are described elsewhere [3,4]. The positive electrodes were prepared by casting mixtures of 80 wt% HE-NCM (BASF SE, Germany), 10 wt% Super P carbon black (TIMCAL, Switzerland) and 10 wt% PDVF-Kynar flex binder (Arkema, France) suspended in NMP solvent (Sigma-Aldrich, USA) onto the titanium metal current collectors of the DEMS cells via doctor-blading. After vacuum-drying the electrode overnight, the DEMS cells were assembled in an argon-filled glove box.

Results

Figure 1 compares the intensities of the relevant mass signals $I_{m/z}$ from the electrochemically generated gases and volatile compounds. The m/z= 44 and m/z= 32 signals are assigned to CO_2 and O_2 gas, respectively.

According to the evolution of $I_{m/z}$ signals we confirm that the oxygen release only appears during the first charge and we seem to have a two-step mechanism involving CO_2 gas formation. During the potential plateau at 4.5V and later, a continuous CO_2 release is observed, followed by a minor O_2 release. For higher potentials (>4.7V), the respective intensities of CO_2 and O_2 gas signals increase, and at the beginning of the discharge, very strong peaks are observed for both species. The intense CO_2 peak is mostly the result of the decomposition of the carbonates in the electrolyte. [5-6].

To investigate this two-step mechanism for O_2 and CO_2 gas formation, we plot the normalized $I_{m/z}$ signals versus the potential for the first cycle in Figure 2. We clearly see that the CO_2 and O_2 gas formation are correlated. However a short lag is observed between CO_2 and O_2 formation between 4.45V and 4.55V. Before 4.55V only CO_2 is detected, and above, O_2 is finally detected. This might suggest that a part of the oxygen released by HE-NCM reacts with carbonaceous species to form CO_2, most probably carbonate solvents of the electrolyte.

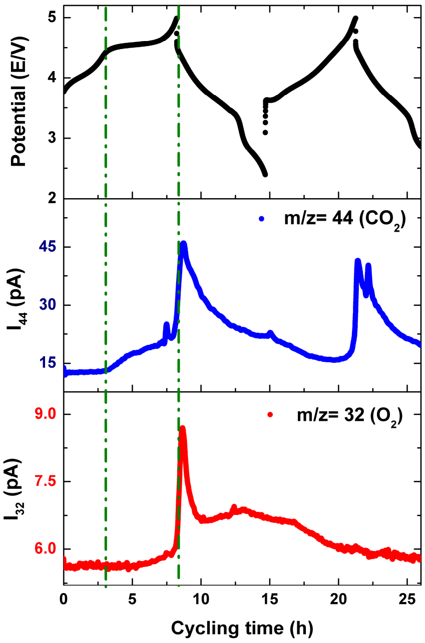

Figure 1. *Plot of mass signal intensities $I_{m/z}$ [A/g] during cycling of HE-NCM vs. Li in EC/DMC 1:1 by wt. (1 M $LiPF_6$).*

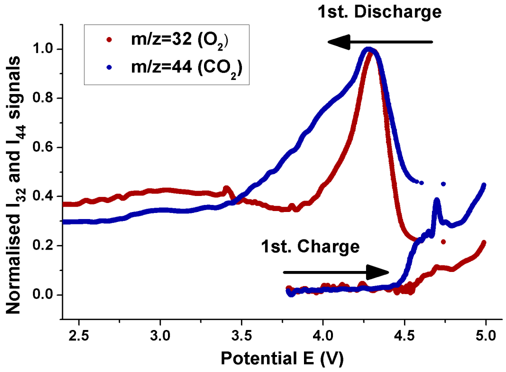

Figure 2. *Normalised mass signal intensities $I_{m/z}$ during cycling of HE-NCM as a function of the potential*

However, after the potential plateau, at higher potentials, O_2 does not participate fully anymore in the oxidation of the carbonates. And this can be detected. At higher potentials (> 4.7V) the strong CO_2 peak confirms that the decomposition of the carbonate solvents (see Ref. [5]) is running without the participation of the O_2 released by HE-NCM.

Furthermore, analysing both CO_2 and O_2 gas evolution during the discharge suggests the lagging of the signals. One explanation could be that the O_2 freshly formed at the HE-NCM material surface is trapped in the porous structure of the electrode.

To confirm these assumptions, another MS gas inlet with faster carrying gas rate has been introduced to reduce the lag of signals as much as possible. This new MS gas inlet setup also improves the sensitivity of the MS channel 32 (O_2 detection). The figure 3 shows the evolution of CO_2 and O_2 gas for the two first cycles.

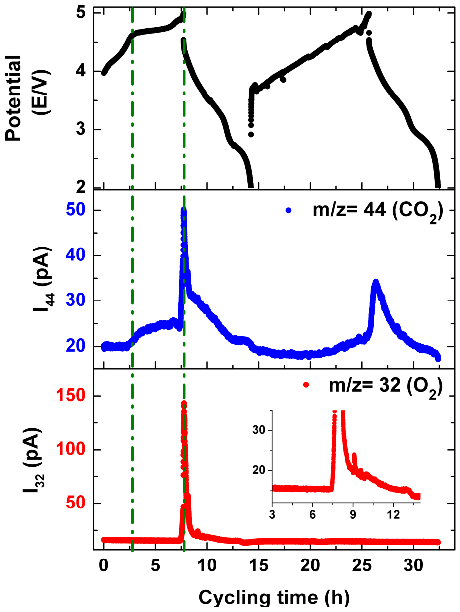

Figure 3. *Plot of mass signal intensities $I_{m/z}$ [A/g] during cycling of HE-NCM vs. Li in EC/DMC 1:1 by wt. (1 M $LiPF_6$).*

Here again, CO_2 gas is only detected during the plateau at 4.5V. At potentials higher than 4.8V, both O_2 and CO_2 gas are detected. This measurement also confirms that we mainly see the O_2 release in the 5V potential range and at the beginning of the discharge.

In Figure 4 we plot the normalised $I_{m/z}$ signals for the first cycle. We clearly see the ongoing and gradual CO_2 formation above 4.5V without any trace of O_2 until 4.8V is reached.

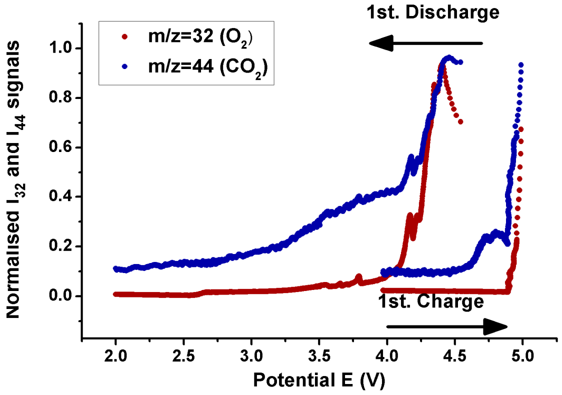

Figure 4. *Normalised mass signal intensities $I_{m/z}$ during cycling of HE-NCM as a function of the potential.*

Afterwards, a measurement is carried out with a 5 hours potentiostatic step at the end of the first galvanostatic charge to maintain the system at 5V. The goal is to see if the strong O_2 release is due to some lag and overpotential or if it is observed during the discharge only.

In Figure 5 we plot the evolution of mass signals intensities for CO_2 and O_2 measured for the first cycle of HE-NCM.

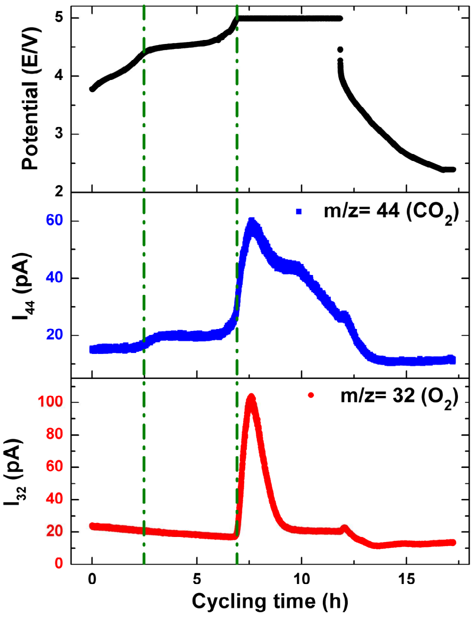

Figure 5. *Plot of mass signal intensities $I_{m/z}$ [A/g] during cycling of HE-NCM vs. Li in EC/DMC 1:1 by wt. (1 M $LiPF_6$).*

We confirm here that CO_2 is the only gas detected during the potential plateau at 4.5V. For potentials above 4.8V and during the potentiostatic step, strong CO_2 and O_2 peaks are clearly observed. The amount of CO_2 is at maximum when some O_2 is still delivered, when no more O_2 is released, then the amount of CO_2 is lowered. This demonstrates both oxidation and further self decomposition of carbonates of the electrolytes at high potentials.

Conclusion

The oxygen radicals released by the active material at the positive electrode during the potential plateau at 4.5V seems to be involved in oxidative reactions with carbonates of the electrolyte. Above 4.7V, the oxygen release is systematically observed accompanied by a strong CO_2 formation, assumed being the result of the carbonate solvents' decomposition at high potentials. Further improvements of the signals detection and data processing are in progress to analyse these data quantitatively.

Acknowledgment

The authors are very grateful for the financial support from BASF SE.

References

[1] M.M. Thackeray, S.-H. Kang, C.S. Johnson *et al.*, J. Mater. Chem. **17**, 3112-3125 (2007).

[2] N. Tran, L. Croguennec, M. Menetrier, *et al.*, Chem. Mater **20**, 4815-4825 (2008).

[3] A. Würsig, W. Scheifele, P. Novák, J. Electrochem. Soc. **154**, A449-A454 (2007).

[4] P. Novák, D. Goers, L. Hardwick *et al.*, J. Power Sources **146**, 15-20 (2005).

[5] M. Moshkovich M. Cojocaru, H.E. Gottlieb *et al.*, J. Electroanal. Chem. **497**, 84–96 (2001).

[6] K. Hayashi, Y. Nemoto, S. Tobishima *et al.*, Electrochem. Acta **44**, 2337-2344 (1999).

In and *ex situ* Raman microscopy applied to the mechanistic study of HE-NCM

P. Lanz, C. Villevieille, P. Novák

phone: +41 56 310 2474, e-mail: patrick.lanz@psi.ch

Li-ion batteries have found a wide range of applications in the portable electronics market and are promising candidates for hybrid electric vehicles and electric vehicles. Advancements in this field are likely to accelerate the adoption of Li-ion batteries by the automotive industry. In this article, we will focus on the positive electrode. Although $LiCoO_2$ has been widely used in industrial applications, it has some major drawbacks, including relatively low practical specific charge (150 Ah/kg), thermal instability, toxicity and high cost.

Layered $Li_{1+a}(Ni_xCo_yMn_z)_{1-a}O_2$ (HE-NCM) has been identified as an attractive alternative with a reduced Co-content. Overlithiation imparts further advantages with respect to cycling stability and rate capability [1]. Improved thermal stability and consistently high specific charges (> 200 Ah/kg) are additional promising features. Investigations of the structure of HE-NCM have revealed the presence of Li_2MnO_3-ordering (Li_2MnO_3 will be abbreviated as LM), with some of the Li being accommodated in the transition metal layers (alternative formula: $Li_2MnO_3 \cdot Li(Ni_{x'}Co_{y'}Mn_{z'})O_2$). Activation and subsequent electrochemical cycling of these LM-domains are responsible for the high specific charge of HE-NCM [2]. During the first charging step, this process leads to a potential plateau at ~4.5 V vs. Li^+/Li, which has been attributed to Li_2O extraction and subsequent oxygen release [3]. Direct evidence of the latter has been provided via differential electrochemical mass spectrometry (DEMS) [4].

In order to further improve the electrochemical properties of HE-NCM, it is important to obtain a detailed understanding of the mechanisms involved. Although many aspects of the first-cycle activation of HE-NCM have already been investigated, several questions remain unanswered. *In situ* Raman spectroscopy constitutes a powerful local characterisation method that provides valuable insights into the structural changes occurring in HE-NCM during electrochemical cycling. Due to the complex nature of HE-NCM and its associated *in situ* Raman spectra, we have also investigated a number of well-defined reference materials relevant to HE-NCM, such as LM, $Li(Ni_{1/3}Co_{1/3}Mn_{1/3})$ (sNCM) and $Li_{1.1}(Ni_{1/3}Co_{1/3}Mn_{1/3})$ (HE-sNCM). It is hoped that this approach will finally allow a more detailed understanding of the activation mechanism of HE-NCM.

Experimental

Electrodes were prepared by casting slurries of 80% active material, 10% Super P and 10% PVDF dispersed in N-methyl pyrrolidone onto stainless steel mesh current collectors via doctor-blading at 200 µm. After vacuum-drying, electrode discs (d = 13 mm) were punched out and calendered to a final thickness of ~80 µm. All experiments were conducted in half cells with metallic Li serving as both counter and reference electrode. The electrolyte consisted of 1 M $LiClO_4$ in EC/DMC.

A schematic diagram of the *in situ* Raman cell used for all Raman experiments presented in this report is shown in Figure 1. This cell design allows access to the back of the working electrode via a glass window. Raman spectra were recorded with a Horiba-Jobin Yvon Labram HR800 microscope equipped with a He-Ne laser (632.8 nm). Depending on the experiment, acquisition times between 60 s and 300 s and acquisition numbers between 1 and 10 were selected.

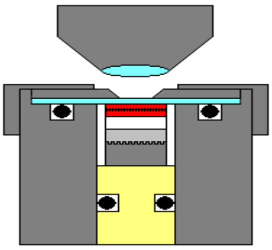

Figure 1. *Schematic diagram of the in situ Raman cell. From top to bottom: objective, glass window, working electrode (coated stainless steel mesh), glass fibre separator, lithium metal, plunger (Ti & PEEK).*

Results

The results of the *in situ* Raman experiments with HE-NCM have already been reported (Annual Report 2011, p. 63). However, a brief discussion is presented in the following paragraph to set the scene for the rest of this report.

Whereas the interpretation of the OCP spectrum of HE-NCM is rather straightforward (E_g at ~500 cm^{-1} and A_{1g} at ~600 cm^{-1}), the reversible bands at ~480 cm^{-1} and ~530 cm^{-1} that evolve during electrochemical cycling have not yet been assigned. It is assumed that they are connected to the potential plateau at 4.5 V vs. Li/Li^+, which has been attributed to the activation of LM-domains in HE-NCM [3]. Therefore, we decided to record separate *in situ* Raman spectra of sNCM and LM (Figure 2).

Apart from a decrease in intensity and a background drift, the *in situ* Raman spectra of sNCM and LM exhibit no striking changes. The decrease in intensity can be explained by improved conductivity of the charged material, which has a negative effect on the penetration depth. Interestingly, the initial intensities cannot be recovered after one complete cycle, which points towards some irreversibility. The slight shift of the A_{1g}-band of sNCM (600 cm^{-1}) is probably due to intercalation.

The most surprising result presented so far is that the *in situ* Raman spectra seem to indicate that LM had not been activated, which appears to be in contrast to the prevailing mechanism for HE-NCM. In order to exclude the possibility that a particle that happened to be inactive (e.g. due to high contact resistance) was measured, we charged LM in standard cells and conducted *ex situ* Raman measurements at various positions of the electrodes. In agreement with the *in situ* experiments, it was shown that LM did not exhibit any changes in its Raman spectra (results not shown).

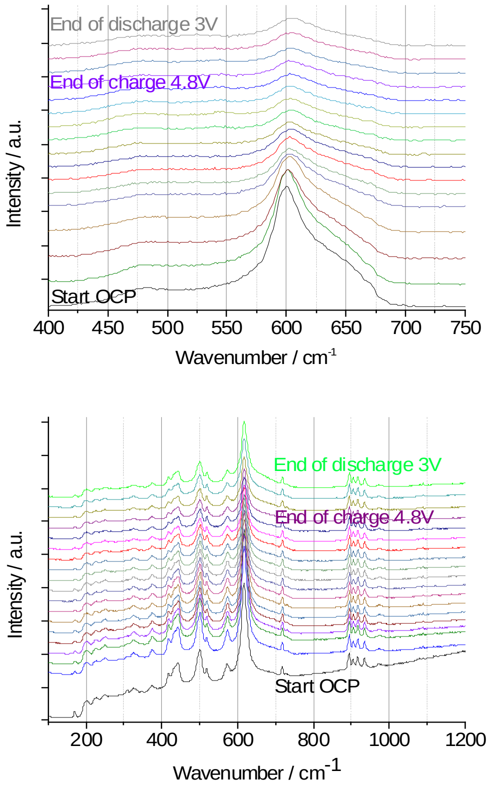

Figure 2. *First cycle in situ Raman spectra of sNCM (top) and LM (bottom). Both materials were synthesised at PSI. The spectra are offset arbitrarily along the intensity axis.*

In a final attempt to activate LM, the material was charged in standard cells, either at elevated temperatures or at increased potential. In the latter case, the galvanostatic step was skipped. On this occasion, an extensive *ex situ* Raman investigation of various pristine and cycled LM as well as NCM materials was conducted. The charged electrodes were rinsed with DMC and glued between two objective slides using epoxy resin. In order to increase the accuracy, calibration was performed not only with silicon but also with highly oriented pyrolytic graphite (HOPG). The results of these experiments are shown in Figures 3.

The *ex situ* Raman spectra presented at the top show some interesting characteristics. When comparing the spectra of sNCM, HE-sNCM and HE-NCM, it is obvious that the curves show an increasing LM-content in the following order: sNCM < HE-sNCM < HE-NCM. This is in perfect agreement with our expectations since the LM-content is proportional to the amount of overlithiation (Li-equivalents: 1, 1.1 and ~1.4, respectively). Note that the most intense LM-band causes the A_{1g}-band to move to higher wavenumbers for increasing overlithiation. Cycled HE-NCM exhibited a distinct shoulder at ~600 cm^{-1} that was absent in cycled HE-sNCM (not shown).

The final two diagrams clearly show that activation of LM can be achieved by using either elevated cycling temperatures or increased potentials. The observations are in agreement with a very recent publication, in which the new bands have been attributed to a spinel-like structure [5]. Our experiments have shown that the activation of LM is highly dependent on various factors. These insights should allow us to achieve LM-activation in future *in situ* experiments.

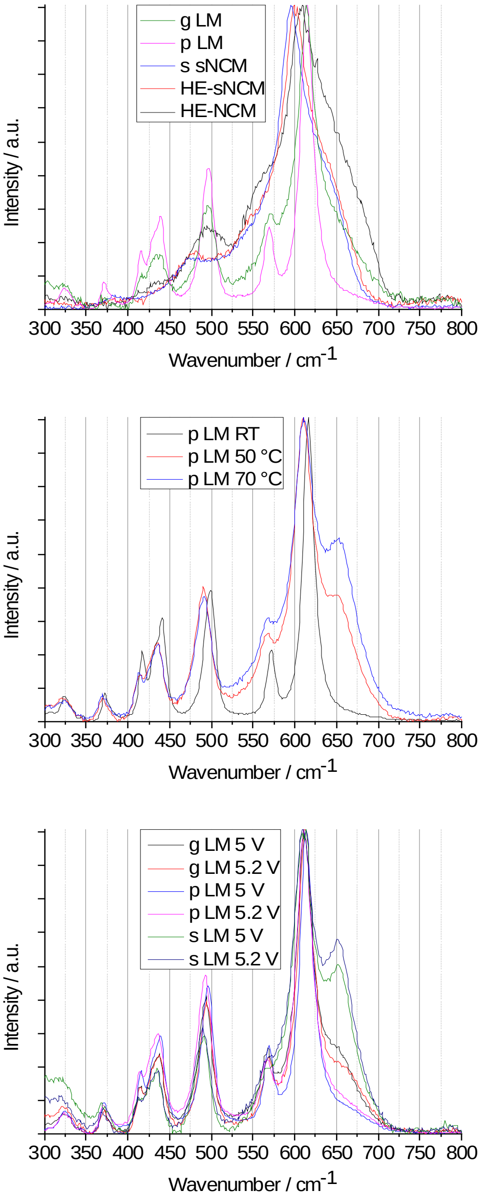

Figure 3. *Normalised ex situ Raman spectra. g: ground, p: pristine, s: self-synthesised (all other materials: BASF SE), RT/50°C/70°C: cycled at the respective temperature, 5V/5.2V: held at the respective potential for 70h.*

Acknowledgements

We are very grateful for the financial support from BASF SE and the technical assistance from Hermann Kaiser.

References

[1] J.M. Kim, N. Kumagai, H.T. Chung, Electrochem. Solid State Lett., **9**, A494-A498 (2006).

[2] M.M. Thackeray, S.H. Kang, C.S. Johnson, J.T. Vaughey, R. Benedek, S.A. Hackney, J. Mater. Chem., **17**, 3112-3125 (2007).

[3] N. Tran, L. Croguennec, M. Menetrier, F. Weill, P. Biensan, C. Jordy, C. Delmas, Chem. Mater., **20**, 4815-4825 (2008).

[4] A.R. Armstrong, M. Holzapfel, P. Novák, C.S. Johnson, S.-H. Kang, M.M. Thackeray, P.G. Bruce, J. Am. Chem. Soc., **128**, 8694-8698 (2006).

[5] S.F. Amalraj et al., Electrochim. Acta, **78**, 32-39 (2012).

Dynamics of ionic liquids in porous carbon electrodes investigated by quasi-elastic neutron scattering

D. Weingarth, J.P. Embs, A. Foelske-Schmitz, A. Wokaun, R. Kötz

phone: +41 56 310 4131, e-mail: daniel.weingarth@psi.ch

Ionic liquids (IL) have attracted remarkable research interest in recent years. Especially in the field of electrochemistry this class of compounds was considered as promising new type of aprotic electrolyte providing a large electrochemical stability window. This makes IL applicable in electrochemical energy storage devices like batteries or capacitors [1].

However, in addition to the electrolyte the characteristics of the electrode material have to be considered because both components interact with each other. For instance, the pore size distribution of the electrode material is known to play a major role for the use of IL in high power devices such as supercapacitors. [2, 3]. Mastragostino and Hall. reported on a better rate performance using mesoporous carbon material due to high viscosity of IL electrolyte and therefore limited pore wetting in case of microporous carbon material.

Triolo et. al [4] have shown in 2003 for the first time that the dynamics in bulk IL can be investigated using quasi-elastic neutron scattering (QENS). Two typical dynamic processes in 1-butyl-3-methyl imidazolium hexafluoro phosphate [BMIM][PF_6] were observed – a fast motion and a jump-like diffusion process. Recently, Embs et. al [5] investigated the dynamic processes in bulk 1-N-Butylpyridinium bis((trifluoromethyl) sulfony)limide [BuPy][TFSI] confirming the two different dynamic processes. A collective jump-like diffusion behaviour as well as a true single particle motion on a ps time scale.

Herein, we report on QENS measurements using [BuPy][TFSI] confined in three different carbon material electrodes as used in supercapacitors. The carbon materials are characterized by different pore size distributions. The findings will be compared to electrochemical measurements, particularly regarding the dynamics in the system.

Experimental

Three different carbon materials YP17 (Kuraray Chemical Japan) BP2000 (Cabot Corp. USA) and an experimental carbon black (Timcal SA, Switzerland) were used for electrode preparation. The electrodes were prepared as already described before [6]. In brief 90 wt. % of carbon material were mixed together with 10 wt. % PTFE binder and isopropanol. This suspension was stirred and heated until a dough like mass is achieved, which is rolled into self-standing electrode sheet with a thickness of about 500 µm. Afterwards the electrode sheets are dried at 120 °C and a vacuum of 20 mbar for at least 24 h.

Nitrogen adsorption measurements were done using a Quantachrome Autosorb instrument. The evaluation of the pore size distribution was done using a NLDFT model with slit/cylindrical pores.

The IL [BuPy][TFSI] was synthesized as described in [5]. According to Karl Fischer titration the water content was below 150 ppm.

Quasi-elastic neutron scattering measurements were done at the cold neutron time-of-flight spectrometer FOCUS at SINQ, PSI. QENS is very sensitive to hydrogen containing samples due to the large incoherent scattering cross section of hydrogen. This means that in the presented experiments we are investigating the dynamics of the cation only, the cross sections of the species present in the anion are comparably small. The incoming neutron wavelength was 5.75 Å, resulting in an energy resolution of about 22 µeV.

A flat Al sample holder (sample size 3 * 4 cm^2), sealed with Pb wires, was used for the experiments. A 1 mm Vanadium plate was measured to calibrate the detectors and to determine the resolution of the spectrometer. Afterwards a piece of the bare carbon electrode was investigated for background determination. The PTFE bound activated carbon sheets were soaked with IL and kept under vacuum for at least 8h to enhance pore filling. The IL + carbon samples were measured for 6 h at a temperature of 310 K. The DAVE software package was used for data reduction. Data measured at constant scattering angles 2Θ as function of time of flight were transferred into Q-E space. These data were divided into 13 groups of constant Q value, the energy range was set to ±1 meV.

QENS allows for an investigation of diffusion, localized motion and jump-like diffusion processes. Figure 1 shows an example of an S(Q,E) spectrum at Q=1.05 $Å^{-1}$ for IL soaked in a BP2000 electrode at 310 K together with the respective fits.

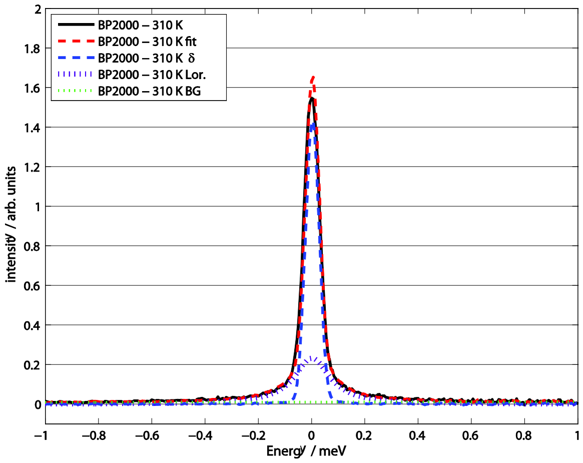

Figure 1. *S(Q,E) of [BuPyr][TFSI] soaked in BP2000 together with the respective fit curves.*

The δ-function represents the contribution of elastic scattering, therefore no information about dynamics can be obtained from this signal. The Lorentz-function corresponds to the peak broadening due to quasi-elastic scattering processes. This contribution is dependent on the scattering vector Q and represents the dynamics in the system, for example diffusion phenomena. A linear background is added to correct for an offset of the zero-line.

A preliminary evaluation of the data can be done using the so-called elastic incoherent structure factor EISF, which is calculated by the ratio of the respective areas of δ and Lorentz function:

$$EISF = \frac{A_\delta}{A_\delta + A_{Lorentz}}$$

The smaller the EISF, the larger the Lorentz contribution and hence the more dynamics in the system.

The electrochemical performance was tested in standard electrochemical cells in three electrode configuration using AC as quasi-reference electrode [7]. The electrode sheets were sandwiched between two Ti pistons, separated with a glassfiber separator, the reference electrode was added through a hole from the side. The scan rate was set to 10 mV s^{-1}.

Results

The Nitrogen adsorption measurements show for all carbons a SA of 1300 -1700 m^{2}g^{-1} (Figure 2). However, the pore size distributions of the three investigated carbon material electrodes show significant differences in the mesoporous regime. While BP2000 exhibits a reasonable amount of mesoporous pore volume (mesopore volume ~ 80 %), YP17 is characterized by almost only micropores (mesopore volume ~ 35%). While the Timcal carbon has a very broad range of different mesopore sizes (mesopore volume ~ 95 %), BP 2000 has some mesoporous channels > 25 nm and some micropores.

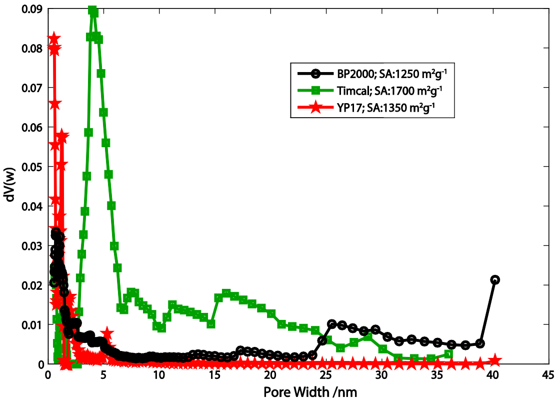

Figure 2. *Pore size distribution of the three investigated carbon electrodes prepared out of YP17, BP2000 and Timcal carbon. SA=specific surface area.*

The effect of pore size distribution on the electrochemical performance is clearly visible in Figure 3. While the specific capacitance at 0 V is comparable for all materials, the current response at the vertex potential ±0.25 V is changed.

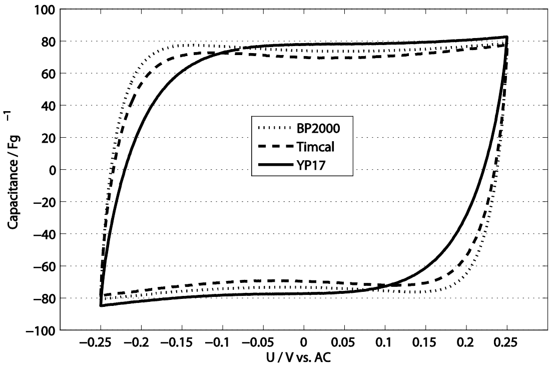

Figure 3. *Cyclic voltammograms using the three different carbon electrodes. Electrolyte: [BuPy] [TFSI]. Scan rate: 10 mVs^{-1}.*

Particularly YP17, the microporous carbon shows the slowest response of the three investigated carbon materials. A comparison of the EISF for the three different systems at 310K is shown in Figure 4. A clear difference between the mesoporous carbons to the microporous YP17 is evident. As already observed in electrochemical measurements, the dynamics in the mesoporous carbon systems are enhanced as compared to the narrow micropores. However, no clear trend can be figured out between the two different mesoporous carbons using this evaluation.

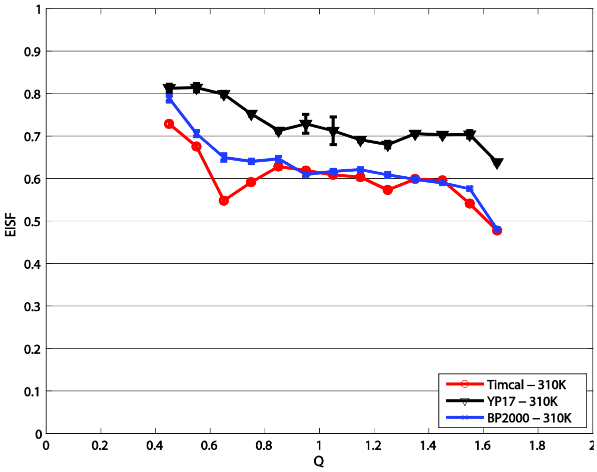

Figure 4. *EISF vs. Q of the three different carbon electrodes, soaked with IL.*

Conclusion

With this study we could clearly show that the pore size distribution of a carbon has a strong influence on the electrochemical behaviour as well as the dynamic motions in the system. Cyclic voltammetry shows clear differences in the current response at the vertex potentials, QENS underlines that the cation dynamics are slowed down with decreasing amount of mesopores. Mesoporous channels as present in BP2000 seem to be sufficient to enhance the dynamics in the system to a great extent. The material does not necessarily need to be completely mesoporous.

Additional temperature dependent measurements as well as a detailed investigation of the effect of confinement on the IL are under way.

References

[1] M. Galinski, A. Lewandowski, I. Stepniak, Electrochim. Acta **51**, 5567-5580 (2006).

[2] M. Lazzari, M. Mastragostino, A.G. Padolfo, V. Ruiz, F. Soavi, J. Electrochem. Soc. **158**, A22-A25 (2011).

[3] F.B. Sillars, S. I. Fletcher, M. Mirzaeian, P. Hall, Energy Environ. Sci. **4**, 695-706 (2011).

[4] A. Triolo, O. Russina, V. Arrighi, F. Juranyi, S. Janssen, C. M. Gordon, J. Chem. Phys. **119**, 8549-8557 (2003).

[5] J.P. Embs, T. Burankova, E. Reichert, R. Hempelmann, J. Phys Chem. B **116**, 13265-13271 (2012).

[6] P.W. Ruch, D. Cericola, A. Foelske-Schmitz, R. Kötz, A. Wokaun, Electrochim. Acta **55**, 4412-4420 (2010).

[7] D. Weingarth, A. Foelske-Schmitz, A. Wokaun, R. Kötz, Electrochem. Commun. **18,** 116–118 (2012).

Core level data of ionic liquids: monitoring charging by *in situ* EC XPS

A. Foelske-Schmitz, D. Weingarth, A. Wokaun, R. Kötz

phone: +41 56 310 4193, e-mail: annette.foelske@psi.ch

From fundamental X-ray photoelectron spectroscopy (XPS) studies of ionic liquids (ILs) charging is known to be a challange [1]. Recently, we showed that preparation of ILs on an activated carbon (AC) support may provide a straightforward opportunity for the determination of reliable binding energies (BE) of ILs [2]. The lack of charging observed on the AC support was referred to the high double layer capacitance (C_{DL}) of the AC when compared to common supports such as metal foils.

Herein, we report on further investigations of charging phenomena using our recently designed *in situ* electrochemical XPS cell [3]. This setup allows recording shifts of core level spectra of the IL electrolyte and measuring the potential of the WE simultaneously. X-ray induced OCP and BE shifts using electrodes providing low and high C_{DL} are compared.

Experimental

The set up of the *in situ* EC XPS cell for ILs has been already described elsewhere [1]. It provides a reaction vessel made from PEEK allowing for *in situ* EC XPS measurements in a three electrode arrangement. PTFE bound AC electrodes are used as counter (CE) and reference electrodes (RE) [4]. The Pt working electrode (WE) was rinsed with acetone and flame annealed prior to use. For the AC WE, BP2000 carbon (Cabot Corp.) was doctor bladed on a carbon coated Al current collector (Exopack Technologies). The IL electrolyte ($EMIMBF_4$, Merck KGaA, 99%) was dried at 100 °C and 10^{-2} mbar for 8 h and stored in a glove box (MBraun, H_2O, O_2 < 1 ppm).

After cell assembly and transfer to the analyzer chamber of the VG ESCALAB 220iXL spectrometer a CV in the potential range of +/- 0.1 V vs. AC RE is recorded (Versastat, PAR) to determine the C_{DL} of the WE. Subsequently, the WE is disconnected from the CE and the OCP values are recorded for a certain period of time having the X-rays off. In order to observe X-ray induced charging of the IL, the Al Kα twin anode is switched on and the OCP measurements are continued. XP spectra are recorded in constant analyzer energy mode at a pass energy of 20 eV.

Results

The evolution of the OCP of a Pt WE (C_{DL} = 5 μF) and an AC WE (C_{DL} = 3000 μF) during X-ray illumination of the IL electrolyte is reproduced in Figure 1. As long as the X-rays are turned off the OCP shows constant values (Figure 1, off). As soon as the X-rays are turned on (t = 0 s in Figure 1) the potentiostat records an OCP shift of the Pt WE. After having the X-rays on for 2000 s an OCP shift by 0.44 V is observed. In contrast to Pt, the OCP of an AC WE remains almost constant for > 7000 s (Figure 1, triangles).

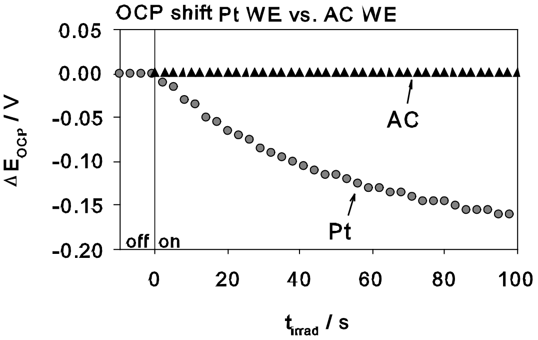

Figure 1. *Development of the OCP of a Pt (circles) and an AC (triangles) WE vs. time after switching the X-rays on.*

In order to investigate if the OCP shift observed on Pt can be directly related to shifts of core level data, N 1s spectra of the IL were recorded after certain irradiation times. For the Pt WE after 2000 s of irradiation the BE of the N 1s line is shifted by 0.44 eV (Figure 2, Pt), i.e. to 402.44 eV if compared to the standard value referenced in [1, 2] (Figure 2, solid vertical line). This shift of BE is in absolute agreement with the OCP shift measured after 2000 s. For the AC WE the BE of the N 1s line was in the range of 402.00 eV +/- 0.05 eV independent on the irradiation time (Figure 2, AC).

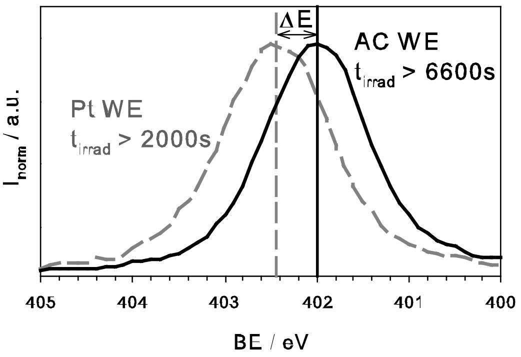

Figure 2. *N 1s spectra of [EMIM][BF$_4$] using a Pt and AC WE after certain X-ray irradiation times.*

Considering equation (1), the lack of charging in case of an AC WE may be explained by the three orders of magnitude higher C_{DL} if compared to Pt.

$$\Delta OCP = i_{photo} * t_{irrad} / C_{DL} \qquad (1)$$

with i_{photo} = photoelectron current, t_{irrad} = irradiation time

In summary, the *in situ* EC XPS data show that shifts of core level spectra of IL are correlated to shifts of the OCP of the WE. The results confirm that AC may be used as support for collecting reference core level data from IL without charging effects and suggest that the IL/support electrochemical interface has to be considered when irradiating/measuring at the IL/UHV interface.

References

[1] I.J. Villar-Garcia, E.F. Smith, A.W. Taylor, F. Qiu, K.R.J. Lovelock, R.G. Jones P. Licence, Phys. Chem. Chem. Phys. **13**, 2797 (2011).

[2] A. Foelske-Schmitz, D. Weingarth, R. Kötz, Surf. Sci. **605**, 1979 (2011).

[3] D. Weingarth, A. Foelske-Schmitz, A. Wokaun, R. Kötz, Electrochem. Commun. **13**, 619 (2011).

[4] D. Weingarth, A. Foelske-Schmitz, A. Wokaun, R. Kötz, Electrochem. Commun. **18**, 116 (2012).

SCIENTIFIC ACHIEVEMENTS 2012

ELECTROCATALYSIS & INTERFACES

Tin oxide as support for Pt-based oxygen reduction electrocatalysts in PEFCs

A. Rabis, E. Fabbri, R. Kötz, T.J. Schmidt

phone: +41 56 310 5172, e-mail: annett.rabis@psi.ch

At present, the most feasible catalyst system for oxygen reduction reaction (ORR) in acidic media is Pt deposited on a high surface area carbon. However, recent investigations show severe corrosion of the carbon support under polymer electrolyte fuel cell (PEFC) operation conditions, leading to a drastic reduction of the catalyst performance [1,2]. Out of several strategies to avoid the effects of carbon corrosion during fuel cell operation metal oxides with high thermodynamic stability in acidic environment are of interest as alternative support materials [3]. Among binary oxides, which are known to be stable in acids [4], we have selected tin oxide compounds as potential catalyst supports. SnO_2 shows good stability towards dissolution in acids and is usually regarded as an oxygen-deficient n-type semiconductor. Furthermore some chemical interaction between Pt and SnO_2 [5] has been observed which might be beneficial for the catalytic activity of Pt supported on SnO_2. The effect of using SnO_2 as support material for Pt-based catalysts was examined. Therefore, SnO_2 thin film model electrodes have been prepared by reactive magnetron sputtering and their electrochemical properties have been investigated by cyclic voltammetry methods. Additionally, Pt was deposited by sputtering on the SnO_2 support and the oxygen reduction activity was determined by rotating disc electrode (RDE) measurements.

Experimental

SnO_2 thin film model electrodes were prepared by reactive magnetron sputtering onto glassy carbon (GC) substrates. Post annealing was performed at 400°C for 4 h in Ar atmosphere. The crystal structure of the resulting metal oxide thin film was analyzed by XRD. XPS measurements were performed to analyze the chemical composition of the surface of the thin films. Additionally, scanning electron microscopy SEM has been performed to study the microstructure of the resulting thin films

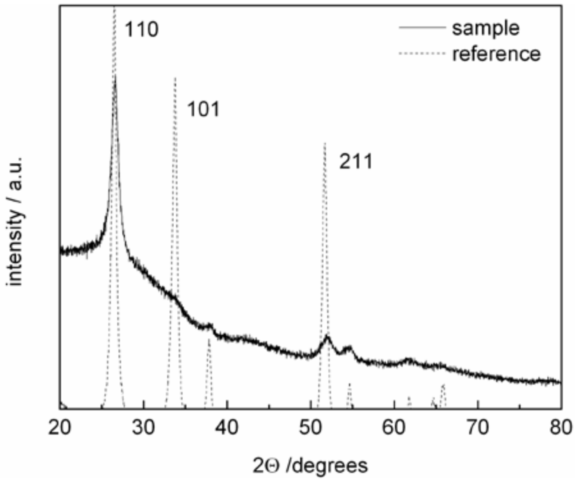

***Figure 1.** XRD spectra of SnO_2 thin films after annealing at 400°C.*

Electrochemical characterization was performed in a standard three-compartment electrochemical cell with 0.1 M $HClO_4$ as electrolyte, a hydrogen reference electrode and a Pt-mesh as the counter electrode. All measurements were performed at ambient temperature and pressure. The CV curves were acquired in Ar-saturated electrolyte at 100 mV/s.

As second step, 2 μg/cm^2 Pt were deposited onto the oxide electrodes by magnetron sputtering. The oxygen reduction reaction (ORR) was measured in an O_2 saturated electrolyte at different rotation rates, and the resulting polarization curves were iR corrected. A cathodic sweep at 5 mV/s has been used after holding the electrode potential for 10 s at 1 V.

Results

A diffractogram of sputtered SnO_2 thin film is depicted in Figure 1 and shows polycrystalline diffraction pattern of cassiterite (rutile SnO_2), as indicated by the dominant peaks from (110) and (211) planes. The mean grain size of SnO_2 was calculated from the (110) peak using Scherrer`s equation to be about 12 nm. It is obvious that the sputter deposited thin films show a preferential orientation. This is a result of the used deposition parameters: P = 80 W, Ar = 3 sccm and O_2 = 7 sccm equivalent to high O_2 content and relative low cathode power. According to Körber et al. [6] a preferential orientation is a result of the oxygen content in the sputter gas and surface energies. They proofed by XRD and ionization potential measurements the possibility of depositing SnO_2 films with preferential orientation on (110) or (101) depending on the oxygen content during magnetron sputtering. Furthermore, they showed that this preferential orientation is accompanied by a reduced or oxidized surface termination. The effect can be explained by the dependence of surface energy on crystal orientation.

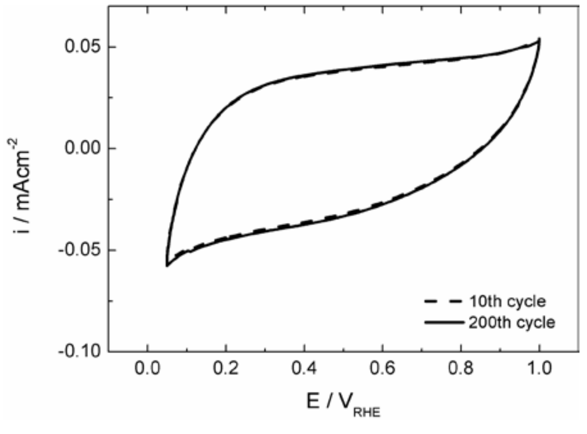

***Figure 2.** CV of SnO_2 thin film deposited on GC obtained at a scan rate of 100 mV/s in 0.1 M $HClO_4$.*

The cyclic voltammogram of annealed SnO_2 thin film deposited on GC in 0.1 M $HClO_4$ at 293 K is shown in Figure 2. Mainly electrical double layer charging of the SnO_2/electrolyte interface is observed under these conditions, indicating the absence of any noticeable reduction/oxidation feature in the potential range of 0.05 to 1.00 V. This could be an indication of an oxidized surface termination which is possibly created as a result of the sputter deposited SnO_2 film with (110) preferential orientation.

After 200 potential cycles between 0.05 and 1.00 V in acidic electrolyte, as shown in Figure 2), no new oxidation–reduction peaks at around 0.6 V, generally attributed to the hydroquinone/quinone reduction/oxidation couple on carbon, appears. This is an indication that the oxide films are still dense and no deterioration of the film upon electrochemical cycling occurs. Furthermore, SEM investigations before and after the electrochemical measurements confirmed the stability of the prepared SnO_2 thin films. This implies the feasibility of such oxide films as supports for model electrode studies. Tus the oxide thin films have been used as supports for 2 µg/cm^2 Pt catalyst deposited by magnetron sputtering.

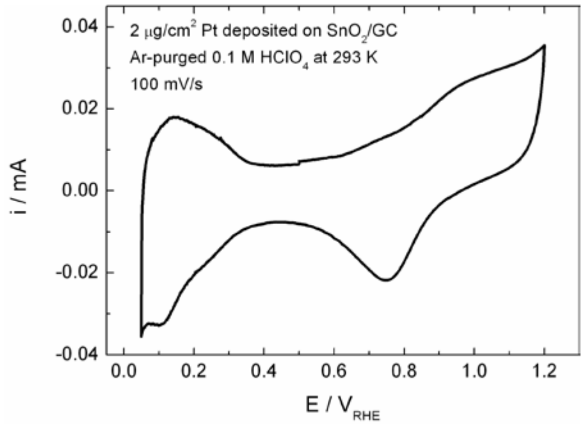

Figure 3. *CV of 2 µg/cm^2 Pt deposited on SnO_2 thin film in 0.1 M $HClO_4$; scan rate 100 mV/s.*

Cyclic voltammogram of Pt/SnO_2 model catalyst recorded in acidic electrolyte is shown in Figure 3. The characteristic Pt features like the hydrogen adsorption potential region, followed by the double layer potential region (0.4 < E < 0.7 V) and the oxide formation potential region are clearly visible.

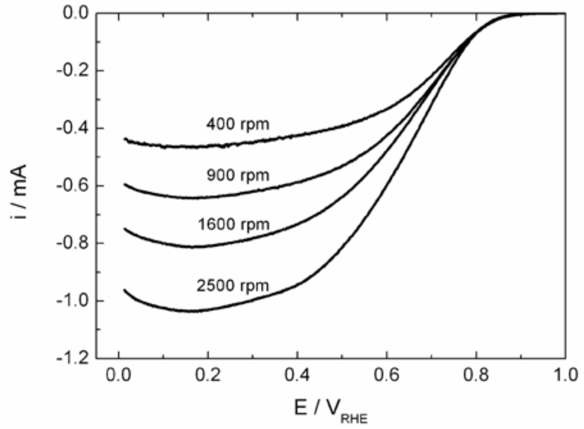

Figure 4. *Polarization curves during ORR on Pt/SnO_2 in 0.1 M $HClO_4$ at a sweep rate of 5 mV/s (2 µg/ cm^2).*

For the purpose of probing the kinetic activity of Pt/SnO_2 thin film model catalyst, a set of polarization curves for the ORR at various rotation speeds (900-2500 rpm) at a scan rate of 5 mV/s were recorded and are shown in Figure 4. The shape of the ORR polarization curves of the Pt/SnO_2 thin film electrode showed very well-defined mass-transfer and kinetic regions similar to those obtained for oxygen reduction on a conventional Pt/C catalyst. Single-step reductions with well-developed limiting current plateaus were observed at all rotation speeds.

From these data, Levich-Koutecky plots (i^{-1} vs. $\omega^{-1/2}$, i @ 0.2, 0.3 and 0.4 V_{RHE}) were prepared and Levich constants of about 2.5*10^{-2} mArpm$^{1/2}$ were determined. For comparison, the theoretical value for a four electron process estimated from the well known Levich equation is 4.5*10^{-2} mArpm$^{1/2}$ (more details see ref 7 and 8). Still using the Levich equation, the number of electrons involved in the ORR on Pt/SnO_2 could be evaluated and it resulted to be 2.6. This can be interpreted as a mixed catalysis of the OR reaction meaning that most of the oxygen is transferred into H_2O_2 and maybe some directly to water. According to this first ring disc measurements between 0.0 and 0.4 V showed some formation of H_2O_2. More investigations on the reaction mechanism of ORR on Pt/SnO_2 are on the way.

Acknowledgements

The authors thank Umicore AG & Co. KG and the Competence Center for Electricity and Mobility Switzerland (CCEM) for financial support within the project DuraCat.

References

[1] M.F. Mathias, R. Makharia, Eletrochem. Soc. Interface **14**, 24 (2005).

[2] H. Schulenburg, J. Phys. Chem. C **115**, 14236 (2005).

[3] A. Rabis, P. Rodriguez, T.J. Schmidt, ACS Catalysis **2**, 864 (2012).

[4] K. Sasaki, F. Takasaki, Z. Noda, ECS Trans **33**, 473 (2010).

[5] T. Okanishi, T. Matsui, K. Eguchi, App. Cat. A General **298**, 181 (2006).

[6] C. Körber, J. Suffner, A. Klein, J. Phys. D: Appl. Phys. **43**, 1 (2010).

[7] B. Schwanitz, A. Rabis, T.J. Schmidt, Chimia **66**, 110 (2012).

[8] N.M. Markovic, H.A. Gasteiger, P.N. Ross, J. Phys. Chem. **99**, 3411 (1995).

Oxide semiconductor-based catalysts for application as cathode materials in polymer electrolyte fuel cells (PEFCs)

E. Fabbri, A. Rabis, T. Binniger, A. Foelske-Schmitz, R. Kötz, T.J. Schmidt

phone: +41 56 310 2795, e-mail: emiliana.fabbri@psi.ch

State-of-the-art polymer electrolyte fuel cell (PEFC) cathodes are based on Pt nanoparticles supported on high-surface area carbons. The recent advances in the experimental techniques coupled with high-level theoretical tools and computational studies have led to significant progress in the atomic level understanding of electrocatalyst behaviour and to the development of advanced catalysts [1]. However, despite the good performance, Pt-supported on carbon suffers from corrosion stability which represents at present one of the main issues hindering PEFC widespread market penetration. Particularly in automotive applications, the cathode of a PEFC can reach under real operation conditions potentials as high as 1.5 V, which cause severe oxidation of the carbon support. Carbon oxidation results in a decrease of the support surface area and in the detachment of the Pt-nanoparticles, with a consequent rapid failure of the fuel cell [2]. In the search of more stable support materials than high surface area carbons, attempts have been made to increase the degree of graphitization of the carbon support. However, even though graphitized carbon shows higher corrosion stability than high surface area carbon black, the corrosion issue is only kinetically delayed and not solved. Other potential candidate materials as Pt supports are carbides, nitrides and oxides. However, carbides or nitrates will all be again thermodynamically driven to oxidation and formation of the respective oxides under the high oxidative conditions of a fuel cell cathode. Furthermore, since the synthesis of carbides is mainly through high temperature processes, this class of materials cannot provide the required specific surface area for a support material. Indeed, for fuel cell application a good catalyst support should provide both adequate stability as well as high surface area in order to reduce the loading of noble metal catalysts. Therefore, the most successful approach in developing a high surface area and corrosion resistant support appears to be the use of transition metal or metal oxides. In fact, this class of materials can achieve high electrochemical stability when used in their highest oxidation state, as well as high surface area when produced by wet chemical synthesis methods. In this work, high surface area 5 at% antimony doped tin oxide ($Sn_{0.95}Sb_{0.05}O_2$) has been synthesized by a modified sol gel synthesis method and its electrochemical stability have been investigated as a function of the processing conditions, which in turns affect the surface chemistry of the oxide support.

Experimental

$Sn_{0.95}$ $Sb_{0.05}O_2$ ($SnSbO_2$) powder has been synthesized by a modified sol gel method. $SnCl_2$ (Aldrich, 99.99%) and Sb_2O_3 (Aldrich, 99.99%) has been used as staring materials. Sb_2O_3 was first dissolved in a 0.1 M HNO_3 aqueous solution until a transparent solution containing antimony nitrates was obtained. Chelation of the metal cations was then achieved by adding citric acid to 0.05 M HNO_3 aqueous solution of tin chloride and aqueous solution of antimony nitrate, in a 3:1 ratio with respect to the total metal cations. Ammonia solution was used as a pH regulator (pH ~4-5) and ethylene glycol was added in the last step to polymerize the organic precursor. The solution was heated under stirring and once the gel was obtained, it was dried at 150 °C overnight. The calcination process was carried out in O_2 at 550 °C for 2 and 10 h. After calcination, the $SnSbO_2$ powders were analyzed by X-ray diffraction (XRD), scanning electron microscopy (SEM), energy-dispersive X-ray spectroscopy (EDX), X-ray photoelectron spectroscopy (XPS) and Brunauer-Emmett-Teller (BET) analysis. For the electrochemical characterization, porous thin films were prepared by drop-coating an electrode ink on glassy carbon disks. The inks were prepared from a suspension made of 75 mg of oxide, 100 μl of Nafion solution, and 25 ml of isopropanol. The working electrodes were immersed in 0.1 M $HClO_4$ electrolyte saturated with pure Ar at room temperature and the measurements were performed using a hydrogen reference electrode (RHE) and a gold counter electrode in a three electrode configuration. Cyclic voltammetry measurements were carried out to evaluate the oxide electrochemical stability.

Results

Thermogravimetric analysis was used to establish the most proper calcination temperature for the $SnSbO_2$ powder precursor. The main weight loss of about 75% occurred between 130 and 550 °C, due to the decomposition of the organic matrix. Therefore, the calcination temperature was set at 550 °C. The annealing time is also an important parameter in the material processing since it can determine the single phase material formation, the crystallinity of the material and also the grain size. The $SnSbO_2$ powder precursors were annealed at 550 °C for 2 and 10 h, and the XRD patterns of the powders after the two annealing processes are reported in Figure 1. Both the annealing processes led to single phase, crystalline $SnSbO_2$ oxides. However, the crystallite sizes, determined by Scherrer equation, were 4±2 nm for the sample annealed at 550 °C for 2 h , and about one order of magnitude larger (35±2 nm) for the $SnSbO_2$ powder annealed at 550 °C for 10 h.

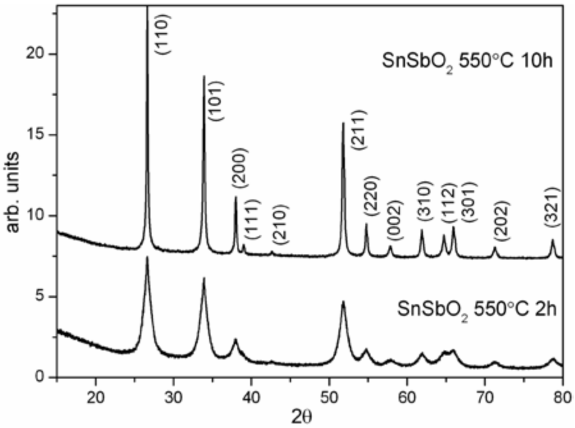

Figure 1. *XRD patterns of $SnSbO_2$ powders annealed at 550 °C for 2 and 10 h; the Miller indices for SnO_2 rutile structure are also included as reference.*

Therefore, the XRD analysis showed that the annealing time of 2 hours was beneficial to produce single phase oxide powders made of nano-crystallites. Besides the crystallite size, the specific surface area was determined using a multi-point BET analysis and the data are summarized in Table 1. Larger surface area was observed for the sample annealed for 2 h and also SEM analysis confirmed smaller particles size distribution for that sample. EDX showed slightly higher values of Sb than the nominal one for both supports (see Table 1). XPS was additionally used to determine the surface chemical composition of the $SnSbO_2$ powders obtained after annealing at 550 °C for 2 and 10 h. The results are also summarized in Table 1. Comparing the EDX and XPS results (bulk vs surface composition, respectively) it is evident that the 10 h annealing process led to surface segregation of Sb at the surface. The careful analysis of the $SnSbO_2$ surface composition is of high importance to develop stable and conductive support materials. Indeed, segregated Sb ions at the interface do not act as n-type donor but instead trap electron pairs reducing the oxide conductivity [3].

Annealing condutuons	BET surface area (m^2/g)	EDX, Sb/Sn ratio	XPS, Sb/Sn ratio
550°C for 2 h	63 ± 5	0.0929 ± 0.005	0.06496 ± 0.005
550°C for 10 h	18 ± 3	0.09051 ± 0.006	0.17096 ± 0.008

Table 1. *BET surface area and Sb at% measured by EDX and XPS for $SnSbO_2$ powders annealed at 550 °C for 2 h and 10 h.*

The electrochemical stability of $SnSbO_2$ powders under the most relevant PEFC cathode conditions is determined by cyclic voltammetry (CV) measurements in 0.1 M $HClO_4$ electrolyte saturated with pure Ar. Long stability tests were performed over 1000 cycles between 50 mV and 1.6 V vs RHE using a scan rate of 50 mVs^{-1}. For comparison the same test was also performed on commonly used carbon support for PEFC electrodes (commercial Vulcan XC72). After the stability test, the CV curve of Vulcan XC72 showed a strong decrease of the peak at about 1.5 V, indicating oxidation of the carbon support [4]. Furthermore, two redox peaks at about 0.55 and 0.6 V vs RHE appeared during cycling due to the formation of quinone/hydroquinone species on the carbon surface.

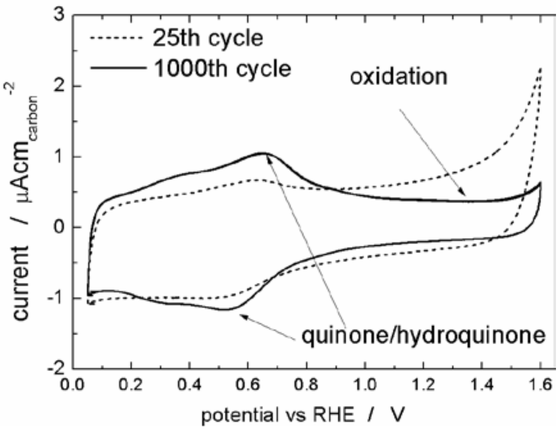

Figure 2. *: CV curves (25th and 1000th cycle) between 0.05 and 1.6 V vs RHE in 0.1 M $HClO_4$ saturated with Ar, at scan rate of 50 mV s^{-1} and at room temperature for Vulcan XC72 support.*

Figure 3 shows the CV curves obtained for the $SnSbO_2$ supports annealed at 550 °C for 2 and 10 h. No evolution of redox couples and only slight changes in the CV curve were observed for the $SnSbO_2$ support annealed at 550 °C for 2 h. Differently, a large decrease in the oxidation and reduction current upon cycling was observed for the $SnSbO_2$ support materials showing large Sb segregation at the surface. To compare the electrochemical stability of the two supports upon cycling, the total charge was determined for the 25th and 1000th cycle. A decrease of about 7% in the total charge was observed for the sample with optimized surface composition, while the decrease in the total charge reached 16% for the sample with Sb surface segregation. These findings point out the importance of the processing conditions in develop oxide support materials, since they can influence the oxide surface chemistry and, in turns, their electrochemical stability under the most relevant PEFC cathode operating conditions.

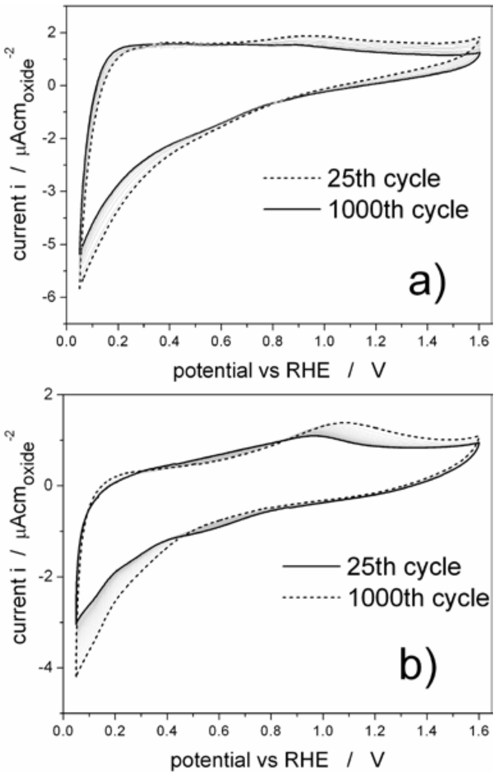

Figure 3 *CV curves (25th and 1000th cycle) between 0.05 and 1.6 V vs RHE in 0.1 M $HClO_4$ saturated with Ar, at scan rate of 50 mV s^{-1} and at room temperature for $SnSbO_2$ supports annealed at 550 °C for 2 h (a) and 10 h (b).*

Acknowledgments

The authors thank Umicore AG & Co. KG and the Competence Center for Electricity and Mobility CCEM for financial support within the project DuraCat.

References

[1] A. Rabis, P. Rodriguez, T.J. Schmidt, ACS Catal. **2**, 864–890 (2012).

[2] F.N. Büchi, M. Inaba, T.J. Schmidt, In Polymer Electrolyte Fuel Cell Durability; Eds.; Springer Science and Business Media LLC: New York p 199-221 (2009).

[3] R.G. Egdell ,T.J. Walker, G. Beamson, J. Electron. Spectrosc. Relat. Phenom. **128**, 59–66 (2003).

[4] M.G. Sullivan, B. Schnyder, M. Bärtsch, D. Alliata, C. Barbero, R. Imhof, R. Kötz, J. Electrochem. Soc. **147**, 2636-2643 (2000).

Iridium-titanium oxide as a stable support for Pt catalyst in PEFC cathodes

T. Binninger, E. Fabbri, R. Kötz, T.J. Schmidt

phone: +41 56 310 5728, e-mail: tobias.binninger@psi.ch

A major obstacle for the commercialization of polymer electrolyte fuel cells (PEFC) is the degradation of the cathode catalyst layer, which is usually made of platinum nanoparticles supported on high surface area carbon. Carbon corrosion (oxidation) at cathode potentials above 0.8 V vs. NHE leads to degradation of the support and detachment of Pt nanoparticles [1]. It is estimated that in automotive applications, a PEFC experiences over 300,000 cycles between 0.55 and 0.90 V [1], and potentials up to 1.5 V can be reached during start/stop conditions. One promising approach to overcome the problem of support corrosion is the use of conductive metal oxides instead of carbon as support for the Pt catalyst. In the following, we present preliminary results on the stability and performance of Pt nanoparticles supported on iridium-titanium oxide ($Ir_xTi_{1-x}O_2$). The oxide and the oxide supported Pt catalyst were produced by Umicore.

Experimental

The electrochemical stability under the most relevant PEFC cathode conditions was determined by cyclic voltammetry (CV) measurements in a three-electrode cell using a digital Metrohm µAutolab 3 potentiostat. Porous thin-film electrodes of the bare $Ir_xTi_{1-x}O_2$ support and of the supported Pt catalyst were prepared from a suspension made from 15 mg of the catalyst powder, 20 µl Nafion 117 as a binder, and 5 ml isopropanol as solvent. 20 µl of the suspension were drop-coated and then dried on glassy carbon disks. The electrodes were immersed in 0.1 M $HClO_4$ electrolyte, prepared from Suprapur 70% perchloric acid (Merck) and ultrapure Milli-Q water, saturated with pure (6.0) argon at room temperature. The measurements were performed using a hydrogen reference electrode (RHE) and a gold counter electrode. In order to simulate start/stop conditions in PEFC operation, stability tests were performed over 1000 cycles between 0.5 and 1.5 V vs. RHE using a scan rate of 50 mV s^{-1}.

The oxygen reduction reaction (ORR) activity was determined by rotating disk electrode (RDE) measurements. RDE measurements were conducted in a three-electrode glass cell and the thin film electrodes were prepared as described above. ORR activities were obtained from the negative-going scans at 5 mV s^{-1} in oxygen-saturated 0.1 M $HClO_4$. All the potentials were corrected for the ohmic drop determined by high frequency ac impedance spectroscopy.

Results

The benchmark support $Ir_xTi_{1-x}O_2$ shows very high stability in the voltage range between 0.5 and 1.5 V vs. RHE. The 50^{th} and the 1000^{th} cycle of the stability test are shown in Figure 1. No significant changes in the CV after 1000 cycles can be observed. For comparison, Figure 2 shows the 25^{th} and the 1000^{th} cyclic voltammogram for a standard carbon support (Vulcan XC72). The decrease of the current at potentials above 1.0 V is a clear evidence of carbon corrosion. At lower potentials around 0.6 V, a redox-couple evolves, which can be attributed to the formation of quinone surface groups [2]. Thus, the corrosion of the carbon support is accompanied by dramatic changes of the CV during stability testing, whereas the minor changes in case of the iridium-titanium oxide support indicate the superior stability properties of the latter.

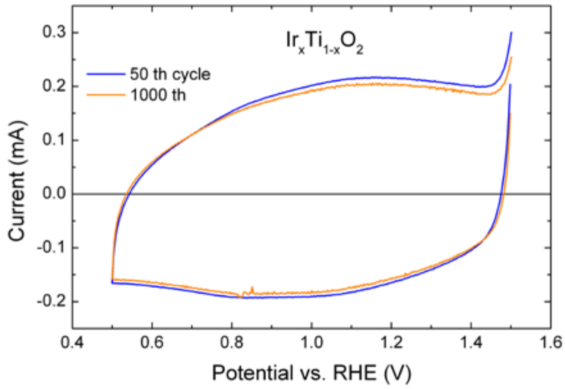

Figure 1. *50^{th} and 1000^{th} CV for the $Ir_xTi_{1-x}O_2$ support at a scan rate of 50 mV s^{-1} in 0.1 M $HClO_4$.*

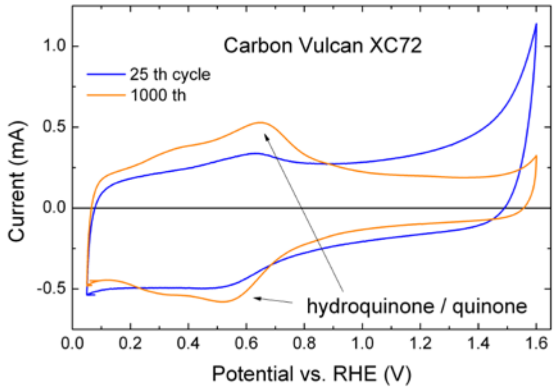

Figure 2. *25^{th} and 1000^{th} CV for a standard carbon support (Vulcan XC72) at a scan rate of 50 mV s^{-1} in 0.1 M $HClO_4$.*

The pure $Ir_xTi_{1-x}O_2$ oxide has considerable ORR activity in the potential range below 0.5 V. In Figure 3, the RDE currents in oxygen saturated electrolyte at different rotation speeds are plotted. Also given is the corresponding CV in argon saturated electrolyte. The much larger currents below 0.5 V in case of oxygen saturation indicate ORR activity of the iridium-titanium oxide. The splitting of the RDE curves for different rotation speeds can be attributed to mass transport losses. The mass transport limiting Levich current can be calculated, and the value of the latter indicates a 4 electron per molecule process for the oxygen reduction, i.e. ORR leading to water as a final product.

The mass transport corrected kinetic current is shown in Figure 4 in a Tafel plot, where the kinetic current is given on a logarithmic scale on the y-axis vs. the electrode potential on the x-axis. The straight line indicates Tafel kinetics but the slope of approx. 400 mV dec^{-1} is unusually high compared to the Tafel slope of 60 mV dec^{-1} for ORR on Pt catalyst. Despite the observed ORR activity of the bare iridium-titanium oxide support, it does not play an important role if Pt nanoparticles are added on the support. Figure 4 also shows the Tafel plot of the kinetic current for the Pt/$Ir_xTi_{1-x}O_2$ catalyst for comparison with the bare $Ir_xTi_{1-x}O_2$ support. It is clearly visible that the kinetic current of the support can be neglected compared to the kinetic current of the supported catalyst.

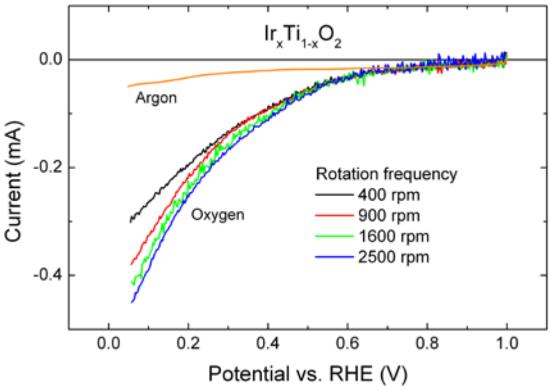

Figure 3. *RDE currents in O_2 saturated 0.1 M $HClO_4$ electrolyte for the bare $Ir_xTi_{1-x}O_2$ support. For comparison, also the CV in Ar saturated electrolyte is shown. Scan rate: 5 mV s^{-1}.*

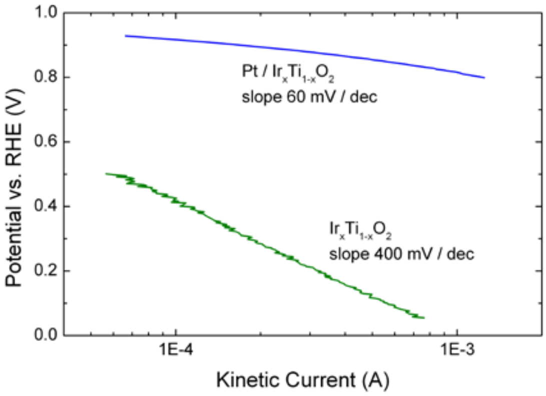

Figure 4. *Kinetic currents in O_2 saturated 0.1 M $HClO_4$ electrolyte for the bare $Ir_xTi_{1-x}O_2$ compared with the supported catalyst Pt/$Ir_xTi_{1-x}O_2$.*

The stability of the Pt/$Ir_xTi_{1-x}O_2$ catalyst was tested for the same conditions as for the support alone. Figure 5 shows the 50th and 1000th cycle of the stability test, and for comparison, Figure 6 plots the same for a commercial carbon supported high-performance PtCo/C catalyst, where the catalyst nanoparticles have a core-shell structure with a PtCo core and a Pt shell. The CV of the Pt/$Ir_xTi_{1-x}O_2$ catalyst only changes little during the stability cycling compared to the large changes in the CV of PtCo/C. However, this interpretation must be taken with care because the CVs are a superposition of the catalyst contribution and the support contribution. The carbon support mainly shows capacitive current in the CV, whereas the CV of the oxide support also contains a strong contribution from surface reduction / reoxidation processes [3]. A separation of the CV currents in Figure 5 into a Pt part and an oxide support part is not straightforward, but it can be expected that the oxide support contribution is significant, so that a loss of electrochemically active Pt surface area (ECSA) will appear to be smaller on the relative scale of the total CV current. Therefore, in order to evaluate the loss of ECSA, we only consider the Pt reduction peak at around 0.7 V in the negative-going scan. The shift of the peak maximum to larger potentials is most probably a catalyst particle size effect [4] and an indication for a growth of catalyst nanoparticles due to Ostwald ripening [1]. The decrease in the peak height can be used to obtain a rough estimate of the ECSA loss, leading to a loss of approx. 30% for the Pt/$Ir_xTi_{1-x}O_2$ catalyst, to be compared to approx. 50% for the PtCo/C. More precise measurements using CO stripping voltammetry will be conducted to confirm this result of a superior stability of the oxide supported Pt.

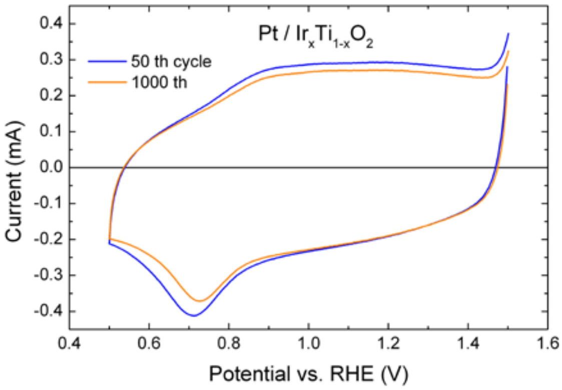

Figure 5. *Stability CV for the Pt/$Ir_xTi_{1-x}O_2$ catalyst at 50 mV s^{-1} in Ar saturated 0.1 M $HClO_4$.*

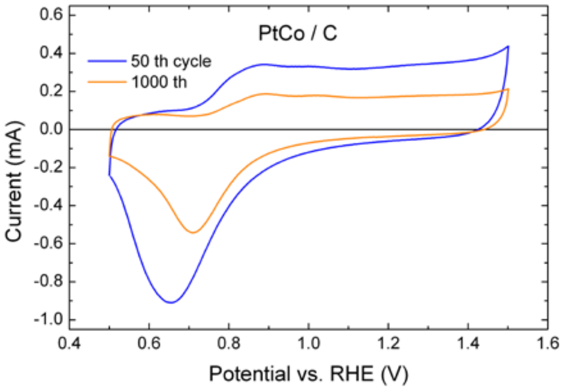

Figure 6. *Stability CV for a commercial high-performance PtCo/C catalyst at 50 mV s^{-1} in Ar saturated 0.1 M $HClO_4$.*

Summarizing, the high suitability of $Ir_xTi_{1-x}O_2$ as a stable support for the Pt catalyst in PEFC cathodes was demonstrated in accelerated laboratory stability tests, which simulate start/stop cycles during fuel cell operation in automotive applications.

Acknowledgements

This work is supported by CCEM Switzerland and Umicore AG & Co. KG within the project DuraCat.

References

[1] F.N. Büchi, M. Inaba, T.J. Schmidt, editors. Polymer Electrolyte Fuel Cell Durability, Springer (2009).

[2] M.G. Sullivan, B. Schnyder, M. Bärtsch, D. Alliata, C. Barbero, R. Imhof, R. Kötz, J. Electrochem. Soc. **147**, 2636-2643 (2000).

[3] L.D. Burke, N.S. Naser, B.M. Ahern, J. Solid State Electrochem. **11**, 655-666 (2007).

[4] F. Maillard, S. Pronkin, E.R. Savinova, Handbook of Fuel Cells, Volume **5**, Chapter 7; W. Vielstich, H. Yokokawa, H. A. Gasteiger, editors; John Wiley & Sons (2009).

Investigation of model Pt catalyts: from nanoparticles to extended surfaces

S. Taylor[1], E. Fabbri, A. Rabis, P. Levecque[1], O. Conrad[1], R. Kötz, T.J. Schmidt

phone: +41 56 310 2795, e-mail: emiliana.fabbri@psi.ch

Polymer electrolyte fuel cells (PEFCs) are electrochemical devices converting chemical energy of hydrogen and oxygen (or air) into electrical energy with relatively high efficiencies and low emissions. For these reasons they have attracted much attention as promising power sources for small stationary, mobile, and portable applications. About two-thirds of the overall voltage losses of a PEFC at high current density are due to the slow oxygen reduction reaction (ORR) kinetics at the positive electrode, and therefore large efforts are currently devoted to search for more active catalysts. However, at present Pt-based catalysts are still recognized as the materials of choice for the ORR in acidic environments [1]. To minimize the amount of Pt required for a given level of activity, the Pt catalyst is generally dispersed as small particles on a high surface area carbon support (Pt/C) which allows higher Pt dispersion and hence larger catalyst surface area compared to unsupported Pt-black. The amount of expensive Pt catalyst used in a PEFC is one of the main deterrents preventing PEFC from entering commercial markets in bulk. In order to decrease the amount of Pt catalyst used and obtain acceptable fuel cell performance a full understanding of the influence of surface morphology and particle size on the oxygen reduction reaction activity is necessary to determine the optimum catalyst properties for the use in PEFCs. The aim of this project is to gain a better understanding of the surface properties of different Pt supported on carbon catalysts from nanoparticles supported on carbon to extended surface catalysts. This was investigated by the preparation of model electrodes sputtered with various Pt loadings from 2 to 100 μgPt/cm^2 on high surface area carbon (Vulcan XC72). A series of electrochemical characterisation measurements including cyclic voltammetery (CV), CO stripping voltammetry, and rotating disk electrode measurements (RDE) has been carried out.

Experimental

The preparation of the model electrodes can be divided into two parts. At first, a Vulcan suspension is made from 75 mg of Vulcan XC72, 100 μl of Nafion® 117 solution (5%, Fluka) and 25 ml 2-propanol (Normapur, VWR Prolabo). The suspension was treated ultrasonically at 60 °C for 2 h. Then 20 μl of the suspension were dispersed onto a polished glassy carbon rotating disk electrode (RDE), and dried overnight at room temperature in an Ar atmosphere. In the second part of the electrode preparation different Pt loadings 2, 10, 20, 50 and 100 μgPt/cm^2, were sputtered onto the electrodes in a magnetron sputtering set-up according to the procedure in reference [2]. The model electrodes were characterized in a three electrode compartment electrochemical cell in 0.1 M $HClO_4$ electrolyte using a hydrogen reference electrode and a Pt-mesh as the counter electrode, at ambient temperature and pressure. The hydrogen electrode was calibrated by hydrogen oxidation/evolution reaction in the same electrolyte. The CV curves were acquired in Ar-saturated electrolyte at 50 mV/s. CO adsorption was achieved at 0.1 V vs. RHE in a CO-saturated (15 min) 0.1 M $HClO_4$ solution, and then the electrolyte was purged with Ar (35 min) to remove the dissolved CO. The oxygen reduction reaction (ORR) was measured in an O_2 saturated electrolyte at different rotation rates, and the resulting polarization curves were iR corrected. A cathodic sweep at 5 mV/s was used after holding the electrode potential for 10 s at 1 V.

Results

The cyclic voltammetry (CV) measurement in Ar-saturated electrolyte for the model electrode with Pt loading of 100 μg$_{Pt}$/cm^2 is shown in Figure 1. The so-called hydrogen underpotential deposition (Hupd) in Ar saturated electrolyte was used to determine the electrochemical surface area (ECSA) of the Pt electrodes.

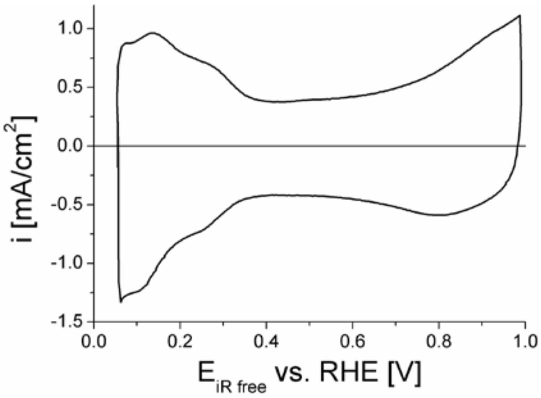

Figure 1. *Cyclic voltammogram for 100 μg/cm^2 Pt sputtered electrode in Ar saturated 0.1 M $HClO_4$ solution. Sweep rate 50: mV/s.*

For the calculation of the Pt surface area, a specific charge of 210 μC/cm$^2_{Pt}$ was used as the adsorption of a monolayer of hydrogen on an atomically flat polycrystalline Pt electrode. The model Pt electrode surface area was also measured by the CO-stripping method (Figure 2); in this case the electrochemically active surface area is determined through the oxidation of a monolayer of CO species adsorbed on the Pt surface (normalization factor of 420 μC/cm$^2_{Pt}$).

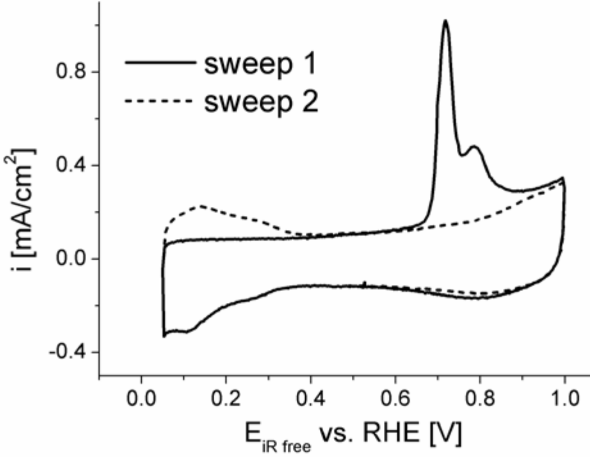

Figure 2. *Cyclic voltammograms for 100 μg/cm^2 Pt sputtered electrode in CO-saturated electrolyte (sweep 1) and after purging the electrolyte with Ar (sweep 2). Sweep rate: 10 mV/s.*

---

[1] HySA/Catalysis Centre of Competence, University of Cape Town, Rondebosch, 7701, Cape Town, South Africa

It is interesting to note the double peak observed in the CO stripping CV for the 100 $\mu g_{Pt}/cm^2$ sample. Maillard et al. reported a similar result for CO oxidation at high Pt loadings where a double voltammetric peak was observed. The authors concluded that the double peak was due to the CO oxidation reaction occurring on Pt agglomerates and on isolated particles. The more negative and the more positive peaks correspond to CO oxidation on Pt agglomerates and on isolated particles, respectively. The intensity of the peaks is indicative of the amount of Pt agglomerates or isolated particles present on the catalyst surface. It was also noted that the CO oxidation reaction is strongly size sensitive [3]; the reaction overpotential of the CO oxidation reaction increases when the particle size decreases below ca. 3 nm and Pt agglomerates show remarkably enhanced catalytic activity in comparison to isolated Pt nanoparticles [3]. It was observed in this study that for low Pt loadings, such as the 10 $\mu g_{Pt}/cm^2$, a single CO oxidation peak occurred at a higher reaction overpotential than the CO oxidation peak related to Pt agglomerates in the 100 $\mu g_{Pt}/cm^2$ sample (Figure 3), in agreement with the findings by Maillard et al. Therefore, CO stripping voltammetry can provide a fingerprint of the particle size distribution and the extent of particle agglomeration, i.e. it can be used as a powerful tool to discriminate between isolated particles and extended Pt surfaces.

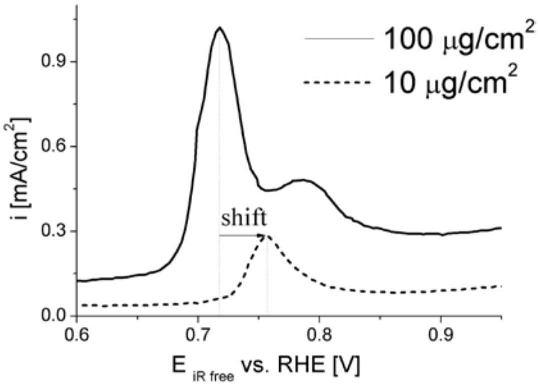

Figure 3. *Cyclic voltammogram showing CO oxidation peaks for sputtered model electrodes with Pt loadings of 100 $\mu g_{Pt}/cm^2$ and 10 $\mu g_{Pt}/cm^2$ in Ar saturated 0.1 M $HClO_4$ solution after holding the electrode potential at 0.1 V for 15 min in CO-saturated electrolyte. Sweep rate 10 mV/s.*

The morphology of the catalyst layer and the dispersion of catalyst particles has a direct effect on the electrochemical surface area (ECSA). Figure 4 illustrates the relationship between Pt loading and ECSA.

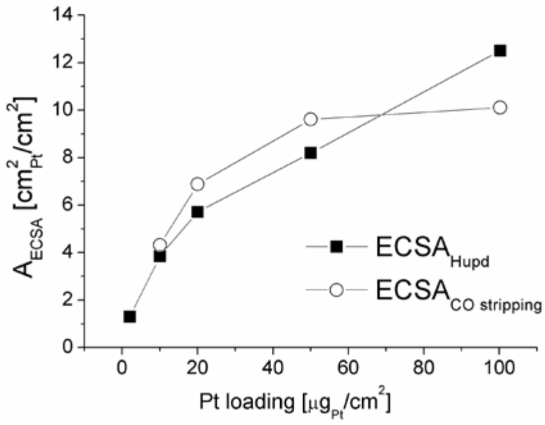

Figure 4. *ECSA vs. Pt loading for sputtered model electrodes from 2 to 100 $\mu g_{Pt}/cm^2$.*

Ideally an increase in Pt loading would produce a linear increase in the ECSA. However, as the Pt loading increases the particles begin to agglomerate and the surface morphology changes from isolated particles to extended surfaces. This agglomeration causes a reduction in the overall ECSA and Pt utilization, resulting in a non-linear Pt-loading/ECSA relationship at higher Pt loadings (Figure 4).

Figure 5 and Figure 6 shows the ORR mass activities ($i_{K,mass}$) and specific activities ($i_{K,spec}$), respectively, for sputtered Pt model electrodes with different Pt loadings. Current densities were taken at constant electrode potential of 0.9 V (RHE) and corrected by ohmic drops and diffusion current using Koutecky-Levich equations. As expected $i_{K,mass}$ decreases and $i_{K,spec}$ increases as Pt loading increases due to the particle size effect. As the Pt loading increases, particle agglomeration increases and hence the active surface area and Pt utilization decreases and consequently $i_{K,spec}$ increases.

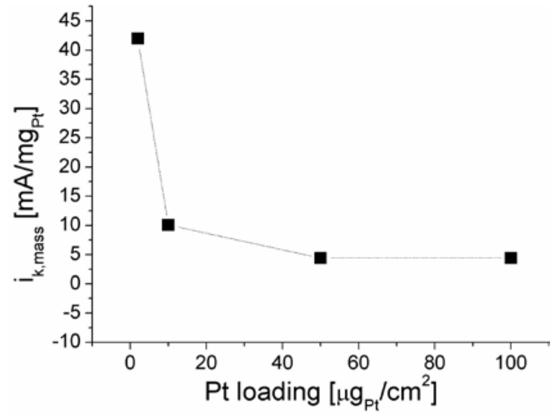

Figure 5. *Comparison of ORR mass activities of sputtered Pt model electrodes with different Pt loadings.*

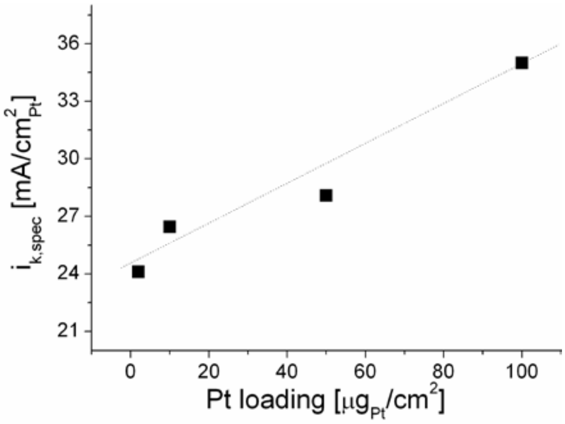

Figure 6. *Comparison of ORR specific activities of sputtered Pt model electrodes with different Pt loadings.*

References

[1] A. Rabis, P. Rodriguez, T.J. Schmidt, ACS Catal. **2**, 864-890 (2012).

[2] B. Schwanitz, A. Rabis, M. Horisberger, G.G. Scherer, T.J. Schmidt, Chimia **66**, 110-119 (2012).

[3] F. Maillard, S. Schreier, M. Hanzlik, E. Savinova, S. Weinkauf, U. Stimming, Phys. Chem. Chem. Phys. **7**, 385 – 393 (2005).

On-line mass spectrometry for electrochemical reduction of CO_2 on copper electrodes

J.V.F. Araújo, M. Özaslan, P. Rodriguez[1], R. Kötz, T.J. Schmidt

phone: +41 56 310 530 4, e-mail: jorge.ferreira@psi.ch

Efficient reduction of CO_2 into liquid fuel has the potential to revolutionise renewable power sources. The electrochemical reduction of carbon dioxide is able to produce hydrocarbons such as methane and ethylene with a reasonable efficiency and reaction rate [1, 2]. Copper has known to be a unique material in its ability to produce a variety of gaseous and aqueous products such as hydrocarbons. Although there is considerable experimental activity on this subject, electrochemical CO_2 reduction is still a reaction with large activation energy and undefined product selectivity [2]. The objective of this study is to investigate the electrochemical reduction of CO_2 for several aqueous electrolytes in order to understand the influence of pH value and of the chemical composition of the electrolyte. The approach is to monitor the reaction by cycling voltammetry and to collect and analyze the reaction products with on-line mass spectrometry [3, 4]. The setup with two pump stages will be presented here and preliminary result of this system will be discussed.

Experimental

The copper polycrystalline disk with 8 mm of diameter (surface area of 0.5 cm^2) was mechanically polished on silicon carbide paper. Using the hanging meniscus configuration the Cu electrode was mounted in a three-neck flask for the electropolishing procedure consisting of three steps. First an anodic potential at 0.4V vs. Hg/$HgSO_4$ is applied in a solution of 930 ml of ortho-phosphoric acid, 45 g of D-mannitol, and 270 ml of Millipore-MilliQ® water during 1 min. Then the oxidised Cu electrode was washed in pure water before the transfer to a second vessel containing a solution of ultrapure 2.5 M H_2SO_4 saturated with argon for 20 min etching. The Cu electrode was removed and protected by a droplet of water. Lastly the Cu is subjected to a cathodic potential (-0.85 V vs. Hg/$HgSO_4$) in 0.5 M KF during 15 min. The Cu electrode was rinsed in pure water and protected from oxidizing ambient air with a droplet of water until potential controlled immersion in the electrochemical cell [5]. [1] University of Birmingham

The electrochemical reduction of CO_2 was performed in a glass electrochemical cell with 60 ml of electrolyte solution. The voltammetry measurements were done with an Autolab potentiostat and a reversible hydrogen reference electrode (RHE). The electrolytes studied were 0.1 M phosphate buffer solutions with pH values of 2, 7, and 12. The electrochemical measurements are done first in Argon, after 20 min. of bubbling, and then in CO_2, with 10 min. of CO_2 gas bubbling. The working electrode was immersed under hanging meniscus configuration with exposed surface are of 0.5 cm^2.

As illustrated schematically in Figure 1, the on-line electrochemical mass spectrometer (OLEMS) setup consists of vacuum system with differential pumping. The differential pumping was promoted by two vacuum pumps; the first stage was pumped with a membrane pump and the second stage with a turbo molecular pump. The two stages were separated with an aperture of 0.2 mm diameter. The electrochemical cell is connected to the vacuum system at the first stage and the electrolyte solution was separated from the vacuum side by a PTFE hydrophobic membrane with pore size of 30 nm. The mass spectrometer is located at the second stage with a vacuum pressure around $5x10^{-5}$ mbar [3]. In order to have good gas collection efficiency the polycrystalline Cu electrode was immersed into the electrolyte solution and pressed on top of PTFE membrane allowing the formation of thin film electrolyte under the electrode surface. The low vacuum pressure at the first stage promoted by the membrane pump avoid the formation of water vapour through the porous membrane and at same time gases moisture still can be collected.

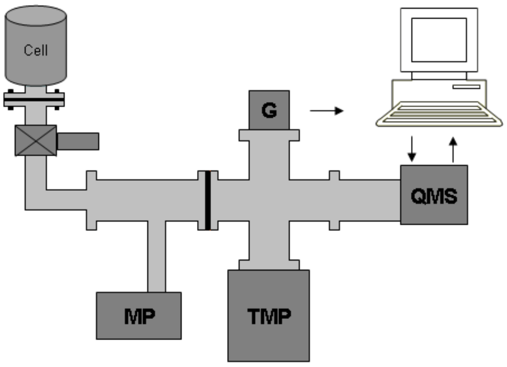

Figure 1. *Schematic drawing of the on-line electrochemical mass spectrometer. Cell-electrochemical cell, MP-membrane pump, G-gauge, TMP-turbo molecular pump, QMS-Quadrupole mass spectrometer (QMS 220)*

Results

By changing the pH value and keeping the same chemical elements we investigated the electrochemical behaviour of polycrystalline Cu in phosphate buffer electrolyte and its possible reactivity to convert CO_2 into other products. The resulting cyclic voltammograms on polycrystalline Cu in phosphate buffer electrolyte at various pH values are shown in Figure 2. The potential was changed from 0 to −1.25 V and back using a scan rate of 10 mV/s.

At potentials below -0.4 V the reduction current density increases for all pH values both in the presence of Ar and CO_2 mainly because of the formation of hydrogen at pH 2, 7 and 12. At pH 12 the system appears to be most active for H_2 evolution.

From figure 2 the CO_2 reduction activity can only be estimated from a difference between the current curves recorded for Ar and CO_2 saturation, respectively. It was noticed that for acidic media no electrochemical reaction possible can be attributed to CO_2 conversion (even with solution of sulfuric or perchloric acid). On the other hand,

---

[1] University of Birmingham

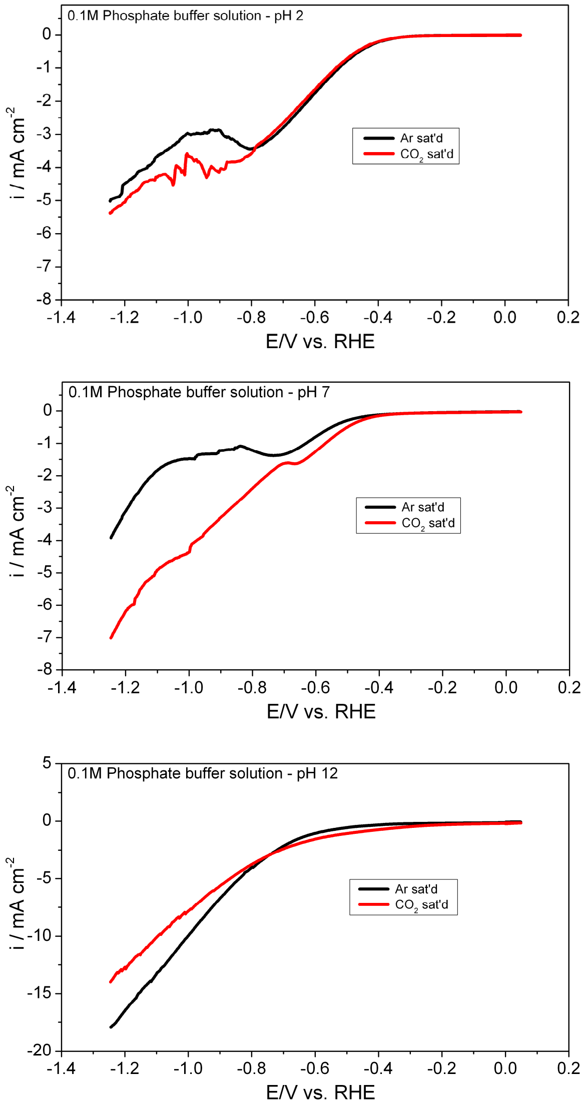

Figure 2. *Cathodic sweep in cyclic voltammetric studies in Phosphate electrolyte solution at various pH saturated with Argon (black line) and afterwards by CO_2 (red line). The scanning rate 10mV/s and start potential of 0 V.*

at neutral pH 7 conversion of CO_2 occurs at lower overpotentials with higher current density compare to the Argon saturated electrolyte. At pH 12 large currents for hydrogen evolution were observed and the presence of CO_2 appears to block this reaction, therefore CO_2reaction intermediates or products are likely to be present.

The simultaneously recorded ion current of H_2 (m/z = 2) during cathodic sweep shows a clear increase of the hydrogen ion concentration with negative going-scan. The hydrogen formation in the CO_2 vs. Ar saturated solution is significantly larger. The onset potential for hydrogen evolution was shifted from -0.4 to -0.55 V, to be observed in parallel in both electrochemical and ion current, respectively. The underlying mechanism for this shift of the HER in the presence of CO_2 is still unclear and a matter of our further studies.

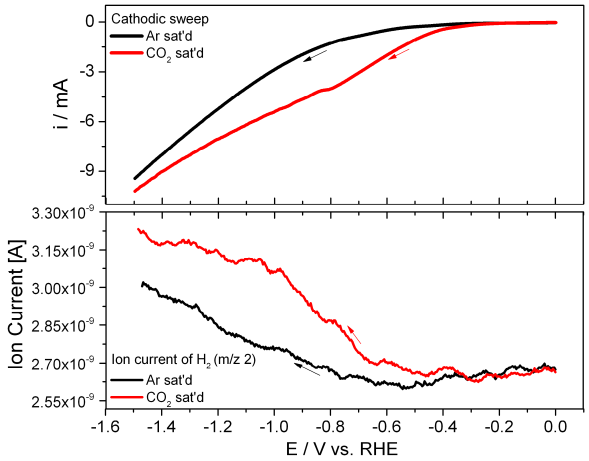

Figure 3. *Cathodic sweep in cyclic voltammetric studies, hydrogen evolution reaction (black and red line) in Phosphate solution at pH 8 in Ar or CO_2 saturated. The scanning rate 10mV/s and start potential of 0 V. The volatile product measured of m/z 2 - H_2 (in ion current) during this potential sweep (black and red line).*

Conclusions

For all of the measurements performed in phosphate buffer on Cu, the Faradaic current was mainly determined by hydrogen evolution. Information about a possible electroreduction of CO_2 activity can only be estimated by comparing the current curves with or without CO_2 saturated electrolyte. The on-line detection of H_2 during the hydrogen evolution reaction demonstrates the potential of *in situ* electrochemical mass spectrometry. CO_2 can be converted into fuel by electrochemical reduction, although there are significant challenges which must be overcome in order to select specific reaction products.

References

[1] M. Gattrell, N. Gupta and A. Co, J. Electroanal. Chem., **594**, 1-19, (2006).

[2] O. Koga, Y. Watanabe, M. Tanizaki, Y. Hori, Electrochim. Acta **46** 3083-3090, (2001).

[3] H. Baltruschat, J. Am. Soc. Mass Spectrom. **15**, 1693, (2004).

[4] K.J.P. Schouten, Z. Qin, E.P. Gallent and T.M. Koper, J. Am. Chem. Soc. **134**, 9864-7 (2012).

[5] G.M. Brisard, E. Zenati, Langmuir **11**, 2221-2230, (1995).

Preparation of thin platinum films by pulsed laser deposition

S.E. Temmel, E. Fabbri, R. Kötz, C. Schneider, T. Lippert, T.J. Schmidt

phone: +41 56 310 2128, e-mail: sandra.temmel@psi.ch

The oxygen reduction reaction (ORR) occurring at the cathode side of polymer electrolyte fuel cells (PEFCs) suffers from poor kinetics, resulting in overpotentials of about 0.3 to 0.4 V. Pt-based catalysts are still recognized as the materials of choice for PEFC cathodes and in the last decades several efforts have been devoted to maximize its catalytic activity towards ORR. According to previous studies, the main possibilities for increasing the ORR kinetics are (i) reducing the interatomic Pt-Pt bond distance and hence modifying the physical structure of Pt, (ii) shifting the d-band center and in turn influencing the electronic structure or (iii) tailoring the termination of the Pt (hkl) surface and hereby manipulate the specific adsorption of species from the electrolyte [1-3].

The main goal of the present work is to gain further understanding of the relation between Pt interatomic distance and surface termination and its electrocatalytic activity towards ORR. A novel class of Pt-based catalyst will be developed by fabricating epitaxial thin films of Pt on single crystal strontium titanate (STO) or strontium ruthenate (SRO) using pulsed laser deposition. First, the appropriate ablation parameters for Pt should be found, with focus on minimizing the formation of Pt microdroplets, often the limiting factor when ablating metals [4].

Experimental

Pulsed laser deposition (PLD), a technique popular for its ability to transferring the target stoichiometry onto thin films, has already been applied for growing complex films [5]. In short, in PLD, an intense laser beam is focused onto the target where its absorption leads to the melting and evaporation of the surface layer. Subsequently, partly ionized species are ejected, producing the so-called “ablation plume”, which in turn interacts with the incoming laser beam and background ambient. The plume expands further and is directed forward towards the substrate (mostly heated to facilitate diffusion) to condense and grow a film of the ablated material.

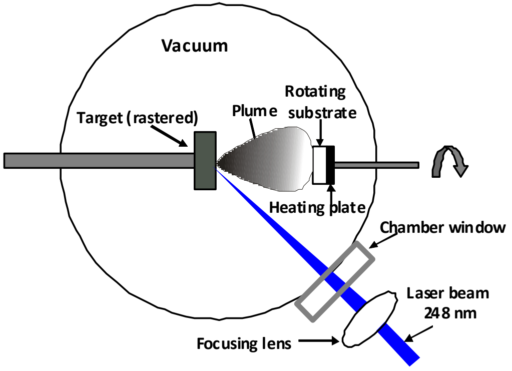

Figure 1. *Illustration of a chamber for pulsed laser deposition.*

Thin Pt films were grown (RT, p= $3x10^{-7}$ mbar) on Si (100) by pulsed laser deposition using a KrF excimer laser (248 nm, 3 Hz, 28 kV). The target (positioned at a distance of 2-4 cm normal to the substrate) was rastered by the laser beam (spot size= $1.1x10^{-2}$ cm^2, Fluence F= 3-4 J/cm^2) under a 45° angle for a total number of 2600 pulses. No background gas was introduced at this point of the research. In addition, in order to minimize the formation of Pt microdroplets, lower fluences and off-axis configurations were also tried. In the off-axis configuration the substrate position is shifted for 5-10 mm in horizontal direction; consequently, the ablation plume does not hit the center of the substrate anymore. Prior to deposition, the substrates were ultrasonically cleaned in ethanol, acetone and isopropanol for 2 min each. The Pt target was preablated for 30 min to smoothen and clean its surface. X-ray reflectometry (XRR) was used to measure the thickness of the films. Scanning electron microscope (SEM) and atomic force microscopy (AFM) images were recorded to analyze the surface morphology and the number and size of microdroplets.

Results

Thin Pt films (~30 nm) with a surface roughness below 1 nm were successfully prepared. It was found that the film growth was strongly dependent on the parameters applied and that very high fluences (>3.5 J/cm^2) were necessary to ablate Pt. AFM images showed that the number and size (d= 10-100 nm) of Pt microdroplets could be successfully reduced to a negligible amount (Figure 2, right side) by increasing the target-substrate distance from 2 to 4 cm, compared to the initially prepared Pt thin films (Figure 2, left side). SEM images confirmed those findings (data not shown). Lower fluences, off-axis configurations and varying the size of the spot size did not result in any further improvement.

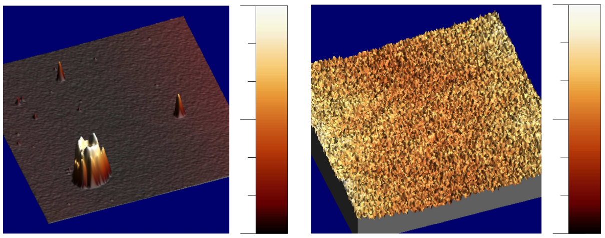

Figure 2. *AFM images of Pt films deposited on Si (100) in vacuum at RT, 4 J/cm^2, $3x10^{-7}$ mbar with a target-substrate distance of 2 cm (left side, 8x8 µm Δz =80 nm) and 4 cm (right side, 500x500 nm, Δz =0.65 nm).*

In the next step, threshold fluences and ablation rates for Pt will be established. STO(100) will be used as substrate of choice to investigate the heteroepitaxial growth of Pt at different deposition conditions (e.g. temperature, no.of pulses, background gas) and to study its influence on the film growth and in turn on its physical and electrochemical properties.

References

[1] V. Jalan, E.J. Taylor, J. Electrochem. Soc **130**, 2299-2302 (1983).

[2] T. Toda, J. Electrochem. Soc. **10**, 146 (1999).

[3] V.R. Stamenkovic, B. Fowler, B.S. Mun, G. Wang, P.N. Ross, C. Lucas, N.M. Marković, Science **315**, 493–497 (2007).

[4] H.U. Krebs, Pulsed laser deposition, R. Eason, ed., Wiley, 363-382 (2007).

[5] C.W. Schneider, T. Lippert, Material Science, P. Schaaf, ed., Springer:Berlin, 89-112 (2010)

THE ELECTROCHEMISTRY LABORATORY
FACTS & NUMBERS

STRUCTURE 2012

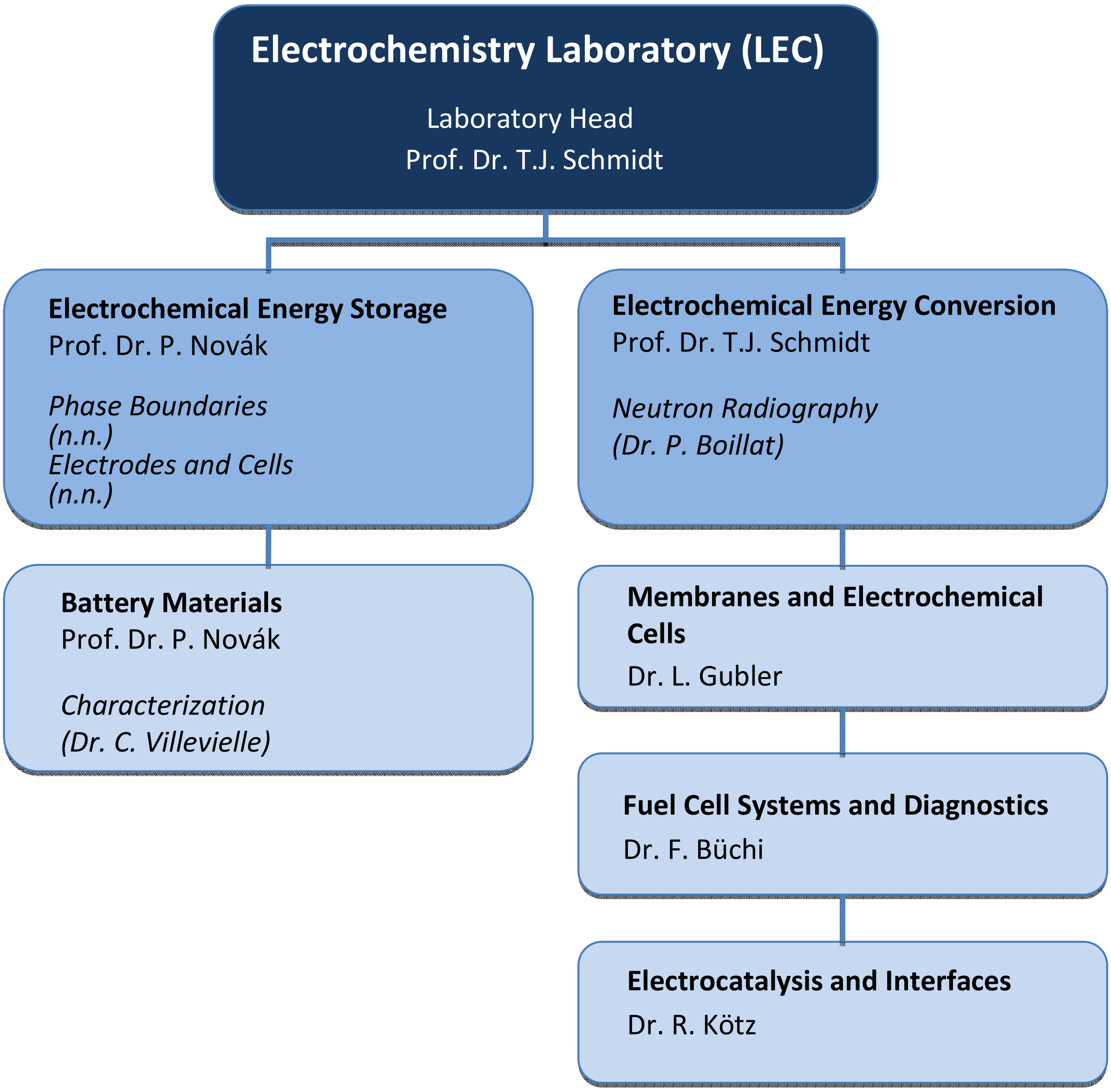

Electrochemistry Laboratory (LEC)

Laboratory Head
Prof. Dr. T.J. Schmidt

Electrochemical Energy Storage
Prof. Dr. P. Novák

Phase Boundaries
(n.n.)
Electrodes and Cells
(n.n.)

Battery Materials
Prof. Dr. P. Novák

Characterization
(Dr. C. Villevielle)

Electrochemical Energy Conversion
Prof. Dr. T.J. Schmidt

Neutron Radiography
(Dr. P. Boillat)

Membranes and Electrochemical Cells
Dr. L. Gubler

Fuel Cell Systems and Diagnostics
Dr. F. Büchi

Electrocatalysis and Interfaces
Dr. R. Kötz

ECL-PERSONNEL 2012

Staff

Dr. Jérôme **B**ERNARD (Scientist)
Felix BERNAUER (Engineer)
Dr. Pierre BOILLAT (Project Leader)
Lukas BONORAND (Engineer)
Dr. Felix BÜCHI (Group Leader)
Dr. Christa BÜNZLI (Post Doctoral Researcher)
Dr. Elias **C**ASTEL (Post Doctoral Researcher)
Dr. Emiliana **F**ABBRI (Scientist)
Dr. Annette FOELSKE (Scientist)
Dr. Nuria **G**ARCIA-ARAEZ (Scientist)
Cordelia GLOOR (Assistant)
Thomas GLOOR (Technician)
Dr. Juan Luis GÓMEZ (Post Doctoral Researcher)
Dr. Lorenz GUBLER (Group Leader)
Dr. Marcel **H**OFER (Scientist)
Dr. Erik **J**ÄMSTORP-BERG (Post Doctoral Researcher)
Christoph JUNKER (Technician)
Hermann **K**AISER (Technician)
Isabella KALT (Assistant)
Dr. Rüdiger KÖTZ (Group Leader)
Renzo **M**ARCOLONGO (Technician)
Christian MARMY (Technician)
André MEIER (Technician)
Prof. Dr. Petr **N**OVÁK (Section Head)
Dr. Pierre **O**BERHOLZER (Post Doctoral Researcher)
Dr. Mehtap ÖZASLAN (Scientist)
Pia **R**EICHEL (Technician)
Dr. Rosa ROBERT (Scientist)
Dr. Paramaconi RODRIGUEZ-PEREZ (Scientist)
Dr. Jörg ROTH (Scientist)
Dr. Sebastien **S**ALLARD (Scientist)
Dr. Tsuyoshi SASAKI (Scientist)
Prof. Dr. Thomas J. SCHMIDT (Laboratory Head)
Jürg **T**HUT (Technician)
Dr. Sigita **U**RBONAITE (Scientist)
Dr. Claire **V**ILLEVIEILLE (Project Leader)

PhD Students

Tobias **B**INNINGER
Johannes BIESDORF
Peter BLEITH
Yves BUCHMÜLLER
Sebastian **E**BERHARDT
Jens ELLER
Tom ENGL
Jorge **F**ERREIRA DE ARAUJO
Moritz **H**ANTEL
Michael HESS
Kaewta **J**ETSRISUPARB
Stefan **K**REITMEIER
Patrick **L**ANZ
George **N**EOPHYTIDES
Pierre **O**BERHOLZER
Annett **R**ABIS
Sandra **T**EMMEL
Daniel **W**EINGARTH
Zhuoxiang **Z**HANG
Mark ZURBRÜGG

DISSERTATIONS 2012

Dr. Pierre Oberholzer

Analysis of water transport in polymer electrolyte fuel cells using neutron imaging

Ph.D. Thesis No. 20548, ETH Zürich, July 2012.

Examiners: Prof. Dr. A. Wokaun, ETH Zürich
Prof. Dr. J.F. Mesot, PSI Villigen
Dr. G.G. Scherer, PSI Villigen
Dr. P. Boillat, PSI Villigen

Dr. Jens Eller

X-ray tomographic microscopy of polymer electrolyte fuel cells

Ph.D. Thesis No. 20916, ETH Zürich, December 2012.

Examiners: Prof. Dr. A. Wokaun, ETH Zürich
Prof. Dr. M. Stampanoni, ETH Zürich
Prof. Dr. T.J. Schmidt, PSI/Villigen/ETH Zürich
Dr. F.N. Büchi, PSI Villigen

EXCHANGE STUDENTS, DIPLOMA THESES, SUMMER STUDENTS, GUEST SCIENTISTS

Tobias Rapp	*Electrochemical energy conversion for high power densities in microfluidic fuel cells* ETH Zürich, February 2012 (Electrocatalysis and Interfaces).
Sebastian Schmidt	*Development of a concept for measuring peak temperatures in PEFCs using thermochromic colors* ETH Zürich, January - March 2012 (Fuel Cell Systems and Diagnostics).
Simon Tschupp	*Synthesis and characterization of metal nanoparticles of different shape and composition for the electrochemical reduction of CO and CO_2* ETH Zürich, February - July 2012 (Electrocatalysis and Interfaces).
Noh Heeju	*The stability of electrolytes depending on carbon electrodes and temperature change by the new stability criterion* ETH Zürich, February – May 2012 (Electrocatalysis and Interfaces).

Rocco Gaudenzi	*Verbesserung von Befeuchtungskonzept für XTM-Setup von PEFC* ETH Zürich, March – May 2012 (Fuel Cell Systems and Diagnostics).
Urs Cabalzar	*Untersuchung des Kaltstartverhaltens von H2/O2 Brennstoffzellen* ETH Zürich, March – September 2012 (Fuel Cell Systems and Diagnostics).
Tom Fedtke	*Analyse des Wärme- und Massentransports in einer Brennstoffzelle für Röntgentomographie - Aufnahmen mit Hilfe numerischer Simulation* Hochschule Wissmar, Germany, March – September 2012 (Fuel Cell Systems and Diagnostics).
Benjamin Miserere	*Charakterisierung von Membranen in Brennstoffzellentests* Arts et Métiers ParisTech, Metz, France, April – August 2012 (Membranes and Electrochemical Cells).
Regina Hafner	*Fuel cell membranes containing an electronically conducting polymer* ETH Zürich, May – August, 2012 (Membranes and Electrochemical Cells).
Annetta Platek	*Präparation und Charakterisierung von Graphen und/oder Graphitoxid für Doppelschicht-Kondensatoren* Poznan University of Technology, Poland, June – October 2012 (Electrocatalysis and Interfaces).
Justyna Piwek	*Auswertung von Tomographiedaten und Mitarbeit bei Brennstoffzellen-Versuchen im Labor* Poznan University of Technology, Poland June – October 2012 (Fuel Cell Systems and Diagnostics).
Irmgard Weissensteiner	*Unterstützung der BZ-X-Ray Tomographie* Montanuniversität Leoben, Österreich, July – September 2012 (Fuel Cell Systems and Diagnostics).
Iván Garcia Torregrosa	*Investigation of solid polymer electrolyte for Li-S batteries* Université de Picardie Jules Verne, France, July - August 2012 (Battery Materials).
Ivan Gugler	*Untersuchung der Energieflüsse der H2O-Tankstelle in Brugg* EPF Lausanne, July – September 2012 (Fuel Cell Systems and Diagnostics).
Alfredo Iranzo	*Simulation of the impact of water on fuel cell performance based on available neutron imaging data* University of Sevilla, Spain, July – August 2012 (Neutron Radiography).
Susan Taylor	*Characterization of Pt electrocatalysts for oxygen reaction reduction (ORR)* University of Cape Town, South Africa, August – November 2012 (Electrocatalysis and Interfaces).
Lukas Lutz	*Syntheses of Mn-based oxides by a new sol-gel route: materials for positive electrodes in Li-ion batteries* ETH Zürich, September – December 2012 (Battery Materials).
Rhiyaad Mohamed	*Oxygen reduction reaction activity of perovskite oxide in alkaline media* University of Cape Town, South Africa, October – December 2012 (Electrocatalysis and Interfaces).

SEMINAR, INVITED SPEAKERS

Zenonas Jusys, Universität Ulm, Germany	*Development and application of novel techniques in electrocatalysis research* January 09, 2012.
Olaf Conrad, University of Cape Town, South Africa	*HySA - Centres of competence in hydrogen and fuel cell technology in South Africa* March 21, 2012.
Jeffrey S. Allen, Michigan Technological University, USA	*Pore-level of multiphase water and thermal transport in low temperature fuel cells* March 29, 2012.
A.Z. Weber, LBNL Berkeley, USA	*Understanding ionomer-related transport and morphology in polymer-electrolyte fuel cells* April 05, 2012.
Robert Savinell, Western Case University, Cleveland, USA	*Redox-flow cell / HT PEFC based on PBI/PA* May 03, 2012.
Josef Meier, MPI Düsseldorf, Germany	*Ex-situ investigation of fuel cell catalyst stability* September 05, 2012.
Nada Zamel, Fraunhofer ISE, Freiburg, Germany	*Effective properties of PEM fuel cells* September 12, 2012.
Katherina Baber, Universität Stuttgart, Germany	*Water management in PEM fuel cells: A coupling concept for one-phase free flow and two-phase porous-media flow accounting for drop formation at the GDL-GC interface* September 19, 2012.
Masaki Matsui, Mie University, Japan	*Recent update of post Li-ion technologies (Focus on multivalent batteries and aqueous based Li-air batteries)* October 19, 2012.
Gleb Yushin, Georgia Institute of Technology, School of Materials Science and Engineering, Atlanta, USA	*Nanostructured materials for energy storage applications* December 19. 2012.

AWARDS

Marcel Hofer	*Best posters award* High power density PE fuel cell system development based on hydrogen/oxygen International Advanced Mobility Forum, Geneva, March, 7-8, 2012.
Kaewta Jetsrisuparb	*Graduate student award* in recognition of the outstanding paper contributed to Symposium F, Solid Proton Conductors (in honour of Professor G. Alberti) E-MRS 2012 Spring Meeting, Strasbourg, France, May 14-18, 2012.
Claire Villevieille	*Young Investigator Award* 16th Int. Meeting on Lithium Batteries, Jeju, Korea, June 17-22, 2012.
Emiliana Fabbri	*Kepler Prize 2012 for European Young Scientists* European Academy of Sciences (EURASC) Symposium on Future of Science in the 21st Century: Sustainability. Belgium, Liege, October 25-26, 2012.

Marcel Hofer

Kaewta Jetsrisuparb (right)

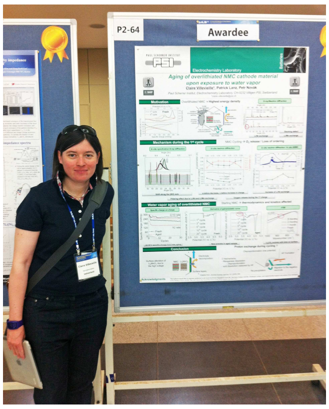
Claire Villevieille

Emiliana Fabbri (3rd from right)

CONFERENCES – SYMPOSIA

ModVal 9
Campus Sursee, April 2-4, 2012.

ModVal 9 is the 9th symposium in the series of annual events initiated by the Swiss Federal Office of Energy in 2004.

The symposium provides a platform for idea exchange encompassing academic institutions as well as industry. ModVal aims at disseminating new results in research, promoting personal contacts, and stimulating new collaborations.

Plenary lectures:

Prof. Gerbrand Ceder, Massachusetts Institute of Technology, USA
Prof. Jürgen Fleig, Technische Universität Wien, Austria
Dr. Michael L. Perry, United Technologies Research Center, USA

Organizers from Paul Scherrer Institut:

Dr. Felix N. Büchi
Dr. Lorenz Gubler
Prof. Petr Novák
Prof. Thomas J. Schmidt

Book of Abstracts: http://dx.doi.org/10.3929/ethz-a-007050000

28th One-Day-Symposium
Paul Scherrer Institut, May 02, 2012.

Electrochemistry for renewable energy storage

Organizers: Thomas J. Schmidt, Rüdiger Kötz, Isabella Kalt

Contributions from:

Daniel Chartouni, ABB Group, Baden-Dättwil
Manfred Waidhas, Siemens, Erlangen, Germany
Sebastian Fiechter, Helmholtz Zentrum, Berlin, Germany
Robert Savinell, Case Western Reserve University, Cleveland, USA
Cord H. Dustmann, Batterie Consult GmbH, Meiringen
Göran Andersson, ETH Zürich

From left to right: Felix Büchi, Sebastian Fiechter, Rüdiger Kötz, Robert Savinell, Andreas Reiner, Lorenz Gubler, Isabella Kalt, Thomas J. Schmidt, Göran Andersson, Daniel Chartouni, Cord H. Dustmann, Petr Novák.

REVIEW ACTIVITIES OF THE LABORATORY

Journals

Accounts of Chemical Research ♦ ACS Catalysis ♦ ACS Applied Materials & Interface ♦ Angewandte Chemie International Edition

Carbon ♦ Chemical Communications

Electrochimica Acta ♦ Electrochemistry Communications ♦ Energy & Environmental Science

Fuel Cells

High Performance Polymers

International Journal of Hydrogen Energy

Journal of the American Chemical Society ♦ Journal of Applied Electrochemistry ♦ Journal of Catalysis ♦ Journal of the Electrochemical Society ♦ Journal of Materials Chemistry of RSC ♦ Journal of Membrane Science ♦ Journal of New Materials for Electrochemical Systems ♦ Journal of Physical Chemistry ♦ Journal of Power Sources ♦ Journal of Solid State Electrochemistry ♦ Journal of Synchotron Radiation

Materials

Nature Materials ♦ Nature Chemistry ♦ Nature Communications ♦

Physical Chemistry Chemical Physics

Science ♦ Solid State Ionics

Organisations

Alexander von Humboldt-Stiftung, Germany

CCEM-CH

ETH Zürich Research Commission

Helmholtz Society, Germany

SNF (Schweizerischer Nationalfonds)

External Dissertations: Review activities

Thomas J. Schmidt :

- J. Durst, Université de Grenoble
- F. Hasché, TU Berlin
- M. Oezaslan, TU Berlin

Felix N. Büchi :

- Zhe Peng, Université Montpellier 2

INDUSTRIAL PARTNERS

The Laboratory had the pleasure to collaborate with the following industrial partners during the year 2012:

BASF SE, Ludwigshafen**,** Germany

Belenos Clean Power Holding, Biel/Bienne

Freudenberg FCCT SE & Co. KG, Fuel Cell Component Technologies, Weinheim, Germany

Heraeus Quarzglas GmbH & Co. KG, Kleinostheim, Germany

IBM Zürich Research Laboratory, Rüschlikon

Liebherr-Aerospace Lindenberg GmbH, Lindenberg, Germany

SolviCore GmbH & Co. KG, Hanau, Germany

TIMCAL SA, Bodio

Umicore AG & Co. KG, Hanau, Germany

DOCUMENTATION

PROJECT COLLABORATIONS WITH EXTERNAL PARTNERS

BFE

F.N. Büchi Projektleiter	*X-ray micro-tomography of polymer electrolyte fuel cells*
F.N. Büchi Projektleiter	*Gasanalysis in polymer electrolyte fuel cells*
L. Gubler Projektleiter	*Lebensdauer-Limitierungen von Brennstoffzellen-Membranen: Mechanismen, Methoden und Innovationen*
P. Novák Projektleiter	*Untersuchung zur Machbarkeit einer Salz-Flow-Batterie* with Battery Consult GmbH, Meiringen
J. Roth Projektleiter	*S_Chain Fundamentals* with ZHAW Winterthur and Belenos Clean Power AG

CCEM

T.J. Schmidt Projektleiter	*DURACAT (Highly durable oxide-based catalysts for polymer electrolyte fuel cells)* with ETH Zürich, CSEM Neuchâtel, University of Southampton UK and Umicore AG & Co. KG

EU

P. Boillat Projektleiter	*H2FC (Integrating European infrastructure to support science and development of hydrogen- and fuel cell technologies towards European strategy for sustainable competitive and secure energy)*
L. Gubler Projektleiter	*NOVEL (Novel materials and system designs for low cost, efficient and durable PEM electrolysers)*
J. Roth Projektleiter	*IMPALA (Improve PEMFC with advanced water management and gas diffusion layers for automotive application)*
R. Kötz Member of MC	*COST Action MP1004 (Hybrid energy storage devices and systems for mobile and stationary applications)*
P. Novák Projektleiter	*MAHEATT (Materials for high energy accumulators in traction and tools)*
T.J. Schmidt Projektleiter	*DEMMEA (Understanding the degradation mechanisms of membrane-electrode-assembly for high temperature PEMFCs and optimization of the individual components)*

Industry

P. Boillat Projektleiter	*Diagnostics of polymer electrolyte fuel cells* Automotive Industry
F.N. Büchi Projektleiter	*Stack and system development* Belenos Clean Power, Biel/Bienne
J.L. Gómez-Cámer Projektleiter	*Graphite für Lithiumionen-Batterien* TIMCAL SA, Bodio

L. Gubler Projektleiter	*Development of components for fuel cells* Belenos Clean Power, Biel/Bienne
P. Novák Projektleiter	*Forschungsnetzwerk „Elektrochemie und Batterien“* BASF SE, Ludwigshafen, Germany
P. Novák Projektleiter	*Projekt HE-Lion (Hochenergie-Lithiumionenbatterien für die Zukunft)* BASF SE, Ludwigshafen, Germany
T.J. Schmidt Projektleiter	*Advanced degradation studies on PBI/H_3PO_4 based MEAs for High Temperature PEFCs* BASF SE, Ludwigshafen, Germany
T.J. Schmidt Projektleiter	*Micro-fluidic redox flow cells* IBM Zürich Research Laboratory, Rüschlikon
S. Urbonaite Projektleiterin	*Spezialkohlenstoffe* Heraeus Quarzglas GmbH & Co. KG, Kleinostheim, Germany

Schweizerischer Nationalfonds

L. Gubler Projektleiter	*Antioxidant strategies for the stabilization of fuel cell membranes against oxidative stress*
L. Gubler Projektleiter (Co-PI)	*Connecting the renewable energy to green mobility using hydrogen as energy carrier under the Belenos Clean Power initiative (GreenPower)* EPFL, CSEM, PSI, Belenos Clean Power
R. Kötz Projektleiter	*Graphite oxides and graphene for electrochemical energy storage* PSI, ETH Zürich
P. Novák Projektleiter	*Synthetic solid electrolyte interphase on carbon electrodes for lithium-ion batteries*
P. Novák Projektleiter	*New oxyphosphates as high specific charge electrode materials for lithium-ion batteries*

TEACHING ACTIVITIES

University Level Teaching

Prof. Dr. P. Novák,	*Elektrochemie* ETH Zürich, HS 2012
Prof. Dr. T.J. Schmidt, Prof. Dr. A. Wokaun, Dr. F: Noembrini	*Renewable Energy Technology II* ETH Zürich, SS 2012
Prof. Dr. T.J. Schmidt, Prof. Dr. M. Quack	*Advanced Kinetics* ETH Zürich, SS 2012

Lecture Courses at Other Schools

Dr. P. Boillat	*Imaging water in fuel cells – introduction to neutron imaging* PSI Summer School on Condensed Matter Research 2012, Zugerberg, August 11-17, 2012.
Dr. P. Oberholzer	*Instrumentation and research at PSI: Imaging of liquid water in operating polymer electrolyte fuel cells* European Technical School on Hydrogen and Fuel Cells 2012, Heraklion, Greece, September 24-28, 2012.

Dr. P. Oberholzer	*Ground breaking research at PSI: Neutron imaging combined with helox pulse analysis in fuel cells* European Technical School on Hydrogen and Fuel Cells 2012, Heraklion, Greece, September 24-28, 2012.

Contributions to Courses at Universities, FHL, and other Institutes

Dr. L. Gubler	*Renewable energy technologies II* ETH Zürich, May 8, 2012

PUBLICATIONS

Books and Reviewed Book Chapters

H.A. Gasteiger[1], V. Ramani[1], F.N. Büchi, A. Weber[1], T. Fuller[1], P. Shirvanian[1], D.C. Hansen[1], K. Shinohara[1], H. Nakagawa[1], M. Edmunson[1], D.J. Jones[1], H. Uchida[1], P. Strasser[1], C. Coutanceau[1], S. Mitsushima[1], R. Mantz[1], K. Swider-Lyons[1], W. Xing[1], T.J. Schmidt (Editors)	*Polymer electrolyte fuel cells 12* ECS Transactions **50** (2012) The Electrochemical Society, Pennington, NJ, USA. ISBN 978-1-62332-001-0; ISSN 1938-6737 (online); ISSN 1938-5862 (print); ISSN 2151-2051 (CD-ROM). [1] external editors
I. Kalt, R. Kötz, G.G. Scherer, T.J. Schmidt	*PSI Electrochemistry Laboratory Annual Report 2011* ISSN 1661-5379 (2012).
I.A. Schneider, M.H. Bayer, S. von Dahlen	*Submillimeter resolved transient techniques for polymer electrolyte membrane fuel cell characterisation: local in situ diagnostics for channel and land areas* doi.org/10.1016/j.jelechem.2012.11.011,Part III, Chapter 12, 351-391, in Polymer Electrolyte Membrane and Direct Methanol Fuel Cell Technology (PEMFCs and DMFCs), Edited by C. Hartnig, C. Roth, Woodhead Publishing Limited, Cambridge, UK (2012), ISBN 978-1-84569-774-7 (2012).
H. Schulenburg, C.R. Roth[1], F. Scheiba[2]	*Advanced microscopy techniques for the characterization of polymer electrolyte membrane fuel cell components* doi.org/10.1016/j.jelechem.2012.11.011,Part I, Chapter 2, 26-60, in Polymer Electrolyte Membrane and Direct Methanol Fuel Cell Technology (PEMFCs and DMFCs), Edited by C. Hartnig, C. Roth, Woodhead Publishing, Cambridge, UK (2012), ISBN 978-1-84569-774-7 (2012). [1] TU Darmstadt, Germany [2] IFW Dresden, Germany
F.N. Büchi, L. Gubler, P. Novák, T.J. Schmidt	*9th Symposium on fuel cell and battery modeling and experimental validation (ModVal 9)* Campus Sursee, April 2-4, 2012. Book of Abstracts: http://dx.doi.org/10.3929/ethz-a-007050000

Peer Reviewed Papers

S. Balog, U. Gasser, K. Mortensen[1], H. Ben youcef, L. Gubler, G.G. Scherer	*Structure of the ion-rich phase in DVB cross-linked graft-copolymer proton-exchange membranes* doi:10.1016/j.polymer.2011.11.023, Polymer **53**, 175-182 (2012). [1] University of Copenhagen, Denmark
M.H Bayer, I.A Schneider	*Dynamic response of a subsaturated polymer electrolyte fuel cell in counterflow mode* doi:10.1002/fuce.201100154, Fuel Cell 12, 320-325 (2012).
M.H Bayer, I.A Schneider	*Application of the Kramers Kronig relations to locally resolved impedance data of polymer electrolyte fuel cells* doi.org/10.1016/j.jelechem.2012.11.011, J. Electroanal. Chem. **689**, 42-45 (2012).

P. Boillat, P. Oberholzer, A. Kaestner, R. Siegrist, E.H. Lehmann, G.G. Scherer, A. Wokaun	*Impact of water on PEFC performance evaluated by neutron imaging combined with pulsed helox operation* doi:10.1149/2.017207jes, J. Electrochem. Soc. 159, F210 (2012).
P. Boillat, P. Oberholzer, F. Neuschütz, T.J. Schmidt, A. Wokaun	*An electrochemical method for high accuracy measurements of water transfer in fuel cells* doi:10.1016/j.elecom.2012.05.019, Electrochem. Commun. **22**, 12 (2012).
D. Cericola, R. Kötz	*Hybridization of rechargeable batteries and electrochemical capacitors: principles and limits* doi:10.1016/j.electacta.2012.03.151, Electrochim. Acta 72, 1-17 (2012).
A. Foelske-Schmitz, A. Peitz, V.A. Guzenko, D. Weingarth, G.G. Scherer, A. Wokaun, R. Kötz	*In situ electrochemical STM study of platinum nanodot arrays on highly oriented pyrolythic graphite prepared by electron beam lithography* doi:10.1016/j.susc.2012.07.040, Surf. Sci. 606, 1922–1933 (2012).
R. Francke[1], D. Cericola, R. Kötz, D. Weingarth, S.R. Waldvogel[1]	*Novel electrolytes for electrochemical double layer capacitors based on 1,1,1,3,3,3-hexafluoroisopropanol* doi:10.1016/j.electacta.2011.12.050, Electrochim. Acta **62**, 372-380 (2012). [1] Mainz University, Mainz, Germany
R. Francke[1], D. Cericola, R. Kötz, S.R. Waldvogel[1]	*Azolylborates for electrochemical double layer capacitor electrolytes* doi:10.1016/j.nimb.2011.08.071, Zeitschrift für Physikalische Chemie **226**, 141-149 (2012). [1] Mainz University, Mainz, Germany
V.A. Godbole, C. Villevieille, H.-H. Sommer, J.-F. Colin, P. Novák	*A structural and electrochemical study of* $Ni_{0.5}TiOPO_4$ *synthesized via modified solution route* doi:10.1016/j.electacta.2012.05.094, Electrochim. Acta **77**, 244-249 (2012).
L. Gubler, W.H. Koppenol[1]	*Kinetic simulation of the chemical stabilization mechanism in fuel cell membranes using cerium and manganese redox couples* doi:10.1149/2.075202jes, J. Electrochem. Soc. **159**, B211-B218 (2012). [1] ETH Zürich
M.M. Hantel, T. Kaspar[1], R. Nesper[1], A. Wokaun, R. Kötz	*Partially reduced graphite oxide as electrode material for electrochemical double layer capacitors* doi:10.1002/chem.201200702, Chem. Eur. J. **18**, 9125–9136 (2012). [1] ETH Zürich
M.M. Hantel, T. Kaspar[1], R. Nesper[1], A. Wokaun, R. Kötz	*Partially reduced graphite oxide as anode for Li-capacitors* doi:10.1149/2.005201eel, ECS Electrochem. Lett. **1**, A1-A3 (2012). [1] ETH Zürich
M.M. Hantel, V. Presser[1], J.K. McDonough[1], G. Feng[2], P.T. Cummings[2], Y. Gogotsi[1], R. Kötz	*In-situ electrochemical dilatometry of onion-like carbon and carbon black* doi:10.1149/2.006212jes, J. Electrochem. Soc. **159,** A1897-A1903 (2012). [1] Drexel University, Pennsylvania, USA [2] Vanderbilt University, Nashville, Tennessee, USA
A. Idhil, C.N. Borca, A. Uldry, N. Zema[1], S. Turchini[1], D. Catone[1], A. Foelske-Schmitz, D. Grolimund, M. Samaras[2]	*The influence of Cr-composition on the local magnetic structure of FeCr alloys* doi:10.1016/j.nimb.2011.08.071, Nuc. Instrum. Methods Phys. Res. Sect. B **284**, 1-5 (2012). [1] CNR, Roma, Italy [2] University of Applied Science, Rapperswil

S. Kreitmeier, G.A. Schuler, A. Wokaun, F.N. Büchi	*Investigation of membrane degradation in polymer electrolyte fuel cells using local gas permeation analysis* doi:10.1016/j.jpowsour.2012.03.071, J. Power Sources **212**, 139-147 (2012).
S. Kreitmeier, M. Michiardi, A. Wokaun, F.N. Büchi	*Factors determining the gas crossover through pinholes in polymer electrolyte fuel cell membranes* doi:10.1016/j.electacta.2012.07.013, Electrochim. Acta **80**, 240-247 (2012).
S. Kreitmeier, A. Wokaun, F.N. Büchi	*Local catalyst support degradation during polymer electrolyte fuel cell start-up and shutdown* doi:10.1149/2.019212jes, J. Electrochem. Soc. **159**, F787-F793 (2012).
N. Linse, G.G. Scherer, A. Wokaun, L. Gubler	*Quantitative analysis of carbon corrosion during fuel cell start-up and shut-down by anode purging* doi:10.1016/j.jpowsour.2012.07.037, J. Power Sources **219**, 240-248 (2012).
P. Oberholzer, P. Boillat, R. Siegrist, A. Kästner, E.H. Lehmann, G.G. Scherer, A. Wokaun	*Simultaneous neutron imaging of six operating PEFCs: experimental set-up and study of the MPL effect* doi:10.1016/j.elecom.2012.03.038, Electrochem. Commun. **20**, 67 (2012).
P. Oberholzer, P. Boillat, R. Siegrist, R. Perego, A. Kästner, E.H. Lehmann, G.G. Scherer, A. Wokaun	*Cold-start of a PEFC visualized with high resolution dynamic in-plane neutron imaging* doi:10.1149/2.085202jes, J. Electrochem. Soc. **159**, B235 (2012).
A. Rabis, P. Rodriguez, T.J. Schmidt	*Electrocatalysis for polymer electrolyte fuel cells: Recent achievements and future challenges* doi:10.1021/cs3000864, ACS Catalysis **2**, 864-890 (2012).
T. Rosén, J. Eller, J. Kang, N.I. Prasianakis, J. Mantzaras, F.N. Büchi	*Saturation Dependent Effective Transport Properties of PEFC Gas Diffusion Layers* doi:10.1149/2.005209jes, J. Electrochem. Soc. **159**, F536-F544 (2012).
J. Roth, J. Eller, F.N. Büchi	*Effects of Synchrotron Radiation on Fuel Cell Materials* doi:10.1149/2.042208jes, J. Electrochem. Soc. **159**, F447-F455 (2012).
H. Schneider, A. Garsuch[1], A. Panchenko[1], O. Gronwald[1], N. Janssen[1], P. Novák	*Influence of different electrode compositions and binder materials on the performance of lithium-sulfur batteries* doi:10.1016/j.jpowsour.2011.12.061, J. Power Sources **205**, 420-425 (2012). [1] BASF SE, Ludwigshafen, Germany
J.O. Schumacher[1], J. Eller, G. Sartoris[1], T. Colinart, B.C. Seyfang	*2+1D modelling of a polymer electrolyte fuel cell with glassy-carbon microstructures* doi:10.1080/13873954.2011.642390, Math. Comp. Model. Dyn. **18**, 355–377 (2012). [1] Institute of Computational Physics, Zurich University of Applied Sciences, Winterthur
B. Schwanitz, A. Rabis, M. Horisberger, G.G. Scherer, T.J. Schmidt	*Sputtered cathodes for polymer electrolyte fuel cells: Insights into potentials, challenges and limitations* doi:10.2533/chimia.2012.110, Chimia **66**, 110–119 (2012).
A.S. Tremsin[1], J.B. McPhate[1], J.V. Vallerga[1], O.H.W. Siegmund[1], W. Bruce Feller[2], E. Lehmann, A. Kaestner, P. Boillat, T. Panzner, U. Filges	*Neutron radiography with sub-15um resolution through event centroiding* doi:10.1016/j.nima.2012.06.005, Nucl. Instr. Meth. A **688**, 32 (2012). [1] University of California at Berkeley, Berkeley, USA [2] NOVA Scientific, Inc., Sturbridge, USA

P. Verma, P. Novák	*Formation of artificial solid electrolyte interphase by grafting for improving Li-ion intercalation and preventing exfoliation of graphite* doi:10.1016/j.carbon.2012.02.019, Carbon **50**, 2599-2614 (2012).
P. Verma, T. Sasaki, P. Novák	*Chemical surface treatments for decreasing irreversible charge loss and preventing exfoliation of graphite in Li-ion batteries* doi:10.1016/j.electacta.2012.03.140, Electrochim. Acta **82**, 233-242 (2012).
S. von Dahlen, I.A. Schneider	*Local flooding phenomena in channeland land areas occurring during dynamicoperation of a PEFC* doi:10.1002/fuce.201200030, Fuel Cells **12**, 1004-1008 (2012).
S. von Dahlen, M.H. Bayer, I.A. Schneider	*Effect of convective channel-to-channel mass flow in a polymer electrolyte fuel cell* doi:10.1016/j.elecom.2011.11.001, Electrochem. Comm. **14**, 55–58 (2012).
F. Wallasch, M. Abele[1], L. Gubler, A. Wokaun, K. Müller[1], G.G. Scherer	*Characterization of radiation grafted polymer films using CP/MAS spectroscopy and confocal Raman microscopy* doi:10.1002/app.36675, J. Appl. Polym. Sci. **125**, 3500-3508 (2012). [1] Universität Stuttgart, Germany; Universitá degli Studi di Trento, Italy
Y. Yamada[1], T. Sasaki, N. Tatsuda[1], D. Weingarth, K. Yano[1], R. Kötz	*A novel model electrode for investigating ion transport inside pores in an electrical double-layer capacitor: monodispered microporous starburst carbon spheres* doi:10.1016/j.electacta.2012.07.064, Electrochim. Acta **81,** 138– 148 (2012). [1] Toyota Central R&D Labs., Nagakute, Japan
D. Weingarth, I. Czekaj, Z. Fei[1], A. Foelske-Schmitz, P.J. Dyson[1], A. Wokaun, R. Kötz	*Electrochemical stability of imidazolium based ionic liquids containing cyano groups in the anion: A cyclic voltammetry, XPS and DFT study* doi:10.1149/2.001207jes, J. Electrochem. Soc. **159**, H611-H615 (2012). [1] EPF, Lausanne
D. Weingarth, A. Foelske-Schmitz, A. Wokaun, R. Kötz	*PTFE bound activated carbon - A quasi-reference electrode for ionic liquids* doi:10.1016/j.elecom.2012.02.040, Electrochem. Commun. **18**, 116–118 (2012).
M. Zaglio, J. Roth, A. Wokaun, J. Mantzaras, F.N. Büchi	*Transient Bi-Domain 1D PEFC Model* doi:10.1149/2.003201eel, ECS Electrochem. Lett. **1**, F1-F3 (2012).

Conference Proceedings / Other Papers

J. Eller, J. Roth, R. Gaudenzi, S. Irvine, F. Marone, M. Stampanoni, A. Wokaun, F.N. Büchi	*Water distribution in GDL near optimal humidification* ECS Trans. **50**, 477-486 (2012).
M. Hofer, J. Bernard, U. Hannesen[1], D. Corson[1], P. Nguyen[1], P. Morey[2], Y. Leuppi[2], J-F. Affolter[2], A. Closset[1], P. Dietrich, F.N. Büchi, R. Gashi[1]	*Hydrogen/oxygen fuel cell system demonstrating high power density and efficiency* Proc. Electric Vehicle Symposium EVS26, Los Angeles, USA, May 6-9 (2012). [1] Belenos Clean Power Holding, Bienne [2] HEIG-VD, Yverdon-les-Bains
S. Kreitmeier, A. Wokaun, F.N. Büchi	*Polymer electrolyte membrane durability - local degradation at pinholes* ECS Trans. **50,** 927-933 (2012).
T.J. Schmidt	*Electrocatalysis in polymer electrolyte fuel cells: From fundamentals to applications* ECS Trans. **45**, 3-14 (2012).

Dissertations

J. Eller	*X-ray tomographic microscopy of polymer electrolyte fuel cells* Ph.D. Thesis, Nr. 20916, ETH Zürich, December 2012.
P. Oberholzer	*Analysis of water transport in polymer electrolyte fuel cells using neutron imaging* Ph.D. Thesis, No. 20548, ETH Zürich, October 2012.

Diploma / Master Theses

T. Fedtke	*Analyse des Wärme- und Massentransports in einer Brennstoffzelle für Röntgentomographie Aufnahmen mit Hilfe numerischer Simulation* PSI Villigen and Hochschule Wissmar, Germany, November 2012.
R. Hafner	*Fuel cell membranes containing an electronically conducting polymer* PSI Villigen, ETH Zürich, August 2012.
T. Rapp	*Electrochemical energy conversion for high power densities in microfluidic fuel cells* PSI Villigen, IBM Rüschlikon, ETH Zürich, February 2012.

Bachelor / Semester Theses

S. Schmidt	*Development of a concept for measuring peak temperatures in PEFCs using thermochromic colors* PSI Villigen, ETH Zürich, March 2012.
H. Ju	*The stability of electrolytes depending on carbon electrodes and temperature change by the new stability criterion* PSI Villigen, ETH Zürich, June 2012.
S. Tschupp	*Synthesis and characterization of metal nanoparticles of different shape and composition for the electrochemical reduction of CO and* CO_2 PSI Villigen, ETH Zürich, July 2012.

TALKS

Invited Talks

F.N. Büchi	*Das Brennstoffzellen-Postauto in Brugg: Funktion und Zukunftsaussichten der Brennstoffzelle* VöV Fachtagung KTBB, Fribourg, November 14, 2012.
F.N. Büchi	*Effizient unterwegs mit Wasserstoff* 13. Automotive Day, Fachtagung SAE, Biel, November 14, 2012.
E. Fabbri	*Oxide-based catalysts for application as cathode materials in polymer electrolyte membrane fuel cells (PEFCs)* Solid State Electrochemistry Workshop, Heidelberg, Germany, July 15-17, 2012
A. Foelske-Schmitz	*XPS studies of ionic liquids for electrochemical energy storage - closing the pressure gap in electrochemistry research* Colloquium, Justus-Liebig-Universität Giessen, Germany, October 25, 2012.
L. Gubler	*Ion-containing membranes for fuel cells* Adolphe Merkle Institute, Marly, September 18, 2012.

M.M. Hantel	*Partially reduced graphite oxide as electrode material for supercapacitors and Li-capacitors* 63th Annual Meeting of ISE, Prague, Czech Republic, August 19-24, 2012.
M.M. Hantel	*In-situ dilatometry study of the activation process of partially reduced graphite oxide (GOpr)* Nanomaterials Seminar, A.J. Drexel Nanotechnology Institute, Philadelphia, USA, March 6, 2012.
R. Kötz	*EC capacitor fundamentals and technology* AABC Europe, Mainz, Germany, June 18-22, 2012.
R. Kötz	*From graphite to graphene - Novel electrode materials for supercapacitors* 63th Annual Meeting of ISE, Prague, Czech Republic, August 19-24, 2012.
S. Kreitmeier	*Pinhole formation and growth in polymer electrolyte membranes for PEFC* Max-Planck-Institut für Eisenforschung GmbH, Düsseldorf, Germany, March 08, 2012.
P. Novák	*Elucidating the reaction mechanism of* $M_{0.5}TiOPO_4$ *electrode materials* 16th Int. Meeting on Lithium Batteries, Jeju, Korea, June 21, 2012.
P. Novák	*Future of lithium batteries* University of Uppsala, Uppsala, Sweden, March 30, 2012.
P. Novák	*Oxygen, nano, and others: future or buzzwords of lithium batteries?* Power our Future 2012 - The 1st International Forum on Progress and Trends in Battery and Capacitor Technologies, Vitoria-Gasteiz, Spain, March 21, 2012.
P. Novák	*In situ studies of battery electrode materials* Gordon Research Conference “Batteries”, Ventura, USA, March 5, 2012.
P. Novák	*The polymer-like solid electrolyte interphase on carbon electrodes in lithium-ion batteries* 14th International Union of Pure and Applied Chemistry Conference on Polymers and Organic Chemistry (POC 2012), Doha, Qatar, January 8, 2012.
T.J. Schmidt	*Electrocatalysis in polymer electrolyte fuel cells: From fundamentals to applications* Tutorials on Electrocatalysis in Low Temperature Fuel Cells 221st ECS Meeting, Seattle, WA, USA, May 7-11, 2012.
T.J. Schmidt, P. Oberholzer, J. Eller, P. Boillat, F.N. Büchi, A. Wokaun, G.G.Scherer	*MEA analysis on different length scales: From centimeters to nanometers* 6th International Fuel Cell Workshop 2012, University of Yamanashi, Yamanashi, Japan, August 01-03, 2012.
T.J. Schmidt, G. Neophytides, F.N. Büchi	*Advanced degradation studies of high temperature PEFCs* 3rd Carisma International Conference, Copenhagen, Denmark, September 3-5, 2012.
T.J. Schmidt	*Advanced fuel cell diagnostics: Catalysts, components, cells* Chemistry Department, University of Copenhagen, Denmark, September 06, 2012.
T.J. Schmidt	*Brennstoffzellen der Zukunft* Swiss Energy and Climate Summit, Bern, September 13-14, 2012.

T.J. Schmidt	*Short course polymer electrolyte fuel cells* 222nd ECS Meeting, Honolulu, HI, USA, October 7-12, 2012.
T.J. Schmidt	*New electrocatalyst systems and old questions: Can we overcome current PEFC catalysis limits?* Workshop Electrocatalysis: Theory Meets Experiment, Reisensburg, Günzburg, Germany, October 28-31, 2012.
T.J. Schmidt	*The fundamentals of PEFC catalysis* Chemical Engineering Department, University of Cape Town, South Africa, November 16, 2012.

Contributed Talks

P. Bleith, C. Villevieille, P. Novák	$M_{0.5}TiOPO_4$ *as high specific charge battery material* Electrochemistry 2012 - Fundamental and Engineering Needs for Sustainable Development, Munich, Germany, September 18, 2012.
P. Boillat, P. Oberholzer, E.H. Lehmann, G.G. Scherer, A. Wokaun	*Determination of the impact of water in fuel cells using neutron imaging and advanced electrochemical methods* MRS Fall Meeting, Boston, USA, November 27, 2012.
P. Boillat, P. Oberholzer, R. Siegrist, A. Kästner, E.H. Lehmann, G.G. Scherer, A. Wokaun	*Towards high accuracy water transfer measurement in differential cells* 9th Symposium on Fuel Cell Modeling and Experimental Validation (MODVAL 9), Sursee, April 4, 2012.
F. N. Büchi, S. Kreitmeier	*Polymer electrolyte membrane durability - local degradation at pinholes* 222nd ECS Meeting, Honolulu, HI, USA, October 7-12, 2012.
J. Eller	*Insight into the 3D water distribution in PEFC gas diffusion layer by in-situ X-ray tomographic microscopy* 9th Symposium on Fuel Cell and Battery Modeling and Experimental Validation (ModVal 9), Sursee, April 2-4, 2012.
E. Fabbri, A. Rabis, A. Foelske, D. Kramer[1], R. Kötz, T.J. Schmidt	*Durable oxide-based catalysts for application as cathode materials in polymer electrolyte membrane fuel cells (PEFCs)* 222nd ECS Meeting, Honolulu, HI, USA, October 7-12, 2012. [1] University of Southampton, UK
E. Fabbri, A. Rabis, A. Foelske-Schmitz, R. Kötz, T.J. Schmidt	*Oxide semiconductor-based catalysts for application as cathode materials in polymer electrolyte fuel cells (PEFCs)* MRS Fall Meeting, Boston, MA, USA, November 25-30, 2012.
A. Foelske-Schmitz, D. Weingarth, A. Wokaun, R. Kötz	*Reliable binding energies of ionic liquids: monitoring charging by in situ electrochemical XPS* Bunsentagung 2012, Leipzig, Germany, May 17-19, 2012.
A. Foelske-Schmitz, D. Weingarth, A. Wokaun, R. Kötz	*X-ray photoelectron spectroscopy studies on ionic liquid electrolytes - from post mortem to in situ electrochemical XPS* Electrochemistry 2012, Munich, Germany, September 17-19, 2012.
L. Gubler, K. Jetsrisuparb, Y. Buchmüller, Z. Zhang, L. Bonorand	*Insights into the degradation mechanism of radiation grafted fuel cell membranes* Characterization and quantification of MEA degradation processes, Grenoble, France, September 26-27, 2012.
L. Gubler, K. Jetsrisuparb, Z. Zhang, L. Bonorand	*Polymer design aspects of radiation grafted fuel cell membranes* XIII International Symposium on Polymer Electrolytes (ISPE-13), Selfoss, Iceland, August 26-31, 2012.
L. Gubler, W.H. Koppenol	*Pulse radiolysis: a tool for studying radical attack on fuel cell membrane materials* 10th Meeting of the Ionizing Radiation and Polymers Symposium (IRaP'2012), Cracow, Poland, October 14-19, 2012.

M. Heß, D. Cogswell[1], M.Z. Bazant[1], P. Novák	*Modeling of the staging phenomena and elastic energy in graphite for lithium-ion batteries* 9th Symposium on Fuel Cell and Battery Modeling and Experimental Validation (ModVal 9), Campus Sursee, April 4, 2012. [1] MIT, Cambridge, MA, USA
M. Hofer	*Hydrogen/oxygen fuel cell system demonstrating high power density and efficiency* Electric Vehicle Symposium, EVS26, Los Angeles, USA, May 6-9, 2012.
K. Jetsrisuparb, Z. Zhang, H. Ben youcef, G.G. Scherer, A. Wokaun, L. Gubler	*Synthesis and properties of chemically modified membranes by radiation co-grafting of styrene and methacrylonitrile* E-MRS 2012 Spring Meeting, Strasbourg, France, May 14-18, 2012.
S. Kreitmeier	*Polymer electrolyte membrane durability - local degradation at pinholes* 222nd ECS Meeting, Honolulu, HI, USA, October 7-12, 2012.
S. Kreitmeier	*Local catalyst support corrosion during PEFC start and stop* 9th Symposium on Fuel Cell and Battery Modeling and Experimental Validation, Sursee, April 8-9, 2012.
W. Liu[1], A. Rabis, A. Foelske, R. Kötz, J. Yuan[1], A.K. Herrmann[1], P. Rodriguez, A. Eychmüller[1], T.J. Schmidt	*PtPd aerogels as a new class of high surface area catalysts towards oxygen reduction* 222nd ECS Meeting, Honolulu, HI, USA, October 7-12, 2012. [1] TU Dresden, Germany
F.C.F. Mornaghini[1], P. Ulmann[1], D. Cericola[1], T. Hucke[1], M.E. Spahr[1], J.L. Gómez Cámer, P. Novák	*Carbon conductive additives and their influence on the performance of lithium-ion battery electrodes* IBA Pacific Power Source Symposium, Waikoloa, Hawaii, USA, January 10, 2012. [1] TIMCAL SA, Bodio
G. Neophytides, F.N. Büchi, T.J. Schmidt	*Investigation of degradation aspects of High Temperature PEFC MEAs with along the channel locally resolved measurements* 63rd ISE Annual Satellite Meeting, Český Krumlov, Czech Republic, August 26-29, 2012.
P. Oberholzer, P. Boillat, R. Siegrist, A. Kästner, E.H. Lehmann, G.G. Scherer, A. Wokaun	*Simultaneous neutron imaging of 6 cells: set-up and results (MPL study)* 9th Symposium on Fuel Cell Modeling and Experimental Validation (MODVAL 9), Sursee, April 4, 2012.
A. Rabis, M. Horisberger, E. Fabbri, R. Kötz, T.J. Schmidt	*Tin oxide as support material for Pt-based electrocatalysts in PEFCs with improved durability* 63th ISE Annual Meeting, Prague, Czech Republic, August 19-24, 2012.
A. Rabis, B. Schwanitz, M. Horisberger, G.G. Scherer, T.J. Schmidt	*Pt-Electrocatalysts: From nanoparticles to extended surfaces* MRS Fall Meeting, Boston, MA, November 25-30, 2012.
P. Rodriguez, W. Liu, A. Rabis, A. Foelske, R. Kötz, J. Yuan[1], A.K. Herrmann[1], A. Eychmüller[1], T.J. Schmidt	*PtPd aerogels as a new class of high surface area catalysts towards oxygen reduction* Swiss Chemical Society Fall Meeting Zürich 2012, September 13, 2012. [1] TU Dresden, Germany
J. Roth	*Effects of gas flow rate on the water distribution in the cathode GDL of a PEFC: an in-situ x-ray tomographic microscopy study* 9th Symposium on Fuel Cell and Battery Modeling and Experimental Validation, Sursee, April 8-9, 2012.
T. Sasaki, Y. Ukyo[1], P. Novák	*An unknown memory effect of* $LiFePO_4$ 16th Int. Meeting on Lithium Batteries, Jeju, Korea, June 21, 2012. [1] Toyota Central R&D Labs., Nagakute, Japan

T. Sasaki, Y. Ukyo[1], P. Novák

An unknown memory effect of $LiFePO_4$ as the positive electrode for Li-ion batteries
53rd Battery Symposium in Japan, Fukuoka, Japan, November 15, 2012.
[1] Toyota Central R&D Labs., Nagakute, Japan

T. Sasaki, C Villevieille,
M. Heß, Y. Ukyo[1], P. Novák

Detection of a solid solution in $LiFePO_4$-$FePO_4$ by an in situ method
53rd Battery Symposium in Japan, Fukuoka, Japan, November 15, 2012.
[1] Toyota Central R&D Labs., Nagakute, Japan

O. Waser[1], A. Güntner[1],
M. Heß, P. Novák,
S.E. Pratsinis[1]

Size controlled flame synthesis of CuO nanoparticles for Li-ion batteries
European Aerosol Conference EAC 2012, Granada, Spain, September 4, 2012.
[1] ETH Zürich

D. Weingarth, A. Foelske-Schmitz, A. Wokaun, R. Kötz

PTFE bound activated carbon – A quasi reference electrode for ionic liquids and its application
ECS 12 - Pacific RIM Meeting on electrochemical and solid-state science, Honolulu, USA, October 7-12, 2012.

Z. Zhang, K. Jetsrisuparb,
A. Wokaun, L. Gubler

In situ characterization of styrene-based radiation grafted membranes with nitrile groups in the fuel cell
Characterization and quantification of MEA degradation processes, Grenoble, France, September 26-27, 2012.

PATENT APPLICATIONS

J. Roth

A method for recovering metal and/or metal compounds which are bound in polymer material
Patent Application No. EP12151609, 2011.

T.J. Schmidt, P. Rodriguez,
A. Rabis, A. Foelske, R. Kötz,
A. Eychmüller[1], W. Liu[1],
J. Yuan[1], N. Gaponik[1],
A.-K. Herrmann[1]

Hochoberflächiger trägerloser Katalysator für elektrochemische Prozesse und Verfahren zu seiner Herstellung
Patent Application No. EP12177908.6, 2012.
[1] TU Dresden, Germany

POSTERS

M. Hofer, J. Bernard,
U. Hannesen[1], D. Corson[1],
P. Nguyen[1], P. Morey[2],
Y. Leuppi[2], J-F Affolter[2],
A. Closset[1], P. Dietrich,
F.N. Büchi, R. Gashi[1]

High power density PE fuel cell system development based on hydrogen/oxygen
International Advanced Mobility Forum 2012, Geneva, March 7-8, 2012.
[1] Belenos Clean Power Holding, Biel/Bienne
[2] HEIG-VD, Yverdon-les-bains

S. Pérez-Villar, H. Schneider,
P. Novák

In situ FTIR microscopy vs. conventional in situ FTIR spectroscopy: impact of VC on the SEI film in li-ion batteries
The 1st International Forum on Progress and Trends in Battery and Capacitor Technologies, Vitoria-Gasteiz, Spain, March 21, 2012.

G. Neophytides, T.J. Schmidt,
F.N. Büchi, I.A. Schneider

Along the channel locally resolved measurements of high temperature PEFC MEAs
9th Symposium on Fuel Cell and Battery Modeling and Experimental Validation (ModVal 9), Sursee, April 2-4, 2012.

L. Bonorand, P. Reichel,
J. Thut, L. Gubler,
G.G. Scherer, Y. Leterrier,
J. Thivolle, F. Oliveira,
J.-A. E. Månson

Novel high performing fuel cell membranes based on fluorinated polymers
Nano-Tera Annual Plenary Meeting, Zürich, April 26, 2012.

J. Eller, J. Roth, F. Marone, M. Stampanoni, A. Wokaun, F.N. Büchi	*Insight into the 3D water distribution in PEFC gas diffusion layer by In-situ X-ray tomographic microscopy* 28 th One-Day-Symposium Electrochemistry Laboratory, PSI Villigen, May 2nd, 2012.
P. Lanz, C. Villevieille, P. Novák	*In situ raman microscopy of* $Li_2MnO_3{\cdot}Li(Mn_xNi_yCo_z)O_2$ *electrodes for lithium-ion cells* E-MRS 2012 Spring Meeting, Strasbourg, France, May 14-18, 2012.
D. Weingarth, A. Foelske-Schmitz, A. Wokaun, R. Kötz	*Electrochemical stability limits of ionic liquids: Facing the reference problem* Bunsentagung, Leipzig, Germany, May 17-19, 2012.
D. Cericola, F. C. F. Mornaghini, P. Ulmann, Th. Hucke, J. L. Gómez-Cámer, P. Novák, M. E. Spahr	*Effect of carbon conductive additives and conductive coatings on the impedance of lithium-ion battery electrodes* 16 th Int. Meeting on Lithium Batteries, Extended Abstracts, Jeju, Korea, June 21, 2012.
M. Heß, P. Novák	*Kinetics of thin graphite layers during lithium intercalation* 16 th Int. Meeting on Lithium Batteries, Extended Abstracts, Jeju, Korea, June 21, 2012.
T. Sasaki, Y. Ukyo, P. Novák	*An unknown memory effect of* $LiFePO_4$ 16 th Int. Meeting on Lithium Batteries, Extended Abstracts, Jeju, Korea, June 21, 2012.
H. Sommer, K. Leitner, A. Kaestner, E. Lehmann, P. Novák	*Neutron Imaging into an operating lithium-ion battery* 16 th Int. Meeting on Lithium Batteries, Extended Abstracts, Jeju, Korea, June 21, 2012.
C. Villevieille, P. Novák	*Aging of overlithiated NMC cathode material upon exposure to water vapor* 16 th Int. Meeting on Lithium Batteries, Extended Abstracts, Jeju, Korea, June 21, 2012.
J. Roth, J. Eller, F.N. Büchi	*Reproducibility of the Water Distribution in Porous Structures of Polymer Electrolyte Fuel Cells* Gordon Research Conference, Les Diablerets, June 24-29, 2012.
P. Bleith, C. Villevieille, P. Lanz, P. Novák	*Structural investigations of* $Li_2MnO_3\ Li(Ni_xCo_yMn_z)O_2$ *Neutron diffraction, in situ X-ray diffraction and in situ Raman spectroscopy* 3rd Workshop on the Simultaneous Combination of Spectroscopies with X-ray Absorption, Scattering and Diffraction Techniques, Zurich July 5, 2012.
J. Eller, J. Roth, R. Gaudenzi, S. Irvine, F. Marone, M. Stampanoni, A. Wokaun, F.N. Büchi	*Permeability of the liquid water phase in GDL near optimal humidification* Gordon Research Conference on Fuel Cells, Smithfield RI, USA, August 5-10, 2012.
J. L. Gómez-Cámer, F. Mornaghini, D. Cericola, P. Ulmann, T. Hucke, M. E. Spahr, P. Novák	*Lithium-bismuth alloy as a reference electrode for electrochemical impedance spectroscopy* 63rd Annual Meeting of the International Society of Electrochemistry, Prague, Czech Republic, August 19-24, 2012.
Z. Zhang, K. Jetsrisuparb, A. Wokaun, L. Gubler	*Performance and degradation of radiation grafted poly(styrene sulfonic acid-co-methacrylonitrile) membranes in the fuel cell* 63rd Annual Meeting of the International Society of Electrochemistry, Prague, Czech Republic, August 19-24, 2012.
O. Waser, A. Güntner, M. Heß, P. Novák, S. E. Pratsinis	*Size controlled flame synthesis of CuO nanoparticles for li-ion batteries* European Aerosol Conference EAC 2012, Granada, Spain, September 2-7, 2012.

A. Rabis, E. Fabbri, R. Kötz, T.J. Schmidt	*Potential of tin oxide-based support materials for durable cathode catalysts in PEFCs* Swiss Chemical Society (SCS) Fall Meeting, ETH Zürich, September 13, 2012.
M. J. Schmid, K. R. Bickel, H. Sommer, P. Novák, R. Schuster	*Microcalorimetric studies on the electrochemical lithium bulk deposition and intercalation in graphite* Electrochemistry 2012 - Fundamental and Engineering Needs for Sustainable Development, Munich, Germany, September 18, 2012.
H. Sommer, K. Leitner, A. Kaestner, E. Lehmann, P. Novák	*Neutron imaging into an operating lithium-ion battery* Electrochemistry 2012 - Fundamental and Engineering Needs for Sustainable Development, Munich, Germany, September 18, 2012.
S. Urbonaite, A. Garsuch, P. Novák	*Lithium-sulfur battery development* 222nd ECS Meeting, Honolulu, Hawaii, USA, October 7-12, 2012.
Y. Buchmüller, G.G. Scherer, A. Wokaun, L. Gubler	*Mechanistic studies on grafting of glycidyl methacrylate (GMA) and styrene onto poly(ethylene-alt-tetrafluoroethylene) (ETFE)* 10th Meeting of the Ionizing Radiation and Polymers Symposium (IRaP’2012), Cracow, Poland, October 14-19, 2012.

CONFERENCES & WORKSHOPS ORGANIZATIONS

F.N. Büchi, L. Gubler, P. Novák, T.J. Schmidt	*9th Symposium on fuel cell and battery modeling and experimental validation (ModVal 9)* Campus Sursee, April 2-4, 2012. Organizing Committee
F.N. Büchi, T.J. Schmidt, H.A. Gasteiger[1], A.Weber[1], E. Cho[1], C. Coutanceau[1], M. Edmundson[1], T.F. Fuller[1], D.C. Hansen[1], D.J. Jones[1], R.A. Mantz[1], S. Mitsushima[1], H. Nakagawa[1], S. Narayanan[1], V. Ramani[1], K. Shinohara[1], P. Shirvanian[1], P. Strasser[1], K. Swider-Lyons[1], Y. Tak[1], H. Uchida[1], W. Xing[1], L. Zhung[1]	*Polymer electrolyte fuel cells 12 (PEFC 12)* 222nd ECS Meeting, Honolulu, Hawaii, USA, October 7-12, 2012. [1] Co-Organizers
P. Novák	*16th Int. meeting on lithium batteries* Jeju, Korea, June 17-22, 2012. Member of Scientific Committee
T.J. Schmidt, M. Arenz[1], V.R. Stamenkovic[1], S. Mitsushima[1]	*Electrocatalysis and interfacial electrochemistry for energy conversion and storage* MRS Fall Meeting, Boston, MA, USA, November 25-30, 2012. Lead Organizer [1] Co-Organizers

MEMBERS IN EXTERNAL COMMITTEES

R. Kötz	*Electrochimica Acta* Associate Editor
P. Novák	*Int. Meetings on Lithium Batteries LLC* Director & Chair of the Organization Subcommittee

PAUL SCHERRER INSTITUT

Paul Scherrer Institut, 5232 Villigen PSI, Switzerland
Tel. +41 56 310 21 11, Fax +41 56 310 21 99
www.psi.ch